STUDIES ON THE PROPERTIES OF NANOSTRUCTURED NICKEL TUNGSTATE

Thesis submitted to Mahatma GandhiUniversity in
partial fulfilment of the requirements for the degree of
DOCTOR OF PHILOSOPHY IN PHYSICS
Under the Faculty of Science

By

Hitha H

Under the supervision of

Dr. Thomas Varghese

DEPARTMENT OF PHYSICS
NEWMAN COLLEGE, THODUPUZHA

March 2021

MAHATMA GANDHI UNIVERSITY

CERTIFICATE ON PLAGIARISM CHECK

1.	Name of the Research Scholar	**HITHA H**
2.	Title of the Thesis/Dissertation	Studies on the Properties of Nanostructured Nickel Tungstate
3.	Name of the Supervisors	Dr. Thomas Varghese
4.	Department/Institution/ Research Centre	Department of Physics Newman College, Thodupuzha
5.	Similar Content (%) identified	**1 % (One)**
6.	Acceptable Maximum Limit	25%
7.	Software Used	Urkund
8.	Date of Verification	10-03-2021

**Report on plagiarism check, items with % of similarity is attached*

Checked by (with Name, Designation & Signature) :

Mini G Pillai
10/03/2021

MINI G PILLAI
DEPUTY LIBRARIAN
MAHATMA GANDHI UNIVERSITY LIBRARY
KOTTAYAM - 686 560

10/3/21

Name & Signature of the Researcher : Hitha H

Name & Signature of the Supervisor : Dr. Thomas Varghese

Dr. THOMAS VARGHESE
RESEARCH GUIDE
DEPT. OF PHYSICS
NEWMAN COLLEGE
THODUPUZHA-685585

Name & Signature of the HoD/ HoI (Chairperson of the Doctoral Committee) :

DR. THOMSON JOSEPH
PRINCIPAL-IN-CHARGE
NEWMAN COLLEGE
THODUPUZHA

URKUND

Urkund Analysis Result

Analysed Document:	Hitha H - Studies on the Properties of Nanostructured Nickel Tungstate.pdf (D97804993)
Submitted:	3/10/2021 7:41:00 AM
Submitted By:	library@mgu.ac.in
Significance:	1 %

Sources included in the report:

https://bmcchem.biomedcentral.com/articles/10.1186/1752-153X-7-80
https://www.sciencedirect.com/science/article/pii/S1381116905007922
https://www.researchgate.net/publication/319505492_Photocatalytic_and_antibacterial_studies_of_indium-doped_ZnO_nanoparticles_synthesized_by_co-precipitation_technique
https://www.researchgate.net/publication/322179135_Synthesis_and_enhanced_photocatalytic_property_of_Ni_doped_ZnS_nanoparticles
https://www.researchgate.net/publication/255748282_Hydrothermal_synthesis_characterization_and_optical_properties_of_wolframite_ZnWO4_nanorods
https://www.researchgate.net/publication/267870540_Effect_of_8_MeV_electron_beam_irradiation_on_the_structural_and_optical_properties_of_CeO2_nanoparticles
https://www.researchgate.net/publication/302484237_Synthesis_structural_and_optical_properties_of_pure_ZnO_and_Co_doped_ZnO_nanoparticles_prepared_by_the_co-precipitation_method
https://www.researchgate.net/publication/269040150_Influence_of_Cu_doping_on_the_structural_electrical_and_optical_properties_of_ZnO
https://www.ias.ac.in/public/Volumes/boms/042/04/0141.pdf
https://www.researchgate.net/publication/319287265_Structural_Optical_and_Dielectric_Properties_of_Transition_Metal_MFe_2_O_4_M_Co_Ni_and_Zn_Nanoferrites

Instances where selected sources appear:

20

10/3/21

Mini G Pillai
10/03/2021

MINI G PILLAI
DEPUTY LIBRARIAN
MAHATMA GANDHI UNIVERSITY LIBRARY
KOTTAYAM - 686 560

Dr. Thomas Varghese
Associate Professor
Department of Physics
Nirmala College, Muvattupuzha
www.nsrc.in
Email :tv@nirmalacollege.ac.in

Certificate

This is to certify that the thesis entitled **"Studies on the Properties of Nanostructured Nickel Tungstate"** is an authentic record of the original research work carried out by **Ms. Hitha H** in the Research Department of Physics, Newman College, Thodupuzha, under my guidance in partial fulfilment of the requirements for the award of the degree of Doctor of Philosophy under the faculty of science of Mahatma Gandhi University, Kottayam. The work presented in this thesis has not been submitted for any other degree or diploma earlier. It is also certified that **Ms. Hitha H** has fulfilled the course requirements for the Ph.D degree of the University.

Muvattupuzha
12-03-2021

Dr. Thomas Varghese
(Supervising teacher)

Dr.THOMAS VARGHESE
RESEARCH GUIDE
DEPT. OF PHYSICS
NEWMAN COLLEGE
THODUPUZHA-685588

DECLARATION

I hereby declare that the present work entitled ***"Studies on the Properties of Nanostructured Nickel Tungstate"*** *is a bonafide report of the original research work done by me under the supervision of Dr. Thomas Varghese, in the Department of Physics, Newman College, Thodupuzha, Kerala in partial fulfilment of the requirements for the degree of Doctor of Philosophy in physics. Also, this thesis or any part thereof has not been previously formed the basis for the award of any degree or diploma of any other University or Institution.*

Thodupuzha **Hitha H**

28-07-2021

ACKNOWLEDGEMENT

I take this opportunity to convey my heartfelt gratitude to various persons who extended their whole-hearted support and help during the period of my research work. First and foremost I thank God Almighty for his blessings bestowed upon me in the accomplishment of this research work.

I wish to express my deep gratitude and profound thanks to Dr. Thomas Varghese, my guide, for his excellent guidance and invaluable support without which I could not have completed this work successfully.

I am grateful to the Principal and faculty members of the Department of Physics, Newman College, Thodupuzha with a special mention to Dr. Joe Jacob, HOD, Research co-ordinator for all the help rendered.

I would like to thank all the members of the NSRC family, who helped me in my struggle to complete my Ph.D. I thank Dr.Aloysius Sabu, Dr.Priyanka, Dr.Babitha K.K, Dr.Sreedevi A, Dr. Sheena P.A, Seenamol Stephen, Francis Xavier, Anjali Jose, SoumyaKuriakose and Mathew John for their helpful feedbacks, co-operation and support. I remember with sincere gratitude the aid rendered by Mohammed, former student of Nirmala College.

I express my heartfelt gratitude to Principal and faculty members of Department of Physics, Nirmala College, Muvattupuzha for all the facilities provided to carry out my research work. I remember Dr.Jaseentha O.P and Soba teacher for their help, support and inspiration.

I acknowledge SAIF, Kochi, Department of Physics M.G. University, SAIF MG University, Department of Physics CUSAT, IIT Madras, STIC Cusat, S.B College Changanacherry for various experimental measurements.

I also take this opportunity to thank all my teachers for inspiring and motivating me. I owe my special thanks to my friends Neetu and Sharanya for being there for me in all my harsh times.

I express my heartfelt gratitude to my parents. They have always been there as a source of encouragement and moral support and whose love and prayers made me to complete my work successfully. I would like to acknowledge with gratitude the support and love of my family members during the crucial phase of my life. I am deeply indebted to my husband Adv. Ashok Kumar T. R and my daughter Anwitha Ashok Kumar for their immense understanding and support during the research period that helped me to complete the research work successfully. I thank everybody who has helped me in making this thesis possible.

Hitha H

Dedicated to

Kannettan and Molu

CONTENTS

Chapter 3: EFFECT OF CALCINATION TEMPERATURE ON THE PROPERTIES OF NANOPHASE $NiWO_4$ 35-74

Chapter 4: EFFECT OF COBALT DOPING ON THE PROPERTIES OF $NiWO_4$ NANOPARTICLES 75-112

Chapter 6: THERMAL, STRUCTURAL, OPTICAL, MAGNETIC AND ELECTRICAL PROPERTIES OF NiWO$_4$/SnPc NANOCOMPOSITES................151-184

Chapter 7: PHOTOCATALYTIC ACTIVITY OF NIWO$_4$, ITS DOPED AND COMPOSITE FORMS..185-198

PREFACE

The effective generation of mixed metal oxide nanomaterials has found tremendous importance due to their wide applications in interdisciplinary fields. Among the various mixed metal oxides, the transition metal tungstates with the formula MWO_4 have attracted much attention due to their unique properties.In the group of MWO_4, nickel tungstate ($NiWO_4$) is an important inorganic salt due to its appropriate potential for application in various fields of industries, such as catalystsand humidity sensors, microwave devices, photoanodes, optical fibre and scintillator materials.

Various studies reportthe synthesis and characterization of $NiWO_4$ nanoparticles. The effect of calcination on the properties of $NiWO_4$ nanoparticles is important to know the structural details of the $NiWO_4$ sample. Reports on the influence of cobalt doping on the structural, optical, electrical and magnetic properties of $NiWO_4$ nanoparticles are sparse. Also, no studies have been reported on the structural, optical, electrical and magnetic properties of bismuth-doped $NiWO_4$ and $NiWO_4$/ Sn Pcnanocomposites. Hence, more extensive and systematic studies of Bi-doped $NiWO_4$ nanoparticles and nanocompositeare needed. The photocatalytic activities of the $NiWO_4$ nanoparticles under UV irradiation are reported. Very low degradation efficiency is seen in most cases due to its wide bandgap. So tuning of the bandgap and improving the photocatalytic activity is a major concern.

The work presented in this thesis comprises the analysis of the properties of pure nickel tungstate, its doped and composite forms. Along with that, the photocatalytic activity of the samples are also studied.

The thesis entitled **“Studies onthe Properties of Nanostructured Nickel Tungstate”** is organized into eight chapters. Chapter 1 contains the introduction, literature survey, statement of the research problem, objectives and scope of the present study. Chapter 2 discuss the various characterization techniques used for the analysis of the materials. The effect of calcination temperature on different properties of nanocrystalline $NiWO_4$ is discussed in chapter 3.

Chapter 4 and 5 describe the effect of cobalt and bismuth doping in $NiWO_4$ respectively. Structural, optical, magnetic and electrical properties of $NiWO_4$ are varied by doping with these elements. Improvement of conductivity by doping are also discussed in these chapters.

The formation of $NiWO_4$/SnPc composite and their properties are analysed in chapter 6. Chapter 7 deals with the photocatalytic activity of nickel tungstate samples. The conclusions drawn based on systematic analysis are summarized in Chapter 8 and the scope for future work in this field is indicated at the end of this chapter.

Most of these results and discussion have been published/ communicated in peer reviewed national/international journals.

PUBLICATIONS

1. Influence of Bi^{3+} doping on structural, optical and photocatalytic degradation properties of NiWO4 nanocrystals, **Hitha H**, Mathew John, Anjaly Jose, SoumyaKuriakose, Thomas Varghese, ***Journal of Solid State Chemistry***(Elsevier)295 (2021) 121892.
2. Effect of Bi^{3+} substitution on structural and electrical properties of polycrystalline $NiWO_4$ nanoparticles, **Hitha H**, Mathew John, Anjaly Jose, SoumyaKuriakose, Thomas Varghese, ***Journal of Materials Science: Materials in Electronics*** (Springer), October 2020, DOI: 10.1007/s10854-020-04630-x
3. Structural modifications, and extended optical properties of $Ni_{1-x}Co_xWO_4$ nanoparticles, **Hitha H**, Mathew John, Anjaly Jose, SoumyaKuriakose, Thomas Varghese, ***Journal of Solid State Chemistry*** (Elsevier) 290, 121546 (2020) https://doi.org/10.1016/j.jssc.2020.121546
4. Structural and optical modification of $NiWO_4$ – Formation of NiWO4/SnPcnanocomposite for improved photocatalytic activity, **Hitha H**, Anjaly Jose, Mathew John, Thomas Varghese, ***Materials Chemistry and Physics*** (Elsevier) (2019); DOI:https://doi.org/10.1016/ j.matchemphys.2019.122080
5. *Structural, optical and magnetic properties of nanophase $NiWO_4$ for potential applications,* **Hitha H**, Anjali Jose, A. Sreedevi, K.P. Priyanka and Thomas Varghese, ***European Physical Journal B*** (Springer). 2018 (DOI:10.1140/epjb/e2018-90382-3)
6. Dependence of Dielectric Parameters and AC Conductivity on Frequency in Polycrystalline NiWO4, **Hitha H**, SoumyaKuriakose, Mathew John, Anjaly Jose and Thomas Varghese, ***AIP Conf. Proc.*** 2263, 050005 (2020); https://doi.org/10.1063/5.0016852

7. Synthesis, characterization and photocatalytic activity of $NiWO_4$ nanoparticles, **Hitha H**, Anjaly Jose, Thomas Varghese,***AIP Conference Proceedings*** 2082, 030017 (2019); https://doi.org/10.1063/1.5093835

Papers Published Other Than This Work

1. Influence of finite size and surface effects on the structural, electrical and magnetic properties of nanostructured nickel oxide, Sheena PA, **Hitha H**, Sreedevi A, Thomas Varghese, ***Journal of Materials Science: Materials in Electronics*** (Springer) 31, 5769–5778 (2020); DOI: 10.1007/s10854-020-03147-7
2. Synthesis and Characterization of $La_2(WO_4)_3$Nanophosphors via Chemical Precipitation Method, SoumyaKuriakose, **Hitha H**, Anjaly Jose, Mathew John,Thomas Varghese, ***AIP Conf. Proc.*** 2263, 060001 (2020); https://doi.org/10.1063/5.0016855
3. Structural and optical characterization of lanthanum tungstate nanoparticles synthesized by chemical precipitation route and their photocatalytic activity, SoumyaKuriakose, **Hitha H**, Anjali Jose, Mathew John, Thomas Varghse,***OpticalMaterials*** (Elsevier)(2019); https://doi.org/10.1016/j.optmat.2019.109571
4. Microstructural characterization and modified spectral response of cobalt doped NiO nanoparticles, Sheena PA, **Hitha H**, Sreedevi A, Thomas Varghese, ***Materials Chemistry and Physics*** (Elsevier) (2019); DOI: 10.1016/j.matchemphys.2019.03.033
5. Synthesis and characterization of iron cerium tungstate nanoparticles and their dielectric studies, Anjaly Jose,Aneesh George, Shinju Benny, **Hitha H**, Thomas Varghese,***AIP Conference Proceedings***2082, 030005 (2019); https://doi.org/10.1063/1.5093823

6. **CeO_2/CoPcNanocomposite for Potential Applications in Electronics***,* K. K. Babitha, K. P. Priyanka,**Hitha H**, S. Rintu Mary, E. M. Mohammed, S. Sankararaman& Thomas Varghese,***Journal of Electronic Materials*** (Springer), 2017; DOI 10.1007/s11664-017-5653-z

Presentations

1. Dependence of dielectric parameters and AC conductivity on frequency in polycrystalline $NiWO_4$, **Hitha H**, SoumyaKuriakose, Mathew John, Anjaly Jose and Thomas Varghese, Rusa sponsored International conference on Science and Technology of advanced materials (STAM 20)14-16 January 2020 held at Marathanasius College, Kothamangalam.
2. Synthesis, characterization and photocatalytic activity of $NiWO_4$ nanoparticles, **Hitha H**, Anjaly Jose, Thomas Varghese, International conference on Optoelectronic and Nano Materials for advanced technology (icOnMAT 2019) held during 3-5 January, 2019 at Cochin University of Science and Technology.

LIST OF FIGURES

Fig. No.	Caption	Page No.

Fig. No.	**Caption**	**Page No.**

LIST OF TABLES

Table. No.	Title	Page No.

Table. No. Title Page No.

LIST OF ABBREVIATIONS

BQ	:	Benzoquinone
CIE	:	International Commission on Illumination (CommissionInternationale de l'Eclairage)
CPE	:	Constant phase element
DTA	:	Differential Thermal Analysis
DTG	:	Differential Thermo Gravimetry
EDS	:	Energy Dispersive X-ray Spectroscopy
FT-IR	:	Fourier Transform Infrared Spectroscopy
FWHM	:	Full Width at Half Maximum
HRTEM	:	High Resolution Transmission Electron Microscopy
Hz	:	Hertz
IPA	:	Isopropyl alcohol
JCPDS	:	Joint Committee on Powder Diffraction Standards
nm	:	Nanometer
MB	:	Methylene blue
PL	:	Photoluminescence
RhB	:	Rhodamine blue
SAED	:	Selected Area Electron Diffraction
FE-SEM	:	Field emissionScanning Electron Microscopy
TEM	:	Transmission Electron Microscopy
TGA	:	Thermo Gravimetric Analysis
UV-VIS- NIR	:	UV-Visible-Near infrared
VSM	:	Vibrating sample magnetometer
XRD	:	X-ray Diffraction

Chapter - 1

INTRODUCTION

Currently, the effective generation of mixed metal oxide nanomaterials has found tremendous importance due to their wide applications in interdisciplinary fields. Among the various mixed metal oxides, the transition metal tungstates with the formula MWO_4 have attracted much attention due to their unique chemical, physical, structural, and photoluminescence properties [1,2]. In this group of MWO_4, nickel tungstate ($NiWO_4$) is an important inorganic salt due to its appropriate potential for application as catalysts and humidity sensors in various fields. Also, $NiWO_4$ could be used extensively in other fields such as microwave devices, photoanodes, scintillator materials, microwave applications and optical fibre [1–6].

This thesis comprises the experimental study of the properties of $NiWO_4$ nanoparticles synthesized by the direct chemical precipitation method. The structural, optical, magnetic and electrical properties of $NiWO_4$ are discussed. The effect of calcination temperature on the properties of the $NiWO_4$ is studied. The effect of different dopants on the properties of pristine $NiWO_4$ is studied. In addition to this, the possibility of the formation of nanocomposite with Tin phthalocyanine (SnPc) is analysed. The variation in the properties of pristine $NiWO_4$ by the nanocomposite formation is also analysed. Photocatalytic properties of pure $NiWO_4$ and its doped and composite forms are also investigated and discussed.

1.1 Synthesis and different properties of $NiWO_4$

The chemical and physical properties of metal tungstates are in general depend on the synthesis route. Until today, different processes are proposed for the synthesis of nano-sized $NiWO_4$ crystals with different morphologies. These proposed methods are co-precipitation [7], polymeric precursor method [8], modified citrate complex technique [9,10], hydrothermal method [11,12], molten salt method [13], spray pyrolysis [14] and solution combustion synthesis [15]. Each method has its benefits and related limitations. Among these methods, the chemical precipitation method is found to be easy and economic even though it needs a post thermal treatment.

The physico-chemical properties of $NiWO_4$ depend on its structure. Crystalline $NiWO_4$ has a wolframite type structure which is a build-up of hexagonally close-packed oxygen with octahedral sites filled by Ni^{2+} and W^{6+} cations [14]. The wolframite type tungstates are monoclinic with the space group *P2/c* and symmetry point group C_{2h}^4 [16]. Literature reports the structure of $NiWO_4$ using the Fourier difference method. In it oxygen atoms have a distorted hexagonal close packing with Ni and W atoms each occupying one-fourth of the octahedral interstices. Like octahedrals are joined by edges and different octahedra are joined by corners [14,17–19].

Literature reports FT-IR absorption bands in between 400-1000cm^{-1} for $NiWO_4$ nanoparticles. These bands are attributed to metal-oxygen vibrations [20,21]. It is reported that the bands below 500 cm^{-1} are due to the vibrations of NiO_6 polyhedra. Other bands can be assigned to the vibrations in WO_6^{6-} entity [17,22,23].

Group theoretical analysis carried out to find the Raman active modes of $NiWO_4$ reported that six internal stretching vibration modes are there in monoclinic wolframite structure through every six W-O bonds in WO_6 octahedra provide 36 lattice modes [17,24].

The optical properties of nickel tungstate play an important role in several applications of it. UV absorption starts at 350 nm in $NiWO_4$ and the absorption peak appears at about 250 nm within the UV range. Nickel tungstate shows light-absorbing properties in UV, VIS and NIR region wavelengths [7,18,25]. A few theoretical and experimental works are reported regarding the absorption properties of $NiWO_4$ crystals [16,26]. Literature reports experimental data regarding the optical bandgap values of $NiWO_4$. It ranges from 2.95 to 3.20 eV which are all due to the electronic structure of $NiWO_4$ [13,27]. A few works report a low bandgap for $NiWO_4$ [28]. Studies carried out by Montini et. al [29] and Pandey et.al [14] reveal that $NiWO_4$ nanocrystals exhibit both direct and indirect bandgaps. In certain works $NiWO_4$ exhibit a high bandgap [14,30]. Hao et. al [31] report a detailed study of the bandgap of $NiWO_4$ in different works. In the case of $NiWO_4$, the valance band is formed by hybridized O_{2p} and Ni_{3d} states, and the Ni_{3d} states contribute mainly to the upper part of the valance band. The conduction band is formed by the empty W_{5d} states with an admixture of the empty Ni_{3d} states at the bottom of the band [18]. Literature report the presence of both direct and indirect bandgaps in $NiWO_4$ [25,32,33]. The direct transition is attributed to the spin-orbit valance band to the conduction band. The indirect transitions are due to the tungstate ion. The phonons involved in the indirect band to band transitions are due to the internal vibrations of the tungstate (WO_4^-) ion [14].

Photoluminescence emission (PL) ranges from 350-550 nm for $NiWO_4$ nanoparticles. This is due to the intrinsic emission of WO_4^{2-} anion due to excitonic absorption or recombination process [23]. Transition metal tungstates is a self-activated luminescent system [34]. Its intrinsic luminescence is due to the presence of WO_6^{6-} ions [22,35]. But NiO_6 polyhedra also contribute towards the PL emission [17].

Literature reports the antiferromagnetic nature of $NiWO_4$ with a Neel temperature of 64K [36]. But the nanocrystalline $NiWO_4$ is found to have paramagnetic behaviour due to the incomplete 3d levels present in Ni [37,38].

The complex electronic structure of transition metal tungstates offers unique physical and chemical properties for potential applications. Thermo-physical, DC conductivity and dielectric measurements of these transition metal tungstates are mentioned in the literature [39–41]. Nickel tungstate with a wolframite structure is considered an important candidate for the fields of sensors, catalysis and photovoltaic electrochemical cells. $NiWO_4$ is a p-type conducting material below 660K. Literature reports a conductivity of 10^{-7} – 10^{-3} S/cm for the nickel tungstate at different temperatures [42–46].

1.2 Doping with transition metal and semimetal ions and $NiWO_4$/Tinphthalocyanine nanocomposite structure

Properties of $NiWO_4$ can be modified by different means such as doping and composite formation. Cobalt is considered one of the most effective doping species due to its abundant electronic states and also it appears to suit well the tailoring of the electronic structure [47,48]. To vary the magnetic functionality existing in semiconductor, it is suitable to dope with a magnetically active transition metal [49,50]. The dopant cobalt plays this role effectively in many cases that are already reported [51].

Doping with semimetal bismuth has attracted much attention because of its unique properties [52,53]. Bi^{3+} ion exhibits outstanding optical properties in inorganic solid-state crystal lattices. These properties are attributed to their intrinsic multiple energy levels [54–57]. It is found that Bi nanoparticles also exhibit plasmonic properties akin to noble metal nanoparticles [58]. This makes Bi a promising candidate in many fields such as sensors, fluorescence, surface-enhanced spectroscopy and photocatalysis [59–61]. No works regarding bismuth doping in $NiWO_4$ is reported to the best of our knowledge.

A wide variety of inorganic/organic composites have found application in different fields [62,63]. Literature report the inorganic semiconductor/Mpc nanocomposite and their potential applications [41,64–68]. Metal phthalocyanines [MPc] are coloured, organic, p-type semiconducting compounds which show high chemical and thermal stability. Since they have unique optical and electronic properties, they can be used in organic solar cells [69–71], chemical sensors [72] and electronic devices such as field-effect transistors [73,74] and optic data storage [75]. Tin phthalocyanines are important due to their chemical and spectroscopic properties, and their applications in photocatalysis and the biomedical field. The SnPc as a metalloporphyrin has an inherent ability to absorb UV-visible light. It possesses a relatively long excited-state lifetime and can be used for optical amplification in this region. The ability to absorb light in the UV-visible part of the spectrum is due to the presence of sp^2 hybridization carbon atoms in SnPc. Moreover, Sn(II) ions induce some strain on the phthalocyanine framework as the ion is large. Due to this strain metal ion is slightly displaced leading to the breakage of planar symmetry of MPcs. This nonplanar symmetry modifies the crystalline properties of the compound.

1.3 Applications of pristine, doped and composites of $NiWO_4$

Based on the literature, it is acknowledged that $NiWO_4$ possesses desirable physico-chemical properties with possible applications in areas such as magnetism [16], photocatalytic degradation of dyes [76], supercapacitor type hybrid- electrodes [77], active electrocatalyst in hydrogen evolution reaction [78], selective detection of sub-ppm level p-Xylene [79], gas or humidity sensing, photoelectron chemical water oxidation [12] and photoluminescence [80].

Literature reports different nanocomposites having visible light photocatalysis [28,81]. Bandgap tuning is done with the formation of composite with different compounds [82,83]. It is reported that $NiWO_4$ also find application in lithium-ion batteries[84]. Recently electrochemical studies were carried out with the help of $NiWO_4$ [12,14,84–87]. In biosensing fields also $NiWO_4$ acts as a potential candidate [11]. Catalytic properties of $NiWO_4$ is found application in the reduction of NO by CO [88].

1.4 Background of the study

Literature reports various synthesis methods for the synthesis of $NiWO_4$ with desired properties. The hydrothermal synthesis route is preferred for the synthesis of $NiWO_4$ with the smallest particle size[11]. Direct chemical precipitation methods is an easy and economic method of synthesis along with assuring high purity sample [89]. By varying the reactant's concentrations Pourmatazair et. al [23] report the optimization done for the synthesis of $NiWO_4$. They varied the concentrations and flow rate to obtain $NiWO_4$ nanoparticles with the lowest particle size and desired properties.

Literature reports the dependence of the vibrational modes of nanoparticles on the particle size variation introduced by the different synthesis methods and also due to the calcination effect [90,91]. Different methods adopted for the synthesis also produce significant changes in the morphology of the samples. Literature reports the self-assisted methods

[27,92]and green synthesis method [93,94] which produce significant changes in the morphologies. These changes in the morphology introduced active centres for reactions and make the $NiWO_4$ particles applicable in photocatalytic and electrochemical applications.

The optical properties of $NiWO_4$ particles highly depend on the synthesis method and particle size variation [91,95–99]. The formation of valance band and conduction band is formed by the hybridization taking place between oxygen, tungsten and nickel atoms [18]. Literature reports variation of band gaps from 2.6 to 3.2 eV. Different synthesis methods provide different band gaps and are reported in Hao et. al [25]. Theoretical works using DFT are also carried out for bulk and nanocrystalline $NiWO_4$ [26]and reports the existence of both direct and indirect band gaps formed in the case of $NiWO_4$ [100]. Ligand field theory also gives a clear explanation for the low energy absorption properties of $NiWO_4$ samples [14].

Nickel tungstate has intrinsic luminescence nature [17]. It has inherent defects like cation vacancies that can act as a luminescence centre. Generally, $NiWO_4$ has photoluminescence emission in the range of 350-550 nm [34]. The main peaks can be attributed to the WO_6 entity. In addition to that NiO_6 sublattice also contribute to the luminescence emission [22]. The intensity of emission is significant in the case of luminescence applications. It is related to the crystal defects or imperfections that can be introduced into the lattice [101]. Literature reports the luminescence emission of $NiWO_4$ and it follows the general transition metal tungstate with wolframite structure [34,101,102].

No detailed study is found regarding the magnetic properties of $NiWO_4$. They are found to be in paramagnetic form at room temperature [36]. In $NiWO_4$, the tungstate sublattice influences the magnetic properties.

Contribution from Ni counterpart is negligible considering the magnetic nature. Variation in the magnetic properties can be achieved by doping or making composite with magnetically active materials.

Literature reports that below 660K, $NiWO_4$ exhibit p-type behaviour [44,103]. At higher temperature, it may have both p and n-type contributions. Due to the defective nature of $NiWO_4$, it shows high conductivity of the order of 10^{-4}S/m compared to other wolframite transition metal tungstate [27,44,46]. The conduction mechanism in $NiWO_4$ is reported to be due to the hopping of charge carriers. To improve the conductivity and dielectric constant doping with suitable elements are preferred.

Many works have been reported based on cobalt doping in $NiWO_4$ matrix involving different synthesis routes and exploring the electrochemical and photocatalytic properties [104–106]. Due to the electronic band structure of Co, it can tune the electrical properties and photocatalytic activity of $NiWO_4$.

Nowadays, Bi is widely used to improve the photocatalytic activity of various semiconductor photocatalysts [90,107–112]. Li et.al [90] reports the photocatalytic activity of Bi-doped anatase TiO_2 nanospheres. This study explains the variation in particle size with variation in doping percentage. It also describes the change in photocatalytic activity according to the particle size variation. Rangaraj et.al [113] reports the photocatalytic activity of Bi^{3+} doped TiO_2 nanocatalyst. This work suggests that the presence of Bi^{3+} in TiO_2 catalyst substantially enhanced the photocatalytic degradation under UV light. Li et. al [112] studied the visible light active photocatalysis and influence of Bi on photocatalytic activity of $NaTa_{1-x}Bi_xO_3$. Wang et.al [114] also reports the optical absorption properties of Bi^{3+} doped $NaTaO_3$ nanoparticles. This study explains a change in bandgap introduced by Bi doping. To the best of our knowledge, no work is done to improve the structural, optical, electrical, and photocatalytic properties of $NiWO_4$.

$NiWO_4$ is a promising candidate for environmental purification and solar water splitting through photocatalysis [99]. The photocatalytic properties of pure $NiWO_4$ nanocrystals at room temperature present interesting applications regarding the purification of the environment. These include photodegradation of methanol [27], 4-chlorophenol [106], methylene blue [115], methyl orange, 4-nitrophenol [83], rhodamine blue and alizarin red [25,25,31]. The major limiting factor in photocatalytic activities is the rapid recombination of photogenerated electron and hole pairs. To overcome this problem and to improve the overall catalytic performance of $NiWO_4$ photocatalysts, many techniques have been developed such as element doping, morphology control, noble metal deposition and semiconductor coupling. The most effective methods are found to be elemental doping and the formation of nanocomposites. Literature report different nanocomposite formations to improve the catalytic activity of $NiWO_4$ and the optical bandgap tuning for visible-light-driven photocatalytic activity.

From the literature survey conducted, it is evident that synthesis route and conditions play a major role in the structural, optical, electrical, and magnetic properties of $NiWO_4$. Particle size variations also affect the different properties of $NiWO_4$. Doping with suitable elements or forming nanocomposite with different compounds help to tune the properties of $NiWO_4$. This helps in making the $NiWO_4$ a suitable candidate for catalytic and other applications.

1.5 Scope of present study and objectives

Various studies report the synthesis and characterization of $NiWO_4$ nanoparticles. The effect of calcination on the properties of $NiWO_4$ nanoparticles is important to know the structural details of the $NiWO_4$ sample. Reports on the influence of cobalt doping on the structural, optical, electrical and magnetic properties of $NiWO_4$ nanoparticles are sparse. Also, no study has been reported on the structural, optical, electrical and magnetic properties of bismuth-doped $NiWO_4$ and $NiWO_4$/SnPc nanocomposites. Hence, more extensive and systematic studies of Bi-doped $NiWO_4$ nanoparticles and nanocomposite are needed. The photocatalytic activities of the $NiWO_4$ nanoparticles under UV irradiation are reported. Very low degradation efficiency is seen in most cases due to its wide bandgap. So tuning of the bandgap and improving the photocatalytic activity is a major concern. The present research work is mainly focussed on the synthesis and characterization of nanocrystalline $NiWO_4$, cobalt doped $NiWO_4$, bismuth-doped $NiWO_4$ and $NiWO_4$/SnPc nanocomposites. Along with that photocatalytic activity of $NiWO_4$, bismuth-doped $NiWO_4$ and $NiWO_4$/SnPc nanocomposite are also investigated.

The main objectives of this research work are:

- To synthesize $NiWO_4$ nanoparticles by direct chemical precipitation method.
- To investigate on the effect of calcination on the structural, optical, magnetic and electrical properties of $NiWO_4$ nanoparticles.
- To study the effect of cobalt doping on the properties of $NiWO_4$ nanoparticles.
- To study the effect of bismuth doping on the properties of $NiWO_4$ nanoparticles.

- To synthesis of $NiWO_4$/SnPc nanocomposite by solvent evaporation method and their characterization.
- To study the photocatalytic activity of $NiWO_4$, its doped and composite forms under UV irradiation, using Rhodamine blue and Methylene blue dyes.

References

[1] D.L. Stern, R.K. Grasselli, J. Catal. 167 (1997) 570–572.

[2] H. Wang, F.D. Medina, Y.D. Zhou, Q.N. Zhang, Phys. Rev. B. 45 (1992) 10356–10362.

[3] D.F. Nelson, W.S. Boyle, Appl. Opt. 1 (1962) 181.

[4] C.W.E. van Eijk, Phys. Med. Biol. 47 (2002).

[5] R.C. Pullar, S. Farrah, N.M.N. Alford, J. Eur. Ceram. Soc. 27 (2007) 1059–1063.

[6] R. Sundaram, K.S. Nagaraja, Mater. Res. Bull. 39 (2004) 581–590.

[7] J.M. Quintana-Melgoza, J. Cruz-Reyes, M. Avalos-Borja, Mater. Lett. 47 (2001) 314–318. .

[8] R.S.Æ. Silva, A.L.M.D.O.Æ.J.M.F.Æ. Ma, S.C. De Souza, Æ.F.T.G.V.Æ.E. Longo, M.G. Santos, Influence of the thermal treatment in the crystallization, (2009) 167–172.

[9] M. Kuriyama, K. Kohra, S. Takagi, J. Phys. Soc. Japan. 12 (1957) 151–156.

[10] J.H. Ryu, J.W. Yoon, C.S. Lim, K.B. Shim, Key Eng. Mater. 317–318 (2006) 223–226.

[11] S. Mani, V. Vediyappan, S.M. Chen, R. Madhu, V. Pitchaimani, J.Y. Chang, S. Bin Liu, Sci. Rep. 6 (2016) 2–9.

[12] M.I. Ahmed, A. Adam, A. Khan, M.N. Siddiqui, Z.H. Yamani, M. Qamar, Mater. Lett. 177 (2016) 135–138.

[13] S.M. Alshehri, J. Ahmed, A.M. Alzahrani, T. Ahamad, New J. Chem. 41 (2017) 8178–8186.

[14] P.K. Pandey, N.S. Bhave, R.B. Kharat, Electrochim. Acta. 51 (2006) 4659–4664.

15] L. Niu, Z. Li, Y. Xu, J. Sun, W. Hong, X. Liu, J. Wang, S. Yang, ACS Appl. Mater. Interfaces. 5 (2013) 8044–8052.

[16] F.J.O. Rosal, A.F. Gouveia, J.C. Sczancoski, P.S. Lemos, E. Longo, B. Zhang, L.S. Cavalcante, Inorg. Chem. Commun. 98 (2018) 34–40.

[17] A. Kuzmin, J. Purans, Radiat. Meas. 33 (2001) 583–586.

[18] A. Kuzmin, A. Kalinko, R.A. Evarestov, 9 (2011) 502–509.

[19] R.E.A. Cryst, J.D.J. Amer, B.Y.R. Keeling, (1957) 1–5.

[20] A. Molla, M. Sahu, S. Hussain, Nat. Publ. Gr. (2016) 1–11.

[21] S.F. Matar, A. Largeteau, G. Demazeau, 12 (2010) 1779–1785.

[22] L.M. De Oliveira, J.M. Ferreira, C.A. Paskocimas, S.J.G. Lima, E. Longo, A. Gouveia, D. Souza, 77 (2008) 210–216.

[23] S.M. Pourmortazavi, M. Rahimi-Nasrabadi, M. Khalilian-Shalamzari, M.M. Zahedi, S.S. Hajimirsadeghi, I. Omrani, Appl. Surf. Sci. 263 (2012) 745–752.

[24] S.M. Murni Zawawi, R. Yahya, A. Hassan, H.N. M Ekramul Mahmud, M. Noh Daud, 2013. https://doi.org/10.1186/1752-153X-7-80.

[25] M. Hao, X. Meng, Y. Miao, Solid State Sci. 72 (2017) 103–108.

[26] N. Doudin, S. Pomp, M. Blatnik, R. Resel, M. Vorokhta, J. Goniakowski, C. Noguera, Surf. Sci. 659 (2017) 20–30.

[27] F.J.O. Rosal, A.F. Gouveia, J.C. Sczancoski, P.S. Lemos, E. Longo, B. Zhang, L.S. Cavalcante, Inorg. Chem. Commun. (2018) https://doi.org/10.1016/j.inoche.2018.10.001.

[28] A. Habibi-Yangjeh, M. Shekofteh-Gohari, Sep. Purif. Technol. 184 (2017) 334–346.

[29] T. Montini, V. Gombac, A. Hameed, L. Felisari, G. Adami, P. Fornasiero, Chem. Phys. Lett. 498 (2010) 113–119.

[30] P. Parhi, T.N. Karthik, V. Manivannan, J. Alloys Compd. 465

(2008) 380–386.

[31] M. Hao, X. Meng, Y. Miao, Synthesis of $NiWO_4$, Solid State Sci. 72 (2017) 103–108.

[32] M. Hao, D. Fa, L. Qian, Y. Miao, (2019). https://doi.org/10.1166/jnn.2018.15288.

[33] P.K. Pandey, N.S. Bhave, R.B. Kharat, j.mat.let.59 (2005) 3149–3155.

[34] L.S. Cavalcante, M.A.P. Almeida, W. Avansi, R.L. Tranquilin, E. Longo, N.C. Batista, U.E. Paulista, (2012). https://doi.org/10.1021/ic300948n.

[35] F.J.O. Rosal, A.F. Gouveia, J.C. Sczancoski, P.S. Lemos, E. Longo, B. Zhang, Inorg. Chem. Commun. 98 (2018) 34–40.

[36] R.C. Sherwood, H.J. Williams, J.J. Rubin, B. Telephone, W.A. Bonnbr, M. Hill, 25 (1964) 1447–1451.

[37] R. Talebi, J. Mater. Sci. Mater. Electron. (2016). https://doi.org/10.1007/s10854-015-4192-8.

[38] F. Gul, M. Athar, M.A. Farid, (2018). https://doi.org/10.1007/s10832-018-0130-5.

[39] N. Aloysius, M.S. Rintu, E.M. Muhammed, T. Varghese, Nanosyst. Physics, Chem. Math. 4 (2016) 599–603.

[40] A. Sreedevi, K.P. Priyanka, K.K. Babitha, O.P. Jaseentha, T. Varghese, EPJ Plus, (2016). https://doi.org/10.1140/epjp/i2016-16007-9.

[41] A. Sreedevi, K.P. Priyanka, K.K. Babitha, S.I. Sankararaman, 3 (2017) 1–10. https://doi.org/10.1140/epjb/e2017-80149-9.

[42] Electrical transport properties of $CIIWO4$, 14 (1980) 449–454.

[43] L. Niu, Z. Li, Y. Xu, J. Sun, W. Hong, X. Liu, J. Wang, S. Yang, ACS Appl. Mater. Interfaces. 5 (2013) 8044–8052.

[44] R. Bharati, R.A. Singh, B.M. Wanklyn, J. Mater. Sci. 18 (1983) 1540–1542.

[45] R. Bharati, R.A. Singh, B.M. Wanklyn, J. Mater. Sci. 15 (1980) 1293–1296. https://doi.org/10.1007/BF00551819.

[46] R. Bharati, ELECTRICAL CONDUCTION IN MANGANESE TUNGSTATE, 43 (1982) 641–644.

[47] I. Juhnevica, M. Maiorov, K. Tanel, Co doped ZnO nanowires as visible light photocatalysts, 56 (2016) 54–62. https://doi.org/10.1016/j.solidstatesciences.2016.04.008.

[48] C. Dhandapani, R. Narayanasamy, S.N. Karthick, K. V Hemalatha, S. Selvam, P. Hemalatha, M. Suresh, S.D. Kirupha, H. Kim, Opt. - Int. J. Light Electron Opt. (2016).

[49] J. Hays, K.M. Reddy, N.Y. Graces, M.H. Engelhard, V. Shutthanandan, M. Luo, C. Xu, N.C. Giles, C. Wang, S. Thevuthasan, A. Punnoose, 266203 (2007). https://doi.org/10.1088/0953-8984/19/26/266203.

[50] J. Singh, N.K. Verma, Structural , optical and magnetic properties of cobalt-doped CdSe nanoparticles, 37 (2014) 541–547.

[51] M.A. Shafique, S.A. Shah, M. Nafees, K. Rasheed, R. Ahmad, Effect of doping concentration on absorbance , structural , and magnetic properties of cobalt-doped ZnO nano-crystallites, (2012) 1–7.

[52] B.O. Brien, M. Plaza, L.Y. Zhu, L. Perez, C.L. Chien, P.C. Searson, Magnetotransport Properties of Electrodeposited Bismuth Films, (2008) 12018–12023.

[53] A.J. Caruana, M.D. Cropper, S.A. Stanley, Surf. Coat. Technol. (2015). https://doi.org/10.1016/j.surfcoat.2015.02.002.

[54] F. Kang, H. Zhang, L. Wondraczek, X. Yang, Y. Zhang, D.Y. Lei, M. Peng, acs.chem.mater. (2016). https://doi.org/10.1021/acs.chemmater.6b00277.

[55] F. Kang, G. Sun, P. Boutinaud, F. Gao, Z. Wang, J. Lu, Y.Y. Li, S. Xiao, solid solution, (2019). https://doi.org/10.1039/c9tc01385g.

[56] V.A. Online, Journal of Materials Chemistry C, (2013) 8033–8040.

[57] R.V. Yadav, R.S. Yadav, A. Bahadur, A.K. Singh, S.B. Rai, acs.inorgchem. (2016). https://doi.org/10.1021/acs.inorgchem.6b01439.

[58] G. Blasse, A. Bril, Investigations on Bi3 + Activated Phosphors, 217 (1968). https://doi.org/10.1063/1.1667905.

[59] R. Xie, N. Hirosaki, T. Suehiro, F. Xu, A Simple , Efficient Synthetic Route to Sr 2 Si 5 N 8 : Eu 2 + -Based Red Phosphors for White Light-Emitting Diodes, (2006) 5578–5583.

[60] C. Emitting, P. Ba, C. Sio, Increased Eu 2 + Content and Codoping Mn 2 + Induced Tunable Full-, (n.d.).

[61] E. Cavalli, F. Angiuli, F. Mezzadri, M. Trevisani, M. Bettinelli, P. Boutinaud, M.G. Brik, 385503 (n.d.). https://doi.org/10.1088/0953-8984/26/38/385503.

[62] S. Guo, Y. Zhu, Y. Yan, Y. Min, J. Fan, Q. Xu, Applied Catalysis B : 185 (2016) 315–321.

[63] J. Low, B. Cheng, J. Yu, Appl. Surf. Sci. 392 (2017) 658–686. https://doi.org/10.1016/j.apsusc.2016.09.093.

[64] A. Sreedevi, K.P. Priyanka, K.K. Babitha, O.P. Jaseentha, T. Varghese, Structural and optical modifications of the Ag 2 WO 4 / CoPc nanocomposite for potential applications, epjp (2016) 2–9. https://doi.org/10.1140/epjp/i2016-16007-9.

[65] K.K. Babitha, K.P.P.A. Sreedevi, B. Abraham, J. Mater. Sci. Mater. Electron. (2016). https://doi.org/10.1007/s10854-016-5636-5.

[66] K.K. Babitha, Structural Modifications and Extended Spectral Response of CeO 2 / CoPc Nanocomposites for Potential Applications, 8 (2016) 1–8. https://doi.org/10.1111/ijac.12542.

[67] K.K. Babitha, K.P. Priyanka, H. Hitha, S. Rintu Mary, E.M. Mohammed, S. Sankararaman, T. Varghese, J. Electron. Mater. 46 (2017). https://doi.org/10.1007/s11664-017-5653-z.

[68] N.A. Sabu, X. Francis, J. Anjaly, S. Sankararaman, T. Varghese,

Enhanced structural and optical properties of the polyaniline-calcium tungstate (PANI-CaWO4) nanocomposite for electronics applications, (2017) 2–8.https://doi.org/10.1140/epjp/i2017-11562-1.

[69] B.F. Yang, K. Sun, S.R. Forrest, Efficient Solar Cells Using All-Organic Nanocrystalline Networks, (2007) 4166–4171. https:// doi.org/10.1002/adma.200700837.

[70] D.A. Links, Interfacial modification of organic photovoltaic devices by molecular, (2012) 3713–3724. https://doi.org/10.1039/ c2cp40198c.

[71] C.W. Tang, Two-layer organic photovoltaic cell, 183 (2003). https://doi.org/10.1063/1.96937.

[72] R.A. Collins, K.A. Mohammed, J. Phys. D. Appl. Phys. 21 (1988) 154–161. https://doi.org/10.1088/0022-3727/21/1/021.

[73] H.G. Kim, J.S. Jang, S.T. Hur, S.W. Choi, S.S. Kim, H. Tada, H. Takezoe, K. Ishikawa, Thin Solid Films. 519 (2011) 2011–2014.

[74] L. Rapp, S. Nénon, A.P. Alloncle, C. Videlot-Ackermann, F. Fages, P. Delaporte, Appl. Surf. Sci. 257 (2011) 5152–5155.

[75] C. Schünemann, C. Elschner, A.A. Levin, M. Levichkova, K. Leo, M. Riede, Thin Solid Films. 519 (2011) 3939–3945. https://doi.org/10.1016/j.tsf.2011.01.356.

[76] N. Helaïli, A. Boudjamaa, M. Kebir, K. Bachari, Environ. Sci. Pollut. Res. 24 (2017) 6481–6491. https://doi.org/10.1007/s11356-016-8296-3.

[77] S. Chen, G. Yang, Y. Jia, H. Zheng, J. Mater. Chem. A. 5 (2017) 1028–1034. https://doi.org/10.1039/c6ta08578d.

[78] S.F. Anis, B.S. Lalia, G. Palmisano, R. Hashaikeh, J. Mater. Sci. (2017). https://doi.org/10.1007/s10853-017-1633-1.

[79] T.H. Kim, C.H. Kwak, J.H. Lee, ACS Appl. Mater. Interfaces. 9 (2017) 32034–32043. https://doi.org/10.1021/acsami.7b10294.

[80] X. Wei, X. Jiang, J. Wei, S. Gao, Chem. Mater. 28 (2016) 445–458.

https://doi.org/10.1021/acs.chemmater.5b02336.

[81] M. Pirhashemi, A. Habibi-Yangjeh, Sep. Purif. Technol. 193 (2018) 69–80. https://doi.org/10.1016/j.seppur.2017.11.007.

[82] T. Zhu, M.N. Chong, E.S. Chan, J.D. Ocon, J. Alloys Compd. 762 (2018) 90–97. https://doi.org/10.1016/j.jallcom.2018.05.147.

[83] M.M.J. Sadiq, U.S. Shenoy, D.K. Bhat, J. Phys. Chem. Solids. 109 (2017) 124–133. https://doi.org/10.1016/j.jpcs.2017.05.023.

[84] T. Peng, C. Liu, X. Hou, Z. Zhang, C. Wang, H. Yan, Y. Lu, X. Liu, Y. Luo, Electrochim. Acta. 224 (2017) 460–467. https://doi.org/10.1016/j.electacta.2016.11.154.

[85] S. Rahimnejad, J.H. He, W. Chen, K. Wu, G.Q. Xu, RSC Adv. 4 (2014) 62423–62429. https://doi.org/10.1039/c4ra10650d.

[86] V.K.V.P. Srirapu, A. Kumar, P. Srivastava, R.N. Singh, A.S.K. Sinha, Electrochim. Acta. 209 (2016) 75–84. https://doi.org/10.1016/j.electacta.2016.05.042.

[87] J. Zhu, W. Li, J. Li, Y. Li, H. Hu, Y. Yang, Electrochim. Acta. 112 (2013) 191–198.

[88] J.M. Quintana-Melgoza, A. Gómez-Cortés, M. Avalos-Borja, React. Kinet. Catal. Lett. 76 (2002) 131–140. https://doi.org/10.1023/A:1015629815029.

[89] E.S. Babu, B.J. Rani, G. Ravi, R. Yuvakkumar, R.K. Guduru, V. Ganesh, S. Kim, Mater. Lett. 220 (2018) 209–212. https://doi.org/10.1016/j.matlet.2018.03.018.

[90] H. Li, D. Wang, P. Wang, H. Fan, T. Xie, Chem. - A Eur. J. 15 (2009) 12521–12527. https://doi.org/10.1002/chem.200901193.

[91] H.Y. He, Mater. Res. Innov. 12 (2008) 138–141. https://doi.org/10.1179/143307508X333659.

[92] U. Nithiyanantham, S.R. Ede, S. Anantharaj, S. Kundu, Cryst. Growth Des. 15 (2015) 673–686. https://doi.org/10.1021/cg501366d.

[93] K. Buvaneswari, M. Ganagaraj, GREEN SYNTHESIS OF NiWO 4

NANOPARTICLES USING PHYLLANTHUS AMARUS EXTRACT, (n.d.) 194–201.

[94] R. Karthiga, B. Kavitha, M. Rajarajan, A. Suganthi, Materials Science in Semiconductor Processing Photocatalytic and antimicrobial activity of NiWO 4 nanoparticles stabilized by the plant extract, 40 (2015) 123–129. https://doi.org/10.1016/j.mssp.2015.05.037.

[95] A. Sreedevi, K.P. Priyanka, K.K. Babitha, N.A. Sabu, T.S. Anu, T. Varghese, Chemical synthesis, structural characterization and optical properties of nanophase a -Ag 2 WO 4, (2015). https://doi.org/10.1007/s12648-015-0664-1.

[96] S.J. Naik, U. Subramanian, R.B. Tangsali, A. V Salker, Optical absorption and photoluminescent studies of cerium-doped cobalt tungstate nanomaterials, 115404 (n.d.). https://doi.org/10.1088/0022-3727/44/11/115404.

[97] D. Errandonea, D. Mart, Optical absorption of divalent metal tungstates : Correlation between the band-gap energy and the cation ionic radius, 37002 (2008). https://doi.org/10.1209/0295-5075/83/37002.

[98] N.M. Batra, OPTICAL CHARACTERIZATION SINGLE CRYSTALS OF CuWO, 50 (1989) 2–5.

[99] S.M. Alshehri, J. Ahmed, A.M. Alzahrani, T. Ahamad, New J. Chem. 41 (2017) 8178–8186. https://doi.org/10.1039/c7nj02085f.

[100] T. Ejima, T. Banse, H. Takatsuka, Y. Kondo, M. Ishino, N. Kimura, 120 (2006) 59–63. https://doi.org/10.1016/j.jlumin.2005.12.012.

[101] V.M. Longo, S. Cavalcante, E.C. Paris, C. Sczancoski, P.S. Pizani, M.S. Li, J. Andr, E. Longo, D. De Física, Hierarchical Assembly of CaMoO 4 Nano-Octahedrons and Their Photoluminescence Properties, (2011) 5207–5219.

[102] C. Zhang, D. Guo, C. Hu, Y. Chen, H. Liu, H. Zhang, X. Wang,

Large-scale synthesis and photoluminescence of cobalt tungstate nanowires, 035416 (2013) 1–8. https://doi.org/10.1103/ PhysRev B.87.035416.

[103] A.K. Bhattacharya, R.G. Biswas, A. Hartridge, J. Mater. Sci. 32 (1997) 353–356. https://doi.org/10.1023/A:1018545131216.

[104] S. Shepard, M. Smeu, Comput. Mater. Sci. 143 (2018) 301–307. https://doi.org/10.1016/j.commatsci.2017.11.021.

[105] M. Feng, D. An, H. Zhang, G. Ma, C. Zhang, Z. Ma, Facile synthesis of cobalt / nickel tungstate and its application in hybrid supercapacitor, 5 (2017) 1954–1960.

[106] S.M.E.M.M. Rashad, Novel Synthesis of Cobalt Nickel Tungstate Nanopowders and its Photocatalytic Application, (2014). https://doi.org/10.1007/s10876-014-0735-z.

[107] Y. Hu, Y. Cao, P. Wang, D. Li, W. Chen, Y. He, X. Fu, Y. Shao, Y. Zheng, Appl. Catal. B Environ. 125 (2012) 294–303. https://doi.org/10.1016/j.apcatb.2012.05.040.

[108] J. Yang, T. Xie, C. Liu, L. Xu, Materials (Basel). 11 (2018). https://doi.org/10.3390/ma11081359.

[109] Z. Zhang, W. Wang, L. Wang, S. Sun, ACS Appl. Mater. Interfaces. 4 (2012) 593–597. https://doi.org/10.1021/am2017199.

[110] I. Razdobreev, H. El Hamzaoui, V.Y. Ivanov, E.F. Kustov, I. Razdobreev, H. El Hamzaoui, V.Y. Ivanov, E.F. Kustov, B. Capoen, I. Razdobreev, H. El Hamzaoui, V.Y. Ivanov, E.F. Kustov, B. Capoen, M. Bouazaoui, Optical spectroscopy of Bismuth-doped pure silica fiber preform To cite this version : Optical spectroscopy of bismuth-doped pure silica fiber preform, (2013).

[111] A. Phuruangrat, P. Dumrongrojthanath, N. Ekthammathat, S. Thongtem, T. Thongtem, Light-Driven Photocatalytic Properties of Bi 2 WO 6 Nanoplates, 2014 (2014).

[112] T.S. Natarajan, K. Natarajan, H.C. Bajaj, R.J. Tayade, J.

Nanoparticle Res. 15 (2013). https://doi.org/10.1007/s11051-013-1669-3.

[113] S. Rengaraj, X.Z. Li, P.A. Tanner, Z. Pan, G.K.H. Pang, Photocatalytic degradation of methylparathion-an endocrine disruptor by Bi 3+-doped TiO 2, n.d. https://www.sciencedirect.com/science/article/pii/S1381116905007922

[114] X. Wang, H. Bai, Y. Meng, Synthesis and optical properties of Bi3+ doped NaTaO3 nano-size photocatalysts, Ingentaconnect.Com. (2010).

[115] G. Munusamy, K. Varadharajan, Investigation of γ-AlOOH and NiWO4-coated boehmite micro/nanostructure under UV/visible light photocatalysis, Res. Chem. Intermed. 5 (2018). https://doi.org/10.1007/s11164-018-3588-5.

◆

Chapter - 2

CHARACTERIZATION TECHNIQUES

2.1 Introduction

Material characterization is the fundamental process that can be done for the systematic and scientific analysis of the properties of materials. Different characterization techniques are performed for the detailed analysis of the properties of $NiWO_4$ nanoparticles and their doped and nanocomposite forms. The present research work includes the synthesis of $NiWO_4$ nanoparticles, its doped and composite forms along with their characterization. The results are discussed in detail in the foregoing chapters. This chapter provides the information of different characterization techniques used in the study.

The thermal stability of the $NiWO_4$ samples is analysed using thermogravimetric (TG) and differential thermal analysis (DTA). Structural characterization of thermally stable $NiWO_4$ is done with X-ray powder diffraction (XRD) and transmission electron microscopy (TEM). Surface morphology is identified with the help of field emission scanning electron microscopy (FESEM). Chemical composition of the elements present is analysed with energy-dispersive X-ray spectroscopy (EDS). The important part in the structure identification, the bonds present is identified with the help of Fourier transform infrared spectroscopy (FTIR) and Raman spectroscopy. Optical properties of the nickel tungstate nanoparticles are analyzed using Ultraviolet-visible- near-infrared spectroscopy (UV-VIS-NIR) and photoluminescence (PL) spectroscopy. The magnetic properties of the samples are studied with the help of vibrating sample magnetometer

(VSM). Electrical studies are carried out by dielectric and impedance measurements.

2.2 Method of Synthesis

In the present work, pure and doped $NiWO_4$ samples are synthesized by direct chemical precipitation method. The nanocomposite samples of $NiWO_4$/SnPc are prepared by the solvent evaporation method. The detailed description of the synthesis procedure of the samples is given in the respective chapters.

2.3 Characterization Techniques

2.3.1 Thermal analysis

Thermogravimetric analysis (TGA) is a technique of thermal analysis in which the mass of a sample is measured with increasing the temperature. With the temperature change, there may be weight loss or gain. This mass change indicates the chemical and physical phenomena taking place in the sample over time by the increase in temperature. The thermogravimetric data collected are complied and plotted. The plot has a mass or percentage of initial mass on the y-axis and temperature on the x-axis. This plot is referred to as a TGA curve. The first derivative of the TGA curve which is called the derivative thermogravimetric (DTG) curve is also plotted to determine changing points in the TGA curve. It is useful for the interpretation of the process involved during temperature change [1].

In differential thermal analysis, the difference in temperature of the material under study and an inert reference is measured as a function of temperature while both the sample and reference are made to undergo identical thermal cycles. Exothermic or endothermic changes taking place in the sample can be detected relative to the inert reference. So from the

DTA curve, transformations such as glass transitions, crystallization, melting and sublimation can be identified [2].

Thermal analysis of the pure $NiWO_4$, doped $NiWO_4$ and $NiWO_4$/SnPc nanocomposite samples are done with *Perkin Elmer STA 6000*, heating from ambient temperature to 880^0C at a rate of 20^0C/min.

2.3.2 Structural characterization

The structural characterization of samples is important as it helps to identify the structure of the sample and the structural variations take place in the case of doped and composite samples. The different analytical techniques used in the present research work are XRD, TEM, FE-SEM, EDS, FT-IR and Raman spectroscopy.

2.3.2.1 Powder X-ray diffraction

XRD mainly helps to identify the phase of a crystalline material and provide information on unit cell dimensions. It also used for the study of crystal structures and atomic spacing. The interaction of the incident X-rays with the sample produces constructive interference when conditions satisfy Bragg's law represented by the equation,

$$n\lambda=2d_{hkl}\sin\theta \tag{2.1}$$

This law relates the wavelength of the X-ray (λ) to the diffraction angle (2θ) and the lattice spacing (d_{hkl}) in a crystalline sample [3].

In the present work, XRD analysis is carried out using the instrument *Bruker AXS D8 Advance* X-ray diffractometer with features Cu-Kα radiation of λ = 1.5406 Å, X-ray tube voltage = 35 kV and current =35 mA are used. The scan is taken in the 2θ range from 0 to 80^0 at increments of 0.02^0 with a step time of 29.1s. The XRD patterns obtained is compared with the X-ray powder data file of the Joint Committee on Powder Diffraction Standards (JCPDS) to identify the crystal phase and structure.

The lattice parameters of the monoclinic structure are determined [4,5] using the formula,

$$\frac{1}{d^2} = \frac{1}{sin^2\beta}\left(\frac{h^2}{a^2} + \frac{k^2 sin^2\beta}{b^2} + \frac{l^2}{c^2} - \frac{2hlcos\beta}{ac}\right), \qquad (2.2)$$

where'd' is the spacing between the planes corresponds to the Miller indices (hkl); a, b, c and β are the lattice parameters.

The average crystallite sizes of nanoparticles are calculated from XRD patterns using Scherrer equation,

$$D = \frac{k\lambda}{\beta_{hkl}\cos\theta}, \qquad (2.3)$$

where D is the crystallite size in nm, k the shape factor, which usually takes a value of about 0.9, λ the radiation wavelength (0.15406 nm for Cu-K_α radiation), β_{hkl} the full width at half maximum (FWHM) of the peak 2θ angle [6,7].

Williamson–Hall (W-H) Method

Williamson- Hall analysis [7] is carried out to find out the contribution of size and micro-strain to line broadening of the XRD spectrum. Crystallite size and micro-strain 'ε' on peak broadening are estimated from W-H equation,

$$\beta_{hkl}\cos\theta = \frac{k\lambda}{D} + 4\varepsilon\sin\theta, \qquad (2.4)$$

where ε is the micro-strain of the system. The variation of $\beta_{hkl}cos\theta$ against $4sin\theta$ is plotted for the samples. By linear fitting, crystallite size is estimated from the y-intercept and micro-strain ε is obtained from the slope of the fitted line.

2.3.2.2 Transmission electron microscopy

In this microscopic technique, a beam of electrons is transmitted through the sample to form an image from the interaction of the electrons with the sample. TEM is capable of imaging at a significantly higher resolution than the light microscope. This is due to the smaller de Broglie wavelength of electrons. In TEM imaging, bright-field pictures are usually obtained at smaller angles and consist of a mixture of elastic, thermal diffuse, and inelastic scattering. In bright-field TEM imaging, the transmitted beam, as well as a small amount of reflections, is select by cutting out all the other electrons to form the image. So a magnified image can be obtained from this. In high-resolution transmission microscopy (HRTEM), both the transmitted and several diffracted electron beams are used to form the image. So the resolution is improved in HRTEM comparing to bright field imaging because higher spatial frequencies are included in HRTEM. Due to the high resolution of this technique, lattice arrangements, defects, dislocations within the sample can be identified using this HRTEM. Selected area electron diffraction (SAED) is obtained by operating TEM in diffraction mode. The SAED image helps to identify the nature of the sample. The SAED pattern consists of a pattern of dots in the case of a single crystal, small spots making up rings in the case of a polycrystalline and diffused rings for amorphous solid material [8].

For TEM studies, $NiWO_4$ samples are dispersed in ethanol using an ultrasonic bath. A drop of the suspension is placed on a copper grid coated with carbon film. After drying, the copper grid containing the nanoparticles is placed on a holder for the imaging process. TEM micrographs of the samples are taken using a *JEOL JEM 2100* accelerated by 200 kV with a resolution of 0.23 nm. Further analysis such as particle size calculation from the bright-field image, lattice spacing calculations from HRTEM and SAED are done using *ImageJ* software.

2.3.2.3 Field emission scanning electron microscopy

FE-SEM is the microscopy that works with electrons instead of light. It is used to analyse the topographic details on the surface of the samples. In the present research work to analyse the surface morphology of $NiWO_4$ samples, FE-SEM images are taken using the instrument *FEI (Model- Nova Nano SEM 450)* operating at15 kV. For the surface analysis of the doped and composite samples, the instrument *∑IGMA* ^{TM} *(ZEISS)* operating at 5 kV is used.

2.3.2.4 Energy-dispersive X-ray spectroscopy

The energy-dispersive X-ray spectroscopy is used to analyse the chemical composition of the samples. When a sample is bombarded with a focused beam of electrons, it emits X-ray spectrum. The EDS makes use of this spectrum to obtain a localized chemical analysis. All elements from atomic number 4 to 92 can be detected in principle. In some instruments, it is difficult to analyse 'light' elements ($Z < 10$). It can be used for qualitative elemental analysis and also standardless quantitative analysis. Qualitative analysis involves the identification of the lines in the spectrum. Quantitative analysis (determination of the concentrations of the elements present) entails measuring line intensities for each element in the sample and the same elements in the calibration standards of known composition. In the present work, the analysis of the $NiWO_4$ samples is carried out with the help of EDS detector *OXFORD XMX N.*

2.3.2.5 Fourier transform infrared spectroscopy

It is a technique used to obtain an infrared spectrum of absorption or transmission of a sample in solid, liquid or gaseous phase. FT-IR identifies the presence of organic and inorganic compounds in the sample. Depending on the infrared absorption frequency range, the specific molecular groups existing in the sample can be determined.

In the present study, Fourier transform infrared spectra of the $NiWO_4$ samples are recorded by FT-IR spectrophotometer (*Thermo Nicolet, Avatar 370*) in the range 4000 to 400 cm^{-1}. The spectral output is recorded by transmittance (*%T*) as a function of wavenumber ($1/\lambda$) cm^{-1}.

2.3.2.6 Raman spectroscopy

Raman spectroscopy is a non-destructive chemical analysis technique which provides detailed information about chemical structure, phase, crystallinity and molecular interactions. It is based upon the interaction of light with the chemical bonds within a material. This spectroscopic technique is used to identify the vibrational modes of a molecule. A Raman spectrum features several peaks, showing the intensity and wavelength position of the Raman scattered light. Each peak corresponds to a specific molecular bond vibration. So the structural properties can be analysed with the help of a Raman spectrum. In the present research work, *Alpha 300 RA AFM & RAMAN* (WITec GmbH, 532 nm DPSS laser) is used to carry out the Raman analysis.

2.3.3 Optical characterization

In this section, two important optical characterization techniques namely UV-VIS-NIR absorption spectroscopy and photoluminescence spectroscopy are discussed.

2.3.3.1 Ultraviolet-visible- near-infrared spectroscopy

UV-VIS-NIR spectroscopy is a powerful analytical technique to determine the optical properties of a material. It includes absorption and reflectance spectroscopy in the UV–Vis-NIR spectral regions. Molecules containing π-electrons or nonbonding electrons (n-electrons) can absorb ultraviolet or visible light energy and be excited to higher anti-bonding molecular orbitals [9]. In UV–Vis spectroscopy, molecules undergo electronic transitions in the ultraviolet or visible region. This transition is from highest occupied molecular orbit in the valence band to lowest unoccupied molecular orbital in the conduction band. This kind of transition is possible only when the incident photon energy is equal to or greater than the energy difference between possible electronic transition states. As a result, a sharp increase in the absorption at an energy close to bandgap is observed in the spectrum.

Bandgap energy

To find the bandgap energy, data is collected from UV-VIS- NIR spectrophotometer in the diffuse reflectance mode. The optical bandgap (E_g) of samples are determined by fitting data to Tauc transition equation [10]

$$\alpha hv = A(hv - E_g)^n, \qquad (2.5)$$

where α is the optical absorption coefficient, hv the photon energy, E_g the bandgap and A is a constant. In equation **(2.5),** n=1/2 gives the direct transition and n=2 gives the indirect transition[11]. The absorption co-efficient ‘α’ is calculated from the diffuse reflectance data using the equation,

$$\alpha = [\,1 - R]^2 / 2R, \qquad (2.6)$$

where R is the reflectance. Both direct and indirect optical bandgap energies of samples are measured by plotting $(\alpha hv)^2$ and $(\alpha hv)^{1/2}$ as a function of photon energy respectively (Tauc plot) and extrapolating the linear portion of the curves to absorption equal to zero.

Absorption spectra of the samples are obtained using a double-beam UV–Visible spectrophotometer (*Varian, Cary 5000 model*) with a scan rate of 600 nm/min. The spectra are recorded in the range of 224–1976 nm.

2.3.3.2 Photoluminescence spectroscopy

Photoluminescence spectroscopy is a non-destructive method of probing the electronic structure of materials. The light which is directed onto a sample is absorbed and it excites an electron to a higher energy level. This is known as the photoexcitation process. This excess energy can be dissipated by the sample through the emission of light and it is called photoluminescence. Photoexcitation causes electrons within a material to move into permissible excited states. When these electrons return to their equilibrium states, the excess energy is released by a radiative process or by a non-radiative process. The energy of the emitted light is related to the difference in energy levels between the electron states involved in the transition. The energy corresponding to the emission peaks is given by,

$$E = h\nu = hc/\lambda \text{ in eV,} \tag{2.7}$$

where λ is the wavelength in nm corresponding to the emission peak.

Photoluminescence spectra of the samples are recorded by a *Horiba fluorescence spectrometer* using broadband 450W Xenon arc lamp as a source with a resolution of 0.2 nm. The emission spectra are recorded in the range 350–650 nm at an excitation wavelength of 350 nm using a slit width of 3 nm.

CIE Chromaticity diagram

In 1931, the Commission International de l'Eclairage (CIE) developed a standard three colour system for specifying colours. The CIE colour model is a visual perception system based on three colours namely red (X), green (Y), and blue (Z) recognized by the colour receptors in the eye. These primaries (X, Y, Z) are called the trichroma values. The chromaticity coordinates (x, y, and z) are calculated as the fractional values of the three primaries. Since the sum of x, y and z equal 1, two of the fractional values are sufficient to define an unknown colour. Thus a two-dimensional chromaticity diagram can be plotted with the x coordinate along the abscissa, and the y coordinate along the ordinate. The two-dimensional chromaticity diagram forms a parabolic curve where the pure spectral colours located on the edge. Fig. 2.1 shows the 1931 chromaticity diagram.

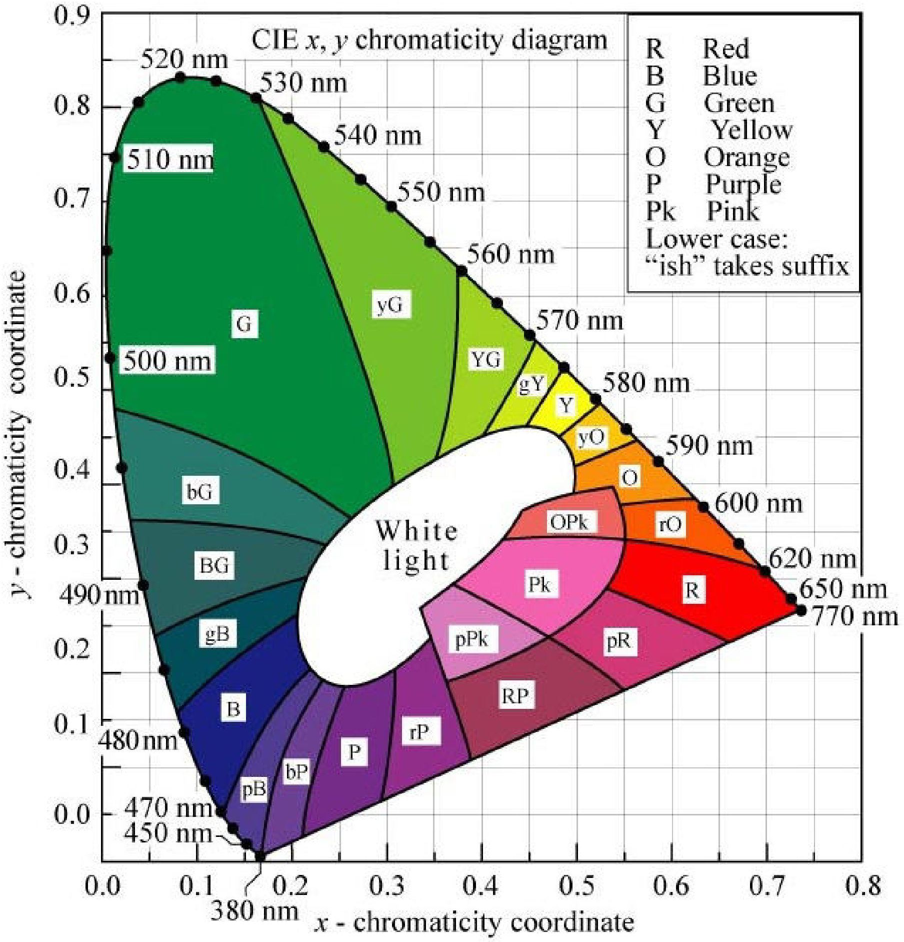

Fig. 2.1 1931 CIE chromaticity diagram [12]

2.3.4 Vibrating sample magnetometry

Vibrating sample magnetometry belongs to the direct class of magnetic measuring techniques in which the macroscopic magnetization of the sample is sensed. VSM measures the magnetic moment of a sample when it is vibrated perpendicular to a uniform magnetizing field. The magnetic moment is measured based on Faraday's law [13]. In the present research work, magnetic measurements of the samples are carried out in a vibrating sample magnetometer (*Lakeshore VSM 7410*) at room temperature in an applied magnetic field sweeping between ± 15000 Oe.

2.3.5 Dielectric and AC conductivity studies

Dielectric measurements are important as they provide electrical characteristics of the materials. Measurement of dielectric properties involves measurements of the complex relative permittivity (ε^*) of the material. Complex permittivity consists of a real and imaginary part. The real part of the complex permittivity, also known as dielectric constant is a measure of the amount of energy from an external electrical field stored in the material. The imaginary part is known as the loss factor. It is a measure of the amount of energy loss from the material due to an external electric field. Its value is zero for lossless materials. The ratio of the imaginary part to the real part of the complex permittivity is called loss tangent it is represented by $\tan\delta$. The loss tangent is also called as tangent loss or dissipation factor.

The frequency-dependent properties of materials at room temperature can be explained with the help of complex permittivity (ε^*), complex impedance (Z^*) and dielectric loss or dissipation factor. Different parameters and their interconnecting relations are given below:

Complex permittivity, $\boldsymbol{\varepsilon^* = \varepsilon' - j\,\varepsilon''}$ **(2.7)**

Complex impedance, $\boldsymbol{Z^* = Z' + j\,Z'' = 1/(j\omega C_0\varepsilon^*)}$ **(2.8)**

Dielectric loss or dissipation factor, $\boldsymbol{\tan\delta = \varepsilon''/\varepsilon' = Z'/Z''}$ **(2.9)**

Where $\omega = 2\pi f$, C_0 is the geometrical capacitance.

The real part of the dielectric constant of a material can be evaluated by forming a capacitor with the same material as a dielectric medium. From the capacitance value obtained, the real part of dielectric constant can be calculated

$$\boldsymbol{\varepsilon' = C_p\, d/(\varepsilon_0\, A),} \qquad \textbf{(2.10)}$$

where C_p is the capacitance of the specimen, d the thickness of the pellet, A the cross-sectional area and ε_0 the permittivity of free space (8.85 x 10^{-12} Fm^{-1}).

For a better understanding of the dielectric behaviour of the samples, the complex impedance spectroscopic technique is employed. In complex impedance diagrams (Nyquist plot), the imaginary part of the impedance $Z''(\omega)$ is plotted against the real part of impedance $Z'(\omega)$. The grain and grain boundary contributions to the overall impedance can be resolved by fitting the experimental response to that of an equivalent circuit. In the present study, the fitting is done with the help of EIS spectrum analyser.

The AC conductivity of samples is investigated to analyze their conduction mechanism. The AC conductivity is calculated using the formula,

$$\boldsymbol{\sigma_{ac} = \varepsilon'\varepsilon_0\omega \tan\delta,} \qquad \textbf{(2.11)}$$

where ε' is the real part of complex permittivity, ε_0 is the permittivity of free space, ω is the angular frequency and $\tan\delta$ is the loss tangent of system.

In general, the electrical conductivity depends on the number of free charge carriers available and their mobility. The real part of AC conductivity σ consists of two parts,

$$\boldsymbol{\sigma = \sigma(T) + \sigma(\omega, T),} \qquad \textbf{(2.12)}$$

The first term is the frequency-independent DC conductivity, which is due to band conduction. The second term is the AC conductivity due to hopping of charge carriers. This term is a frequency-dependent term [14]. The variation of AC conductivity can be described by the universal Jonscher's power law [15].

$$\boldsymbol{\sigma(\omega, T) = \sigma_{ac} = A\omega^{s}}, \quad \textbf{(2.13)}$$

where ω is the angular frequency of the applied field, and *A* and *n* are constants which depend on both the temperature and composition. The constant *s* is the frequency exponent which varies between zero and unity.

In the present work, the dielectric and impedance spectra are measured in the frequency range of 50 Hz- 5 MHz at room temperature by using *Wayne Kerr H- 6500B* model impedance analyser.

References

[1] A.W. Coats, J.P. Redfern, Thermogravimetric analysis. A review, Analyst. 88(1963)

[2] D.J.W. Robert Bud, Instruments of Science, 1998.

[3] W.A. Dollase, Solid state chemistry and its applications by A. R. West , 1985.

[4] R.D. Dobrott, X-Ray Diffraction Methods, in: Charact. Solid Surfaces, Springer US, Boston, MA, 1974: pp. 147–178.

[5] B. D. Cullity, Elements of X-Ray Diffraction (Addison-Wesley, MA, 1967)

[6] T. Varghese, K.M. Balakrishna, Nanotechnology: An introduction to synthesis, properties and applications of nanomaterials, Atlantic Publishers, New Delhi, 2011.

[7] G. K. Williamson and W. H. Hall, Acta Metall. 1, 22 (1956)

[8] B. M, W. E, principles of optics, Cambridge university press, Cambridge, 1997.

[9] H. Wang, P.K. Chu, Surface Characterization of Biomaterials, in: Charact. Biomater., Elsevier Inc., 2013: pp. 105–174.

[10] J. Tauc, Amorphous and liquid semiconductors, (1973).

[11] E.I. Ross-Medgaarden, I.E. Wachs, Structural Determination of Bulk and Surface Tungsten Oxides with UV-vis Diffuse Reflectance Spectroscopy and Raman Spectroscopy, (2007).

[12] S. Gage, D. Evans, M.W. Hodapp, H. Sorensen, Optoelectronics Applications Manual, McGraw Hilll, Newyork, 1977.

[13] B.D. Cullity, C.D. Graham, Introduction to magnetic materials, Second Edition, 2011.

[14] M.A. El Hiti, AC electrical conductivity of Ni-Mg ferrites, J. Phys. D. Appl. Phys. 29 (1996) 501–505.

[15] A.K. Jonscher, Dielectric relaxation in solids, J. Phys. D. Appl. Phys. 32 (1999) R57.

◆

Chapter - 3

EFFECT OF CALCINATION TEMPERATURE ON THE PROPERTIES OF NANOPHASE $NiWO_4$

3.1 Introduction

The important steps to obtain nanophase nickel tungstate with desired applications are the synthesis of nanoparticles with suitable size and morphology, and explore its unique properties. This chapter describes the synthesis and characterization of nickel tungstate nanoparticles. The effect of calcination temperature on the structural, vibrational, optical, magnetic and electrical properties of $NiWO_4$ nanoparticles is also discussed.

3.2 Synthesis of nickel tungstate nanoparticles

Method of direct precipitation is used to synthesize $NiWO_4$ nanoparticles. This is a simple, easy to handle and more economical synthesis route. All chemicals used for the synthesis of $NiWO_4$ are of analytical grade and are used without further purification. The specific chemicals used are nickel (II) nitrate hexahydrate, $Ni(NO_3)_2.6H_2O$ (98%, Merck) and sodium tungstate, $Na_2WO_4.2H_2O$ (98%, Merck). Distilled water is used in all the synthesis procedures.

In a typical synthesis, 0.1 M solutions of $Ni(NO_3)_2.6H_2O$ (Sol A) and $Na_2WO_4.2H_2O$ (Sol B) are made by dissolving 2.91 g of nickel nitrate and 3.29 g of sodium tungstate in 100 ml of distilled water separately. Sol B is added to sol A and stirred using a magnetic stirrer. After completing the precipitation, the above solution is washed several times with distilled water. The washing process helps to eliminate unreacted nitrate and sodium ions from the obtained product. The precipitate obtained is dried at 80^0C for 15 h. The dried powder sample is calcined at three different temperatures namely 500, 600 and 700^0C for 3 h to get three different samples to study the effect of calcination temperature. The samples obtained after calcination at 500, 600 and 700^0C are designated as S1, S2 and S3, respectively. The colour of the nanocrystalline nickel tungstate powder changed from light ochre to dark ochre as the temperature is increased from 500 to 700^0C. A schematic representation of the synthesis of nanocrystalline $NiWO_4$ is shown in Fig.3.1.

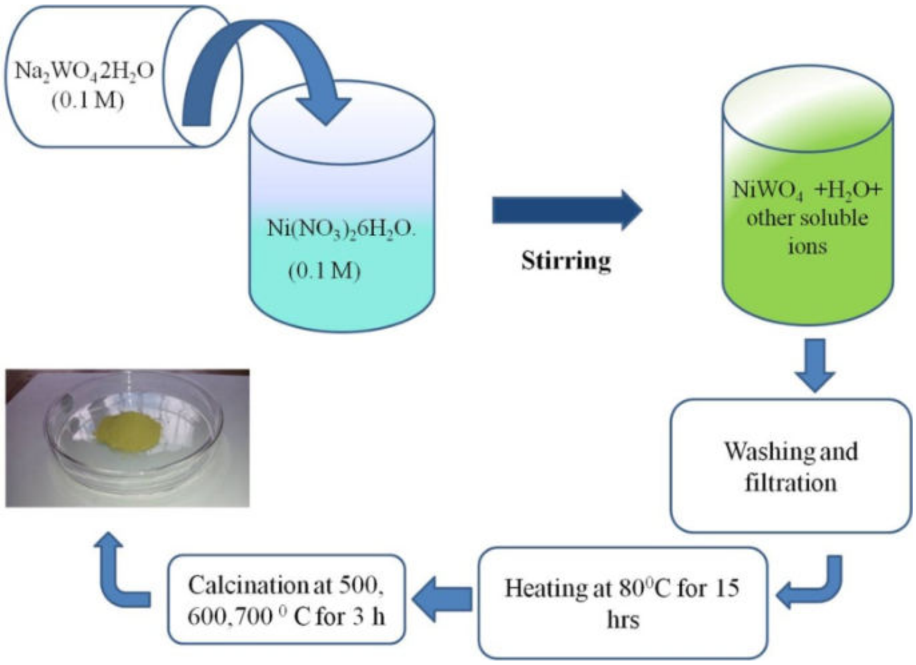

Fig. 3.1 The scheme of preparation of nanophase nickel tungstate using direct precipitation method.

3.3 Results and discussion

3.3.1 Thermal analysis

Selection of suitable calcination temperatures is determined from the thermal analysis of nickel tungstate powder. The thermal stability and decomposition of the synthesized $NiWO_4$ are studied using thermogravimetric, derivative thermogravimetric and differential thermal analysis using *Perkin Elmer STA 6000*. TGA/DTG/DTA graphs for nickel tungstate nanoparticles prepared under optimum conditions (before calcination) are shown in Fig.3.2. The sample shows a weight loss of 10% in the temperature range of 50-200^{0}C due to dehydration of surface absorbed moisture and gases. This loss of weight is confirmed from the DTG curve as a broad peak observed from the ambient temperature to 300^{0}C. A weak endothermic peak is also observed in the same region of the DTA curve. In the TG curve, the dehydration process continues with a small weight loss of 4% in between 200-440^{0}C. This loss in weight may be attributed to the releasing of the trapped water in the crystalline structure of the sample. The profile reaches a plateau above 440^{0}C. The nickel tungstate nanoparticles are thermally stable, and there is no weight loss above 440^{0}C. Based on the results, the calcination temperatures are chosen as 500, 600 and 700^{0}C.

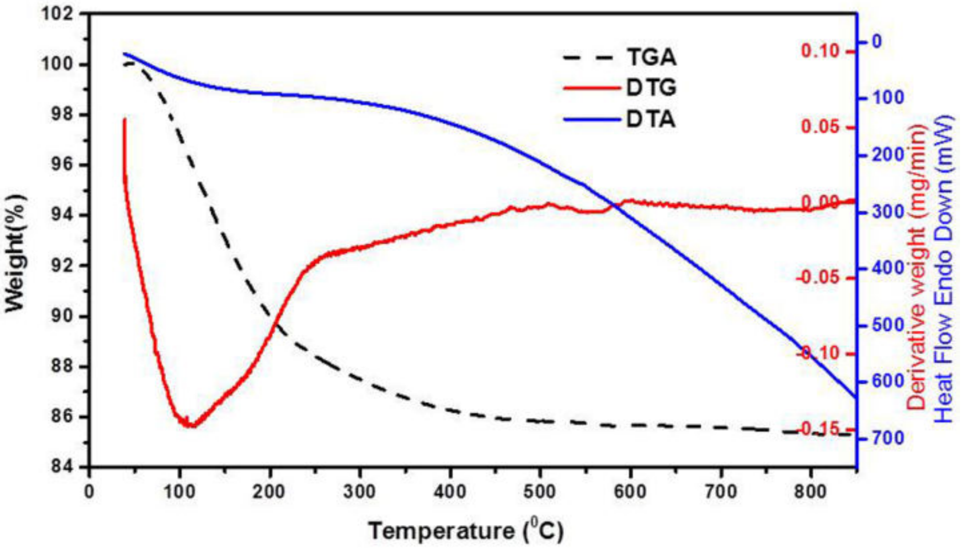

Fig. 3.2 TGA/DTG/DTA curves of $NiWO_4$ nanoparticles.

3.3.2 Analysis of structural properties

The structural analyses of the synthesized nanocrystalline $NiWO_4$ are carried out by following the procedure described in *section 2.3.2* and the effect of calcination temperature is also studied.

3.3.2.1 Powder XRD analysis

Crystalline structure, phase purity and average crystallite size of $NiWO_4$ nanoparticles are determined using XRD patterns. Fig. 3.3 shows the X-ray diffractograms of the $NiWO_4$ samples calcined at 500 (S1), 600 (S2) and 700^0C (S3) taken by a *Bruker AXS D8 Advance* X-ray diffractometer with Cu-Kα radiation ($\lambda = 1.5406$ Å). From the Fig.3.3, it is evident that as calcination temperature rises, intensities of diffraction peaks raise and become sharper, indicating an increase of crystalline nature. Along with that, there is a decrease in full width at half maximum. The XRD patterns obtained agree well with the JCPDS file No. 72-0480. The same crystalline structure is observed for the samples S1, S2 and S3. The XRD patterns of the $NiWO_4$ samples S1, S2 and S3 correspond to wolframite monoclinic structure with *P2/c* space group. In this structure, oxygen atoms are hexagonally close-packed and the metal ions occupy a quarter of all the octahedral sites [1, 2]. The lattice parameters are determined using the formula given in *section2.3.2.1* and their values are compared with the JCPDS values and are presented in Table 3.1.

The average crystallite sizes of $NiWO_4$ nanoparticles calcined at different temperatures are calculated from XRD patterns using the Scherrer equation. Average crystallite sizes estimated for samples S1, S2 and S3 are 14.74, 25.13 and 28.10 nm, respectively. From these values, it can be concluded that crystallite size increases with the increase in calcination temperature.

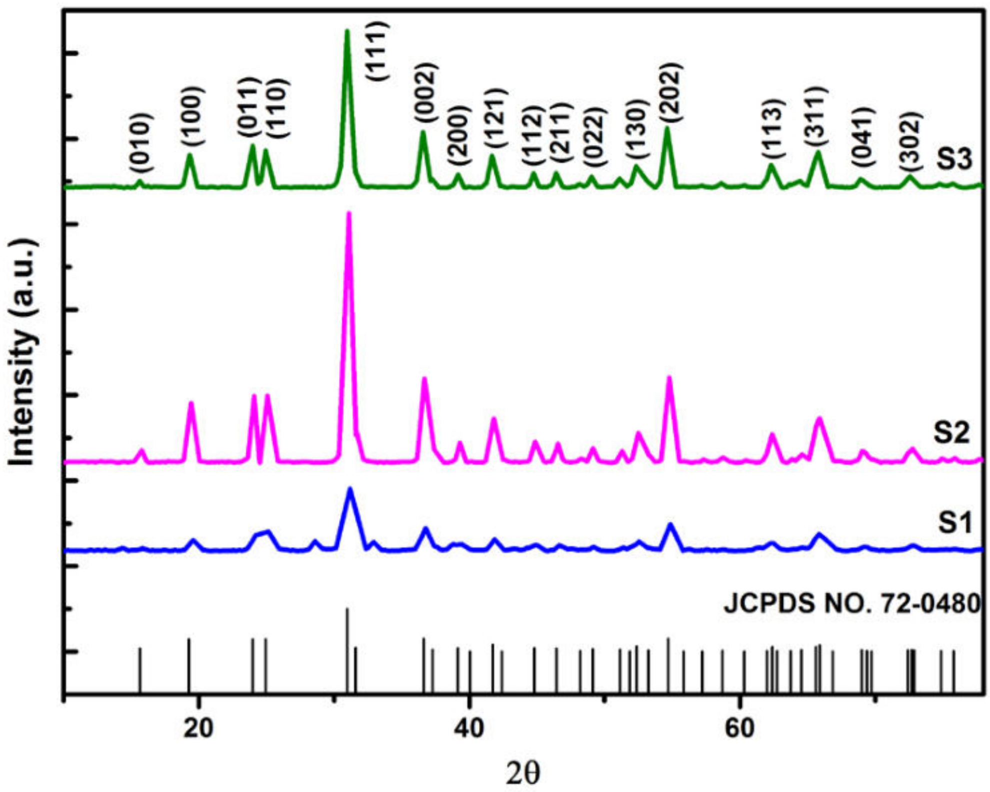

Fig. 3.3 X-ray diffraction patterns of $NiWO_4$ samples calcined at different temperatures.

Table 3.1 Lattice parameters of $NiWO_4$ samples calcined at different temperatures.

Lattice parameter	Sample (S1)	Sample (S2)	Sample (S3)	JCPDS values
a (Å)	4.655±0.093	4.582±0.091	4.592±0.091	4.599
b (Å)	5.439±0.108	5.612±0.112	5.667±0.113	5.660
c (Å)	4.986±0.9972	4.900±0.98	4.907±0.09814	4.906
β	91.943	89.920	89.864	90.030

Williamson–Hall analysis as described in *section2.3.2.1* is carried out to calculate the contributions of size and micro-strain to XRD line broadening. The particle size and micro-strain ‘ε’ on peak broadening of nanocrystalline $NiWO_4$ are estimated for different calcination temperatures using W–H plots. The W-H plots of samples S1, S2 and S3 are shown in Fig. 3.4. Geometric parameters of $NiWO_4$ nanoparticles are presented in Table 3.2.

Table 3.2 Geometrical properties of $NiWO_4$ samples.

Sample	**Average crystallite size (Scherrer equation) (nm)**	**Unit cell volume (10^{-30} m^3)**	**W-H Method**	
			Crystallite size (nm)	**Micro-strain (*10^{-3})**
S1	14.74±0.29	126.18	15.88±0.31	2.63±0.05
S2	25.13±0.75	125.99	24.30±0.24	0.68±0.01
S3	28.10±0.56	126.69	30.27±0.60	0.47±0.01

It can be seen from Table 3.2 that the crystallite sizes estimated from the Scherrer equation and W–H analysis for all the samples are nearly in agreement. Crystallite size increases with an increase in calcination temperature. It can also be seen that the micro-strain for $NiWO_4$ calcined at 500^0C is high, which decreases with the increase in calcination temperature. Micro-strain in crystals may be due to the structural imperfections and surface effects [2, 3]. In the case of calcined samples S2 and S3, the decrease in micro-strain may be due to the removal of defects like dislocations, edges or cuts during the calcination process [3]. So from this analysis, it can be concluded that the increase of calcination temperature leads to the reduction in the micro-strain.

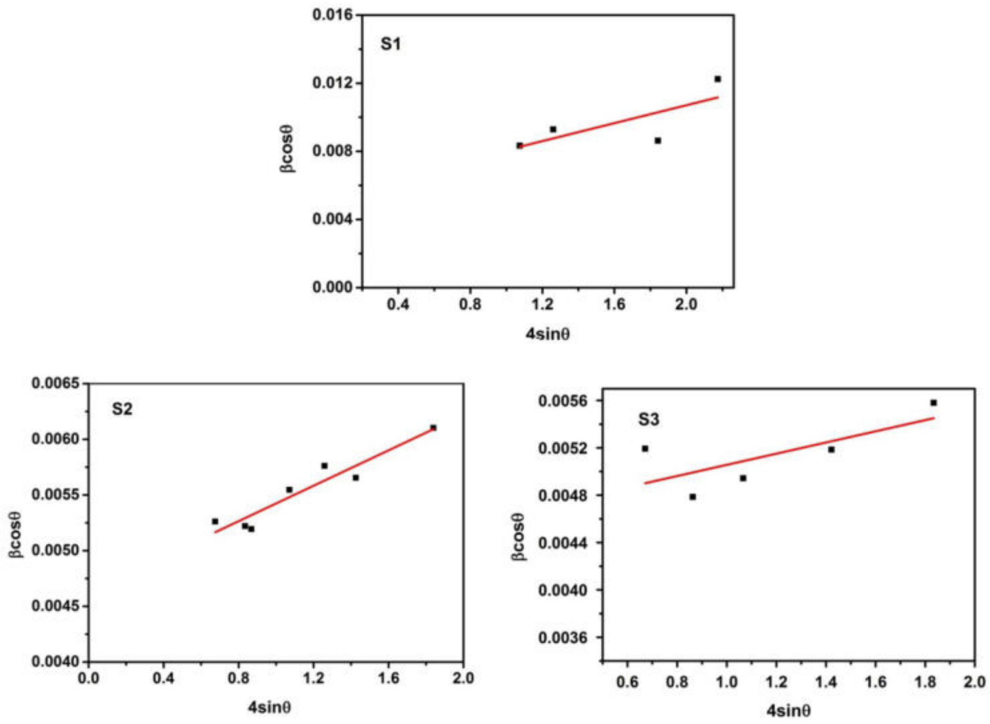

Fig. 3.4 W-H plots of $NiWO_4$ samples

3.3.2.2 TEM analysis

Transmission electron microscopy images of $NiWO_4$ samples are taken by a *JEOL/JEM 2100* (Source: LaB6 and voltage: 200 kV). TEM bright field images of $NiWO_4$ samples (S1, S2 and S3) are shown in Fig.3.5. The bright field images of $NiWO_4$ samples show that nanoparticles formed are not having an exact spherical shape. Moreover, they are found to be agglomerated. From Fig. 3.5, it is evident that the particle size increases with the increase in calcination temperature. The particle size distribution obtained from TEM images is presented in Fig.3.6. The particle size ranges from 8 to 20 nm for S1, 16-30 nm for S2 and 24-38 nm for S3. The average particle size for samples S1, S2 and S3 are 14.84, 28.05 and 32.31 nm respectively. Fig. 3.7 shows the HRTEM images of all the samples. From the figure, it can be seen that all the samples show lattice fringes formed due to the crystal planes formed in the particles. The SAED patterns of nanocrystalline $NiWO_4$ samples are presented in Fig. 3.8. In the figure, all samples show bright spots that confirm the crystalline nature of the samples. The crystal planes which show high-intensity peaks in the XRD can be indexed from the SAED pattern. The calculated inter-planar spacing(d_{hkl}) values from SAED patterns are compared with the XRD results to index the planes. The comparison of d_{hkl} values with XRD values for different planes of $NiWO_4$ samples are presented in Table 3.3.

Table 3.3 Inter-planar spacing (d_{hkl}) and the corresponding planes of samples S1, S2 and S3.

S1			**S2**			**S3**		
Plane	**Measured fromSAED d (A^0)**	**Measured from XRD d (A^0)**	**Plane**	**Measured fromSAED d (A^0)**	**Measured from XRD d (A^0)**	**Plane**	**Measured fromSAED d (A^0)**	**Measured from XRD d (A^0)**
(010)	5.543	5.587	(010)	5.409	5.611	(010)	5.395	5.654
(100)	4.401	4.533	(111)	2.886	2.875	(110)	3.388	3.567
(011)	3.448	3.537	(112)	1.994	2.018	(111)	2.882	2.886
(002)	2.591	2.447	(130)	1.723	1.742	(002)	2.386	2.454
(112)	2.046	2.017	(311)	1.345	1.416	(211)	1.914	1.955
(130)	1.695	1.740				(220)	1.809	1.785
(302)	1.268	1.298				(311)	1.391	1.418

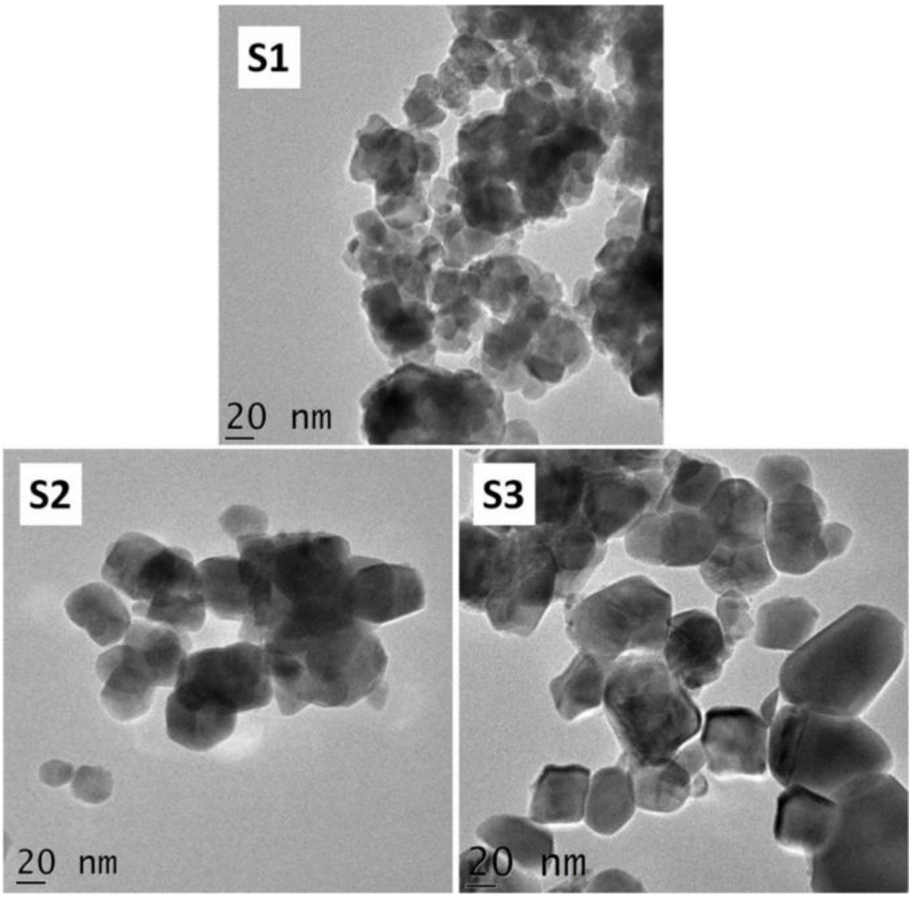

Fig.3.5 TEM bright-field images of $NiWO_4$ samples.

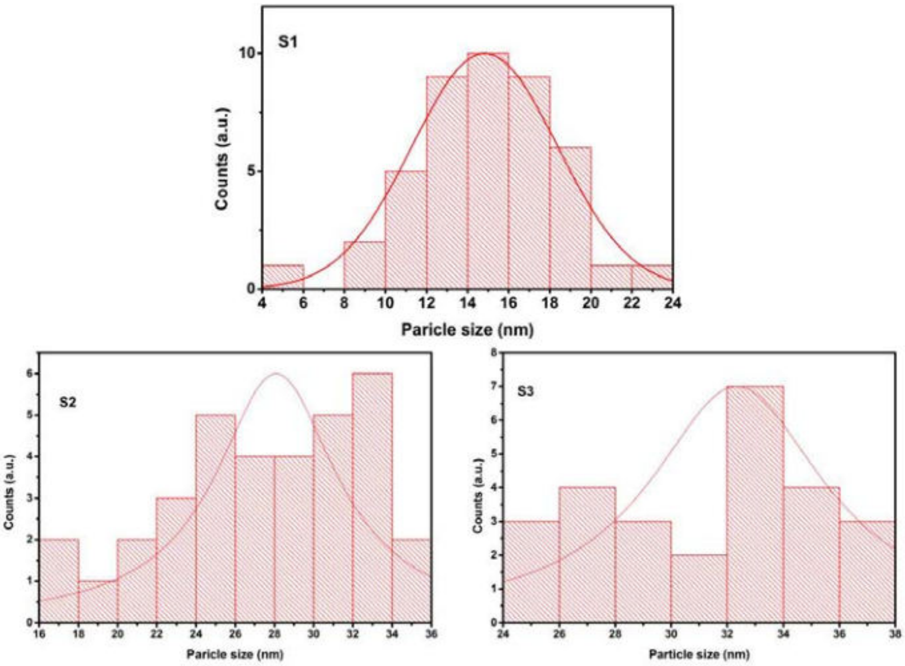

Fig.3.6 Size distribution graphs of $NiWO_4$ samples.

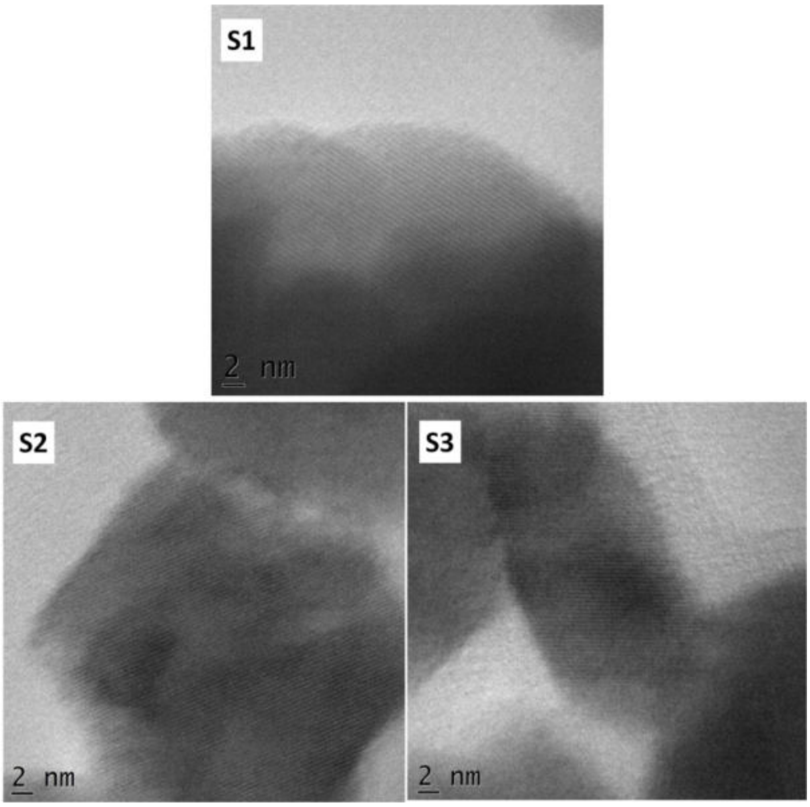

Fig.3.7 HRTEM images of $NiWO_4$ samples.

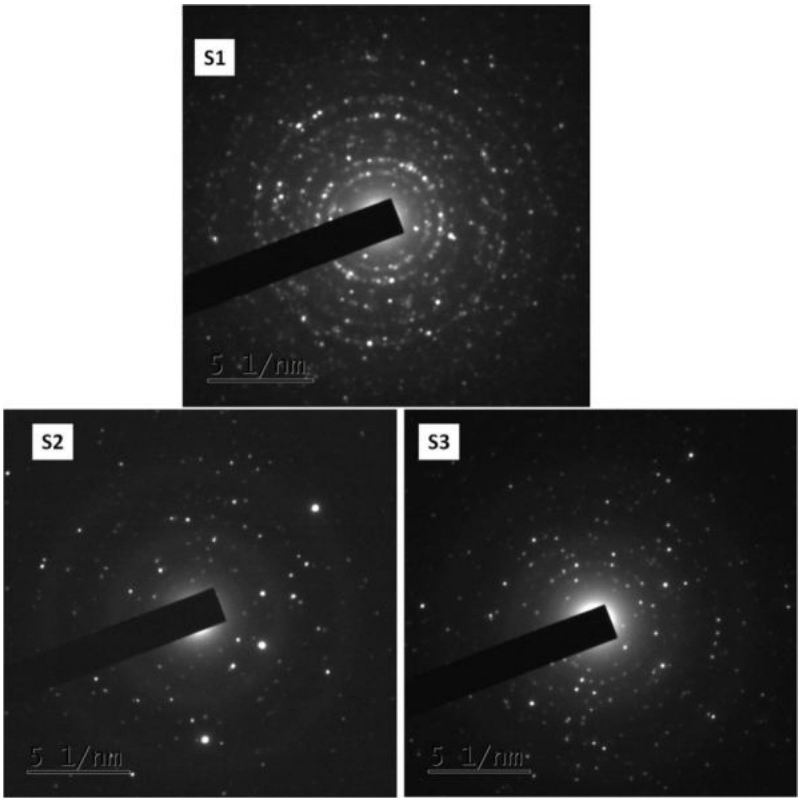

Fig.3.8 SAED patterns of $NiWO_4$ samples.

3.3.2.3 FE-SEM and EDS analysis

The surface morphology of the nickel tungstate nanoparticles is studied with the help of field emission scanning electron microscopy. The micrographs of the samples are taken using the instrument *FEI (Model- Nova Nano SEM 450)* operating at 15 kV. Fig. 3.9 shows the FE-SEM images of the $NiWO_4$ samples with a magnification of 150000. From the figure, it can be seen that spherical nanoparticles combined to form clusters which result in coral-like structures. As the calcination temperature increases, the spherical nanoparticles are changing their shapes to cube-like structures [2].

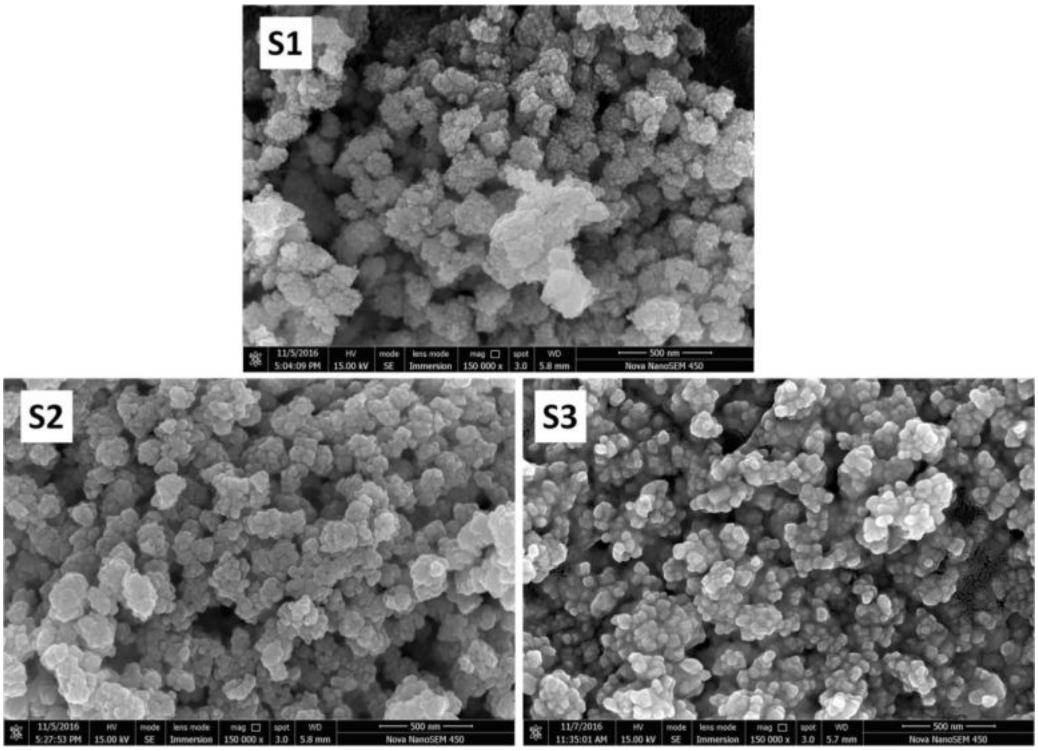

Fig. 3.9 FESEM images of $NiWO_4$ samples at different calcination temperatures.

The energy-dispersive X-ray spectroscopy is used to analyse the chemical composition of the as-prepared samples. This is done with the help of *BRUKER EDS detector (Model- XFlash 6/10)*. The EDS image of the $NiWO_4$ sample calcined at 500^0C is shown in Fig. 3.10. The image confirms the presence of Ni, W and O in the correct stoichiometric ratio. Also, no impurities are observed in the synthesized $NiWO_4$ samples. Table 3.4 gives the EDS data for all the three samples S1, S2 and S3. For the sample S1, Ni and W are in the correct stoichiometry with a negligible oxygen deficiency. For sample S2 the same behaviour is observed with a slight increase in oxygen deficiency. For S3, Ni and W are in high percentage with comparatively large oxygen deficiency. From EDS analysis, it can be found that calcination introduces slight variation in atomic percentages. Mainly, oxygen deficiency is found to be increasing with the increase in calcination temperature.

Table. 3.4 EDS data of $NiWO_4$ samples S1, S2 and S3.

Sample	Elements	Atomic number	Series	Wt. %	At.%
S1	W	74	L- Series	58.91	15.64
	O	8	K- Series	22.62	69.00
	Ni	28	K- Series	18.47	15.36
S2	W	74	L- Series	58.9	15.74
	O	8	K- Series	22.31	68.53
	Ni	28	K- Series	18.79	15.73
S3	W	74	L- Series	59.88	16.96
	O	8	K- Series	20.04	65.23
	Ni	28	K- Series	20.08	17.81

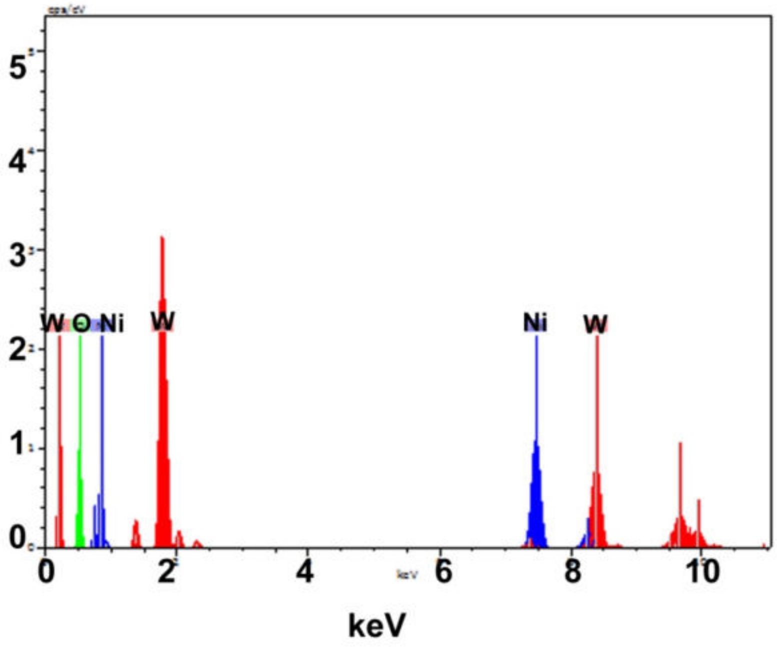

Fig. 3.10 EDS image of the $NiWO_4$ sample calcined at 500^0C.

3.3.2.4 FT-IR analysis

FT-IR spectra of the samples S1, S2 and S3 are recorded by FT-IR spectrophotometer (*Thermo Nicolet, Avatar 370*) in the range 3750 to 450 cm^{-1}. Fig.3.11 shows FT-IR spectra of $NiWO_4$ samples calcined at different temperatures. The wide peaks at about 3414 cm^{-1} confirm the presence of moisture. The main absorption bands of wolframite type structure appear in the range of 450-1000 cm^{-1}. In comparison with previous investigations [4], these peaks are attributed to the vibration bands of the $NiWO_4$. Fig. 3.12 represents the FT-IR spectra of S1, S2 and S3 in the range 300 – 1200 cm^{-1}. The bands at 944 and 997 cm^{-1} correspond to the stretching modes of the W=O terminal bond present in each octahedron of WO_3 [2,5]. The bands at 869 and 806 cm^{-1} arise from vibrations of the WO_2 present in the W_2O_8 groups. The absorption band at 622 cm^{-1} is typical of a two-oxygen bridge (W_2O_2) and corresponds to the asymmetric stretching of the same units [2,6-9]. The observed absorption below 500 cm^{-1} corresponds to the asymmetric stretching vibrations of the NiO_6 polyhedra [2,10, 11]. On an increase in calcination temperature, noticeable changes are observed in the positions of vibration bands of $NiWO_4$ samples. The vibration bands shift slightly due to lattice expansion and anharmonic effects that reflect the rigidity of the tungstate lattice. From the Fig.3.12, it can be seen that for the samples S2 and S3, the bands at 997 and 944 cm^{-1} are disappeared. This may be due to the absence of the stretching of the W-O bond with an increase in calcination temperature. An additional band at 690 cm^{-1} for S2 and S3 are formed. This may be due to distortions induced in some W=O terminal bonds with the increase in temperature. In Table 3.5, IR active modes obtained for the $NiWO_4$ samples are compared with the literature values [12]. To summarize, synthesized nanocrystalline $NiWO_4$ has wolframite structure with the characteristics bonds and changes are observed in the positions of vibration bands with the increase in calcination temperature.

Table 3.5 Comparison of IR- active modes of $NiWO_4$ with the literature values.

Literature value [12](cm^{-1})	**Present work (cm^{-1})**		
	S1	**S2**	**S3**
432	455	456	458
494	---	---	---
523	527	529	527
533	---	---	---
---	623	621	615
681	677	690	690
---	806	819	822
877	869	869	874
961	944	---	---
---	997	---	---

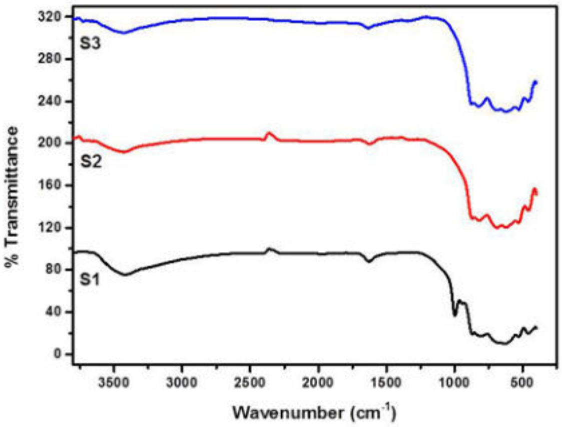

Fig. 3.11 FT-IR spectra of $NiWO_4$ samples calcined at different temperatures.

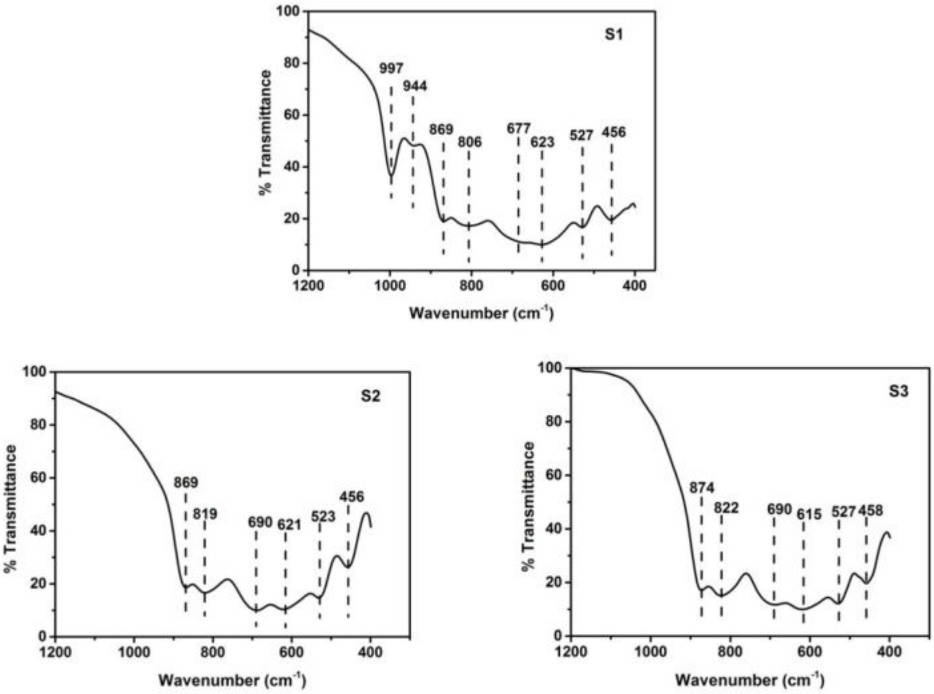

Fig. 3.12 FT-IR spectra of $NiWO_4$ samples for the range of 300-1200 cm^{-1}.

3.3.2.5 Raman analysis

Raman spectroscopy is used to probe short-range ordering in the samples. The Raman spectra of samples are taken by *Alpha 300 RA AFM & RAMAN*. Raman spectra of $NiWO_4$ are sensitive mainly to the tungsten sublattice since the nickel environment shows relatively weak Raman activity. As $NiWO_4$ belongs to the monoclinic, *P2/c* wolframite structure, it would be expected to give six internal stretching modes caused by each of the six W-O bonds in the WO_6 octahedrons. From the site- group method [2,13], it is possible to obtain the following distributions for the Raman first-order modes; $\Gamma = 8A_g+10B_g$. So there are 18 Raman active modes for $NiWO_4$. Fig.3.13 shows the Raman spectra of $NiWO_4$ nanoparticles obtained after calcination at different temperatures.

Table 3.6 compares the phonon active modes of $NiWO_4$ with the literature values [12]. From Fig.3.13 and Table 3.6, it can be seen that Raman spectra of $NiWO_4$ samples at room temperature consisting of 14 Raman active modes in the range of 45-1200 cm^{-1}. The spectra obtained agree with the literature values with a slight difference in the band frequency.

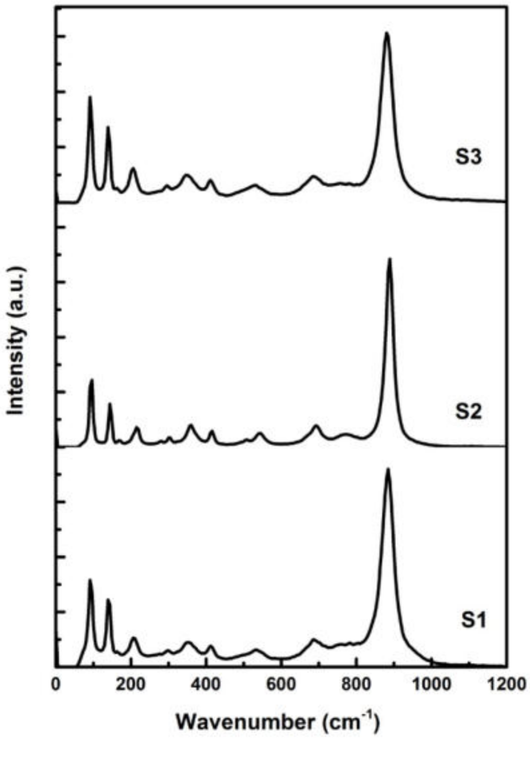

Fig.3.13 Raman spectra of $NiWO_4$ nanoparticles calcined at different temperatures.

Table. 3.6 Raman active modes of $NiWO_4$ samples.

ν (cm^{-1}) [12]	**Phonon symmetry**	**S1 (cm^{-1})**	**S2 (cm^{-1})**	**S3 (cm^{-1})**
97	B_g	91.4	94.7	91.6
149	A_g	139.3	144.4	139.7
174	B_g	163.8	169.1	163
197	B_g	----	----	----
210	B_g	207.7	215.2	205.9
223	A_g	----	----	----
287	A_g	276.2	281.2	296.1
307	A_g	298.7	303.3	----
326	B_g	----	----	----
363	A_g	353.4	359.7	349.1
380	B_g	----	----	----
418	A_g	412.3	416.1	411.5
512	B_g	----	506.6	----
549	A_g	533.1	543.8	531.1
675	B_g	686.6	----	----
697	A_g	717.4	693.4	685.7
775	B_g	783	773.2	781.8
893	A_g	883.8	889.2	880.9

The most intense band observed at 884 cm^{-1} is assigned to the A_g mode. In the case of a regular octahedron, the symmetric stretch is expected to have the maximum frequency. So this band originates from the symmetric stretching of shortest terminal W-O bond [2, 14]. The bands at 783 and 717 cm^{-1} are attributed by B_g and A_g modes, respectively. They are due to the asymmetric stretching of the W-O bonds. The bands at 412, 353 and 207.7 cm^{-1} are assigned to $2A_g$+B_g modes, originate from the bending modes of the regular octahedron [2,15]. Other bands are contributed by asymmetric stretching vibration modes of longer W–O bond, symmetric stretching vibrations of longer W–O bond, deformation vibration of short W–O bonds, and inter-chain deformation modes and lattice modes [2,16, 17]. It can also be seen that Raman peaks shift slightly as calcination temperature is increased, which may be due to particle size elevation.

3.3.3 Analysis of optical properties

UV-VIS-NIR spectroscopic studies and photoluminescence studies of $NiWO_4$ nanoparticles calcined at different temperatures are presented here. The analyses are carried out by following the procedure as given in *section 2.3.3.*

3.3.3.1 UV-VIS-NIR analysis

To characterize the absorption properties, absorption spectra of the $NiWO_4$ samples are obtained using a double-beam UV–Visible spectrophotometer (*Cary 5000 model*) with a scan rate of 600 nm/min. The spectra are recorded in the wavelength range 224–1976 nm. Fig.3.14 shows the optical absorbance spectra of $NiWO_4$ samples calcined at different temperatures. It shows that $NiWO_4$ nanoparticles have good light absorption properties in the ultraviolet, visible and infrared wavelengths. These spectra have main absorption peak in the region 270-315 nm (4.58-3.93 eV). This absorption peak may be attributed to the charge transfer transition in the WO_6 matrix. In metal tungstates, the ultraviolet absorption is attributed to the excitation in O and W within the WO_6 matrix [2,18]. The two peaks in the visible region around 450 nm (2.75 eV) and 740 nm (1.68

eV) are due to the forbidden electronic transition from $^3A_{2g}$ to ^1E_g and the electronic transition from $^3A_{2g}$ to $^1T_{2g}$, respectively [2,19]. The band around 825 nm (1.50 eV) can be assigned to the $^3T_1$ to $^1T_2$ transition in $Ni^{2+}O_4$. So this band represents the presence of $Ni^{2+}O_4$ arising from Frenkel defects which are present in the sample by the dislocation of Ni^{2+} from the octahedral to tetrahedral sites. A broad absorption band is observed in the IR wavelength range 1300-1600 nm. This IR absorption may be due to the presence of Ni^{3+} present in the sample [19]. From the Fig. 3.14, it can also be seen that the absorption peaks are slightly shifted towards higher wavelength region upon calcination at a higher temperature. This redshift is due to particle size elevation of the samples with the increase in calcination temperature [2,20].

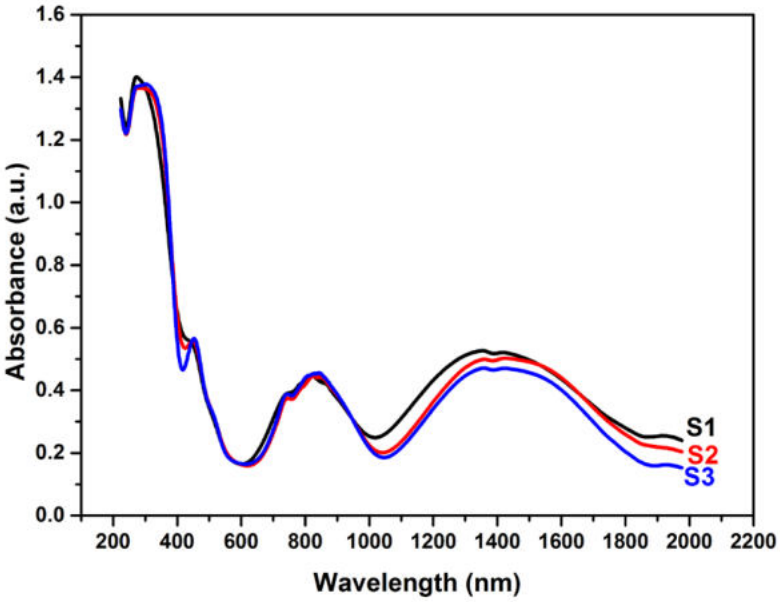

Fig. 3.14 Optical absorbance spectra of $NiWO_4$ samples calcined at different temperatures.

In metal tungstates, there is a chance of having both direct and indirect band transitions [21]. In the case of $NiWO_4$, the valance band is formed by hybridized O_{2p} and Ni_{3d} states, and the Ni_{3d} states contribute mainly to the upper part of the valance band. The conduction band is formed by the empty W_{5d} states with an admixture of the empty Ni_{3d} states at the bottom of the band [12]. Optical absorption below the fundamental absorption edge can be explained by the ligand field theory. According to this theory, optical transitions occur between crystal- field-split levels of the $3d^n$ ion. Even though 3d electrons are not completely localized, electron transfer between the 3d and ligand orbitals and between neighbouring 3d sites occurs to some extent. A cluster NiO_6^{-10}, where Ni atom is octahedrally coordinated by O atoms, is considered to explain the energy levels as the spectral shape of $NiWO_4$ is similar to that of NiO [22]. To analyse the electronic structure of $NiWO_4$, energy levels diagram of NiO_6^{-10} cluster [23] is considered and is shown in Fig.3.15. The figure explains d-d transitions taking place along with the charge transfer transitions in NiO_6. The dashed lines represent those configurations which interact strongly via Ni 3d- O2p hybridization.

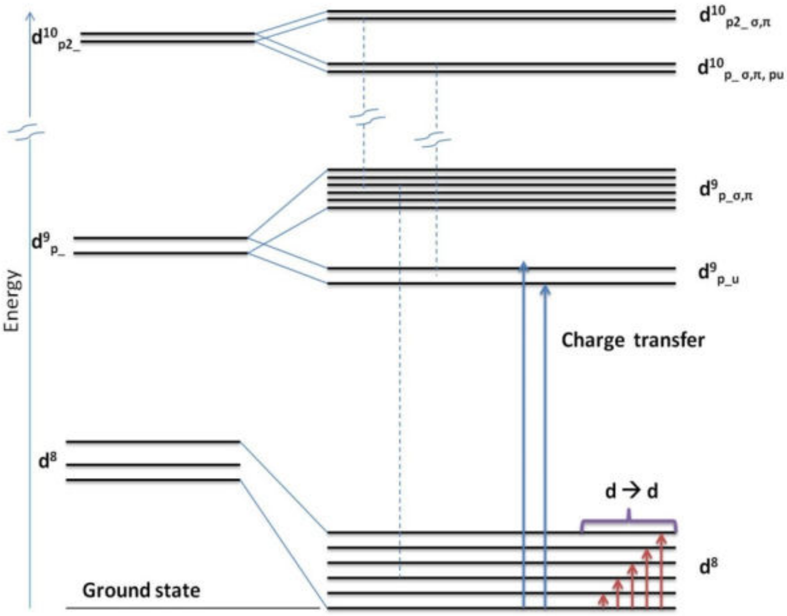

Fig.3.15 Energy level diagram of NiO_6^{-10} cluster.

[$^3A_{2g}$ represents the ground state. In d^8 configuration $^3T_{2g}$, $^1T_{1g}$, $^3T_{1g}$, $^1T_{2g}$, $^1E_{1g}$, $^1A_{1g}$ represent excited states. P_σ and p_π are having symmetry of ^2E_g and $^2T_{2g}$ respectively]

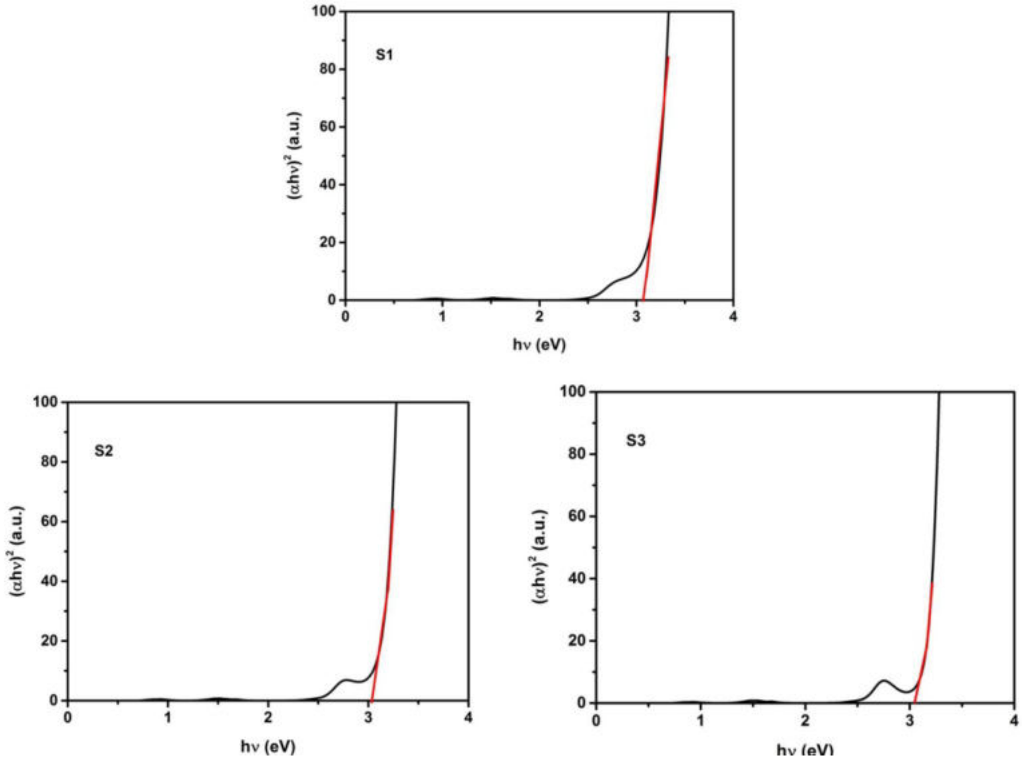

Fig.3.16 Tauc plots for direct bandgap energy of $NiWO_4$ samples calcined at different temperatures.

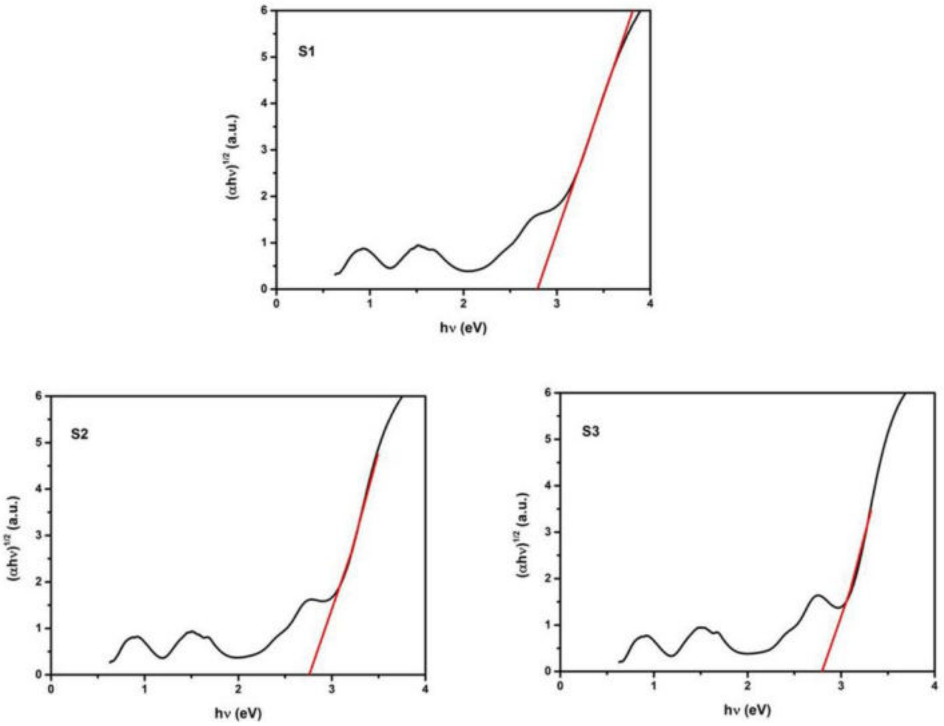

Fig.3.17 Tauc plots for indirect bandgap energy of $NiWO_4$ samples calcined at different temperatures.

From reflectance data, absorption co-efficient ‘α’ is calculated for the $NiWO_4$ samples. Both direct and indirect optical bandgap energies of samples are measured by Tauc plots [23, 24]. In Tauc plot, $(\alpha h\nu)^2$ and $(\alpha h\nu)^{1/2}$ are plotted as a function of photon energy for direct and indirect bandgaps respectively. The linear portion of the curves is extrapolated to absorption equal to zero to get the bandgap value. The Tauc plot for direct and indirect bandgaps of $NiWO_4$ are shown in Fig.3.16 and Fig.3.17 respectively. From Fig.3.16 and 3.17, both direct and indirect optical bandgap values are estimated for samples S1, S2 and S3, and are tabulated in Table 3.7. It can be seen that both direct and indirect bandgap values of samples decrease slightly with the increase in calcination temperature. As calcination temperature increases, the level of the conduction band may be decreased, which in turn results in the reduction of bandgap energy.

Table 3.7 Direct and indirect optical band gaps of $NiWO_4$ samples.

Sample	Direct bandgap (eV)	Indirect bandgap (eV)
S1	3.07	2.80
S2	3.02	2.78
S3	3.02	2.78

3.3.3.2 Photoluminescence analysis

PL studies provide information relating to different energy states available between valance band and conduction band, which are responsible for radiative recombination. Fig. 3.18 shows room temperature PL emission spectra of the synthesized $NiWO_4$ nanoparticles under different calcination temperatures recorded by *Horiba fluorescence spectrometer* (slit width of 3.0 nm), using 350 nm excitation wavelength. Using 350 nm excitation, the PL emissions for $NiWO_4$ nanoparticles are obtained at a wavelength range of 350-550 nm. This may be due to the presence of states within the bandgap of the material that may involve in the emission [24]. As the PL emission mainly results from the recombination of photoexcited electrons and holes, the emission spectra of the $NiWO_4$ samples show similar peak positions with varied PL intensities. Samples S1, S2 and S3 show nearly the same peaks. The patterns are similar to other wolframite compounds with two major peaks at 412 nm (3.01 ev) and 433 nm (2.86 eV). The observed patterns may be originated from the WO_6^{6-} anion along with some defects in the crystal structure [2,25]. The emission peak at 412 nm is mainly attributed to charge transfer transitions within the WO_6 octahedra [24]. The emission peaks of 454 nm (2.74 eV) and 481 nm (2.58 eV) are due to the transitions $^3A_{2g}$ to $^3T_{1g}$ and $^3A_{2g}$ to a $^1T_{2g}$, respectively taking place within the NiO_6 polyhedra [2,26]. They are the d-d transitions for octahedrally co-ordinated Ni^{2+}. As $NiWO_4$ is a self-activated luminescent tungstate [27], the luminescence origin is intrinsic luminescence. So intrinsic defects, such as oxygen vacancies and interstitial atoms may be present in these samples [28].

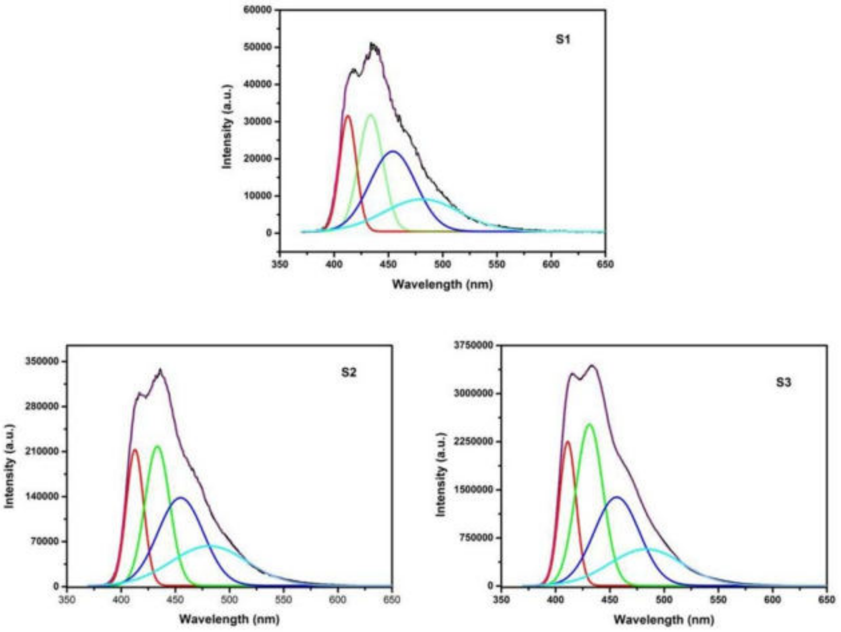

Fig. 3.18 PL spectra of $NiWO_4$ nanoparticles at different calcination temperatures.

Maximum PL emission intensity is obtained for sample S3 and minimum for S1. In short, the increase in calcination temperature results in an increase in PL emission. This increase in PL intensity may be due to the increase in oxygen vacancies caused by the increase in calcination temperature. The high PL emission of S3 makes it a suitable candidate for luminescence application while the low PL emission of S1 makes it a suitable material for photocatalytic applications.

The CIE XYZ colour space encompasses all colour sensations that are visible to a person with average eyesight. CIE XYZ (Tristimulus values) is a device-invariant representation of the colour and it serves as a standard reference. Figure 3.19 shows the CIE chromaticity diagram for the samples S1, S2 and S3. The **x** and **y** chromaticity co-ordinates under the excitation of 350 nm are calculated in the CIE XYZ colour space. The CIE chromaticity coordinates of the samples S1, S2 and S3 are presented in Table 3.8. All three samples show purplish-blue emission. Only slight changes for the chromaticity co-ordinates can be found for $NiWO_4$ samples with the increase in calcination temperature. In short, the results of the PL and CIE chromaticity studies suggest that the $NiWO_4$ nano-phosphors can be used to construct near-ultraviolet (NUV) light excited purplish-blue light-emitting diodes (LEDs).

Table 3.8 Chromaticity coordinates of the samples S1, S2 and S3.

Sample	**S1**	**S2**	**S3**
x	0.1562	0.1527	0.1505
y	0.0889	0.0879	0.0812

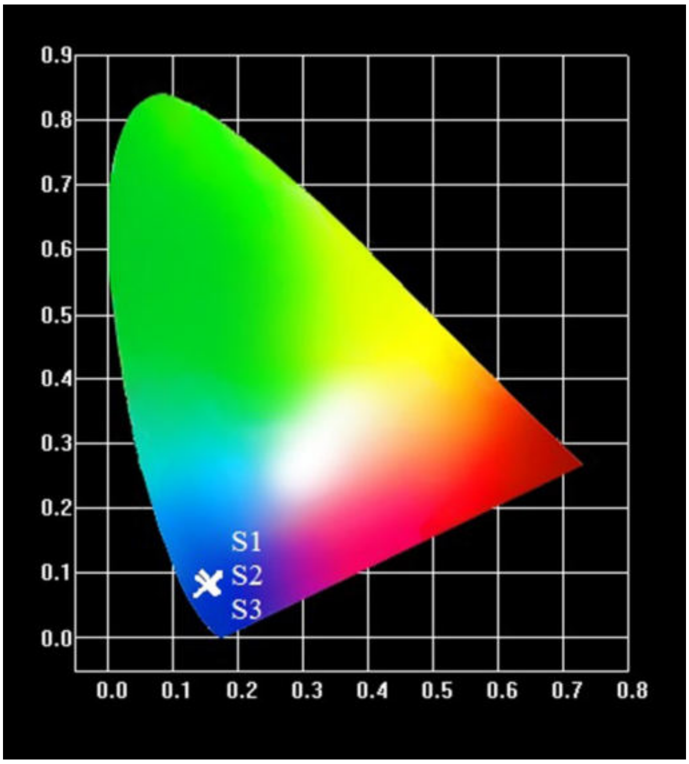

Fig. 3.19 CIE chromaticity diagram of $NiWO_4$ samples.

3.3.4 Analysis of magnetic properties

Fig.3.20 shows the VSM magnetic measurements at room temperature for the $NiWO_4$ nanoparticles calcined at different temperatures. Magnetic measurements of the samples are carried out in a vibrating sample magnetometer (*Lakeshore VSM 7410*) at room temperature in an applied magnetic field sweeping between ± 15000 Oe. From Fig.3.20, $NiWO_4$ shows a paramagnetic behaviour at room temperature. As the calcination temperature increases, the curve shows a shift towards the lower magnetic moment. The magnetic properties of the calcined samples are presented in Table 3.9.

From Table 3.9, it can be concluded that magnetic properties vary with the calcination temperature. The saturation magnetic field is reduced with the increase in calcination temperature or with the increase in particle size. The variation of coercivity and retentivity with particle size is shown in Fig. 3.21. The reduction of coercivity and retentivity with the increase in particle size can be seen. Also, the reduced remanence slightly decreases with the increase in particle size. For the sample calcined at a lower temperature (S1), the internal strain is high, this may lead to the presence of uniaxial magnetic anisotropy. On increasing the calcination temperature, the particle size increases and correspondingly the strain decreases. The magnetic anisotropy also decreases and this may result in the lowering of coercivity and retentivity [2,29].

Table 3.9 Magnetic properties of $NiWO_4$ nanoparticles calcined at different temperatures.

Sample	**S1**	**S2**	**S3**
Coercivity (Oe)	486.42	427.89	362.07
Retentivity (emu/g)	7.69E-03	6.73E-03	4.25E-03
Saturation magnetization (emu/g)	1.63E-01	1.49E-01	1.02E-01
Reduced remanence	4.72E-02	4.52E-02	4.16E-02

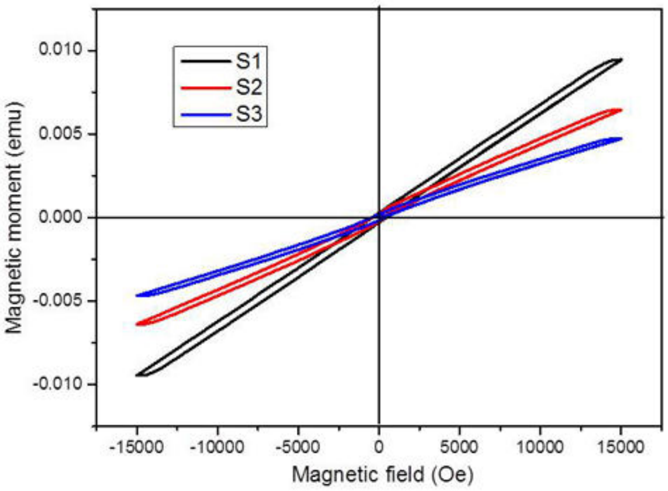

Fig. 3.20 VSM curves of $NiWO_4$ nanoparticles calcined at different temperatures.

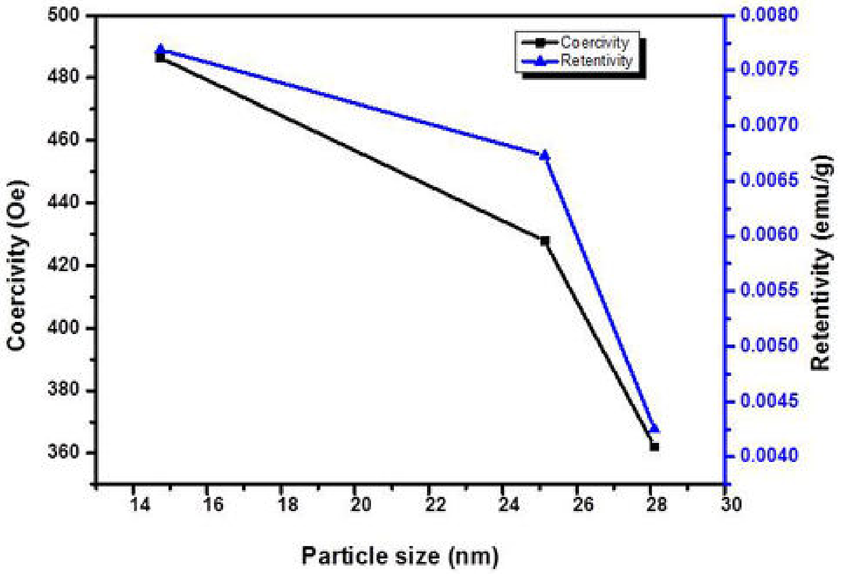

Fig. 3.21 Variation of coercivity and retentivity with particle size.

3.3.5 Analysis of electrical properties

Electrical studies are carried out by following the procedure given in *section 2.3.5*. The electrical measurements are performed by making cylindrical pellets by applying a pressure of 7 GPa using a hydraulic press. The thickness and diameter of the pellets are 1.7 and 13 mm respectively. The pellets are then sintered at 500^0C for 1.5 h. The silver paste is applied to both the faces of the pellets for good electrical contact. The dielectric and impedance spectra are measured in the frequency range 50 Hz-5 MHz at room temperature by using *Wayne Kerr H- 6500B* model impedance analyser.

3.3.5.1 Dielectric analysis

Fig.3.22 represents the room temperature frequency response of the real part of the dielectric constant of $NiWO_4$ samples calcined at 500, 600 and 700^0C. It can be seen from Fig. 3.22 that $NiWO_4$ samples exhibit a similar type of response against frequency. At low frequency, the real part of dielectric constant (ε') is high for the $NiWO_4$ samples, and it decreases with the increase in frequency. It shows a dispersion behaviour at low frequency region 50-1000 Hz. The ε' attains a constant value at high frequency region. The values of ε' for the three samples at different frequencies are listed in Table 3.10. The high value of ε' at low frequency for the samples may be due to the electrode polarization effect. The dispersion behaviour shown by the samples can be explained based on space charge polarization. The theoretical basis for this can be given by Maxwell–Wagner-type interfacial polarization [30, 31] and Koop's phenomenological theory [32]. Both theories explain the consequences of the existence of conducting grains separated by poor conducting grain boundaries. The external electric field causes constrained building up of charges in the grain boundaries. This process produces large polarization and high dielectric constant in the lower-frequency region. But when the frequency increases, grains become more effective as the charge carriers cannot chase the high frequency AC field. So the polarization decreases and correspondingly the value of ε' decreases rapidly.

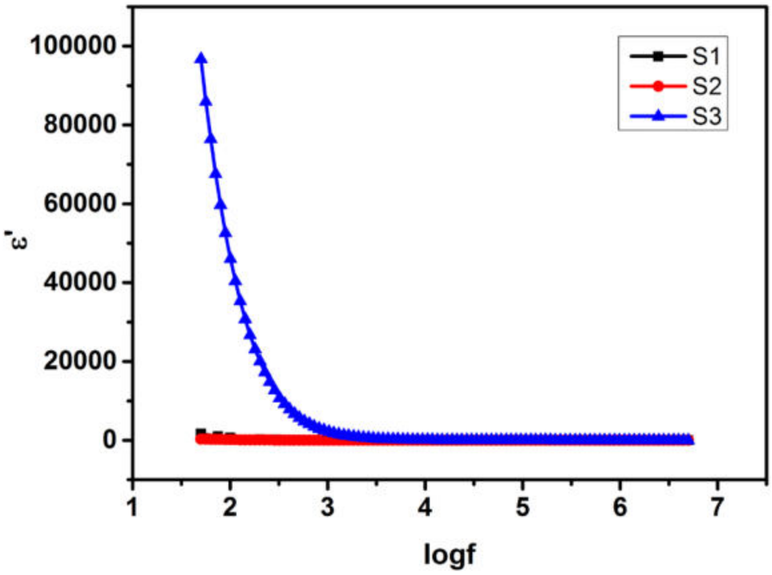

Fig. 3.22 Room temperature frequency response of the real part of dielectric constant for $NiWO_4$ sample calcined at different temperatures.

The energy band structure of the material is important to study the conduction mechanism. It is well known that in the 3d transition metal oxides, the 4s and 4p orbital overlap the 2s and 2p oxygen orbitals. Because of the hybridization of the overlapping orbital, a very high energy gap exists connecting the filled 2p band associated with the oxygen ions and the bottom of the 4s and 4p bands of the transition metal. In nickel tungstate, each nickel ion is bonded to six oxygen ions with octahedral coordination. Exchange splitting and the resulting octahedral crystal splits the 3d-orbital into a lower triplet of t_{2g} symmetry and a higher doublet of e_g symmetry. Therefore, the valence band will consist of a filled O^{2-}: 2p and Ni^{2+}: $3d^8$ [$T_{2g}{}^6$ $E_g{}^2$] bands. The conduction bands are Ni^{2+}: $3d^2$ [$E_g{}^2$] and W^{6+}:5d bands [2, 33, 34]. This type of band structure leads to three possible electronic conduction mechanisms: (i) excitation of electrons from filled O^{2-} : 2p band to a conduction band, (ii) hopping conduction of electrons between neighbouring metal ions and (iii) excitation of d electrons from the filled valence band to empty conduction bands. The possibilities (i) and (iii) may be discarded as it needs a high amount of energy. Here in this work room temperature studies are considered. So the most probable conduction mechanism in the present case may be the hopping of charge carriers.

In $NiWO_4$, short-range self- polarization of the lattice occurs at lower temperature and it traps holes (cationic impurities) at local ionic sites. Hole transport occurs by electron exchange from Ni^{2+} to adjacent Ni^{3+}. It also occurs due to the hygroscopic nature of the compound and possible transition metal impurities. Therefore the material is a p-type conductor below 660 K [33, 35]. In $NiWO_4$, surface defects may lead to the existence of Ni^{3+} ions. Permanent defects are metal vacancies. A nickel cation vacancy produces two acceptor states (holes): Ni^{3+}- V_{M}- – Ni^{3+}, where V_{M}- is a cation vacancy. A Ni^{3+} ion thus introduced into the crystal jumps from one Ni^{2+} site to another. Hence, high conductivity is shown by $NiWO_4$ at room temperature. As $NiWO_4$ contains narrow 3d bands when the carriers hop between Ni^{2+} and Ni^{3+}, local polarization takes place and this is adequate to trap them at one lattice site and leads to the formation of small polarons.

From Table 3.10 it can be analysed that calcination temperature has a significant effect on the dielectric properties of $NiWO_4$ samples. When the calcination temperature of the sample is increased from 500 to 600^0C, there is a reduction in the parameter. But when the calcination temperature is increased to 700^0C, the dielectric constant attains high value in all the frequency regions as compared to S1 and S2. From the dielectric analysis it can be inferred that by changing the calcination temperature, the real part of the dielectric constant of $NiWO_4$ can be varied.

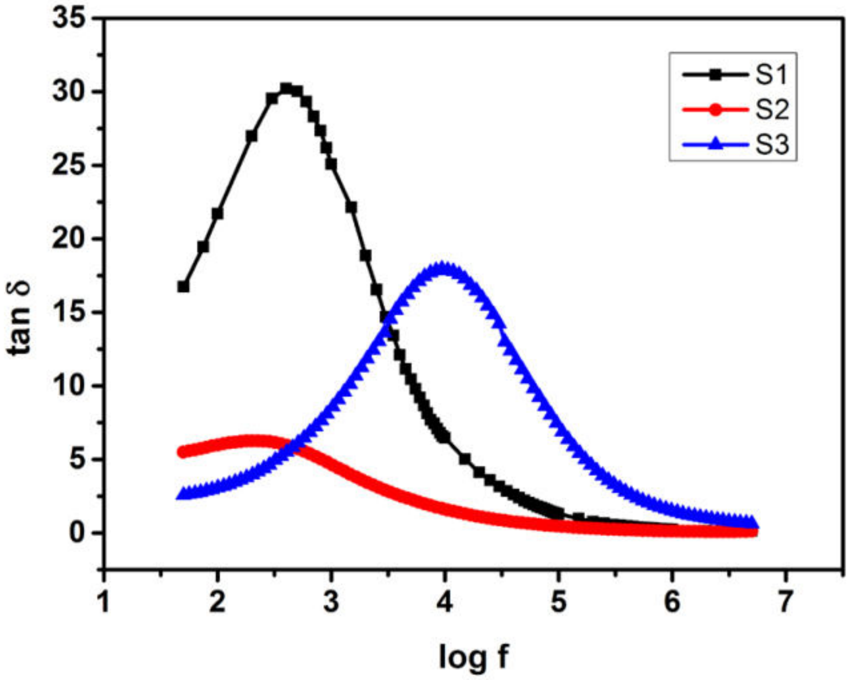

Fig. 3.23 Room temperature frequency response of dissipation factor for $NiWO_4$ nanoparticles calcined at different temperatures.

Table 3.10 Real part of dielectric constant at different frequencies of $NiWO_4$ samples.

Sample	ε' at 50 Hz	ε' at 1000 Hz	ε' at 10^5 Hz
S1	1682	54	10
S2	310	22	6
S3	96727	1814	30

Fig. 3.23 shows the room temperature frequency response of the dissipation factor of $NiWO_4$ samples calcined at 500, 600 and 700^{0}C. For sample S1, there is a peak in the low frequency region. But this peak shifts to a high frequency region by increasing the calcination temperature. The peak in the tanδ curve implies the relaxation process taking place in the samples. For the samples S2 and S3, the loss is small as compared with the sample S1. At high frequencies, all the curves approach zero.

3.3.5.2 Impedance analysis

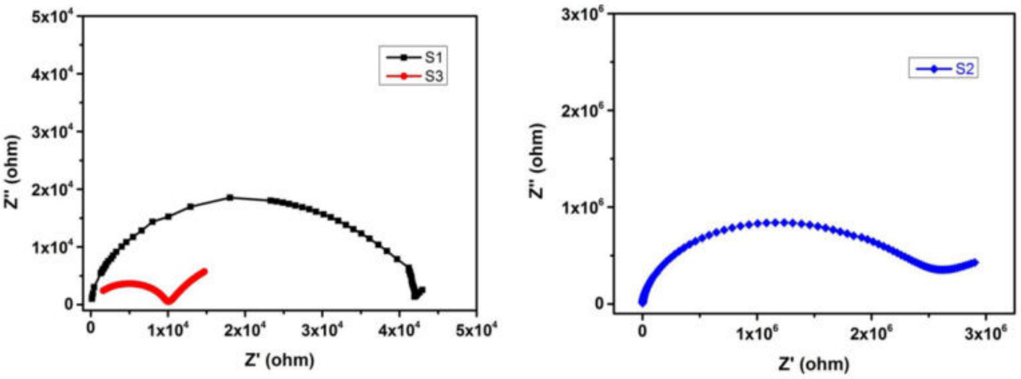

Fig. 3.24 Room temperature Nyquist plots of $NiWO_4$ samples calcined at 500, 600 and 700^{0}C.

Nyquist curves are drawn to understand the type of conduction taking place in $NiWO_4$ samples. The electrical properties of polycrystalline materials have contributions from grains, grain boundaries and specimen electrode interfaces. At low frequencies, the effects of grain boundaries and electrode polarization are dominated. However, at high frequencies, the effect of grains dominates. Both of these contributions can be represented by an equivalent circuit containing parallel R-C elements connected in series [36]. Fig. 3.24 represents the Nyquist plots of the $NiWO_4$ samples calcined at 500, 600 and 700^0C. All the samples show two overlapping semi-circular arcs with their centres lie below the real axis and a line making 45^0 with the real axis in the low frequency region. All the samples show non- Debye type relaxation process as the centre of the arcs lies below the real axis. The $NiWO_4$ sample calcined at 600^0C (S2) shows high impedance at room temperature with a small electrode polarization effect. Sample S3 shows the least impedance. But it has a significant electrode polarization effect. This may be the reason for the high value of ε' for S3 in the low frequency region.

An equivalent circuit based on impedance spectroscopy gives an idea of the physical process happening inside the sample. The fitted Nyquist plots and corresponding equivalent circuits are shown in Fig. 3. 25. The contribution of grain and grain boundaries are represented by parallel RC circuits [36]. To describe the non-Debye behaviour, a suitable approach [37] of replacing the specific capacitance C by a constant phase element (CPE) is used. The impedance of CPE is given by $Z_{CPE}= 1/(CPE(j\omega)^{\beta})$, where $0\leq\beta\leq1$. For the $NiWO_4$ samples, another CPE element is used in series with the parallel R-C elements to represent the electrode polarization effect. The values of the parameters R, C and β for grain and grain boundaries, and CPE value are presented in Table 3.11.

Table 3. 11 Equivalent circuit parameters for $NiWO_4$ samples.

Circuit parameters	S1	S2	S3
$CPE_{electrode}$ (F)	0.008	11.5×10^{-6}	0.0022
$\beta_{electrode}$	0.5	0.415	0.57
Rg (Ω)	200	150000	800
CPE_g (F)	10×10^{-10}	2×10^{-4}	27×10^{-10}
β_g	0.85	0.33	0.89
R_{gb} (Ω)	42000	2331000	9000
CPE_{gb} (F)	25×10^{-9}	3×10^{-7}	1×10^{-9}
β_{gb}	0.91	0.775	0.94

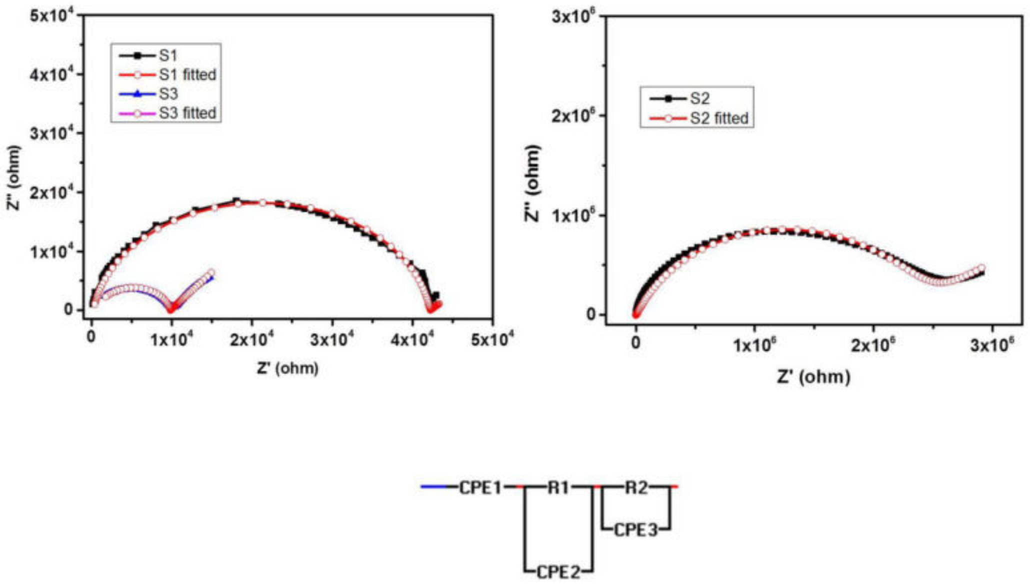

Fig. 3.25 Room temperature Nyquist plots and the corresponding equivalent circuit of $NiWO_4$ samples.

3.3.5.3 AC conductivity

The AC conductivity (σ_{ac}) of $NiWO_4$ samples calcined at different temperatures is investigated to analyze their conduction mechanism.

Variations of AC conductivity as a function of frequency for the $NiWO_4$ samples at room temperature are shown in Fig. 3. 26.

For sample S1, conductivity is found to be constant from 100 to 10^4 Hz and the value is around $8x10^{-5}$ S/m. A slight increase in conductivity occurs with the increase in frequency and reaches a value of $1.52x10^{-4}$ S/m at 1 MHz. A sharp increase in conductivity can be seen after 1 MHz, and AC conductivity attains a maximum value of $4.52x10^{-4}$ S/m at 5 MHz. The σ_{ac} curve of the pure sample shows a frequency-independent region followed by a region where σ_{ac} increases with the frequency. The increasing tendency of σ_{ac} with an increase in frequency may be due to the moving of cations between adjacent sites, and the occurrence of space charges [38]. This represents that the conductivity follows Jonscher's power law, given as $\sigma_{ac} = \sigma_{dc} + A\omega^s$, $0<s<1$, where σ_{dc} is the frequency-independent DC conductivity. According to Jonscher [39], the frequency-dependent conductivity occurs as a result of the relaxation mechanism of charge carriers that are moving. The hopping of charge carrier from one to a new site can be considered as the dislocation of the charge carriers between two potential minima.

Sample S2 shows similar behaviour as S1. AC conductivity shows a linear relationship with frequency in the low frequency region. It shows a slight increase in conductivity from $1.33x10^{-5}$ to $3.35x10^{-5}$ S/m with an increase of frequency from 50 to 10^6 Hz. For this region, the AC conductivity shows nearly frequency-independent behaviour. This is the DC conductivity in the sample. An increase in conductivity is observed after this, and the AC conductivity attains a maximum value $1.64x10^{-4}$ S/m at 5 MHz. The increase in conductivity by S2 at high frequency may be due to the hopping of charge carriers. The conductivity shown by the sample S2 is less than that of S1. This is the expected result from the impedance analysis.

The sample S3 shows slightly different behaviour in conductivity. For the low frequency region, conductivity increases with the increase in frequency up to 1000 Hz. The conductivity changes from 6.94×10^{-4} S/m to 1.05×10^{-3} S/m in this range. This may be due to the influence of electrode polarization effect. After that, it attains a frequency-independent region till 10^6 Hz. A rapid increase in conductivity is observed at higher frequency regime. For the sample S3 conductivity attains a maximum value of 2.3×10^{-3} S/m. Among all the samples, S3 shows high conductivity and low impedance. The increase in conductivity of all samples at high frequency can be explained by the rise in the charge hopping between Ni^{2+} to Ni^{3+}. The hopping rate goes up with the increase in the frequency of the applied field and hence, the conductivity enhances. In short, it can be said that by changing the calcination temperature, the electrical properties of $NiWO_4$ can be varied.

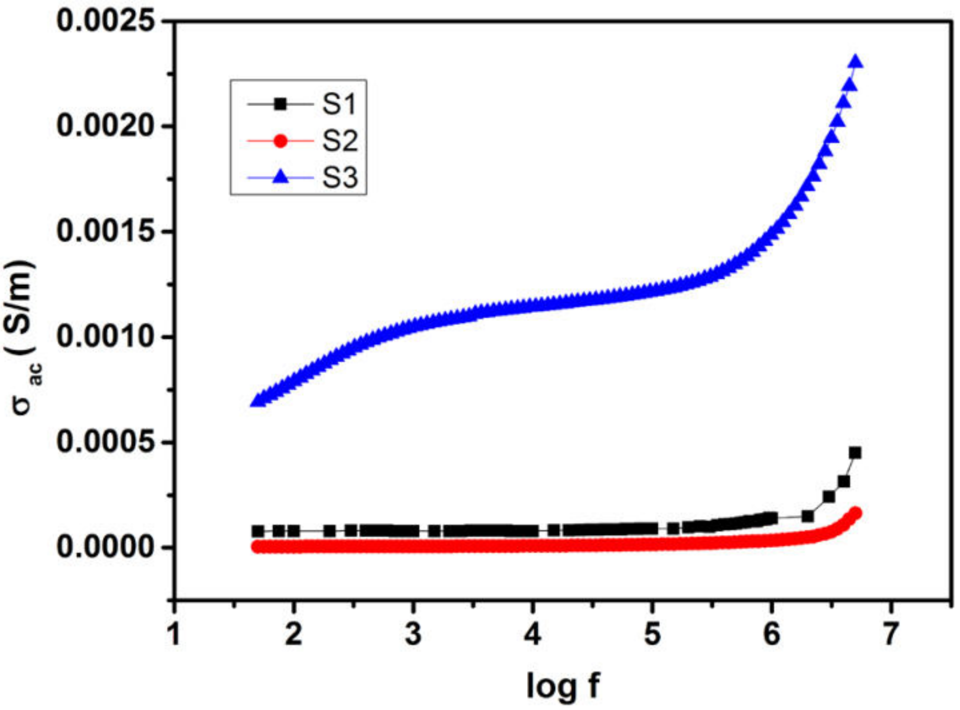

Fig. 3. 26 Variation of AC conductivity with frequency for $NiWO_4$ samples at room temperature.

3.4 Conclusion

- Nanocrystalline $NiWO_4$ samples are successfully prepared by direct chemical precipitation route and the effect of calcination temperature on the structural, optical and magnetic properties of as-synthesized samples are studied.
- $NiWO_4$ samples are found to be thermally stable above 440^0C.
- Synthesized $NiWO_4$ nanoparticles have wolframite monoclinic structure with a space group *P2/c.*
- The average crystallite sizes of the samples are found to be increased with the increase in calcination temperature by thermally promoted crystalline growth.
- FT-IR and Raman spectra confirm the presence of characteristics bonds of $NiWO_4$.
- $NiWO_4$ nanoparticles have both direct and indirect bandgap due to its complex electronic structure. The direct and indirect bandgap energies of the $NiWO_4$ samples are found to be decreasing with the increase in calcination temperature.
- In the UV-VIS-NIR spectrum, a wide absorption peak is observed in the infrared region in addition to the UV and visible absorption.
- The PL emission spectra and CIE chromaticity diagram show purplish-blue emission for $NiWO_4$. Nanocrystalline $NiWO_4$ can be used for making near-ultraviolet (NUV) light excited purplish-blue light-emitting diodes.
- The $NiWO_4$ sample calcined at 500^0C (S1) can be used for photocatalytic application as the PL intensity is low for this sample.
- $NiWO_4$ nanoparticles calcined at different temperatures possess paramagnetic behaviour at room temperature.
- The dielectric properties and AC conductivity show a significant dependence on the calcination temperature.

- Nyquist plot studies and equivalent circuit analyses give the idea that the conduction mechanism is not changed much with the change in calcination temperature.

References

[1] J. Ruiz- Fertes, S. Lopez- Moreno, A. Segura, P. Rodrigues-Hernandez, A. Munoz, A. H. Romeo and J. Gonzales, J Appl. Phy.**107**, 083506 (2010)

[2] H. Hitha, K.P. Priyanka, A. Sreedevi, Anjali Jose, T. Varghese, Eur. Phys. J. B 91 (2018) 287.

[3] R. Di Monte and J. Kaspar, J. Catal. Today **100**, 27 (2005)

[4] M. Mancheva, R. Iordanova and Y. Dimitriev, J. Alloys Compd. **509**, 15 (2011)

[5] M.N. Mancheva, R. S. Iordanova, D. G. Klissurski, G. T. Tyuliev and B. N. Kunev, J. Phys. Chem. C **111**, 1101 (2007)

[6] M. Daturi, G. Busca, M. M. Borel, A. Leclaire and P. Piaggio, J. Phys. Chem. B **101**, 4358 (1997)

[7] V. V. Fomichev and O. I. Kondratov, Spectrochem. Acta A **50**, 1113 (1994)

[8] M. Maczka, J. Kanuza, S. Kojima and J. H. vander Maas, J. Solid state Chem. **158**, 334 (2001)

[9] J. Hanuza and L. Macalik, Spectrochem. Acta A **43**, 361 (1987)

[10] H. Wang, F. D. Medina, Y. D. Zhou and Q. N. Zhang, Phys. Rev. B **45**, 10356 (1992)

[11] J. M. Quintana-Melgoza, A. Gomez-Cortes and M. Avalos-Borja, React. Kinet. Catal. Lett.**76**, 131 (2002)

[12] A. Kuzmin, A. Kalinko and R. A. Evarestov, Cent. Eur. J. Phys. **9**, 502 (2011)

[13] D. L. Rousseau, R. P. Bauman and S. P. S. Porto, J. Raman Spectroscopy **10**, 253 (1981)

[14] F. D. Hard Castle and I. E. Wachs, J. Raman Spectroscopy **26**, 397 (1995)

[15] N. V. Minh and N. M. Hung, Materials Sciences and Application **2**, 957 (2011)

[16] W. Tong, L. Li, W. Hu, T. Yan, X. Guan and G. Li, J. Phys. Chem. C **114**, 15298 (2010)

[17] A. Sreedevi, K. P. Priyanka, K. K. Babitha, N. Aloysius Sabu, T. S. Anu and T. Varghese, Indian J. Phys. 89, 889 (2015)

[18] S.M. M Zawawi, R. Yahya, A. Hassan, H N M E. Mahmud, M.N. Daud, Chem.Cent.J.7(2013)80–89.

[19] A.L.M. de Oliveira, M.R.S. Silva, S.C. de Souza, F.T.G. Vieira, E. Longo, A.G. Souza and M.G. S. Leda, J. Thermal Anal Calorim. **97**, 167 (2009)

[20] P. Prashant Kumar, N.S. Bhave and R.B. Kharat, Electrochim Acta. **51**, 4659 (2006)

[21] S. K. Arora, T. Mathew, N. M. Batra, J. Phys. Chem.solids. Vol. 50, No. 7.(1989) 665- 668.

[22] P.D.C. King, T.D. Veal, F.Fuchs, C.Y. Wang, D.J. Payne, A. Bourlange, H. Zhang, G.R. Bell, V. Cimalla, O. Ambacher, R.G. Egdell, F. Bechstedt, C.F. McConville,Phys.Rev.B**79**(2009) 205211

[22] T. Ejima, T. Banse, H. Takatsuka, Y. Kondo, M. Ishino, N. Kimura, M.Watanabe, I. Matsubara, Journal of luminescence 119-120 (2006) 59-63

[23] E.I. Ross-Medgaarden and I.E. Wachs, J Phys Chem C.**111**, 15089 (2007)

[24] L. S. Cavalcante, M.A.P. Almeida, W. Avansi, R. L. Tranquilin, E. Longo, N. C. Batista, V. R. Mastelaro and M. S. Li, Inorg. Chem. **51**, 10675 (2012)

[25] D. V. Bavykin, S. N. Gordeev, A. V. Morkalenko, A. A. lapkin and F. C. Walsh, J. Phys. Chem. B **109**, 8565 (2005)27.

[26] A. L. M. de Oliveira, J.M. Ferreira, M.R.S. Silva, G.S. Braga, L. E.B. Soledade, M.A. M. M. Aldeiza, C. A. Paskocimas, S.J.G. Lima, E.Longo, A. G. de Souza, I.M. G. dos Santos, Dyes Pigments 77 (2008)210-218

[27] A. Kuzmin and J. Purans, Radiation Measurements **33**, 583 (2001)

[28] V. M. Longo, L. S. Cavalcante, E. C. Paris, J. C. Sczancoski, P. S. Pizani, M. S. Li, J. Andres, E. Longo, J. A. Varela, J. Phys. Chem. C.115 (2011) 5207-5219.

[29] M. A. Santos, E. Orhan, M. A. M. A. de Maurera, L. G. P. Simoes, A. G .Souza, P. S. Pizani, E.R. Leite, J. A. Varela, .J Andres, A. Beltran, E. Longo, Phys. Rev. B. 75 (2007) 165105–165115.

[30] J.C.Maxwell, Electricity and magnetism, vol 1. Oxford University Press, New York, p 88, 1973

[31] K.W. Wagner, Ann Phys 40: (1913).817

[32] C.G. Koop, Phys Rev 83 (1951) 121.

[33] R.Bharati, R.A. Singh, B.M. Wanklyn, J.Mater.Sci. 18(1983) 1540.

[34] H. Hitha, M. John, A. Jose, S. Kuriakose, T. Varghese, J Mater Sci: Mater Electron (2020) 31:21180-21192

[35] A. K. Bhattacharya, R. G. Biswas, A. Hartridge, Journal of materials science 32 (1997) 353-356

[36] J. Ross Macdonald, Impedance Spectroscopy: Emphasizing Solid Materials and Systems, Wiley Interscience Publication, New York (1987)

[37] R. Schmidt, W. Eerenstein, T. Winiecki, F. D. Morrison, and P. A. Midgley, Phys. Rev. B **75** (2007) 245111.

[38] N.K. Karan, D.K. Pradhan, R. Thomas, B. Natesan, R.S. Katiyar, Solid State Ionics 179 (2008) 689.

[39] D.K. Pradhan, B. Behera, P. R. Das, J. Mater. Sci.: Mater. Electron.23 (2011) 779-785.

◆

Chapter - 4

EFFECT OF COBALT DOPING ON THE PROPERTIES OF $NiWO_4$ NANOPARTICLES

4.1 Introduction

$NiWO_4$ has gained significant importance due to its wide applications in various fields of industries such as catalyst, humidity sensors, microwave devices, and optic fibres[1-4]. Properties of $NiWO_4$ can be modified by different means such as doping and composite formation. Cobalt (Co) is considered as one of the most effective doping species due to its abundant electronic states and also it appears to suit well for tailoring the electronic structure [5, 6]. Many works have been reported based on cobalt doping in $NiWO_4$ matrix involving different synthesis routes and exploring the electrochemical and photocatalytic properties [7-9]. As cobalt is a magnetically active transition metal, it is suitable to use this dopant to vary the magnetic functionality existing in a semiconductor, and cobalt plays this role effectively in many cases [10-13].

In this chapter, the effect of Co doping on structural, optical, magnetic and electrical parameters of $NiWO_4$ is discussed by varying the molar concentration of Co from 0.01 to 0.05.

4.2 Synthesis of Co-doped $NiWO_4$ Nanoparticles

The direct chemical precipitation method is used for the synthesis of nanocrystalline Co-doped $NiWO_4$ samples. Cobalt at 0.01, 0.03 and 0.05 molar concentrations are used for making the samples. Initially, two reactant solutions A and B are prepared in 100 ml distilled water at 0.1 M concentration. Solution A is made with $Ni(NO_3)_2.6H_2O$ (98%, Merck) and $Co(NO_3)_2.6H_2O$ (98%, Merck) in a suitable molar ratio. Solution B is prepared using $Na_2WO_4.2H_2O$ (98%, Merck). Solution B is added slowly to solution A under constant stirring. After completing the precipitation, samples are thoroughly washed several times with distilled water and ethanol to remove unreacted ions and hydroxides. The precipitate is then dried at 80^0C for 15 h using a hot air oven. The dried powders are calcined at 500^0C for 3 h to get the Co-doped $NiWO_4$ samples. The pure and 1, 3 and 5 molar percentages doped samples are named as S1, Co1, Co3 and Co5 respectively [14]. The synthesis of the pure sample S1 is described in *section 3.2*.

4.3 Results and discussion

4.3.1 Thermal analysis

To study the thermal stability of cobalt doped $NiWO_4$ samples, thermal analysis is carried out using *Perkin Elmer STA 6000*. The TGA and DTG curves of 1% cobalt doped $NiWO_4$ are presented in Fig. 4.1. The TGA curve shows three weight loss steps. 7% of the weight is lost within 200^0C. Corresponding to this weight loss a broad peak is observed in the DTG curve. This is due to the dehydration of surface absorbed water content. In between 200 to 300^0C, 2% of the weight is lost. From 300 to 450^0C, 4% of the weight is lost. DTG curve shows two peaks corresponding to these weight losses. These peaks can be attributed to the elimination of trapped water content within the crystal. From 450^0C onwards both the curves show a steady nature. So it can be inferred that above 450^0C the sample is thermally stable. So for the Co-doped $NiWO_4$ samples calcination temperature is chosen to be 500^0C.

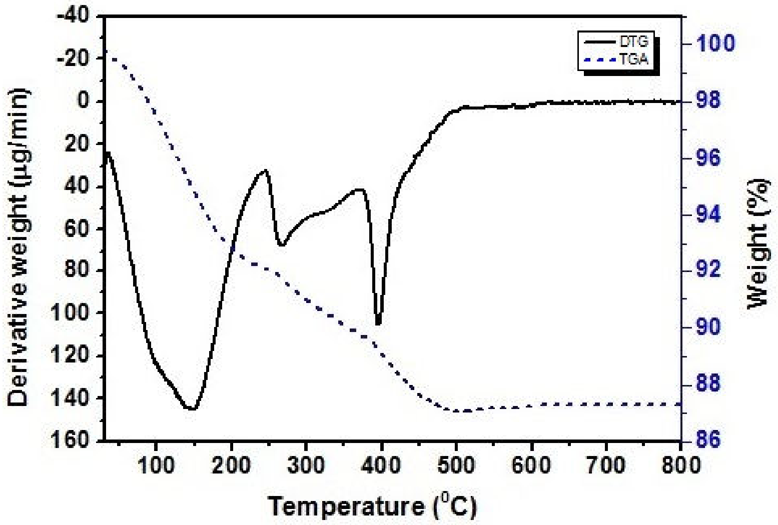

Fig. 4.1 TGA/DTG curves of Co-doped $NiWO_4$ nanoparticles.

4.3.2 Analysis of structural properties

The structural analyses of synthesized Co-doped $NiWO_4$ are carried out by following the procedure described in *section 2.3.2* and the effect of doping on the structural properties of $NiWO_4$ is analysed.

4.3.2.1 Powder XRD analysis

X-ray diffractograms of pure and Co-doped $NiWO_4$ samples are taken by a *Bruker AXS D8 Advance* X-ray diffractometer with Cu-Kα radiation (λ = 1.5406Å). Fig 4.2 shows the X-ray diffraction patterns of pristine and doped samples. All diffraction peaks can be indexed with the monoclinic type structure with space group *2P/c*, which is consistent with JCPDS file no.72-0480. Doping of cobalt does not modify the diffraction profile of $NiWO_4$. $CoWO_4$ possess the same crystal structure as $NiWO_4$. The difference between the ionic radii of Ni^{2+} (0.069 nm) and Co^{2+} (0.065 nm) species are less than 15% and the electronegativity of Ni (1.91) atom is close to that of Co (1.88) atom. These factors may lead Co atoms to get easily incorporated into $NiWO_4$ lattice [15]. There are no secondary phases found (metallic cobalt, cobalt oxide or clusters) under the detection limit of

XRD equipment. This may be due to the good dispersion of the cobalt ion in the crystal lattice of $NiWO_4$ or due to the lower loading of dopant ions prevent observing signals referable to other crystalline phases. The diffraction patterns of pure and Co-doped samples display that the intensity of diffraction peaks decreases with the increase in the concentration of Co^{2+}. The lattice parameters are determined using the formula explained in *section 2.3.2.1* and their values are presented in Table 4.1.

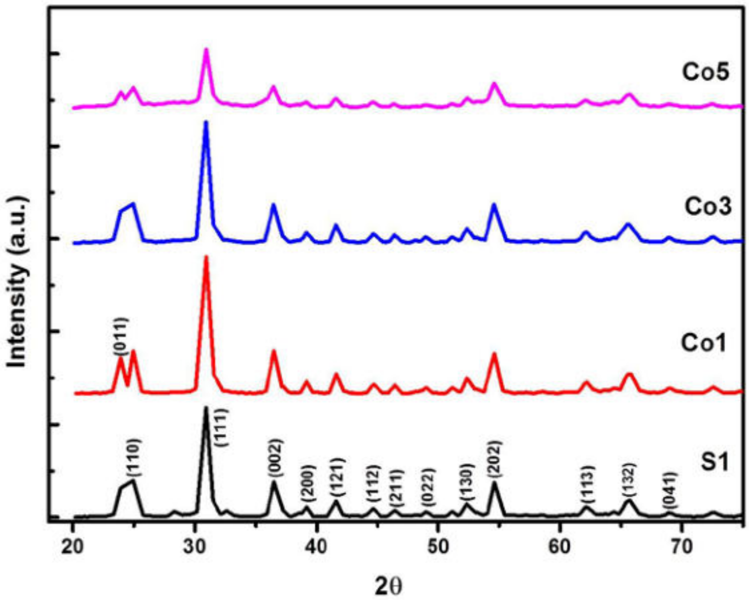

Fig.4.2 X-ray diffractograms of pure and Co^{2+} doped $NiWO_4$ samples.

Table 4.1 Lattice and geometrical parameters of pure and Co^{2+} doped $NiWO_4$ samples.

Sample	Lattice parameters				Geometrical parameters			
	a	b	C	β	Unit cell volume ($x10^{-30}$ m^3)	Average crystallite size (Scherrer formula) (nm)	Average crystallite size (W-H formula) (nm)	Micro-strain ($x10^{-3}$)
S1	4.655±0.093	5.439±0.108	4.986±0.099	91.94	126.18	14.74±0.29	15.88±0.31	2.63±0.05
Co1	4.594±0.091	5.663±0.113	4.917±0.098	89.98	127.92	13.19±0.26	13.86±0.27	1.28±0.02
Co3	4.598±0.091	5.674±0.113	4.921±0.098	89.99	128.38	11.14±0.22	11.63±0.23	1.0±0.01
Co5	4.598±0.091	5.674±0.114	4.919±0.098	89.97	128.33	11.20±0.22	11.24±0.22	0.69±0.01

It can be seen from Table 4.1 that the lattice parameters **a**, **c** and **β** of doped samples show a slight decrease in value when compared with the pure sample. However, a slight increment is observed for **b**. This variation in lattice parameters with cobalt doping concentration is due to the slight difference in ionic radius of Co with the host ion in the lattice [14,16].

The average crystallite sizes of pure and Co^{2+} doped $NiWO_4$ nanoparticles are calculated from XRD patterns using Scherrer equation explained in *section 2.3.2.1.* The average crystallite sizes of pure and doped samples are also presented in Table 4.1. It shows that the average crystallite size of $NiWO_4$ is changed when doped with Co^{2+}, and it decreases with the increase in Co concentration. The reduction in crystallite size is mainly due to the distortion in the host lattice caused by the introduction of Co ions, due to which the nucleation and growth rate of $NiWO_4$ nanoparticles decreases [14,17].

Average crystallite size and micro-strain 'ε' of pure and Co-doped $NiWO_4$ are calculated using Williamson- Hall analysis described in *section 2.3.2.1.* The effect of doping on these parameters is analysed. Fig.4.3 represents the W-H Plot of pure and doped samples of $NiWO_4$. The average crystallite sizes and micro-strains of pure and doped $NiWO_4$ samples are also presented in Table 4.1. From Table 4.1, it can be seen that the average crystallite sizes estimated from the Scherrer equation and W-H analysis for all the samples are in agreement with each other. Variation of average crystallite size and micro-strain calculated from W-H analysis are presented in Fig.4.4. It can be seen that the micro-strain of the doped samples decreases with the increase in Co concentration. The dopant Co is having almost the same ionic radius as Ni with a little bit smaller size than Ni. Hence, Co can replace Ni well and strain may get reduced [18]. From XRD analysis, one can conclude that by increasing the dopant ion (Co^{2+}) concentration, the average crystallite size and the micro-strain of the

$NiWO_4$ sample can be reduced without changing its basic monoclinic crystal structure even though there is a slight change in lattice parameters.

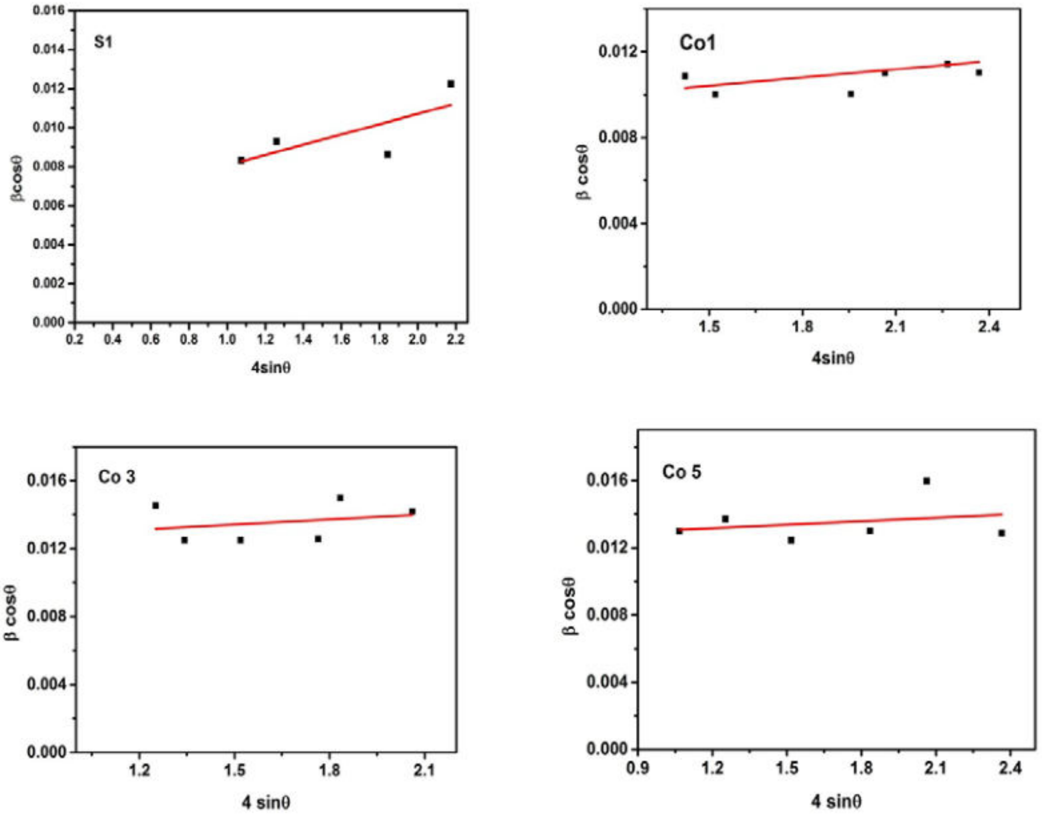

Fig. 4.3 W-H Plots of pure and doped $NiWO_4$ samples.

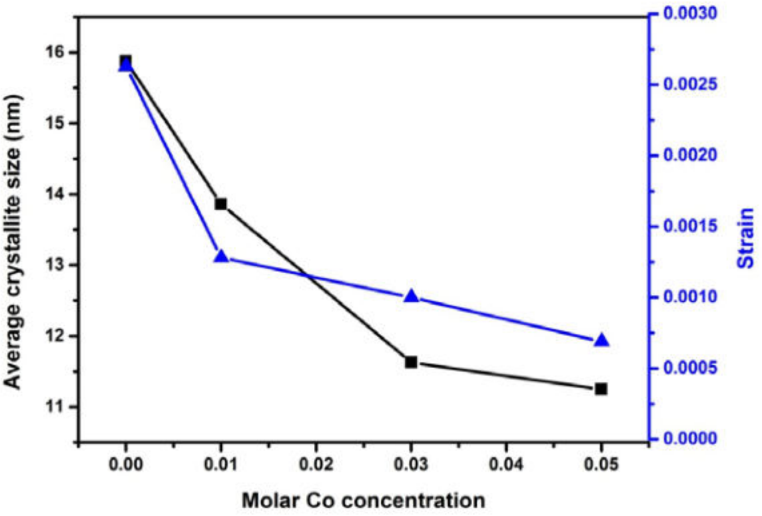

Fig. 4.4 Variation of average crystallite size and micro-strain of $NiWO_4$ with molar Co^{2+} concentration.

4.3.2.2 TEM analysis

TEM analysis of the pure and doped $NiWO_4$ samples is done with the help of *JEOL/JEM 2100* (Source: LaB6 and voltage: 200 kV). Fig. 4.5 represents the TEM bright-field images of pure and Co-doped $NiWO_4$ samples. From the figure, it is evident that particle size decreases with an increase in Co concentration. The average particle size is calculated with the help of a histogram. Fig. 4.6 shows the histogram of particle size of $NiWO_4$ samples. The particle size ranges from 8 to 20 nm for S1, 8 to 18 nm for Co1, 9 to 15 nm for Co3 and 6 to 16 nm for Co5. The average particle size for samples S1, Co1, Co3 and Co5 are found to be 14.84, 13.36, 13.24 and 11.18 nm respectively.

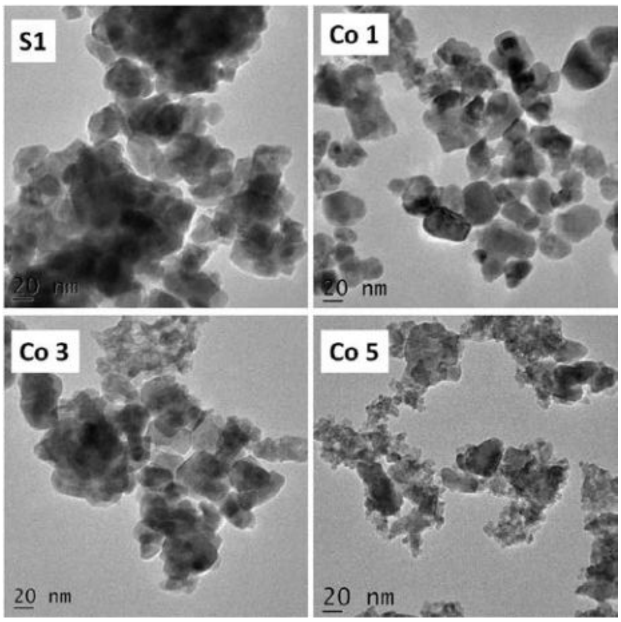

Fig. 4.5 Bright-field images of pure and Co-doped $NiWO_4$ samples.

Fig.4.7 shows the HR-TEM images of pure and Co-doped $NiWO_4$ samples. It illustrates the polycrystalline nature of the pure and doped samples. Selected area electron diffraction images of pristine and Co-doped $NiWO_4$ samples are shown in Fig 4.8. It also confirms the polycrystalline nature of the samples. Crystalline planes that show high-intensity peaks in XRD can be indexed from the SAED images by calculating inter-planar spacing (d_{hkl}) values from the images. The d_{hkl} values of the planes are calculated and crystal planes are identified by comparing them with the XRD values, and these values are tabulated in Table 4.2.

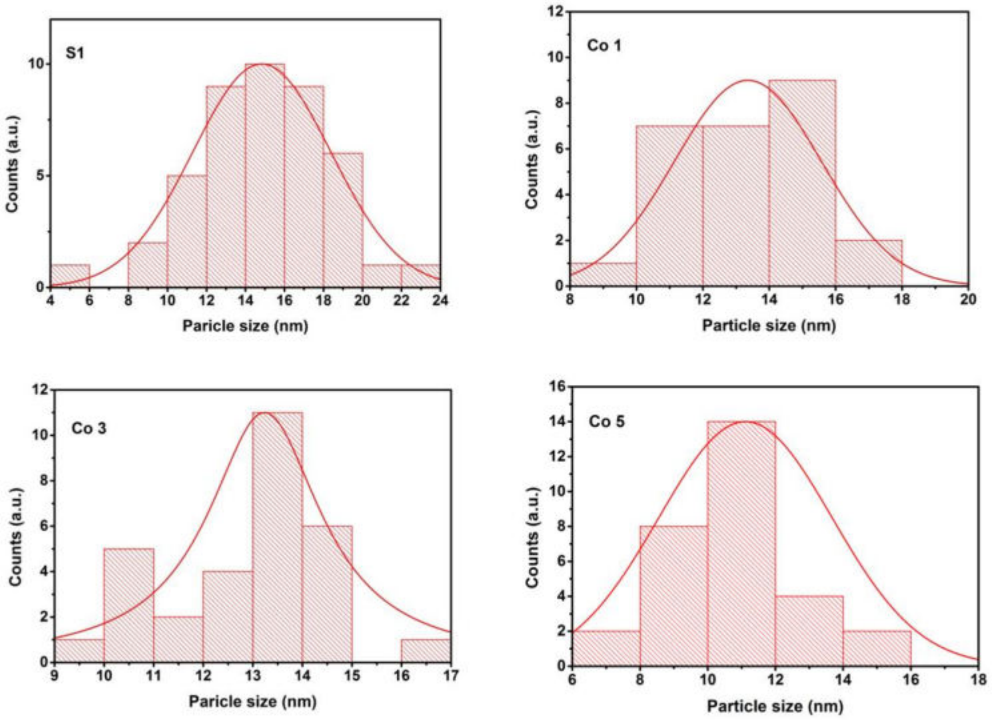

Fig. 4.6 Size distribution graphs of pure and Co-doped $NiWO_4$ samples.

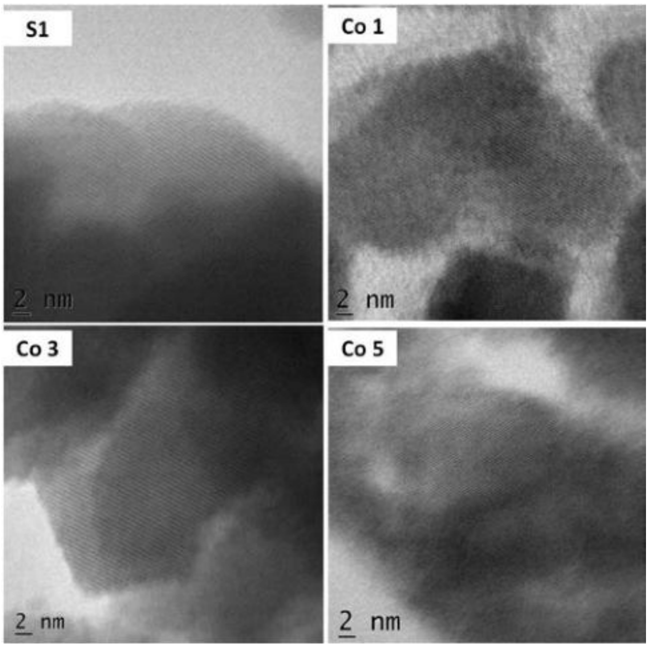

Fig. 4.7 HR-TEM images of pure and Co-doped $NiWO_4$ samples.

Table 4.2 Inter-planar spacing (d_{hkl}) and the corresponding planes of pure and Co-doped $NiWO_4$ samples.

Sample	**Plane**	**Measured from SAED d (A^0)**	**Measured from XRD d (A^0)**
S1	(010)	5.543	5.587
	(100)	4.401	4.533
	(011)	3.448	3.537
	(002)	2.591	2.447
	(112)	2.046	2.017
	(130)	1.695	1.740
	(302)	1.268	1.298
Co1	(100)	4.228	4.289
	(110)	3.345	3.447
	(111)	2.823	2.888
Co3	(110)	3.350	3.432
	(111)	2.832	2.890
	(002)	2.502	2.460
	(211)	1.961	1.956
	(202)	1.657	1.680
Co 5	(110)	3.384	3.564
	(111)	2.849	2.889
	(002)	2.535	2.460
	(112)	1.987	2.031
	(202)	1.657	1.679

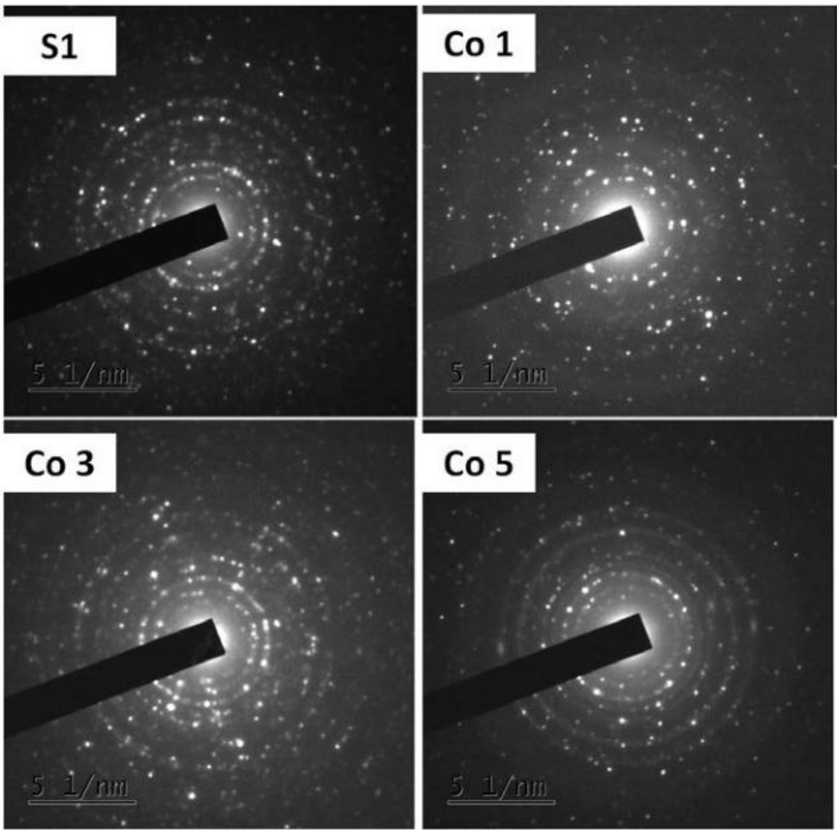

Fig. 4.8 SAED images of pure and Co-doped $NiWO_4$ samples.

4.3.2.3 FE-SEM and EDS analysis

The surface morphology of the pure and cobalt doped $NiWO_4$ samples are analysed using an FE-SEM instrument ∑*IGMA* ^{TM} operating at 5 kV. Fig. 4. 9 represents the FE-SEM images of pure and Co-doped $NiWO_4$ samples. From the figure, it can be inferred that there is no noticeable change in the surface morphology of the doped sample as compared with the pure sample.

Fig. 4.10 represents the EDS image of 1 molar % Co-doped $NiWO_4$ sample. The EDS data for the samples S1 and cobalt doped $NiWO_4$ samples Co1, Co 3 and Co 5 are presented in Table 4.3. From the image and data, it is evident that Co is successfully incorporated into $NiWO_4$. From the EDS data, Co-doped samples are found to be oxygen-deficient as compared to the stoichiometry of pure sample. For doped samples, tungsten and nickel are in the correct proportion. But the atomic percentage of oxygen varies significantly. This oxygen deficiency may lead to the formation of recombination centres or trapping centres [14].

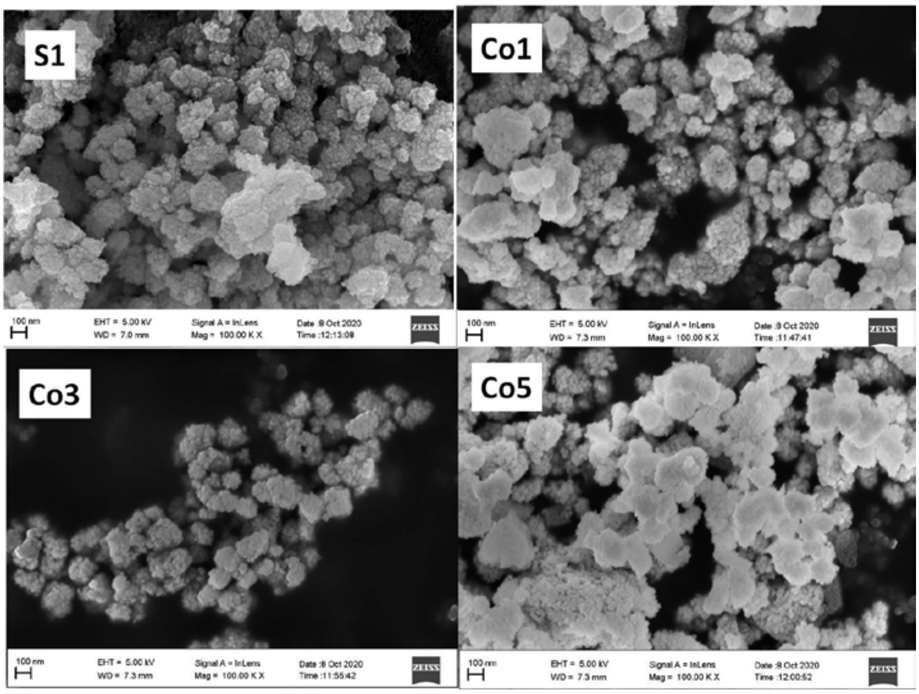

Fig. 4.9 FE-SEM images of pure and doped $NiWO_4$ samples.

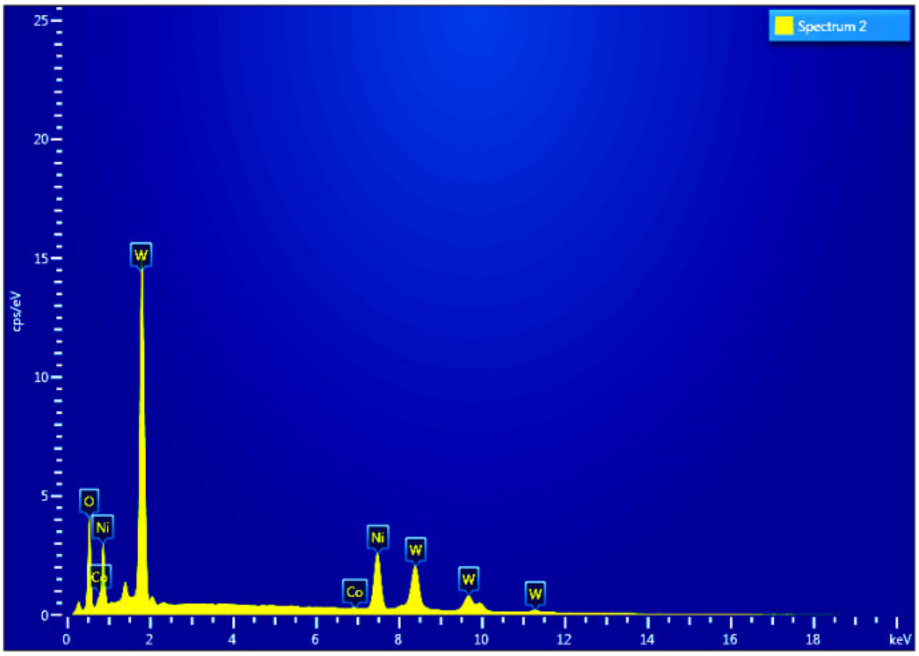

Fig. 4.10 EDS image of 1 molar % Co-doped $NiWO_4$ sample.

Table 4.3 EDS data for pure and Co-doped $NiWO_4$ samples.

Sample	Elements	Atomic number	Series	Wt. %	At.%
S1	W	74	L- Series	58.91	15.64
	O	8	K- Series	22.62	69.00
	Ni	28	K- Series	18.47	15.36
Co 1	W	74	L- Series	61	17.96
	O	8	K- Series	18.72	63.34
	Ni	28	K- Series	19.98	18.42
	Co	27	K- series	0.3	0.28
Co 3	W	74	L- Series	59.3	16.81
	O	8	K- Series	19.87	64.7
	Ni	28	K- Series	19.93	17.69
	Co	27	K- Series	0.9	0.8
Co 5	W	74	L- Series	63.34	20.51
	O	8	K- Series	15.62	58.15
	Ni	28	K- Series	19.74	20.02
	Co	27	K- Series	1.3	1.31

4.3.2.4 FT-IR analysis

FT-IR spectra of pure and Co-doped $NiWO_4$ samples are recorded by FT-IR spectrophotometer (*Thermo Nicolet, Avatar 370*) in the range 1200 to 400 cm^{-1}. Fig. 4.11 shows the FT-IR spectra of pure and Co-doped $NiWO_4$ nanoparticles. In Table 4.4, IR active modes obtained for the pure and Co-doped $NiWO_4$ samples are compared with the literature values of $NiWO_4$ [19] and their band assignments [20-24] are also given. For the pure sample, there are broad intense bands. But the absorption band intensity decreases with an increase in dopant concentration. Moreover, no characteristic peaks correspond to Co-O are not seen in the FT-IR spectra of doped samples with the increment in dopant concentration, which shows that cobalt is well occupied in the host lattice without forming any oxides or hydroxides [14].

Table 4.4 IR active modes of pure and Co-doped $NiWO_4$ samples.

Literature value [19] (cm^{-1})	**Present work (cm^{-1})**				**Band assignment [20-24]**
	S1	**Co1**	**Co3**	**Co5**	
432	455	456	455	450	Deformation modes of W-O bonds in $[WO_6]^{6-}$ or deformation of W-O-W bridges
494	---	---	---	---	
523	527	527	530	527	Asymmetric stretching vibrations of $[WO_6]^{6-}$
533	---	---	---	---	
---	---	614	618	---	Asymmetric stretching of W-O-W bridging bonds
---	623	---	---	---	Asymmetric stretching of W-O-W bridging bonds
681	677	685	691	---	Stretching vibrations of W-O-W bonds
---	806	818	815	---	Vibrations of the WO_2 entity present in the W_2O_8
877	869	868	868	868 (low)	W-O stretching mode in WO_4 tetrahedron
961	944	---	945 (low)	942 (low)	Streching mode of W-O terminal bond
---	997	996	995	1001 (low)	Metal ligand vibrations

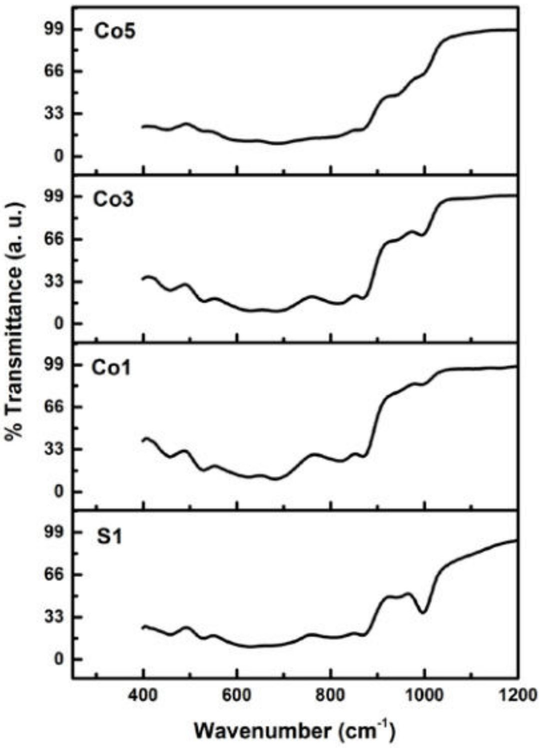

Fig.4.11 FT-IR spectra of pristine and Co-doped $NiWO_4$ nanoparticles.

4.3.2.5 Raman analysis

The Raman spectra of pure and Co-doped $NiWO_4$ samples are taken by *Alpha 300 RA AFM & RAMAN*. The origin of Raman spectra of metal tungstates is explained in *section 3.3.2.5*. Fig. 4.12 shows the Raman spectra of pure and Co-doped $NiWO_4$ nanoparticles. Out of 18 Raman modes that previous literature reports [19, 24], 12 modes are present in all the samples. There are certain modes with very low intensity which are difficult to see in the figure due to the high intensity of other peaks. Table 4.5 represents the phonon active Raman modes of pristine and doped $NiWO_4$ along with the literature values of $NiWO_4$ [19]. The most intense band observed at 879-884 cm^{-1} is assigned to the A_g mode due to the symmetric stretch of the shortest terminal W-O bond [14, 25]. The bands at 783 and 716 cm^{-1} are attributed by B_g and A_g modes respectively, which are due to the asymmetric stretching of the W-O bonds. The bands at 413, 353 and 209 cm^{-1} are assigned to $2A_g$+ B_g modes, originate from the bending modes of the regular octahedron [14, 26]. Other vibrational modes are contributed by asymmetric and symmetric stretching vibrations of longer W–O bonds along with the deformation vibration modes [27, 28]. Fig. 4.12 shows that an increase in dopant concentration leads to variation in line width of the main intense peak. It can also be seen that intense A_g Raman mode shift towards the lower wavenumber side as the Co concentration is increased, which may be due to particle size variation introduced by the variation of Co concentration. Raman scattering is very sensitive to changes in the force constant resulting from slight distortion of the structure, leading to a significant change in the Raman spectra which cannot be shown by XRD spectra. Here the shift in peaks can be attributed to the slight structural disorders in the doped samples due to Co loading. From this observation, it can be concluded that the introduction of Co^{2+} into the lattice leads to the observed changes in the line width and position of the Raman peaks.

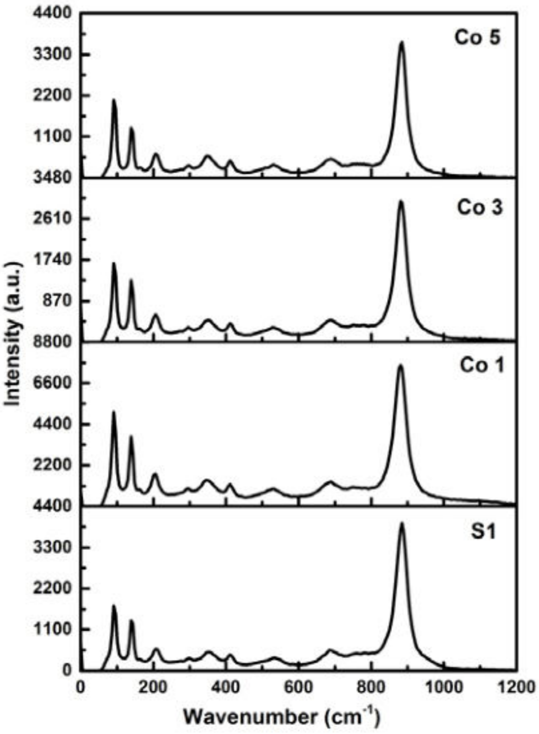

Fig. 4.12 Raman spectra of pure and Co-doped $NiWO_4$ samples.

Table 4.5 Raman active modes of pure and Co-doped $NiWO_4$ samples.

ν (cm^{-1}) [19]	**Phonon symmetry**	**S1 (cm^{-1})**	**Co 1 (cm^{-1})**	**Co 3 (cm^{-1})**	**Co 5 (cm^{-1})**
97	B_g	91.4	91.3	91.3	91.3
149	A_g	139.3	140.7	140.7	140.7
174	B_g	163.8	162.2	162.9	164.3
197	B_g	----	----	----	----
210	B_g	207.7	205.1	207.4	207.4
223	A_g	----	----	----	----
287	A_g	276.2	----	----	----
307	A_g	298.7	295.4	295.42	297.42
326	B_g	----	----	----	----
363	A_g	353.4	349.1	353.4	349.1
380	B_g	----	----	----	----
418	A_g	412.3	411.3	413.5	413.5
512	B_g	----	----	----	----
549	A_g	533.1	529.7	531.7	531.7
675	B_g	686.6	688.7	688.7	690.7
697	A_g	717.4	726.1	----	727.3
----		----	750.9	752.2	747.8
----		----	769.4	761.3	761.1
775	B_g	783	782.7	780.9	778.6
----		----	801.4	799.9	791.7
893	A_g	883.8	879.8	882	884

4.3.3Analysis of optical properties

This section deals with the UV-VIS-NIR spectroscopic and photoluminescence studies of pristine and cobalt doped (1, 3 and 5 molar%) $NiWO_4$ nanoparticles. The analyses are carried out by following the procedure as given in *section 2.3.3*.

4.3.3.1 UV-VIS-NIR analysis

A double-beam UV–Visible spectrophotometer (*Cary 5000 model*) is used to study the absorption properties of pure and Co-doped $NiWO_4$ samples. Absorption spectra of the samples are recorded in the wavelength range 224–1976 nm. Fig.4.13 shows the UV-Vis- NIR absorbance spectra of pure and Co-doped $NiWO_4$ samples. All the samples show an intense absorption peak in the ultraviolet region. The maximum absorption peak for the pure sample is observed at 271 nm (4.58 eV) [14]. From Fig.4.13, the doped $NiWO_4$ samples show the maximum absorption band at 282 nm (4.39 eV). Along with that, an additional band at 353 nm (3.51 eV) is observed for all the doped samples. Thus, the absorption band is broad in the UV regime for the Co^{2+} doped $NiWO_4$ samples [14]. The charge transfer within the WO_6 matrix is the main reason for ultraviolet absorption [29]. The two peaks in the visible region around 445 nm (2.78 eV) and 740 nm (1.68 eV) are seen for both pure and doped samples. These bands are due to the electronic transition from $^3A_{2g}$ to ^1E_g and $^3A_{2g}$ to $^1T_{2g}$, respectively in the $Ni^{2+}O_6$ matrix [14,30].

An additional band is also seen around 592 nm (2.09 eV) for the Co-doped samples. This is due to the d-d transition from $^4A_2$ to $4T_1(p)$ levels of the Co^{2+} ions [14,31]. It is found that the intensity of the band increases with the increase in cobalt concentration. A band around 823 nm (1.50 eV) can be seen in a pure $NiWO_4$ sample and can be assigned to the $^3T_1$ to $^1T_2$ transition in $Ni^{2+}O_4$. So this band represents the presence of $Ni^{2+}O_4$ arising from Frenkel defects in the pure sample with dislocation of Ni^{2+} from the octahedral to tetrahedral sites [14,30]. For the Co-doped samples, a few more peaks are present in this range. These absorption bands occur when Ni^{2+} is situated in a co-ordination environment of low symmetry [32]. Fascinatingly, a broad absorption band in the infrared wavelength ranging from 1300-1600 nm is also seen for all the samples.

From Fig.4.13, it can be seen that absorption in the IR region decreases with the increase in Co^{2+} concentration for the doped $NiWO_4$ samples.

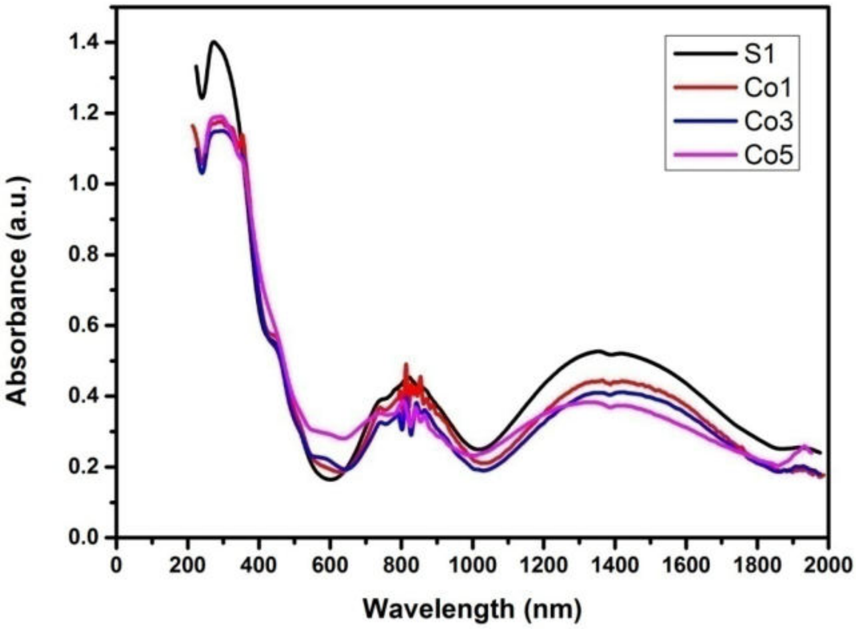

Fig.4.13 Absorbance spectra of pure and Co-doped $NiWO_4$ samples.

From reflectance data, absorption co-efficient ‘α’ is calculated for the pure and Co-doped $NiWO_4$ samples. Both direct and indirect optical bandgap energies of pure and doped samples are measured by plotting $(\alpha h\nu)^2$ and $(\alpha h\nu)^{1/2}$ as a function of photon energy respectively, and extrapolating the linear portion of the curves to absorption equal to zero. The Tauc plot for direct and indirect bandgaps of pure and Co-doped $NiWO_4$ is shown in Fig.4.14. and Fig.4.15 respectively. The optical energy gap values calculated for the samples are tabulated in Table 4.6.

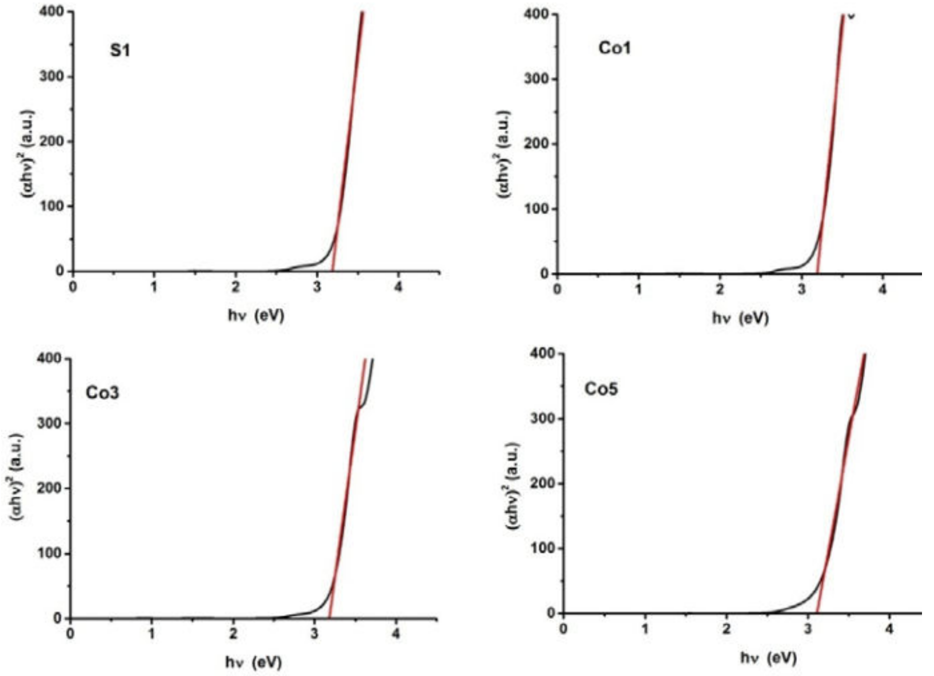

Fig.4. 14 Tauc plot of pure and Co-doped NiWO$_4$ samples for direct bandgap estimation.

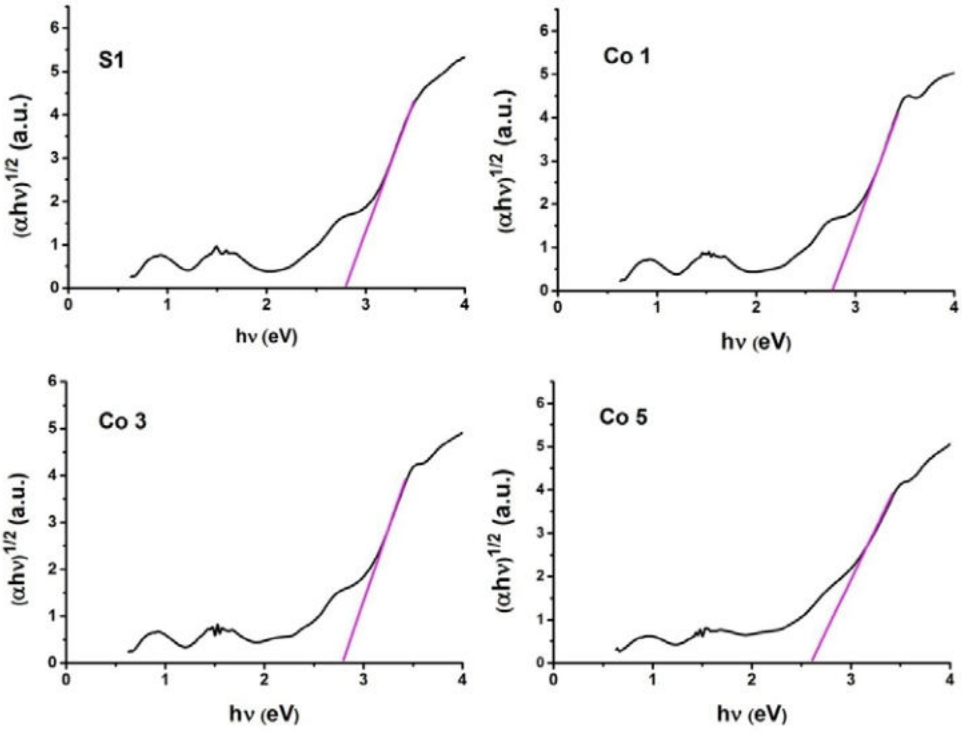

Fig.4. 15 Tauc plot of pure and Co-doped NiWO$_4$ samples for indirect bandgap estimation.

Table 4.6 Direct and indirect optical bandgap values of pure and doped samples

Sample	Direct bandgap (eV)	Indirect bandgap (eV)
S1	3.07	2.80
Co 1	3.19	2.78
Co 3	3.18	2.79
Co 5	3.11	2.60

From Table 4.6, it can be seen that the direct bandgap is increased for doped samples. The quantum size confinement effect is highly pronounced only when the crystallite size of nanocrystalline semiconductor is comparable to its Bohr exciton radius. But, the crystallite sizes of Co-doped $NiWO_4$, calculated from XRD and TEM are far beyond the quantum confinement regime. The widening of the direct bandgap in Co-doped $NiWO_4$ samples can be explained based on Burstein–Moss shift [14,33,34]. In degenerate p-type semiconductors, Fermi level occupies its position within the valence band, and the position varies with the concentration of holes. Thus, the optical bandgap values calculated from UV absorbance are related to the excitation of the electrons from the Fermi level in the valance band to the conduction band, whereas the actual bandgap of the material is related to the excitation of the electrons from the top of the valence band to the bottom of the conduction band. Thus, the optical bandgap widening in Co-doped $NiWO_4$ samples with cobalt doping is attributed to the Burstein–Moss effect. When Co is doped into $NiWO_4$, the free charge concentration gets increased. This in turn results shifting of Fermi level within the valence band. Due to the inclusion of holes or a vacant energy state, the electrons in the valence band make a transition to occupy the available states. This transition and the periodic addition of holes make the Fermi level to shift further below the valence band and thus widen the bandgap [14]. In short, the optical bandgap can be tuned by doping with a suitable molar percentage of cobalt ions into the $NiWO_4$ matrix.

4.3.3.2 Photoluminescence analysis

To analyse the photoluminescence properties of pristine and Co-doped $NiWO_4$ samples, photoluminescence spectra of the samples are taken with the help of *Horiba fluorescence spectrometer* (slit width of 3.0 nm), with an excitation wavelength of 350 nm. Fig.4.16 shows room temperature PL emission spectra of the pure and doped $NiWO_4$ nanoparticles at an excitation wavelength of 350 nm (3.54 eV). Broad emission in the spectral range from 300 to 600 nm is observed for the pure and doped samples, which indicate the presence of several recombination sites and defects [14]. As the PL emission mainly results from the recombination of photoexcited electrons and holes, the PL spectra of the Co-doped samples show variation in PL intensities compared to pure sample. But for doped samples, some additional peaks are formed due to the transitions related to cobalt. The results show that the intensity of PL emission depends on the doping concentration of Co. For a 1 molar % Co-doped sample, the PL intensity is decreased largely. However, the PL intensity for the 3 molar % Co-doped sample increases greatly. As increasing the dopant concentration to 5 molar %, PL intensity is decreased slightly. For the excitation wavelength of 350 nm, two main emission peaks around 412-413 and 433-435 nm are observed, which are similar to other wolframite compounds. Low-intensity shoulder peaks can also be observed in the PL spectra (Fig.4. 17). The observed patterns can originate from the WO_6^{6-} anion along with some defects in the crystal structure [14, 35].

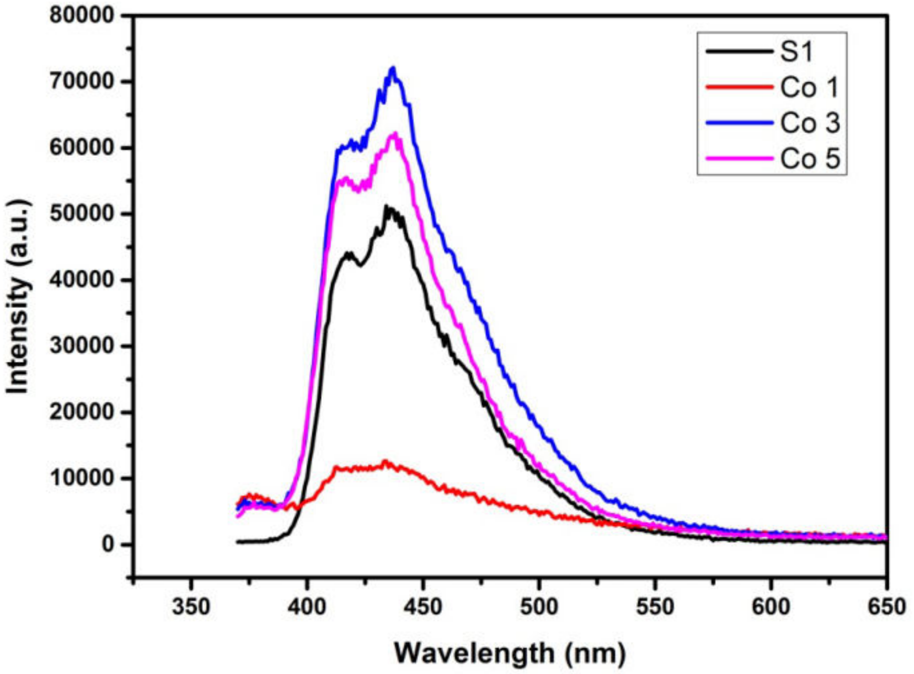

Fig. 4.16 PL spectra of pure and doped NiWO$_4$ samples.

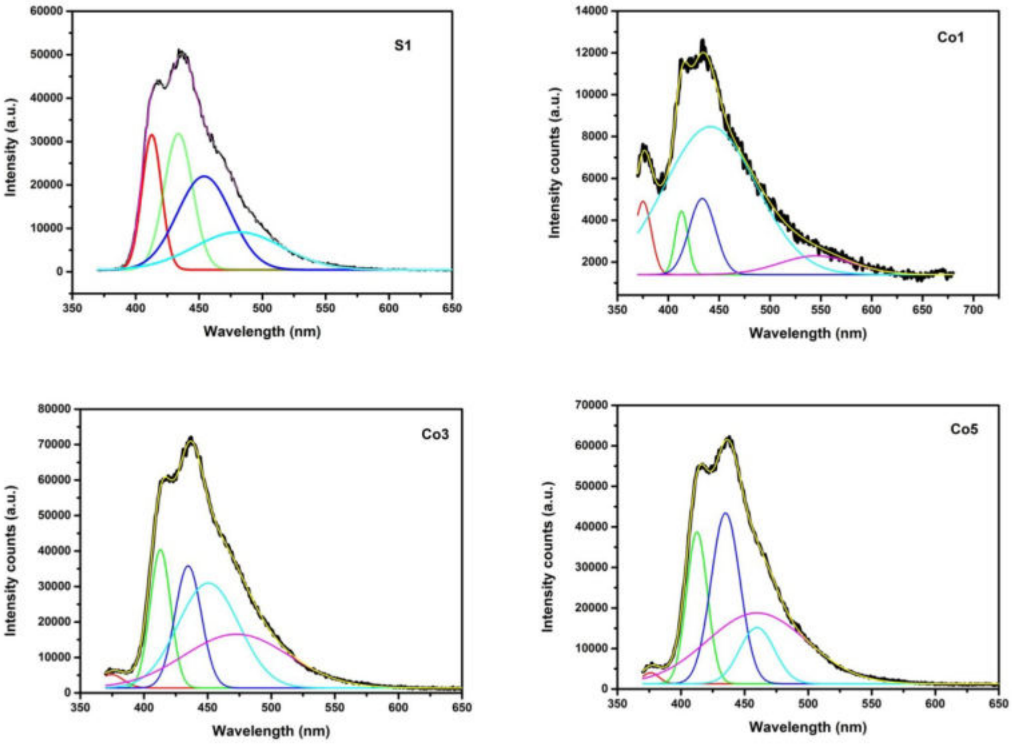

Fig.4. 17 Deconvoluted PL spectra of pure and doped NiWO$_4$ samples.

The emission bands of pure and Co-doped $NiWO_4$ samples present energies ranging between 2.27 and 3.31 eV. The PL spectrum of pure $NiWO_4$ can be decomposed into four Gaussian components of energies G1, G2, G3 and G4. The resulting Gaussian fit is reasonably good. The multi-Gaussian decomposition analyses for pure and doped samples are shown in Fig.4.17. The four deconvoluted bands of the pure sample are having energies 3.01 eV (G1), 2.86 eV (G2), 2.73 eV (G3) and 2.58 eV (G4). G1 is the near band edge transition. G1 and G2 are due to the transitions within the WO_6 complex. G3 and G4 are due to the transitions $^3A_{2g}$ to $^3T_{1g}$ and $^3A_{2g}$ to a $^1T_{2g}$ respectively taking place within the NiO_6 polyhedra [14, 36]. They are the d-d transitions for octahedrally co-ordinated Ni^{2+}. Co-doped $NiWO_4$ samples also show these four bands with slight variations in energy, along with that an additional band G0 is formed. The band G0 can be due to the transition of Co and it could be the emission corresponding to the absorbance at 353 nm that is already discussed in section 4.3.2.1. The presence of G0 influences the bandgap of the doped samples. It can also be noted that the near band edge transition in Co^{2+} doped $NiWO_4$ samples are shifted, which is due to the formation of the additional band. 1 molar % Co-doped sample Co1 shows some changes in the emission spectrum. In the case of Co1 emission band, G4 is absent instead of that an additional band 2.27 eV (G5) is formed which is due to the spin- forbidden transitions from T_{1g} to ^1A_g within WO_6 unit [14, 37].

To analyse the effect of dopant concentration on PL emission, the variation of different peak energies concerning the dopant concentration is considered. G0 component is only for the doped samples, and with the increase in dopant concentration the component is shifted to lower energy. The components G1 and G2 that arises from the tungstate group do not show much variation in energy with the increase in Co concentration. The components related to the NiO_6 group, G3 and G4 show variations in energies with the increase in dopant concentration as the dopant Co affect the Ni^{2+} ions and that may lead to the change in transitions in the NiO_6 cluster. Emission spectra of doped samples show some variations when compared with the pure sample, and the variation is more for sample Co1 as the emission intensity is low for Co1 and all the transitions are equally significant in Co1 [14].

Fig.4.18 shows the CIE chromaticity diagram for the pure and Co-doped $NiWO_4$ samples. The chromaticity coordinates (x and y) are estimated from the CIE XYZ colour space with an excitation wavelength of 350 nm. The CIE coordinates of the pure and Co-doped $NiWO_4$ samples are presented in Table 4.7. Pure sample S1 shows purplish-blue emission. The colour of emission of sample Co1 is blue. The samples Co3 and Co5 show purplish-blue emission similar to S1. Co1 and Co3 show much variation in coordinates of emission, and photo emissions of both the samples come inside the phosphor triangle [14]. In short, the results of PL emission spectra and CIE chromaticity diagram indicate that the intensity and colour of emission of doped $NiWO_4$ samples can be tuned by varying the dopant (Co^{2+}) concentration. All these make pure and Co-doped $NiWO_4$ phosphor materials suitable for the applications such as emissive displays, fluorescent lamps and light-emitting diodes.

Table 4.7 CIE co-ordinates for pristine and Co-doped $NiWO_4$ samples.

Sample	**S1**	**Co1**	**Co3**	**Co5**
x	0.1562	0.2213	0.195	0.1645
y	0.0889	0.2094	0.1317	0.0978

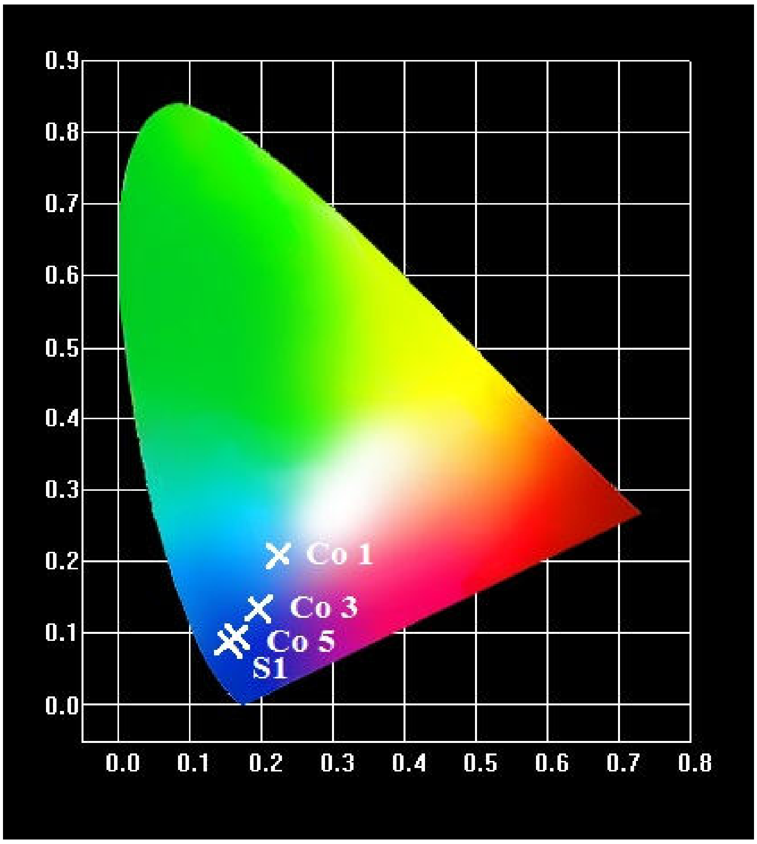

Fig. 4.18 CIE chromaticity diagram of pure and Co-doped $NiWO_4$ samples.

4.3.4 Analysis of magnetic properties

The VSM measurements at room temperature for the pure and Co-doped $NiWO_4$ nanoparticles are carried out in a vibrating sample magnetometer (*Lakeshore VSM 7410*) in an applied magnetic field sweeping between ± 15000 Oe. Fig. 4.19 represents the VSM curves of the pure and Co-doped $NiWO_4$ nanoparticles. The pure sample shows paramagnetic behaviour at room temperature [24]. The magnetic behaviour of pure $NiWO_4$ is discussed in detail in *section 3.3.4*. By doping with cobalt, there is no significant deviation from the magnetic nature of $NiWO_4$. All the doped samples also show paramagnetic nature. From the magnetic studies, it can be concluded that doping by a magnetically active material like Cobalt does not affect the magnetic nature of the $NiWO_4$ sample.

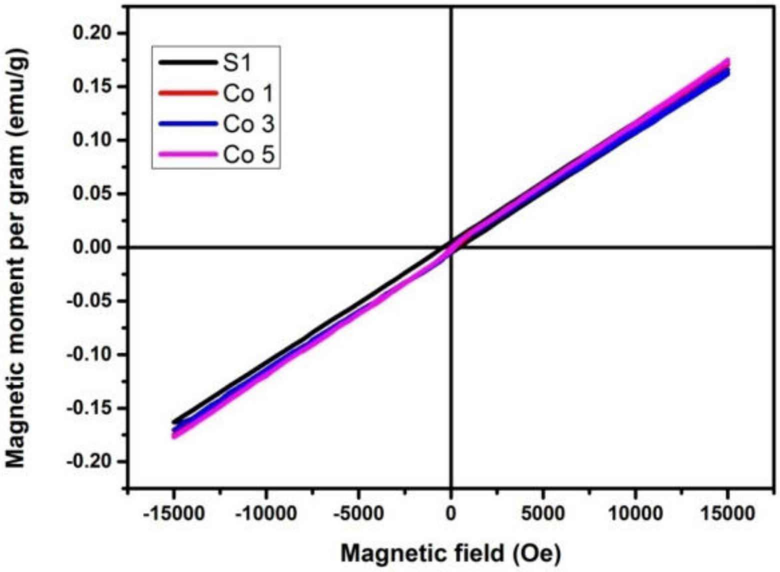

Fig. 4.19 VSM curves of pristine and Co-doped $NiWO_4$ nanoparticles.

4.3.5 Analysis of electrical properties

Electrical studies are carried out by following the procedure given in *section 2.3.5.* The electrical measurements are performed by making cylindrical pellets of pure and doped samples. Pellets are made by applying a pressure of 7 GPa using a hydraulic press. The thickness and diameter of the pellets are 1.7 and 13 mm respectively. The pellets are then sintered at 500^0C for 1.5 h. The silver paste is applied to both the faces of the pellets for good electrical contact. The dielectric and impedance spectra are measured in the frequency range of 50 Hz-5 MHz at room temperature by using *Wayne Kerr H- 6500B* model impedance analyser.

4.3.5.1 Dielectric analysis

Fig.4.20 represents the frequency response of the real part of the dielectric constant of pure and Co-doped $NiWO_4$ samples at room temperature. From Fig.4.20 it can be seen that the Co-doped samples show a very high value of the real part of dielectric constant (ε') when compared to the pure sample. Both pure and Co-doped samples show similar behaviour regarding the variation of the real part of dielectric constant (ε') with frequency. At low frequency, ε' is high for the pure and doped $NiWO_4$ samples. It shows a dispersion at the lower frequency region 50-1000 Hz. The dispersion behaviour shown by the samples can be explained based on space charge polarization. Maxwell–Wagner-type interfacial polarization [38, 39] and Koop's phenomenological theory [40] explains the situation. The value of ε' decreases with the increase in frequency and becomes constant at the high frequency region. The values of ε' for pure and Co-doped $NiWO_4$ samples at selected frequencies are presented in Table 4.8.

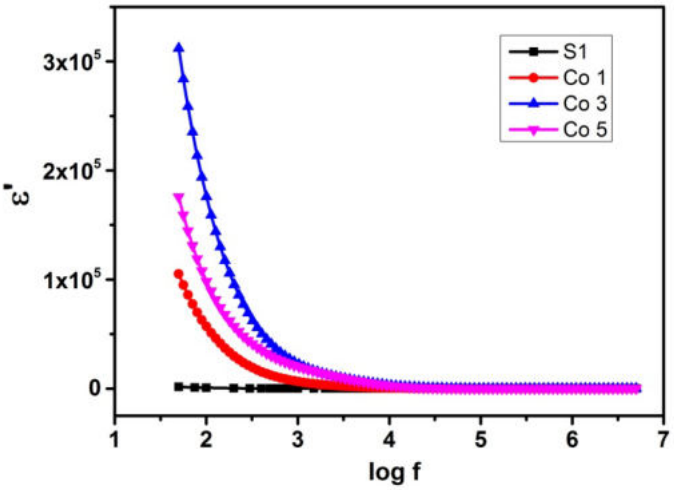

Fig. 4.20 Room temperature frequency response of the real part of dielectric constant for pure and Co-doped $NiWO_4$ sample.

Table 4.8 Real part of dielectric constant at different frequencies for pure and Co-doped $NiWO_4$ samples.

Sample	ε' at 50 Hz	ε' at 1000 Hz	ε' at 10^5 Hz
S1	1682	54	10
Co1	105135	6333	67
Co3	311989	22177	100
Co5	175681	19874	101

From Table 4.8, the Co-doped $NiWO_4$ samples have a very high value of **ε'** in the low frequency region as compared to the pure sample. An increase in permittivity with cobalt doping may be due to the increase in the number of dipoles. This increase in the number of dipoles may happen due to many reasons. One possibility is due to the increase in ionic polarization because of the change in electronegativity of Ni (1.91) and Co (1.88). Since the dopant Co is less electronegative than Ni, makes the ionic bonds weaker. This increases the ionic polarization and hence increases the dielectric constant [41]. It can also be stated that a decrease in particle size leads to an increase in dielectric constant [41]. Here doped samples have a particle size less than the pure sample. So it may also lead to the high ε' of doped samples in the low frequency region. Another possibility is the presence of oxygen ion vacancies which are equivalent to the positive charges giving dipole moments. These dipoles will rotate and give a resultant dipole moment in the direction of the applied field [42]. This is called the rotation direction polarization. For the Co-doped samples, oxygen deficiency increases with doping percentage, which is confirmed from the EDS analysis. This oxygen vacancy may cause rotation direction polarization. So the high value of ε' of doped samples in the low frequency region may be due to the rotation direction polarization along with the space charge polarization. For the high dopant concentration (5 molar% of Co), the dielectric constant decreases. This may be because of the high density of defects introduced in the sample [41].

Fig.4.21 shows the frequency response of loss tangent of pure and Co-doped $NiWO_4$ samples at room temperature. For pure sample, there is a peak in the low frequency region, but this peak shift to the high frequency region for doped $NiWO_4$ samples. The peak in the tanδ curve implies the relaxation process taking place in the samples. Peaking behaviour occurs when the hopping frequency of the ions is equal to the frequency of the applied field. For the doped samples, the loss is small as compared with the pure sample. At high frequencies both the curves approach zero. From the dielectric analysis it can be inferred that by doping with Co, the dielectric constant of $NiWO_4$ can be increased along with a decrease in loss. Hence, the Co-doped $NiWO_4$ nanomaterial can be used in electronic applications.

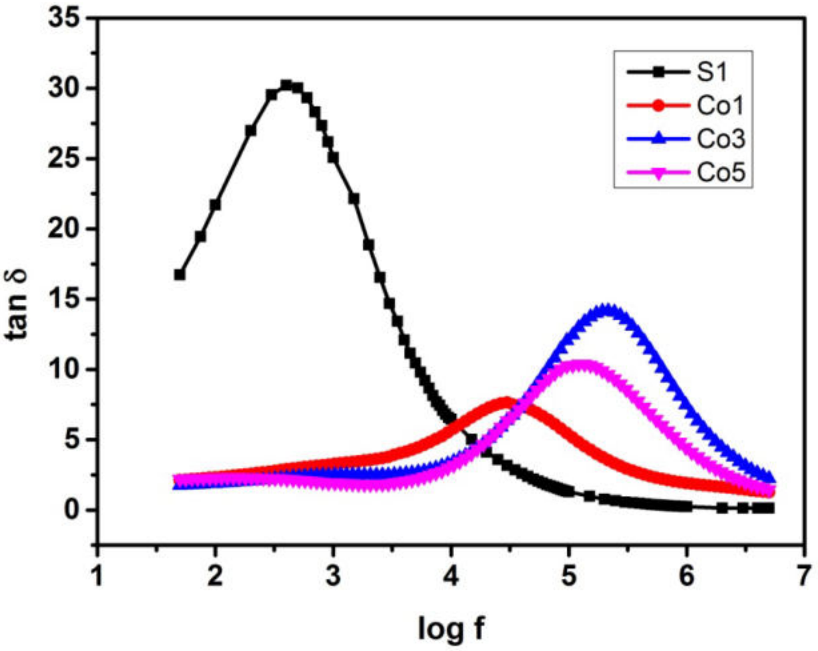

Fig. 4.21 Room temperature frequency response of dissipation factor for pure and Co-doped $NiWO_4$.

4.3.5.2 Impedance analysis

To analyse the conduction mechanism in the pure and Co-doped $NiWO_4$ samples, Nyquist curves are drawn. The electrical properties of polycrystalline material have contributions from grains, grain boundaries and specimen electrode interfaces. Fig. 4.22 represents the Nyquist plots of the pure and Co-doped $NiWO_4$ samples. All the samples show a non-Debye type relaxation process as the centre of the arcs lies below the real axis. The pure $NiWO_4$ sample shows high impedance at room temperature with a very small electrode polarization effect. At the same time, Co-doped $NiWO_4$ samples show small values of real and imaginary parts of complex impedance with a relatively high electrode polarization effect, which might be due to the additional charge carriers formed by the addition of the dopant Co.

An equivalent circuit based on impedance spectroscopy gives an idea of the physical process happening inside the sample. The fitted Nyquist plots and corresponding equivalent circuits are shown in Fig. 4. 23. For the pure sample, two RC circuits connected in series along with a CPE element in series to represent the conduction process. In two RC circuits, one represents the grain and the other represents the grain boundary contribution. In the RC circuits, capacitance is replaced by CPE which represents the non- Debye behaviour shown by the sample. For the Co-doped samples in addition to the two RC elements, another element having a Warburg component with a parallel CPE is used. This additional CPE- W component represents the electrode polarization effect taking place at a lower frequency. Hence, the change in the equivalent circuit for the Co-doped $NiWO_4$ sample indicates the change in the conduction mechanism. The values of the parameters R, C and β for grain and grain boundaries, and CPE value are presented in Table 4.9.

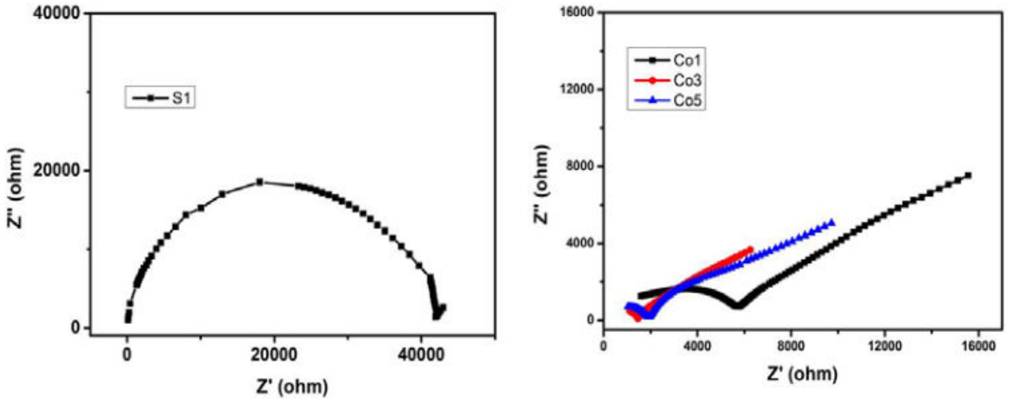

Fig. 4.22 Room temperature Nyquist plots of pristine and Co-doped $NiWO_4$ samples

Table 4. 9 Equivalent circuit parameters for pure and doped $NiWO_4$ samples.

Circuit parameters	**S1**	**Co1**	**Co3**	**Co5**
$CPE_{electrode}$ (F)	0.008	$2x10^{-3}$	$1x10^{-3}$	$2.1x10^{-3}$
$\beta_{electrode}$	0.5	0.59	0.66	0.8
W_1 ($\Omega s^{-1/2}$)	-	1000	300	300
Rg (Ω)	200	5700	1500	2000
CPE_g (F)	$10x\ 10^{-10}$	$4x10^{-8}$	$5x10^{-8}$	$5x10^{-8}$
β_g	0.85	0.69	0.68	0.68
R_{gb} (Ω)	42000	10000	5500	5400
CPE_{gb} (F)	$25x\ 10^{-9}$	$2x\ 10^{-3}$	$2x10^{-3}$	$2x10^{-3}$
β_{gb}	0.91	0.6	0.68	0.73

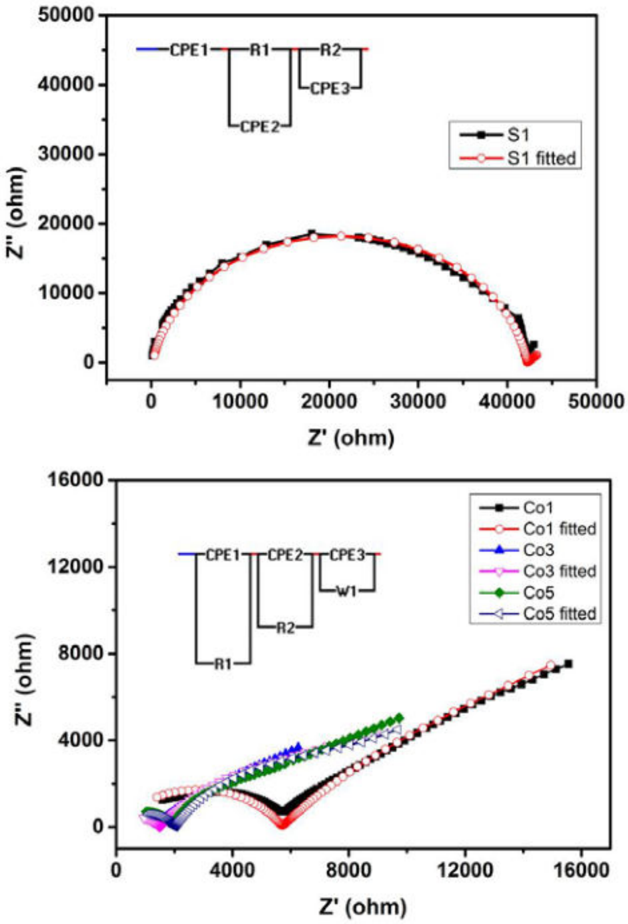

Fig. 4.23 Room temperature Nyquist plots and the corresponding equivalent circuit (inset) of pure and Co-doped $NiWO_4$ samples.

4.3.5.3 AC conductivity

The AC conductivity of pure and Co-doped $NiWO_4$ samples are investigated to analyze their conduction mechanism. Variations of AC conductivity as a function of frequency for pure and doped $NiWO_4$ samples are shown in Fig. 4. 24.

The pure sample shows a frequency-independent region followed by a region where σ_{ac} increases with the frequency. The conductivity of the pure sample follows Jonscher's power law. In the pure sample, an increase in conductivity occurs with the increase in frequency at the high frequency region. This may be due to the hopping of charge carrier from one site to a new site. A detailed explanation of the conductivity of the pure sample is given in *section 3.3.5.3*.

For the Co-doped samples, AC conductivity shows a linear relationship with frequency in the low frequency region. This linear behaviour of the frequency against the AC conductivity in the low frequency region indicates the presence of conductivity influenced by the electrode polarization effect. It is found that conductivity is increased with Co doping. There may be two possibilities for the increase in conductivity. When Co ions are substituted in $NiWO_4$ lattice, more carriers are available in grains and they get sufficient energy at relevant frequencies. This may increase conductivity. Another possibility is that increase in dopant concentration increases the oxygen vacancies. This increases the conductivity of doped samples. But for the sample Co5, the conductivity decreases due to a high density of defects. The presence of Co^{2+} may introduce the defect ions in the system. Sintering and cooling process results in the diffusion process. Due to this diffusion, these defects tend to segregate at the grain boundaries. Substitution of Ni ions with Co ions can take place up to a certain limit. Thus by increasing dopant concentration beyond that, the defect ions will act as a barrier to the flow of charge carriers [41]. This will reduce the conductivity. This may be the reason for the reduction in conductivity of Co5. In short, it can be said that by introducing a dopant like Co^{2+} into the lattice of $NiWO_4$, the conduction mechanism of $NiWO_4$ can be changed and thereby improving its conductivity. Furthermore, the improved conductivity of Co-doped $NiWO_4$ makes it a potential candidate in microelectronic devices.

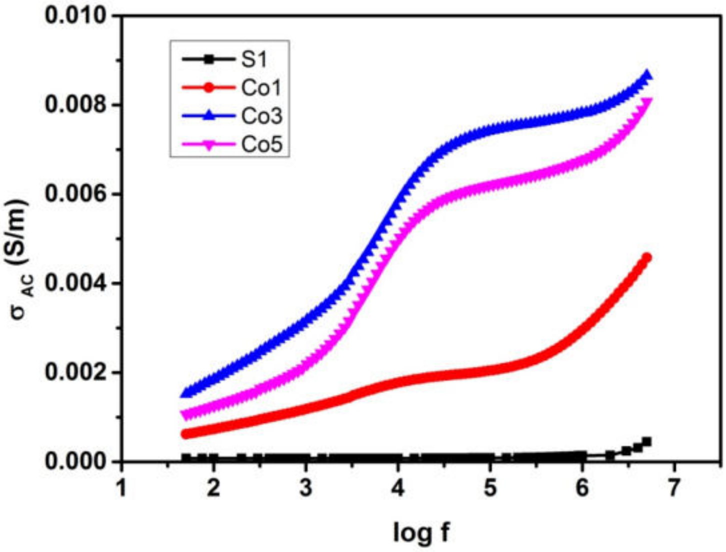

Fig. 4. 24 Variation of AC conductivity with frequency for pure and Co-doped $NiWO_4$ samples at room temperature.

4.4 Conclusion

- The Co-doped $NiWO_4$ nanoparticles are synthesized successfully using the direct chemical precipitation route.
- From XRD studies, it is found that all the doped samples have the same wolframite structure as pure $NiWO_4$.
- By increasing the dopant ion (Co^{2+}) concentration, the average crystallite size and the micro-strain of the $NiWO_4$ sample can be reduced.

- The TEM analysis revealed that the particle size decreases with an increase in Co^{2+} concentration. All the samples show a polycrystalline nature. The SAED patterns confirmed the presence of different crystal planes.
- FTIR and Raman studies confirmed the successful incorporation of cobalt ion (Co^{2+}) in the $NiWO_4$ lattice. All the characteristic vibrational modes of the pure sample are also seen in doped samples.'
- From UV-VIS-NIR analysis it can be inferred that the optical bandgap of the $NiWO_4$ sample can be tuned for potential applications by suitably varying the dopant ion concentration.
- By varying the dopant concentration, PL emission peaks and their intensities can be varied significantly. Correspondingly colour of emission changes for the doped $NiWO_4$ samples. The systematic analyses of the PL properties of Co-doped $NiWO_4$ reveal that these materials can be suitable for applications such as emissive displays, fluorescent lamps and light-emitting diodes.
- The paramagnetic nature of pure sample cannot be changed significantly by doping with a magnetically active Co element.
- The dielectric constant, loss and AC conductivity of $NiWO_4$ can be modified according to variations in Co concentration. So the electrical properties of $NiWO_4$ can be tuned by Co doping.

References

[1] R. Sundaram and K. S. Nagaraja, Mater. Res. Bull. **39** (2004) 581-590

[2] R. C. Pullar, S. Farrah and N. McN Alford, J. Eur. Ceram. Soc. **27** (2007) 1059-1063

[3] P. S. Pandey, N. S. Bhave and R. B. Kharat, Electrochim. Acta **51** (2006) 4659-4664

[4] W. Carel and E. van Eijk, Phys. Res. A **392** (1997) 285-290

[5] C. Dhandapani, R. Narayanasamy, S.N. Karthick, K. V. Hemalatha, S. Selvam, P. Hemalatha, M.S.kumar, S.D. Kirupha, H.J. Kim, Optik (Stuttg). 127 (2016) 10288–10296

[6] A. Šutka, T. Käämbre, R. Pärna, I. Juhnevica, M. Maiorov, U. Joost, V. Kisand, Solid State Sci. 56 (2016) 54–62.

[7] S. M. El-Sheikh, M. M. Rashad, J Clust Sci **26** (2015) 743–757.

[8] M. Feng, D. An, H. Zhang, G. Ma, C. Zhang, Z. Ma, International Journal of Chemical Studies 5(6) 2017, 1954-1960

[9] Yunxia Huang, Chen Yan, Xing Shi, Wen Zhi, Zhimin Li,Yangxi Yan, Maolin Zhang and Guozhong, Nano Energy 48 (2018) 430-440

[10] J. Singh, N. K. Verma, Structural, Bull Mater Sci **37** (2014) 541–547.

[11] J. Hays, K. M. Reddy, N. Y. Graces, M. H. Engelhard, V. Shutthanandan, M. Luo, C. Xu, N. C. Giles, C. Wang, S. Thevuthasan, A. Punnoose, J. Phys.: Condens. Matter **19** (2007) 266203 (24pp)

[12] H. Ji, C. Cai, S. Zhou,W. Liu, Structure, J Mater Sci: Mater Electron **29** (2018) 12917–12926.

[13] M. A. Shafique, S. A. Shah, M. Nafees, K. Rasheed, R. Ahmad, International Nano Letters 2 (2012)31

[14] H. Hitha, M. John, S. Kuriakose, A. Jose, T. Varghese, Journal of Solid State Chemistry (2020) 121546

[15] Yunxia Huang, Chen Yan, Xing Shi, Wen Zhi, Zhimin Li,Yangxi Yan, Maolin Zhang and Guozhong Nano Energy 48 (2018) 430-440

[16] S. Kumar, S. Basu, B. Rana, A. Barman, S. Chatterjee, S.N. Jha, D. Bhattacharyya, N.K. Sahoo, A.K. Ghosh, J. Mater. Chem. C (2014) 481–495

[17] G. Vijayaprasath, R. Murugan, T. Mahalingam, G. Ravi, J. Mater.Sci. **26** (2015) 7205–7213

[18] S.J. Naik, U. Subramanian, R.B. Tangsali, A.V. Salker, J.Phys.D44 (2011) 115404–115410

[19] A. Kuzmin, A. Kalinko and R. A. Evarestov, Cent. Eur. J. Phys. 9 (2011) 502- 509.

[20] T. Mathew, N.M. Batra, S.K. Arora, J.Mater. Sci. 27 (1992) 4003–4008

[21] M. Galceran, M.C. Pujol, C. Zaldo, F. Di´az, M. Aguilo´ , J. Phys. Chem. C 113 (2009) 15497–15506.

[22] H. Zhang, X. Hu, , Sep. Purif. Technol. 34 (2004) 105–108.

[23] G.M. Clark, W.P. Doyle, Acta **22**(1996) 1441-1447.

[24] H. Hitha, K.P. Priyanka, A. Sreedevi, Anjali Jose, T. Varghese, Eur. Phys. J. B 91 (2018) 287.

[25] F. D. Hard Castle and I. E. Wachs, J. Raman Spectroscopy **26**(1995) 397-405.

[26] N. V. Minh and N. M. Hung, Materials Sciences and Application 2 (2011) 957.

[27] W. Tong, L. Li, W. Hu, T. Yan, X. Guan and G. Li, J. Phys. Chem. C **114** (2010) 15298- 15305.

[28] A. Sreedevi, K. P. Priyanka, K. K. Babitha, N. Aloysius Sabu, T. S. Anu and T. Varghese, Indian J. Phys. 89 (2015) 889-897.

[29] S.M. M Zawawi, R. Yahya, A. Hassan, H N M E. Mahmud, M.N. Daud, Chem.Cent.J.7(2013)80–89.

[30] A.L.M. de Oliveira, M.R.S. Silva, S.C. de Souza, F.T.G. Vieira, E. Longo, A.G. Souza and M.G. S. Leda, J. Thermal Anal Calorim. **97** (2009) 167.

[31] S.J. Naik, U. Subramanian, R.B. Tangsali, A.V. Salker, J.Phys.D44 (2011) 115404–115410.

[32] A. B. P. Lever, G. London, P. J. McCarthy, Canad. J. Chem.55 (1977) 3172-3189

[33] A. Fujimori, F. Minami, Phys. Rev. B 30 (1984) 957

[34] N. Rajeswari Yogamalar · A. Chandra Bose, Appl Phys A 103 (2011) 33–42.

[35] L. S. Cavalcante, M.A.P. Almeida, W.Avansi, R. L. Tranquilin, E. Longo, N.C. Batista, V. R. Mastelaro,M. S. Li, Inorg. Chem. 51 (2012) 10675

[36] A. L. M. de Oliveira, J.M. Ferreira, M.R.S. Silva, G.S. Braga, L. E.B. Soledade, M.A. M. M. Aldeiza, C. A. Paskocimas, S.J.G. Lima, E.Longo, A. G. de Souza, I.M. G. dos Santos, Dyes Pigments 77 (2008)210-218

[37] C. Zhang, D. Guo, C. Hu, Y. Chen, H. Liu, H. Zhang, X. Wang, physical review **b** 87 (2013) 035416.

[38] K.W. Wagner, Ann Phys 40: (1913).817

[39] C.G. Koop, Phys Rev 83 (1951) 121.

[40] S.H. Lee, H.M. Cheong, N.G. Park, C.E. Tracy, A. Mascarenhas, D.K. Benson, S.K. Deb, Solid State Ionics 140 (2001) 135-139

[41] C. Jayachandraiah, G. Krishnaiah, Journal of Materials Science, 52(12) (2017) 7058–7066

[42] T. Nisha, R. Rohith, V. Alexander, Chithra. P. G, Indian Journal of Engineering and Materials Sciences. 15(2008) 489-496

◆

Chapter - 5

INFLUENCE OF Bi^{3+} DOPING ON THE PROPERTIES OF $NiWO_4$ NANOCRYSTALS

5.1 Introduction

Modification of structural matrix by dopants is an effective method to achieve changes in the structural, optical and electrical properties of semiconductor materials. Luminescence materials free of rare-earth ion doping are currently an active research area for its potential applications in photo-electronic fields, especially due to the lower cost of raw materials compared to that of rare earth elements. Recently, semimetal bismuth has attracted much attention because of its unique properties [1-3]. Bi^{3+} ion exhibits outstanding optical properties in inorganic solid-state crystal lattices, and such properties are attributed to their intrinsic multiple energy levels [4-7]. It is also found that Bi nanoparticles exhibit plasmonic properties akin to noble metal nanoparticles [8]. This makes Bi as a promising candidate in many fields such as sensors, fluorescence, surface-enhanced spectroscopy and photocatalysis [9-11].

This chapter deals with the influence of Bi^{3+} doping on the structural, optical and electrical properties of $NiWO_4$ nanoparticles. Variation of doping percentage affects the properties of the pure sample, which modifies their luminescence emission and electrical properties.

5.2 Synthesis of Bi-doped $NiWO_4$ nanoparticles

The reagents used for the synthesis of Bi-doped $NiWO_4$ include nickel (II) nitrate hexahydrate [$Ni(NO_3)_2.6H_2O$] (98%, Merck), sodium tungstate [$Na_2WO_4.2H_2O$] (98%, Merck) and bismuth (III) nitrate pentahydrate[$Bi(NO_3)_3.5H_2O$] (98%, Merck). The reagents are used without further purification. Nanocrystalline $NiWO_4$ samples doped with Bi^{3+} at various molar percentages (0, 1, 3 and 5%) are synthesized using direct chemical precipitation method. Two reactant solutions of 0.1 M concentration are prepared. Solution A contains $Ni(NO_3)_2.6\ H_2O$ and $Bi\ (NO_3)_3.5H_2O$ in a suitable molar ratio in 100 ml distilled water. Solution B is made of $Na_2WO_4.2H_2O$ in 100 ml distilled water. Solution A is kept in a magnetic stirrer setup and solution B is added slowly to solution A. Precipitate is formed under constant stirring. After completing the precipitation, samples are carefully washed several times with distilled water and ethanol to remove unreacted ions. The obtained precipitate is dried at 80^0C for 15 h. The dried powders are calcined at 500^0C for 3 h to get the Bi-doped $NiWO_4$ samples. The samples with 0, 1, 3 and 5% of Bi doping are named as S1, B1, B3 and B5 respectively. Synthesis procedures of the pure sample (S1) is described in *section 3.2*.

5.3 Results and discussion

5.3.1 Thermal analysis

To analyse the thermal stability of the Bi-doped $NiWO_4$ samples, thermal analysis is carried out with the help of *Perkin Elmer STA 6000*. TGA and DTG curves of the 1% bismuth-doped $NiWO_4$ are presented in Fig.5.1. The TGA curve shows three weight loss steps. When the temperature is varied from room temperature to 200^0C, 7% of the weight is lost. This may be due to the dehydration of surface absorbed moisture and gases. In 200 – 300^0C temperature range, there is a weight loss of 3% is observed. From 300 to 400^0C there is a weight loss of 2%. These two changes are due to the removal of the water trapped in the crystalline structure of the sample. Corresponding to these three weight-loss steps, three peaks are there in the DTG curve. Above 400⁰C both the graphs attain stability. From this analysis, it is found that Bi-doped $NiWO_4$ samples are thermally stable above 450⁰C. So the calcination temperature for this Bi-doped $NiWO_4$ samples is chosen to be 500⁰C.

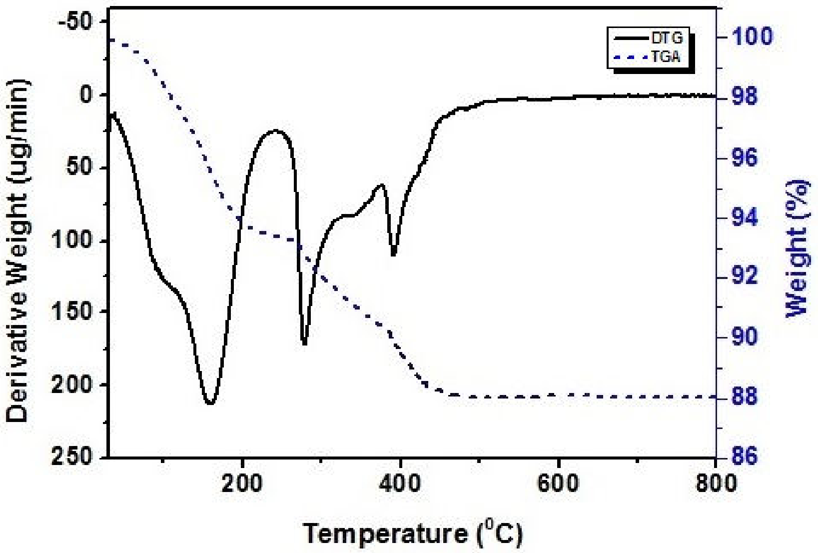

Fig. 5.1 TGA/DTG curves of Bi-doped $NiWO_4$ nanoparticles.

5.3.2 Analysis of structural properties

The structural analyses of synthesized Bi-doped $NiWO_4$ are carried out by following the procedure described in *section 2.3.2.* The effect of doping on the structural properties of pure $NiWO_4$ is analysed by considering the variations in structural properties of the pure sample with the different doping concentrations.

5.3.2.1 Powder XRD analysis

The XRD patterns of pure and Bi-doped nanophase $NiWO_4$ are determined using *Bruker AXS D8 Advance* X-ray diffractometer with Cu-Kα radiation (λ = 1.5406Å). Fig.5.2 shows the X-ray diffractograms of pristine and doped samples. XRD patterns reveal that all samples have the monoclinic phase with space group *2P/c*, which is in good agreement with

JCPDS file no. 72-0480. Variation in diffraction peak intensities by doping concentration can be observed in Fig.5.2. The diffraction intensities of B1 and B3 are large compared to pure sample S1. This is because the dopant used here is Bi^{3+}, which is a larger ion compared to Ni^{2+}. Substitution with a larger ion would imply more scattering centres, which would result increase in intensity. For the 5% doped sample (B5), the diffraction intensities are reduced and some peaks [(010), (112), (211) and (113)] are of very low intensities compared to S1. This may be due to the increased dopant concentration which restricts the crystalline growth [12].

It can be seen from Fig.5.2 that the diffraction peaks of the doped samples show a slight shift towards the lower angle side. Since the dopant Bi^{3+} is a larger ion, there is a chance of an increase in inter-planar spacing (d_{hkl}). This may result in the shifting of XRD peaks to smaller angles. Correspondingly, a small increase in d_{hkl} values is also observed for the doped samples [12]. The shift in peak position and change in d_{hkl} values of the main peak (111) are presented in Table 5.1. The lattice parameters are determined using the formula explained in *section 2.3.2.1* and their values are presented in Table 5.2.

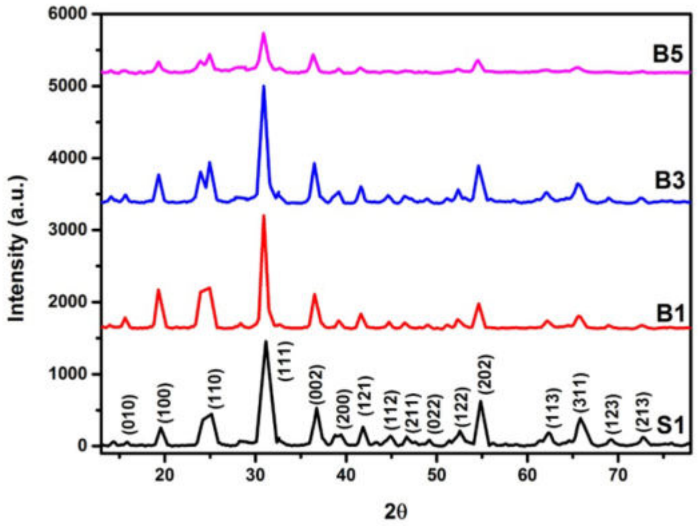

Fig. 5.2 X-ray diffractograms of pure and Bi-doped $NiWO_4$ samples.

Table 5.1 Peak position and *d_{hkl}* values of pure and Bi-doped $NiWO_4$ samples.

Sample	**Peak position of (111) planes (2θ)**	**d spacing of (111) planes (A^0)**
S1	31.17	2.867
B1	30.93	2.888
B3	30.92	2.889
B5	30.88	2.893

Table 5.2 Lattice and geometrical parameters of pure and Bi-doped $NiWO_4$ samples

Sample	**Lattice parameters**				**Geometrical parameters**			
	a	**b**	**c**	**β**	**Unitcell volume ($x10^{-30}$ m^3)**	**Average crystallite size(Scherrer formula) (nm)**	**Average crystallite size (W-H formula) (nm)**	**Micro-strain ($x10^{-3}$)**
S1	4.655±0.093	5.439±0.108	4.986±0.099	91.943	126.18	14.74±0.29	15.88±0.31	2.63±0.05
B1	4.591±0.091	5.665±0.113	4.915±0.098	89.932	127.82	15.56±0.31	15.42±0.30	1.21±0.02
B3	4.599±0.091	5.647±0.112	4.929±0.098	90.181	128.03	13.28±0.26	13.37±0.26	0.63±0.01
B5	4.711±0.094	5.473±0.109	5.064±0.101	92.883	130.4	10.71±0.21	11.73±0.23	0.99±0.02

The average crystallite sizes of pure and Bi^{3+} doped $NiWO_4$ nanoparticles are calculated from XRD data using the Scherrer equation as explained in *section 2.3.2.1,* and their results are presented in Table 5.2. It shows that the average crystallite size is increased for 1 molar % doped sample and decreased for higher molar % (3 and 5) of Bi. For a small dopant percentage, the dopant gets into the lattice and leads to an increase in crystallite size. But when dopant concentration is increased further, the decrease in the size is observed. The reason for the decrease in size is that the dopant ions constrained further growth of nanoparticles because of the relatively large size of Bi^{3+} (1.03 A^0) compared to Ni^{2+} (0.69 A^0) [12,13].

. Crystallite size and micro-strain ‘ε’ are estimated using the W-H equation as explained in *section 2.3.2.1*. Fig. 5.3 shows the W-H plots of pure and Bi-doped $NiWO_4$ nanoparticles. Average crystallite sizes and micro-strains of pure and doped $NiWO_4$ samples obtained by the W-H method are also presented in Table 5.2. From table 5.2, it can be seen that the average crystallite sizes estimated from the Scherrer equation and W-H analysis for all the samples are in agreement with each other. It is found that the micro-strain of the Bi-doped samples is decreased as compared to pure $NiWO_4$. Fig. 5.4 illustrates the variation in crystallite size and microstrain with varying dopant concentration. From XRD analysis, it is concluded that using a heavier dopant ion (Bi^{3+}) vary the average crystallite size and reduce the micro-strain in $NiWO_4$ samples. In short, structural parameters can be modified by varying the dopant (Bi^{3+}) concentration.

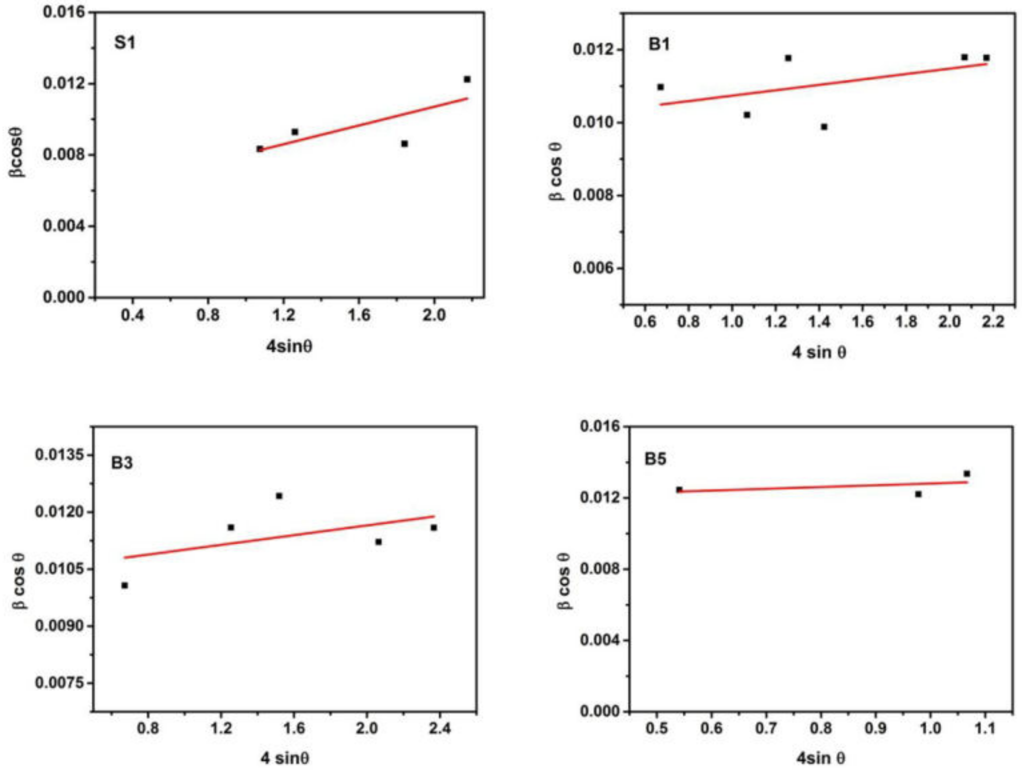

Fig.5.3 WH- plots of pure and Bi-doped $NiWO_4$ samples.

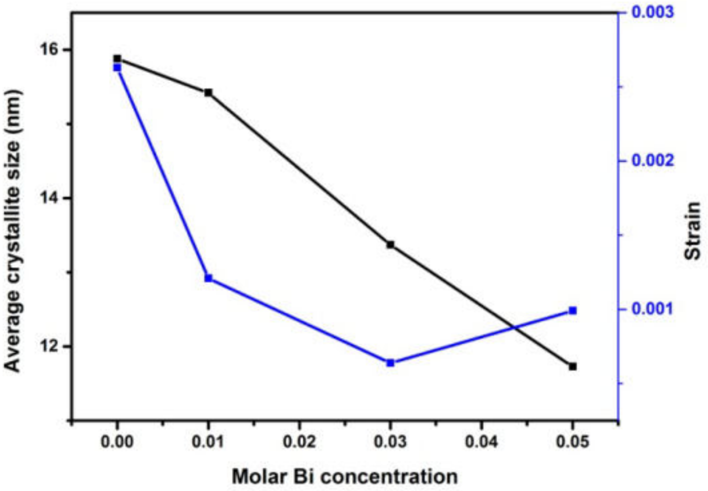

Fig. 5.4 Variation of average crystallite size and micro-strain with Bi^{3+} concentration.

5.3.2.2 TEM analysis

TEM analysis of the pure and Bi-doped samples is done with the help of *JEOL/JEM 2100* (Source: LaB6 and voltage: 200 kV). Fig.5.5 represents the TEM bright-field images of pure and Bi-doped $NiWO_4$ samples. From this figure, it is evident that particle size is varied with the increase in Bi concentration. The particle size is calculated from bright-field images using *Image J* software. The average particle size of pristine and Bi-doped samples is calculated by drawing histograms (Fig. 5.6). The particle size ranges from 8 to 20 nm for S1, 14 to 22 for B1, 8 to 22 for B3 and 8 to 16 for B5. The average particle size is found to be 14.84, 16.95, 14.11 and 11.09 nm for samples S1, B1, B3 and B5 respectively [12]. Fig.5.7, which is the HR-TEM images of pure and Bi-doped samples illustrates the polycrystalline nature of the samples. Selected area electron diffraction images of pristine and Bi-doped $NiWO_4$ samples are shown in Fig 5.8. The SAED patterns of pure and doped $NiWO_4$ samples show bright spots that also confirm the polycrystalline nature of the samples. Different diffraction planes can be identified from these images [12]. The inter-planar spacing (d_{hkl}) of planes are calculated from SAED images and corresponding planes are identified using the XRD results.These planes are tabulated in Table5.3.

Table 5.3 Inter-planar spacing (d_{hkl}) and the corresponding planes of pure and Bi-doped $NiWO_4$ samples.

Sample	**Plane**	**Measured from SAED d (A^0)**	**Measured from XRD d (A^0)**
S1	(010)	5.543	5.587
	(100)	4.401	4.533
	(011)	3.448	3.537
	(002)	2.591	2.447
	(112)	2.046	2.017
	(130)	1.695	1.740
	(302)	1.268	1.298
B1	(010)	5.565	5.665
	(100)	4.305	4.321
	(110)	3.422	3.434
	(111)	2.994	3.004
	(112)	2.021	2.025
	(211)	1.973	1.978
B3	(100)	4.337	4.337
	(110)	3.445	3.457
	(002)	2.543	2.554
	(210)	2.079	2.078
	(122)	1.686	1.698
B5	(100)	4.394	4.421
	(110)	3.447	3.449
	(211)	1,974	1.973
	(131)	1.657	1.680

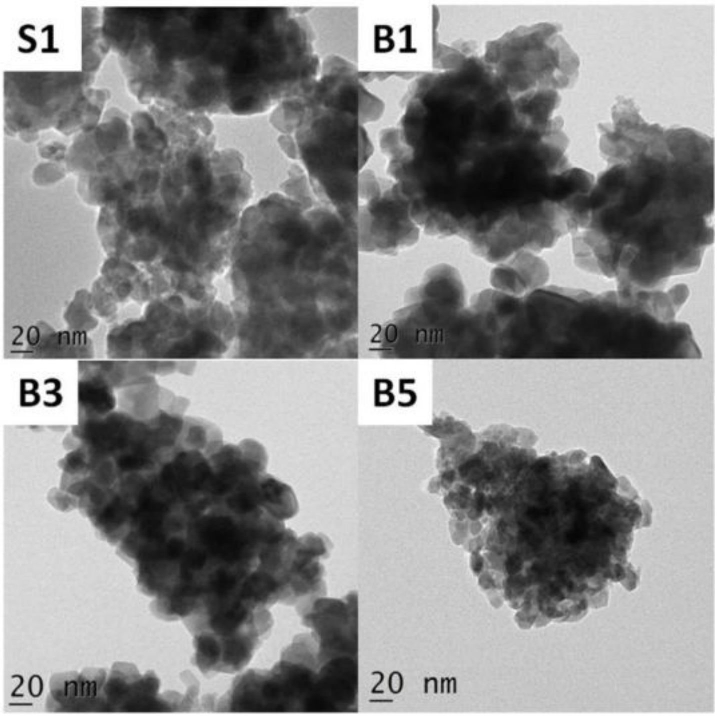

Fig. 5.5 Bright-field images of pure and Bi-doped $NiWO_4$ samples.

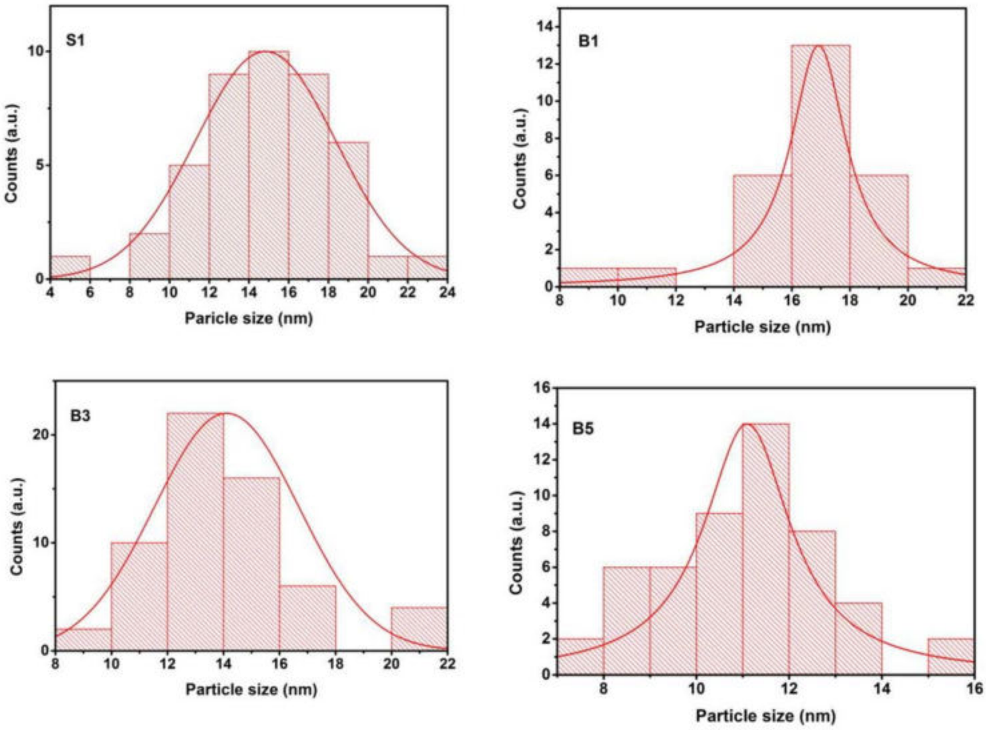

Fig. 5.6 The particle size distribution of pure and Bi-doped $NiWO_4$ samples.

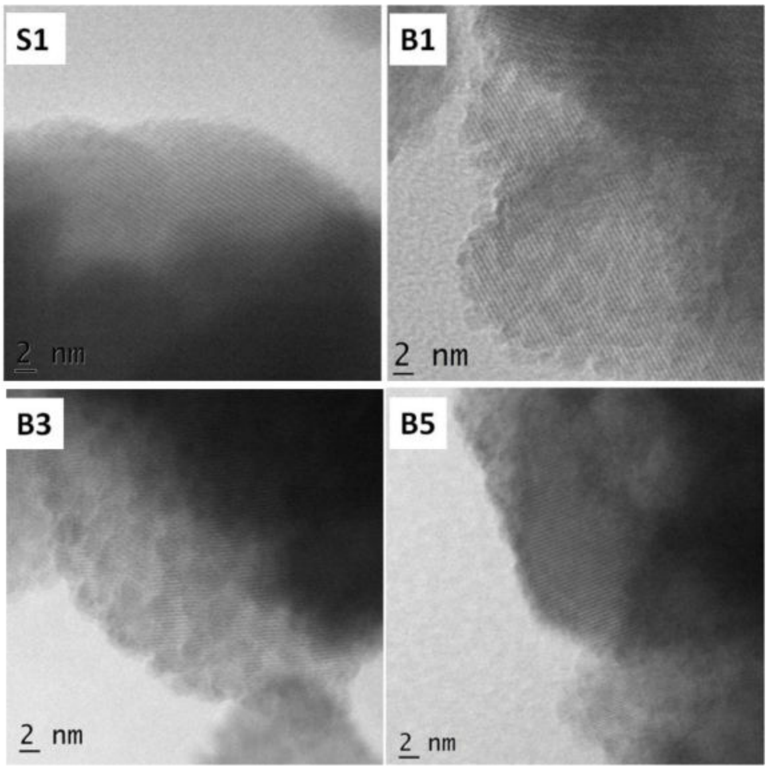

Fig. 5.7 HRTEM image of pure and doped $NiWO_4$ samples.

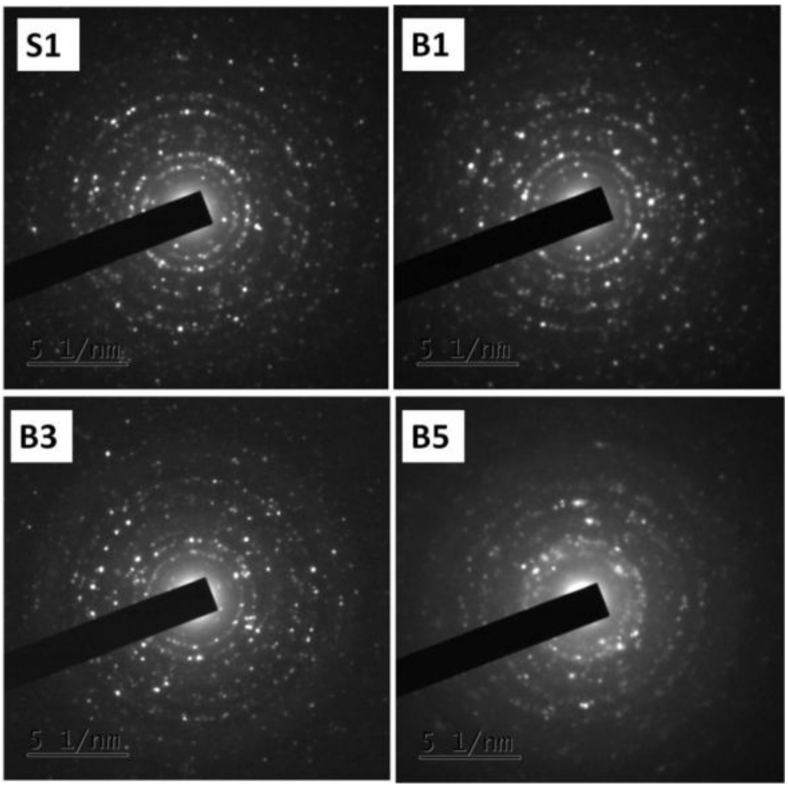

Fig. 5.8 SAED images of pure and Bi-doped $NiWO_4$ samples.

5.3.2.3 FESEM and EDS analysis

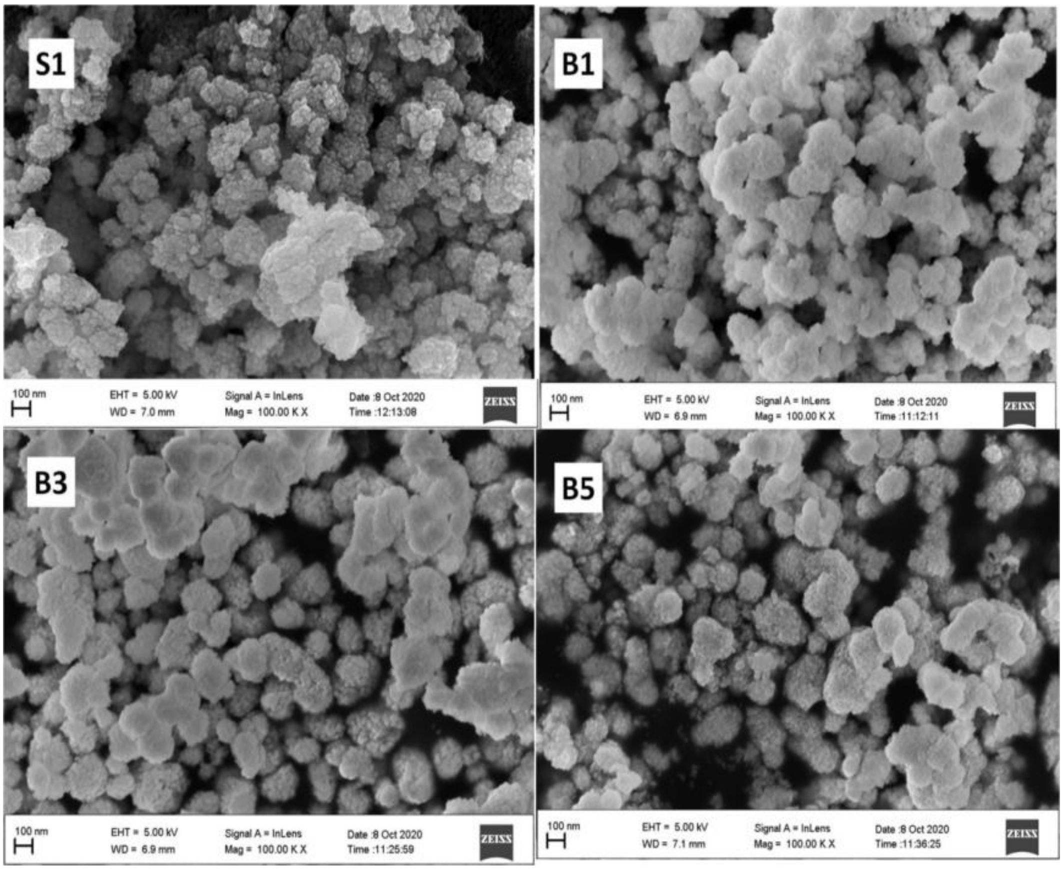

Fig. 5.9 FE-SEM images of pure and doped $NiWO_4$ samples.

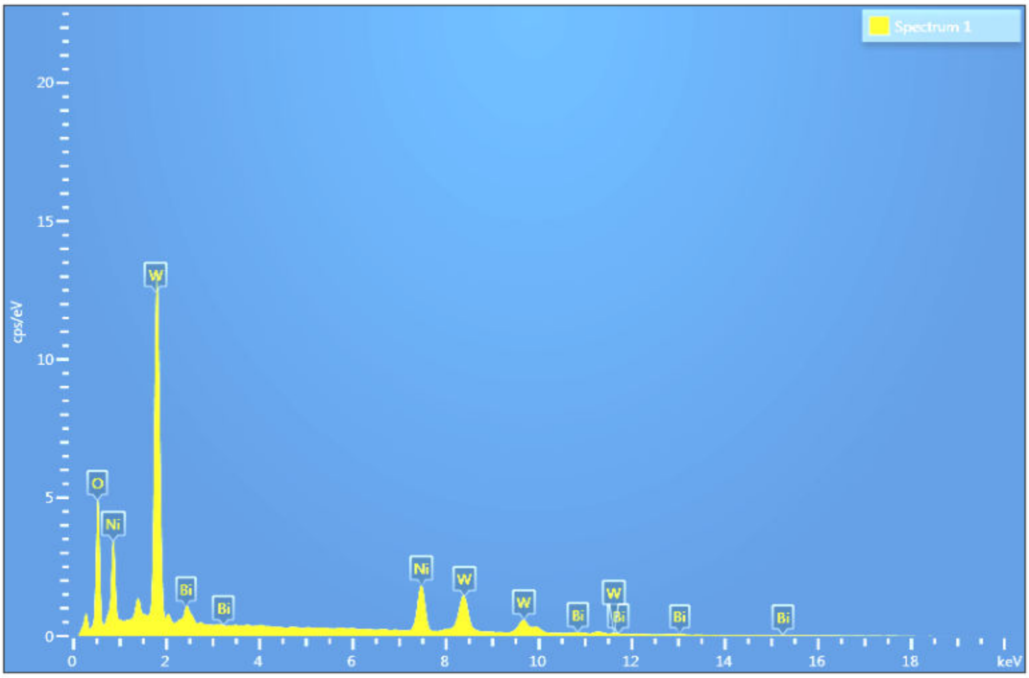

Fig. 5.10 EDS image of Bi-doped $NiWO_4$ sample B1.

Surface morphology of pure and Bi-doped samples are analysed using FE-SEM analysis. It is done with the help of the instrument ∑IGMA ^{TM} operating at 5 k V. Fig. 5.9 shows the FE-SEM images of pure and doped samples. From the figure, it can be seen that all samples show similar kind of structure with variation in size [12]. All the samples show agglomeration. Particles are agglomerated to form coral-like structures.

Table 5.4 EDS data of pure and Bi-doped $NiWO_4$ samples.

Sample	Elements	Atomic number	Series	Wt%	At. %
B0	W	74	L- Series	58.91	15.64
	O	8	K- Series	22.62	69
	Ni	28	K- Series	18.47	15.36
B1	O	8	K series	21.65	67.72
	Ni	28	K series	18.93	16.14
	W	74	L series	58.14	15.83
	Bi	83	M series	1.29	0.31
B3	O	8	K series	20.08	66.26
	Ni	28	K series	17.77	15.97
	W	74	L series	59.83	17.18
	Bi	83	M series	2.32	0.59
B5	O	8	K series	21.07	68.37
	Ni	28	K series	15.83	13.99
	W	74	L series	58.04	16.39
	Bi	83	M series	5.06	1.26

To analyse the elements present and their relative presence in the compound of the pure and doped $NiWO_4$ samples, EDS measurement is performed. Fig. 5.10 shows the EDS images of Bi-doped sample B1. The EDS data of pure and Bi-doped $NiWO_4$ samples are presented in Table 5.4. Table 5.4 confirms the presence of Ni, W, O and Bi in the doped sample.

Elements are found to be in stochiometry. It also confirms the purity of the pure and doped samples, since other impurity elements are absent in the samples [12].

5.3.2.4 FT-IR analysis

FT-IR spectra of pure and Bi-doped $NiWO_4$ nanoparticles are recorded using FTIR spectrophotometer (*Thermo Nicolet, Avatar 370*) in the range of 400-1200 cm^{-1}. Fig. 5.11 shows the FT-IR spectra of pure and Bi^{3+} doped $NiWO_4$ samples. The different modes of vibrations and corresponding band assignments of the pure sample are described in *section 3.3.2.4.* As compared to the pure sample, the doped samples show an additional peak at 691-694 cm^{-1}. This may be owing to the distortion in W=O induced by the presence of Bi^{3+} ion. The different modes of vibrations of pure and doped samples are compared with literature values [15], and are tabulated in Table 5.5.

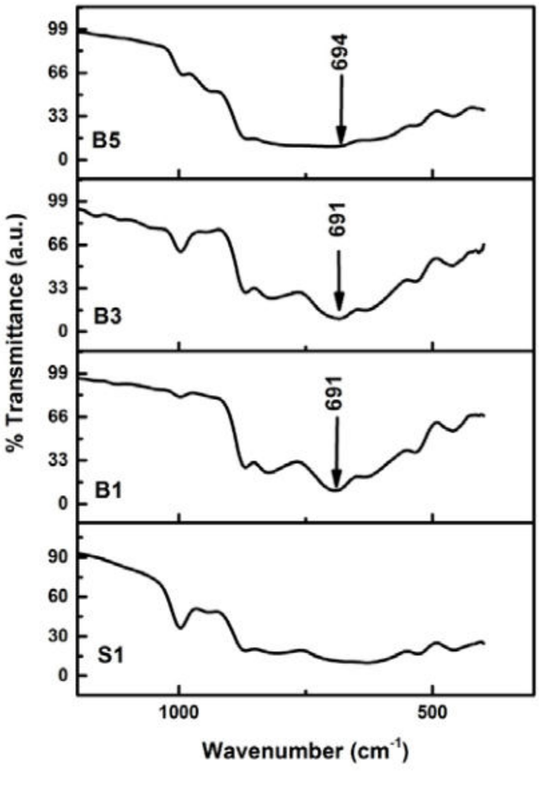

Fig. 5.11 FT-IR spectra of pure and Bi-doped $NiWO_4$ samples.

Table 5.5 IR active modes of pure and Bi-doped $NiWO_4$ samples.

Literature value (cm^{-1}) [15]	**Present work (cm^{-1})**				**Band assignment [14-17]**
	S1	**B1**	**B3**	**B5**	
432	455	460	462	459	Deformation modes of W-O bonds in $[WO_6]^{6-}$ or deformation of W-O-W bridges
494	---	---	---	---	
523	527	---	---	---	Asymmetric stretching vibrations of $[WO_6]^{6-}$
533	---	535	534	531	Asymmetric stretching vibrations of $[WO_6]^{6-}$
---	623	634	630	618	Asymmetric stretching of W-O-W bridging bonds
681	677	694	686	687	Stretching vibrations of W-O-W bonds
---	806	822	818	791	Vibrations of the WO_2 entity present in the W_2O_8
877	869	868	868	866 (low)	W-O stretching mode in WO_4 tetrahedron
961	944	---	---	936 (low)	Streching mode of W-O terminal bond
---	997	996	995	996	Metal ligand vibrations

5.3.2.5 Raman analysis

The Raman spectra of pure and Bi-doped samples are taken by *Alpha 300 RA AFM & RAMAN.* Raman spectra are mainly due to the WO_6 unit, as the NiO_6 shows relatively weak Raman activity. Fig. 5.12 shows the Raman spectra of pure and Bi^{3+}-doped $NiWO_4$ nanoparticles. The intense band is seen around 883-890 cm^{-1} in the samples, and it is A_g mode vibration due to the symmetric stretching of shortest terminal W-O bond within WO_6 unit [14]. The maximum frequency maybe for the symmetric stretch in a regular octahedron. So this band can be assigned to the symmetric stretching [14,18]. The bands at 775-790 cm^{-1} (B_g) and 689-717 cm^{-1}(A_g) are assigned to the asymmetric stretching of the W-O bonds. The bands at 411- 416 and 353-362 are assigned to A_g modes, originate from the bending modes of the regular octahedron [14, 19]. Other bands are due to the asymmetric and symmetric stretching vibrations of longer W–O bond. Deformation vibrations of inter-chain and short W–O bonds are also responsible for other bands [14, 20, 21].

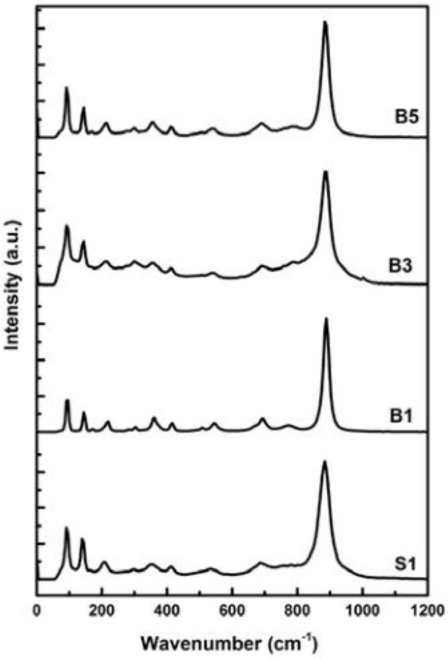

Fig. 5.12 Raman spectra of pure and Bi-doped $NiWO_4$ samples.

By doping with Bi^{3+}, all the modes of pure sample get shifted to the high wavenumber side, which confirms the effect of dopant in the $NiWO_4$ lattice. Since there is no additional mode formation in the Raman spectra of the doped samples, it can be assumed that doping does not change the basic wolframite crystal structure of the pure sample. But only slight distortions in bonds are produced.

Table 5.6 Raman active modes of pure and Bi-doped $NiWO_4$ samples.

ν (cm^{-1}) [15]	**Phonon symmetry**	**S1 (cm^{-1})**	**B1 (cm^{-1})**	**B3 (cm^{-1})**	**B5 (cm^{-1})**
97	B_g	91.4	95.5	93.5	93.5
149	A_g	139.3	144.9	144.9	144.9
174	B_g	163.8	170.8	----	170.8
197	B_g	----	----	----	----
210	B_g	207.7	----	----	----
223	A_g	----	220.2	213.7	215.9
287	A_g	276.2	282.4	278.1	278.1
307	A_g	298.7	303.9	303.9	299.7
326	B_g	----	----	----	----
363	A_g	353.4	361.9	357.6	357.6
380	B_g	----	----	----	----
418	A_g	412.3	415.8	413.5	411
512	B_g	----	508.1	503.8	508
549	A_g	533.1	546.7	540.2	542
675	B_g	686.6	669.1	663.6	----
697	A_g	717.4	694	689.6	690
775	B_g	783	776.7	785	791
893	A_g	883.8	890.53	888	886

5.3.3 Analysis of optical properties

This section deals with the UV-VIS-NIR spectroscopic and photoluminescence studies of pure $NiWO_4$ sample and its doped forms. It also includes a comparative study of the optical properties of pristine and Bi-doped $NiWO_4$ samples. The analyses are carried out by following the procedure as given in *section 2.3.3*.

5.3.3.1 UV-VIS-NIR analysis

UV-VIS-NIR spectra of pure and doped samples of $NiWO_4$ are taken with the help of a double-beam UV–Visible spectrophotometer (*Cary 5000 model*) to study their absorption properties. Fig.5.13 shows the absorption spectra of pristine and Bi-doped samples. Fig.5.13 (a) shows the absorbance spectrum in full wavelength range and Fig.5.13 (b) shows the enlarged version for 200-400 nm wavelength range. All the samples show a broad and high-intensity peak in the UV range. The maximum absorption peak for the pure sample is at 273 nm (4.54 eV). From Fig. 5.13, it can be seen that the doped $NiWO_4$ samples show the maximum absorption band around 273-299 nm (4.54- 4.14 eV). An additional band at 353 nm (3.51 eV) is observed for all the doped samples. This makes the absorption band as a broad one in the UV region for doped samples. The intense ultraviolet absorption is attributed to the excitation in O and W within the WO_6 matrix [12, 22]. The two peaks in the visible region around 454 nm (2.73 eV) and 740 nm (1.68 eV) are seen for both pure and doped samples. These bands are due to the electronic transition from ${}^3A_{2g}$ to ${}^1E_g$ and ${}^3A_{2g}$ to ${}^1T_{2g}$, respectively in $Ni^{2+}O_6$ matrix. A band around 823 nm (1.50 eV) can be seen in pure $NiWO_4$ sample and can be assigned to the ${}^3T_1$ to ${}^1T_2$ transition in $Ni^{2+}O_4$. So this band represents the presence of $Ni^{2+}O_4$ arising from Frenkel defects which are present in the pure sample with dislocation of Ni^{2+} from the octahedral to tetrahedral sites [12, 22]. For doped samples, a few more peaks are present in this range. These absorption bands occur when Ni^{2+} is situated in a co-ordination environment of low symmetry [12, 23]. All the samples show a broad absorption in the IR range, the absorption decreases with the doping in this range. So from this absorption spectra analysis, it can be concluded that the absorption property can be tuned by Bi^{3+} doping.

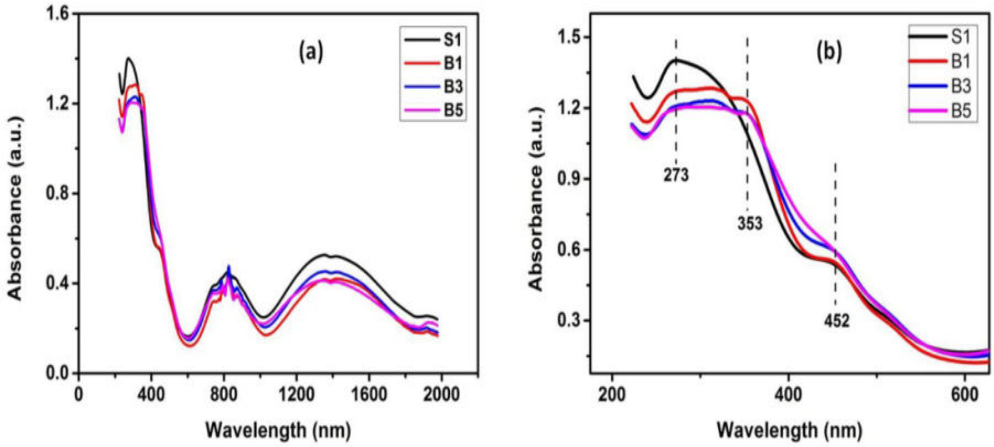

Fig. 5.13 Absorption spectra of pure and Bi-doped NiWO$_4$ samples for (a) the full range of wavelength and (b) enlarged curve of absorbance for 200-600 nm range.

In nickel tungstates, there is a chance of having both direct and indirect band transitions due to its electronic structure and d-d transitions taking place within the d levels [12, 23]. From reflectance data, absorption co-efficient 'α' is calculated for all the samples. Both direct and indirect optical band gap energies of pure and doped samples are measured by plotting $(\alpha h\nu)^2$ and $(\alpha h\nu)^{1/2}$ as a function of photon energy respectively. The energy gap is found by extrapolating the linear portion of the curves to absorption equal to zero. The Tauc plot for direct and indirect bandgaps of pure and Bi-doped NiWO$_4$ is shown in Fig.5.14 and Fig.5.15 respectively. The values of direct and indirect bandgap values are tabulated in Table 5.7.

In the case of NiWO$_4$, the valance band is formed by hybridized O$_{2p}$ and Ni$_{3d}$ states, and the Ni$_{3d}$ states contribute mainly to the upper part of the valance band. The conduction band is formed by the empty W_{5d} states with an admixture of the empty Ni_{3d} states at the bottom of the band [12, 22]. By doping with Bi, which has 6s 6p valance orbital, there are chances for modification of both valance band and conduction band. The 6s orbital of Bi may hybridize with 2p of O to modify the valance band [12, 24] and 6p orbital of Bi also may take part in hybridization to modify the conduction band [12, 25]. When doped with Bi, these changes in the valance band and conduction band may cause variation in the energy gap of the doped $NiWO_4$ samples.

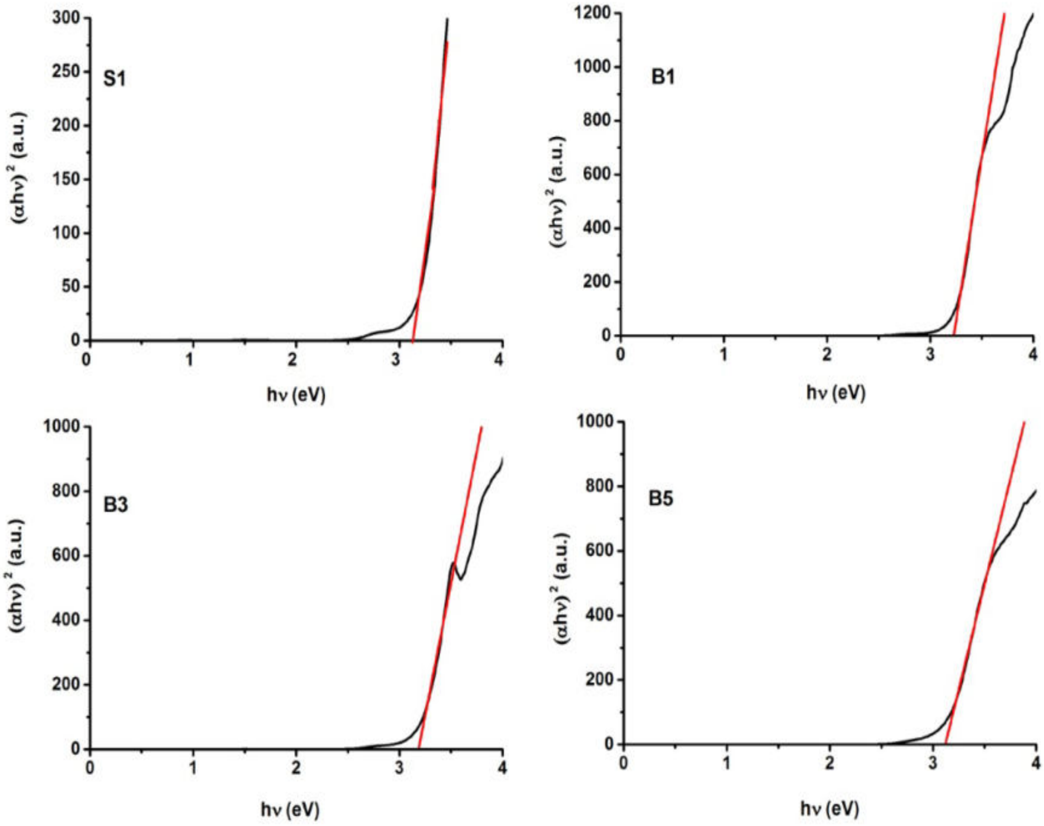

Fig. 5.14 Tauc plots for pure and Bi-doped $NiWO_4$ samples for direct bandgap.

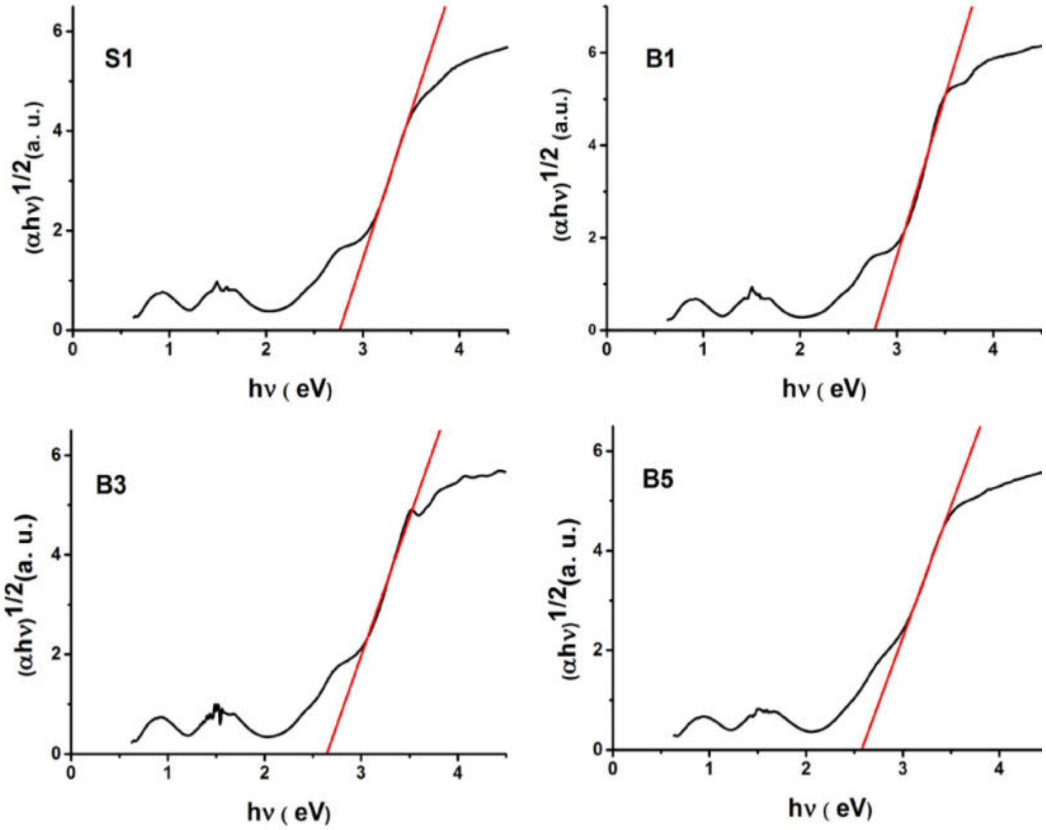

Fig. 5.15 Tauc plots for pure and Bi-doped $NiWO_4$ samples for indirect bandgap.

Table 5.7 Direct and indirect optical bandgaps of pure and doped $NiWO_4$ samples.

Sample	Direct bandgap (eV)	Indirect Bandgap (eV)
S1	3.07	2.80
B1	3.22	2.77
B3	3.18	2.65
B5	3.11	2.58

5.3.3.2 Photoluminescence analysis

PL studies provide information relating to different energy states available, which are responsible for radiative recombination. To analyse the photoluminescence properties of pristine and Bi-doped $NiWO_4$ samples, photoluminescence spectra of these samples are taken with the help of *Horiba fluorescence spectrometer* (slit width of 3.0 nm), with an excitation wavelength of 350 nm. The PL spectra of pure and Bi^{3+} doped $NiWO_4$ samples at room temperature for an excitation wavelength of 350 nm are shown in Fig.5.16. Broad emission in the spectral range from 400 to 500 nm is observed for pure and doped samples. For the excitation wavelength of 350 nm, two main emission peaks around 411-413 and 431-439 nm are observed, which are similar to other wolframite compounds [12]. Shoulder peaks of low intensities are also observed in the PL spectra. The observed patterns can originate from the WO_6^{6-} anion along with some defects in the crystal structure [12, 26, 27]. Doped samples show some additional peaks, and variation in intensity compared to the pure sample. The deconvoluted PL emission spectra of pure and doped samples are shown in Fig.5.17. The peaks at 450, 453, 454, 477 and 481 nm are related to the intensive transition from the ground state $^3A_{2g}$ to the excited state $^3T_1$ of Ni^{2+} ($3d^8$) ions in distorted octahedral coordination [12, 28, 29]. The luminescence properties of Bi-doped samples depend on the local structure. By introducing Bi^{3+} into the $NiWO_4$ lattice, it may enter into the octahedral void (as an interstitial ion) or locate at the site of octahedral symmetry (substituting for the Ni^{2+}). In this system, the radius of Bi^{3+} (1.02 A°) is much larger than that of Ni^{2+} (0.69 A°) and the majority of the Bi^{3+} ions occupy the octahedral voids. In the first case, Bi^{3+} can be considered to be 'isolated' and serves as an intrinsic luminescent centre in the $NiWO_4$ lattice [12, 30]. The emission peaks at 423, 426, 428, 458 and 439 nm are the additional peaks found in the doped $NiWO_4$ samples. They are attributed to the transition from the excited states of Bi^{3+} (triplet states $^3P_0$, $^3P_1$, $^3P_2$ and singlet state $^1P_1$) to the ground state $^1S_0$ [12, 30]. The PL spectrum of 5% Bi-doped $NiWO_4$ sample (B5) shows a new peak of small intensity centred on 605 nm (Fig. 5.17). This broadband is mainly ascribed to the $^3P_1 \rightarrow {}^1S_0$ transition of Bi^{3+} ions [12, 31]. This modification in PL spectra is due to the presence of Bi^{3+} ions in higher concentration.

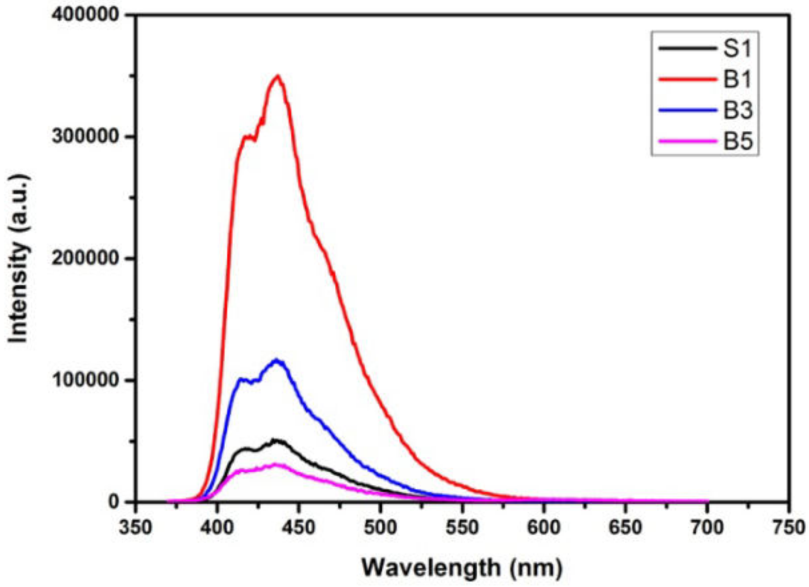

Fig. 5. 16 PL spectra of $NiWO_4$ samples for an excitation wavelength of 350 nm.

From Fig.5.16, the PL intensity varies with varying dopant concentration. The sample B1 (1% Bi^{3+} doped) shows high PL intensity which makes it suitable for luminescence applications. Quenching of PL intensity is observed to be a result of an increase in the concentration of dopant ions. Sample B5 shows very low PL intensity. This 5% Bi-doped $NiWO_4$ sample (B5) can be a suitable candidate for photocatalysis. PL spectral analysis suggests that emission spectra could be tuned by varying the dopant concentration. In short, lower and higher Bi concentrations give luminescence and photocatalytic applications, respectively.

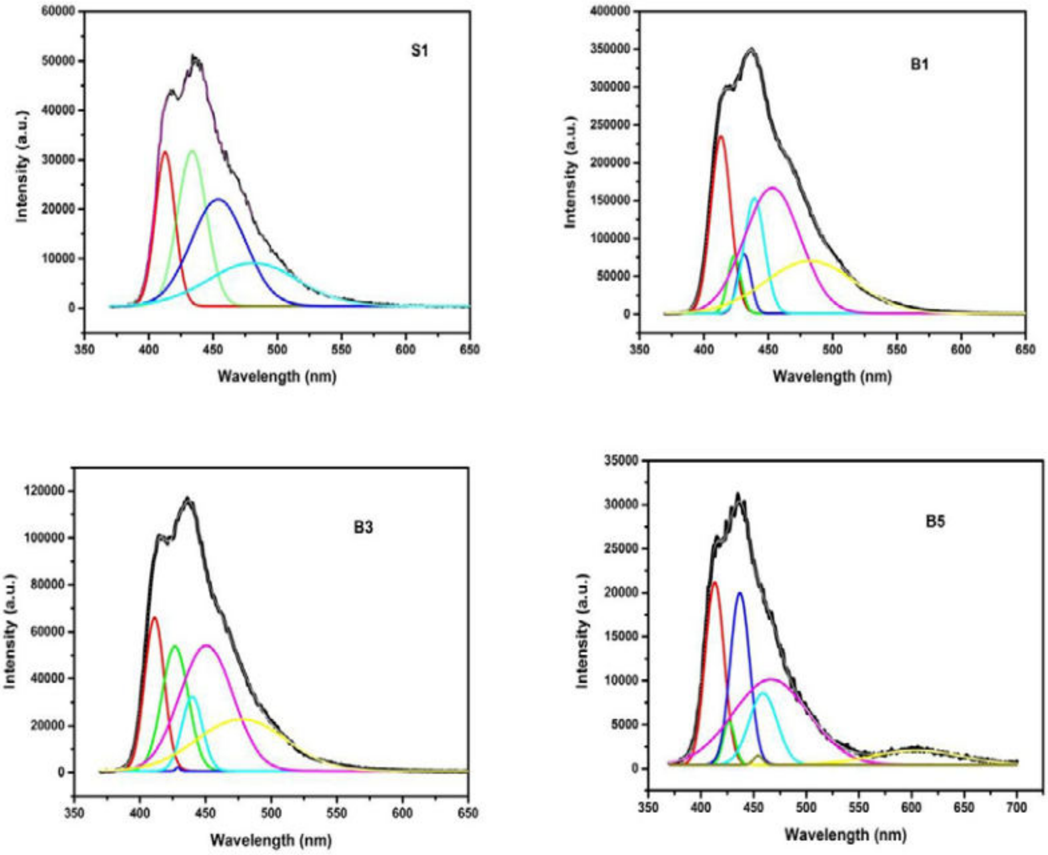

Fig. 5.17 Deconvoluted PL spectrum of pure and Bi-doped $NiWO_4$samples for an excitation wavelength of 350 nm.

Fig. 5.18 shows the CIE chromaticity diagram for the $NiWO_4$ samples S1, B1, B3 and B5. The **x** and **y** chromaticity coordinates are calculated in the CIE XYZ colour space with an excitation wavelength of 350 nm. The CIE coordinates of the pure and doped samples are presented in Table 5.8. Pure sample S1 shows purplish-blue emission. But, samples B1 and B3 show a deep blue emission. The colour of emission changes to purple-blue for sample B5 and its CIE co-ordinates come inside the phosphor triangle. It indicates that the colour of emission of samples can be tuned by varying the concentration of dopant ions.

Table 5.8 CIE co-ordinates for pure and Bi-doped $NiWO_4$ samples.

Sample	**S1**	**B1**	**B3**	**B5**
X	0.1562	0.1511	0.1534	0.1898
Y	0.0889	0.091	0.0806	0.1292

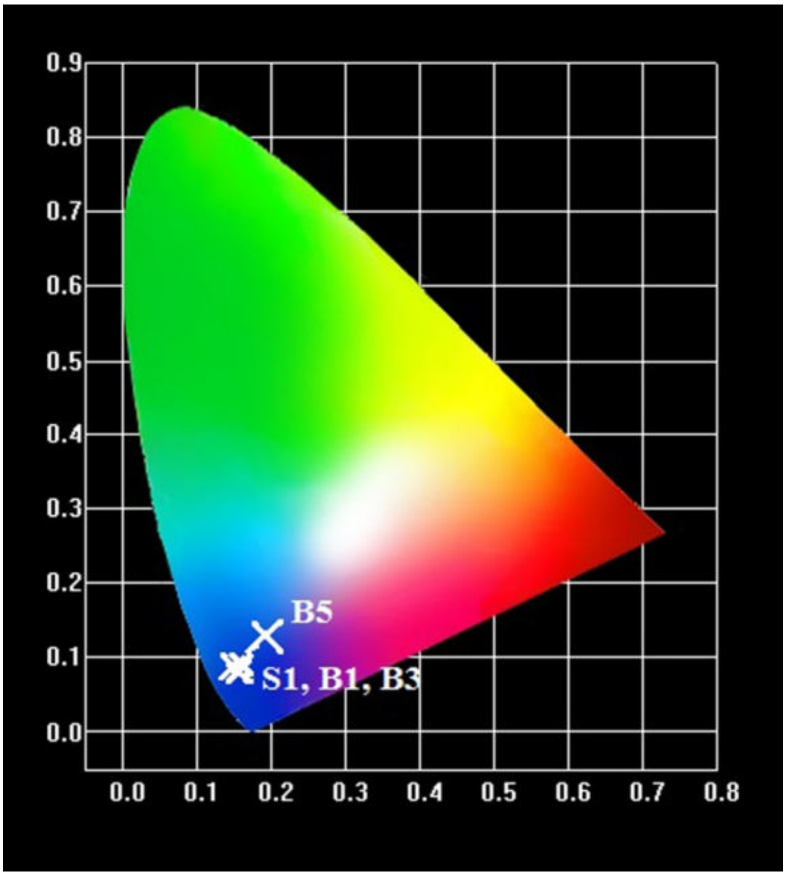

Fig. 5. 18 CIE chromaticity diagram of pristine and Bi-doped $NiWO_4$ samples.

5.3.4 Analysis of magnetic properties

The magnetic measurements at room temperature for the pure and Bi-doped $NiWO_4$ nanoparticles are carried out using a vibrating sample magnetometer (*Lakeshore VSM 7410*) in an applied magnetic field sweeping between ± 15000 Oe. Fig. 5.19 represents the VSM curves of the pure and Bi-doped $NiWO_4$ nanoparticles. The pure sample shows paramagnetic behaviour at room temperature [14]. The magnetic behaviour of pure $NiWO_4$ is discussed in *section 3.3.4.* By doping with bismuth, there is no significant deviation from the magnetic nature of $NiWO_4$. All the doped samples show paramagnetic nature as the pure sample. But, a slight shift in the curve is observed. From the magnetic studies, it can be concluded that bismuth doping does not affect the paramagnetic nature of the $NiWO_4$ sample.

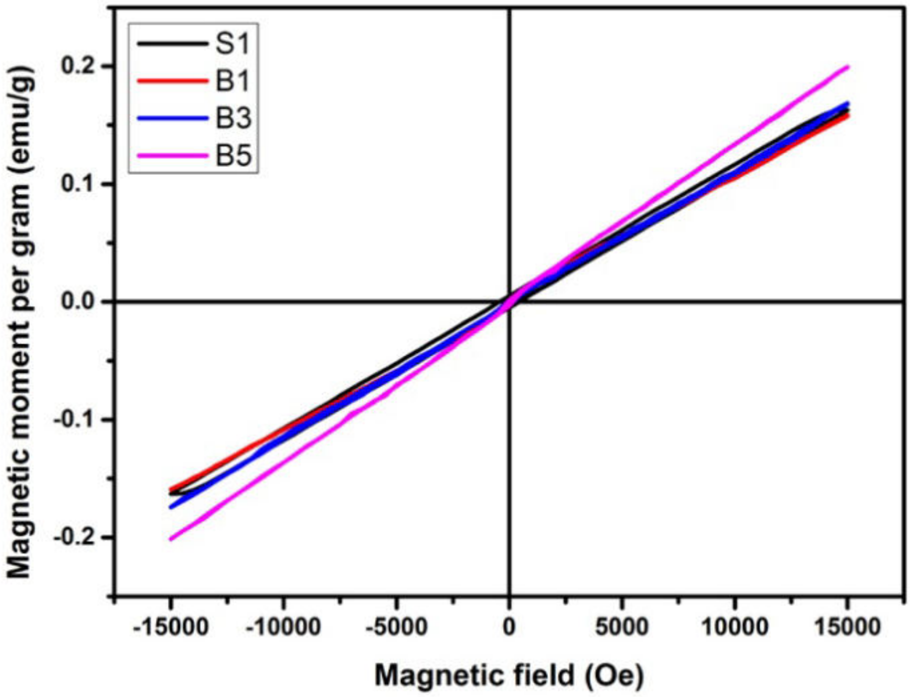

Fig. 5. 19 VSM curves of pure and Bi-doped $NiWO_4$.

5.3.5 Analysis of electrical properties

Electrical studies are carried out by following the procedure given in *Chapter 2, Section 2.3.5.* The electrical measurements are performed by making cylindrical pellets by applying a pressure of 7 GPa using a hydraulic press. The thickness and diameter of the pellets are 1.7 and 13 mm respectively. The pellets are then sintered at 500^0C for 1.5 h. The silver paste is applied to both the faces of the pellets for good electrical contact. The dielectric and impedance spectra are measured in the frequency range of 50 Hz- 5 MHz at room temperature by using *Wayne Kerr H- 6500B* model impedance analyser.

5.3.5.1 Dielectric analysis

Fig.5.20 represents the frequency response of the real part of the dielectric constant of pure and Bi-doped $NiWO_4$ at room temperature. It can be seen from Fig.5.20 that both pure and Bi-doped $NiWO_4$ samples exhibit a similar type of response against frequency. At low frequency, the real part of dielectric constant (ε') is high for the $NiWO_4$ samples, and it decreases with the increase in frequency. But, the value of ε' becomes constant at high frequency. It shows a dispersion at lower frequency region 50-1000 Hz and reaches a constant value at high frequency region, which is listed in Table 5.9. The pure sample shows a constant value 10 at 0.1 MHz frequency which is almost equal to the theoretical value [32]. The doped samples B1, B3 and B5 attain the values 53, 52 and 50 respectively at 0.1 MHz. The very high value of ε' at low frequency for the samples may be due to the electrode polarization effect. The dispersion behaviour shown by the samples can be explained based on space charge polarization, which is a consequence of the presence of conducting grains which are detached by poor conducting grain boundaries. The external electric field causes restricted building up of charges in the grain boundaries. This process produces large polarization and high dielectric constant in the lower-frequency region. This is described by Maxwell–Wagner-type interfacial polarization [33, 34] in conformity with Koop's phenomenological theory [35]. The grains become more effectual in the high frequency region as the charge carriers cannot chase the high frequency AC field. So the value of ε' decreases rapidly when the frequency rises.

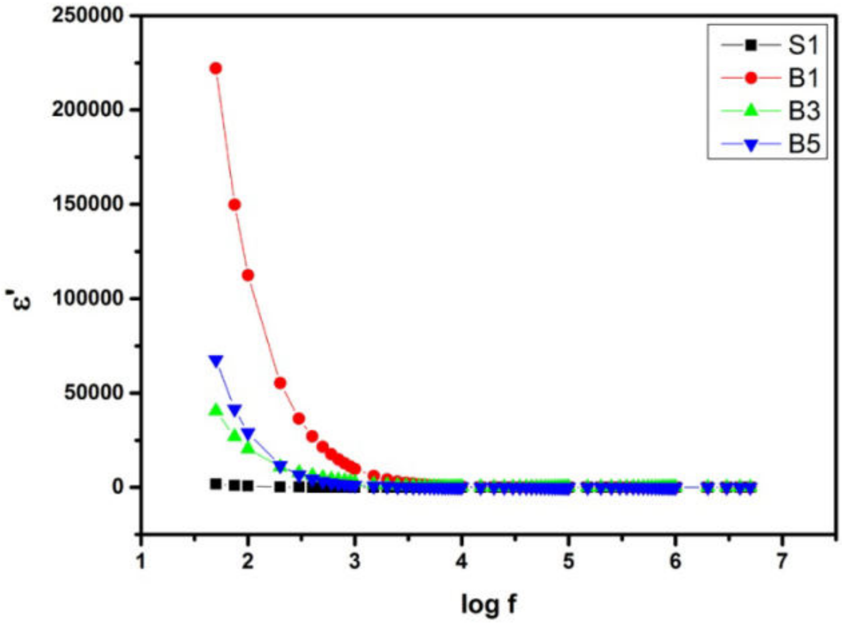

Fig. 5.20 Room temperature frequency response of the real part of dielectric constant for pure and Bi-doped $NiWO_4$ sample.

Table 5.9 Real part of dielectric constant at different frequencies for pure and Bi-doped $NiWO_4$ samples.

Sample	**ε' at 50 Hz**	**ε' at 1000 Hz**	**ε' at 10^5 Hz**
S1	1682	54	10
B1	222136	9768	53
B3	40490	2757	52
B5	67610	1157	50

From Table 5.9, the Bi-doped $NiWO_4$ samples have a very high value of **ε'** in the low frequency region as compared to the pure sample. When an element of 3^+ oxidation state is introduced into the lattice of Ni^{2+}, more cation vacancies are generated to compensate for charge neutrality [36]. In the doped sample, the Bi^{3+} create an additional vacancy which may lead to an increase of charge carrier hopping in doped samples. For the doped sample B1, it is found to have high electrode polarization and accumulation of charge carriers at the boundaries which lead to the high value of **ε'**. But when the doping concentration is increased, a slight decrease in the **ε'** is observed. In the low frequency region, an increase in the accumulation of charge carriers takes place at the grain boundaries, which results in a high value of **ε'**.

Fig. 5.21 shows the frequency response of loss tangent of pure and Bi-doped $NiWO_4$ samples at room temperature. For the pure sample, there is a peak in the low frequency region, but this peak shift to high frequency region for the doped $NiWO_4$. The peak in the tanδ curve implies the relaxation process taking place in the samples. For the doped samples, the loss is small as compared with the pure sample. At high frequencies both the curves approach to zero. From the dielectric analysis it can be inferred that by doping with Bi, the dielectric constant of $NiWO_4$ can be increased along with a decrease in loss. Hence, the Bi-doped $NiWO_4$ nanomaterial can be used in high frequency electronics applications.

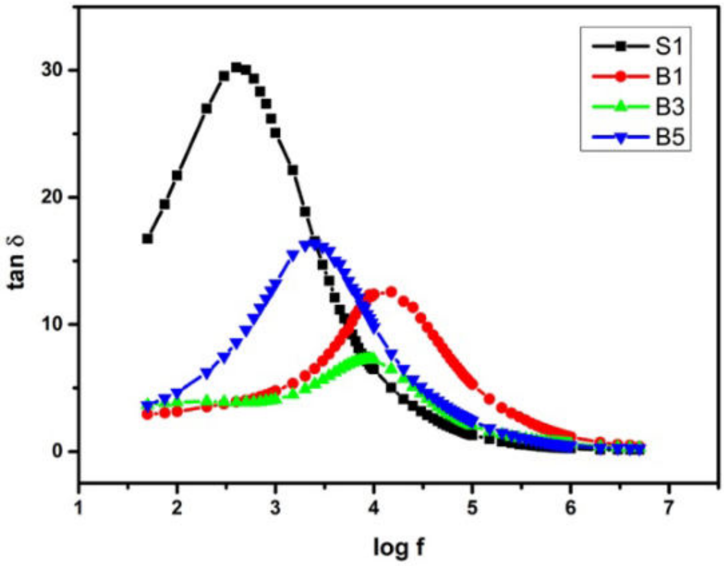

Fig. 5.21 Room temperature frequency response of dissipation factor for pure and Bi-doped $NiWO_4$.

5.3.5.2 Impedance analysis

Nyquist curves are drawn to understand the type of conduction and contributors to conduction in materials. The electrical properties of polycrystalline material have contributions from grains, grain boundaries and specimen electrode interfaces. At low frequencies the grain boundaries are active, and at high frequencies, the grains affect the conductivity. Both of these contributions can be represented by an equivalent circuit containing parallel R-C elements connected in series [37]. Fig. 5.22 represents the Nyquist plots of the pure and Bi-doped $NiWO_4$ samples. All the samples show two overlapping semi-circular arcs with their centres lie below the real axis and a line making 45^0 with the real axis in the low frequency region. All the samples show non- Debye type relaxation process as the centre of the arcs lies below the real axis. The pure $NiWO_4$ sample shows high impedance at room temperature with a very small electrode polarization effect. At the same time, Bi-doped $NiWO_4$ samples show small values of real and imaginary parts of complex impedance with a relatively high electrode polarization effect, which might be due to the additional charge carriers formed by the presence of Bi.

An equivalent circuit based on impedance spectroscopy gives an idea of the physical process happening inside the sample. The fitted Nyquist plots and corresponding equivalent circuits are shown in Fig. 5. 23. To describe the non-Debye behaviour, a suitable approach [38] of replacing the specific capacitance C in the RC circuit with a constant phase element is used. For pure sample, another CPE element is used in series with the parallel R-C elements to represent the electrode polarization effect. The values of the parameters R, C and β for grain and grain boundaries, and CPE value are presented in Table 5.10. For the doped sample, in addition to the two R-C elements, another element having Warburg component with a parallel CPE is used for representing the electrode polarization effect taking place at a lower frequency. Hence, the equivalent circuit becomes complicated for the Bi-doped $NiWO_4$ sample, which indicates the change in the conduction mechanism.

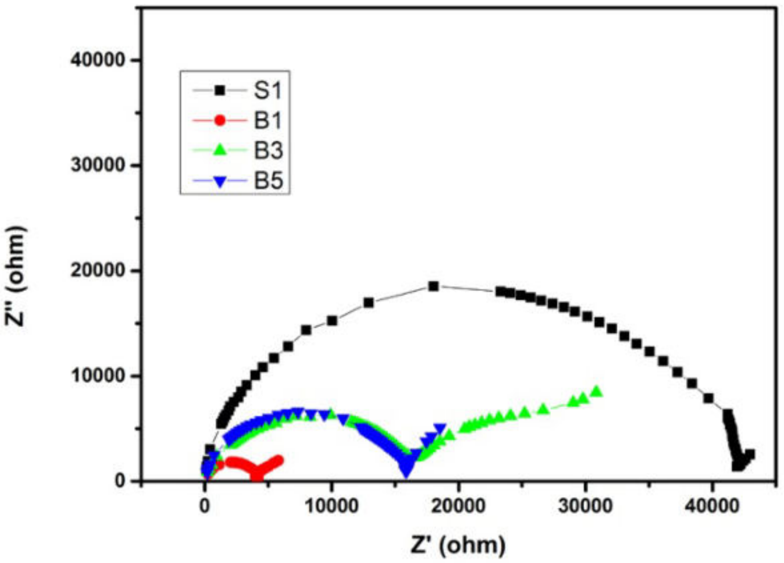

Fig. 5.22 Room temperature Nyquist plots of pristine and Bi-doped samples.

Table 5. 10 Equivalent circuit parameters for pure and doped samples

Circuit parameters	**S1**	**B1**	**B3**	**B5**
$CPE_{electrode}$ (F)	0.008	$993x10^{-8}$	$95x10^{-6}$	$95x10^{-4}$
$\beta_{electrode}$	0.5	0.68	0.85	0.9
W_1 ($\Omega s^{-1/2}$)	-	150	400	620
R (Ω)	-	70	70	90
Rg (Ω)	200	1500	15500	5000
CPE_g (F)	$10x\ 10^{-10}$	$54x10^{-5}$	$64x10^{-7}$	$74x10^{-6}$
β_g	0.85	0.99	0.85	0.75
R_{gb} (Ω)	42000	2100	12700	10750
CPE_{gb} (F)	$25x\ 10^{-9}$	$40x\ 10^{-5}$	$97x10^{-5}$	$110x10^{-7}$
β_{gb}	0.91	0.95	0.72	0.98

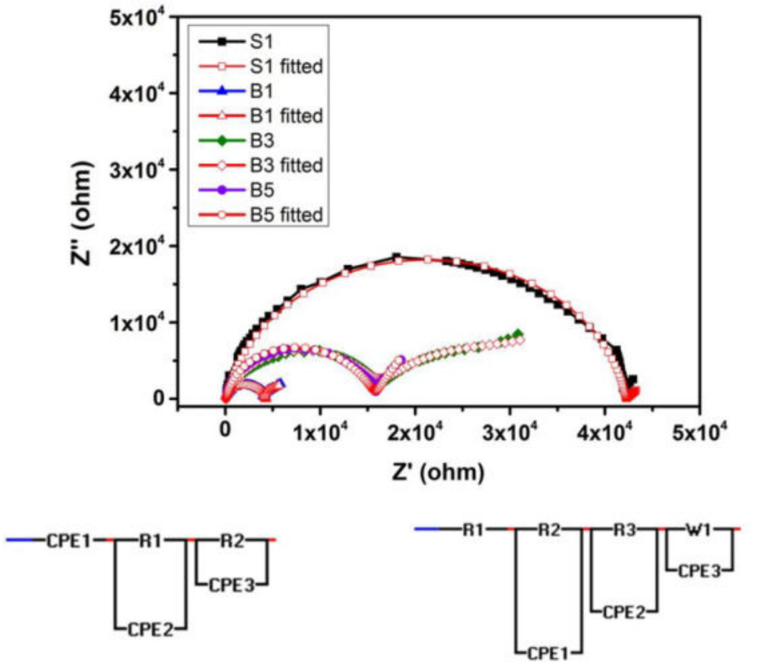

Equivalent circuit for S1

Equivalent circuit for Bi doped samples

Fig. 5.23 Room temperature Nyquist plots and the corresponding equivalent circuit of pure and Bi-doped $NiWO_4$ samples.

5.3.4.3 AC conductivity

The AC conductivity of pure and Bi-doped $NiWO_4$ samples are investigated to analyze their conduction mechanism. Variations of AC conductivity as a function of frequency at room temperature for pure and doped $NiWO_4$ samples are shown in Fig. 5. 24.

For the pure sample, conductivity is found to be constant from 100 to 10^4 Hz and the value is around $8x10^{-5}$ S/m. A slight increase in conductivity occurs with the increase in frequency and reaches a value of $1.52x10^{-4}$ S/m at 1 MHz. A sharp increase in conductivity can be seen after 1 MHz, and AC conductivity attains a maximum value of $4.52x10^{-4}$ S/m at 5 MHz for the pure sample. The σ_{ac} curve of the pure sample shows a frequency-independent region followed by a region where σ_{ac} increases with the frequency. The increasing tendency of σ_{ac} with an increase in frequency may be due to the moving of cations between adjacent sites, and the occurrence of space charges [39]. This represents that the conductivity follows Jonscher's power law, given as $\sigma_{ac} = \sigma_{dc} + A\omega^s$, 0< s<1, where σ_{dc} is the frequency-independent DC conductivity. According to Jonscher [40], the frequency-dependent conductivity occurs as a result of the relaxation mechanism of charge carriers which are moving. The hopping of charge carrier from one to a new site can be considered as the dislocation of the charge carriers between two potential minima.

For the Bi-doped sample B1, AC conductivity shows a linear relationship with frequency in the low frequency region. It increases from $1.9\text{x}10^{-3}$ to $2.8\text{x}10^{-3}$ S/m with an increase of frequency from 100 to 3000 Hz. This linear behaviour of the frequency against the AC conductivity in the low frequency region indicates the presence of conductivity influenced by electrode polarization effect. After that, the curve shows almost constant value till 10^5 Hz. This is the DC conductivity in the sample. A sharp increase in conductivity is observed above 10^5 Hz, and the AC conductivity attains a maximum value $5.74\text{x}10^{-3}$ S/m at 5 MHz. The doped samples B3 and B5 also show a linear portion in the low frequency region as DC conductivity. The curve shows an increasing nature with the increase in frequency. Sample B3 also shows the same kind of behaviour. Up to 1000 Hz, there is an increase in conductivity with an increase in frequency. From 1000 Hz to 0.1M Hz, it shows a constant conductivity region called DC conductivity. Above 0.1MHz, the conductivity increases with the increase in frequency and attains a maximum value of $3.97\text{x}\ 10^{-3}$ S/m. Sample B5 shows almost constant conductivity up to 0.1MHz and after that, the conductivity increases with the frequency and attains a maximum value of $3.3\text{x}10^{-3}$S/m at 5 MHz. The behaviour against the frequency of pure and doped $NiWO_4$ samples at high frequency can be described with the help of Maxwell–Wagner theory and Koop's model [33, 35]. According to this theory, there are two layers in the dielectric structure. Conductive grains, which are separated from each other by grain boundaries that are weak in conduction. The grain boundaries are active in the low frequency region, whereas the grains affect the conductivity at a higher frequency. The increase in conductivity of all samples at high frequency can be explained by the rise in the charge hopping between Ni^{2+} to Ni^{3+}. The hopping rate goes up with the increase in the frequency of the applied field and hence, the conductivity enhances. In short, it can be said that by introducing a dopant like Bi^{3+} into the lattice of $NiWO_4$, cation vacancies can be created and leads to the formation of charge carriers. This changes the conduction mechanism of $NiWO_4$ and thereby improving its conductivity. Furthermore, the improved conductivity of Bi-doped $NiWO_4$ makes it a potential material in microelectronic devices.

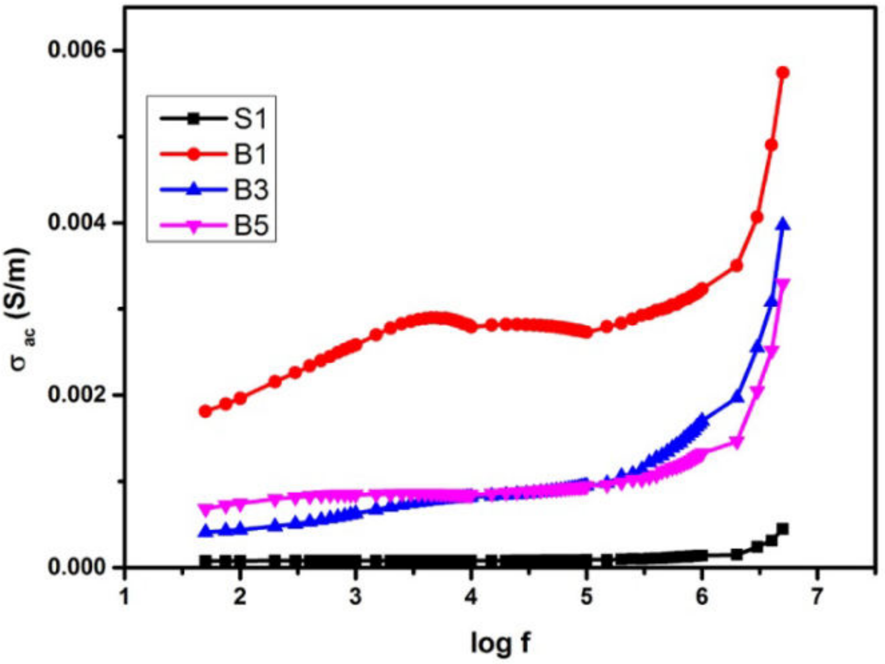

Fig. 5. 24 Variation of AC conductivity with frequency for pure and Bi-doped $NiWO_4$ samples at room temperature.

5.4 Conclusion

- Bi-doped $NiWO_4$ nanoparticles are synthesized using a simple chemical precipitation method.
- By changing the Bi concentration, the average crystallite size and micro-strain of the samples are modified. So the structural parameters are varied by varying the Bi concentration without varying the crystal structure of pure $NiWO_4$ sample
- TEM studies confirmed the particle size variation of Bi-doped $NiWO_4$ and the polycrystalline nature of the samples.
- EDS analysis shows that the doped samples are free from impurity elements and all the samples follow the right stoichiometric ratio.
- FT-IR and Raman spectra confirm the formation of a basic wolframite structure of doped samples.
- UV-VIS-NIR analysis reveals that the optical bandgap slightly changes according to the doping concentration.
- PL analysis revealed the idea that the luminescence properties of the $NiWO_4$ sample can be tuned by varying the dopant concentration. The dopant Bi also acts as a luminescence centre in doped samples.
- Magnetic studies of Bi-doped $NiWO_4$ samples gives the idea that doping with Bi does not change the magnetic behaviour of $NiWO_4$.
- Dielectric studies show that the doped samples exhibit a high value of dielectric constant with low loss. and conductivity of pure $NiWO_4$ sample can be varied significantly by doping with bismuth. The electrical properties of $NiWO_4$ can be tuned by Bi doping.
- Doping of Bi in $NiWO_4$ lattice changed the structural, optical and electrical properties of $NiWO_4$ significantly. These changes make the doped sample applicable in photocatalytic and electrical fields.

References

[1] A.J. Caruana, M.D. Cropper, S.A. Stanley, Surf. Coat. Technol. 271 (2015) 8-12;

[2] B. O'Brien, M. Plaza, L. Y. Zhu, L. Perez, C. L. Chien, P. C. Searson, J. Phys. Chem. C 112 (2008) 12018-12023

[3] F. Y. Yang, K. Liu, K. M. Hong, D. H. Reich, P. C. Searson, C. L. Chien, Science 284 (1999) 1335-1337

[4] F. W. Kang, M. Y. Peng, D. Y. Lei, Q. Y. Zhang, Chem. Mater. 28 (2016) 7807–7815.

[5] F. W. Kang, H. S. Zhang, L.Wondraczek, X. B. Yang, Y. Zhang, D. Y. Lei, M. Y. Peng, Chem. Mater. 28 (2016) 2692–2703.

[6] L. L. Wang , Q. L. Wang , X. Y. Xu , J. Z. Li , L. B. Gao , W. K. Kang , J. S. Shi, J. Wang , *J. Mater. Chem. CJ. Mater. Chem. C Mater. Opt. Electron. Devices* **1** *(*2013) 8033—8040.

[7] R. V. Yadav, R. S. Yadav, A. Bahadur, A. K. Singh, S. B. Rai, Inorg. Chem. 55 (2016) 10928–10935

[8] G. Blasse, A. Bril, Investigations on Bi^{3+}-Activated Phosphors, J. Chem. Phys. 48 (1968) 217–222.

[9] S. H. Miao, Z. G. Xia, J. Zhang, Q. L. Liu, Inorg. Chem. 53 (2014) 10386–10393.

[10] E. Cavalli, F. Angiuli, F. Mezzadri, M. Trevisani, M. Bettinelli, P. Boutinaud, M.G. Brik, J. Phys.: Condens. Matter 26 (2014) 385503

[11] R. J. Xie, N. Hirosaki, T. Suehiro, F. F. Xu, M. Mitomo,Chem. Mater. 18 (2006) 5578–5583.

[12] H. Hitha, Mathew John, Anjaly Jose, Soumya Kuriakose, Thomas Varghese, Journal of Solid State Chemistry 295 (2021) 121892. doi:10.1016/j.jssc.2020.121892

[13] J. Choi, H. Park, M.R. Hoffmann, J. Phys. Chem. C 114 (2009) 783–792

[14] H. Hitha, K.P. Priyanka, A. Sreedevi, Anjali Jose, T. Varghese, Eur. Phys. J. B 91 (2018) 287.

[15] A. Kuzmin, A. Kalinko and R. A. Evarestov, Cent. Eur. J. Phys. 9 (2011) 502- 509.

[16] H. Wang, F. D. Medina, Y. D. Zhou and Q. N. Zhang, Phys. Rev. B **45**, 10356 (1992)

[17] J. M. Quintana-Melgoza, A. Gomez-Cortes and M. Avalos-Borja, React. Kinet. Catal. Lett.**76**, 131 (2002)

[18] D. Hard Castle and I. E. Wachs, J. Raman Spectroscopy **26**, 397 (1995)

[19] N. V. Minh and N. M. Hung, Materials Sciences and Application **2**, 957 (2011)

[20] W. Tong, L. Li, W. Hu, T. Yan, X. Guan and G. Li, J. Phys. Chem. C **114**, 15298 (2010)

[21] A. Sreedevi, K. P. Priyanka, K. K. Babitha, N. Aloysius Sabu, T. S. Anu and T. Varghese, Indian J. Phys. 89 (2015) 889

[22] S.M. M Zawawi, R. Yahya, A. Hassan, H N M E. Mahmud, M.N. Daud, Chem.Cent.J.7(2013)80–89.

[23] G. T. Montini, H. Abdul, F.Laura, A. Gianpiero, F. Paolo, Chem. Phys. Lett. 498 (2010) 115- 116.

[24] L. Zhang, Y.Zhu, Catal. Sci. Technol. 2 (2012) 694–706

[25] L. Zhang, Y. Man, Y. Zhu, ACS Catal. 1 (2011) 841-848

[26] D. V. Bavykin, S. N. Gordeev, A. V. Morkalenko, A. A. Lapkin, F. C. Walsh, J. Phys. Chem. B 109 (2005) 8565-8569

[27] L. S. Cavalcante, M.A.P. Almeida, W.Avansi, R. L. Tranquilin, E. Longo, N.C. Batista, V. R. Mastelaro,M. S. Li, Inorg. Chem. 51 (2012) 10675

[28] A. L. M. de Oliveira, J.M. Ferreira, M.R.S. Silva, G.S. Braga, L. E.B. Soledade, M.A. M. M. Aldeiza, C. A. Paskocimas, S.J.G. Lima,

E.Longo, A. G. de Souza, I.M. G. dos Santos, Dyes Pigments 77 (2008) 210-218

[29] A. Kuzmin, J. Purans, Radiation Measurements 33 (2001) 583-586.

[30] Z. Xiu, S. Liu, F. Xu, W. Yu, J. Yu, G. Feng, Materials Letters 61 (2007) 4800– 4802

[31] F. Kang, X. Yang, M. Peng, L. Wondraczek, Z. Ma, Q. Zhang, J. Qiu, J. Phys. Chem. C 118 (2014) 7515−7522

[32] J. Lv, E. Xiao, M. Liu, X. Dong, Y. Chen, Z. Yue, Z. Qi, F. Shi, Materials Chemistry and Physics (2020)

[33] J.C.Maxwell, Electricity and magnetism, vol 1. Oxford University Press, New York, p 88, 1973

[34] K.W. Wagner, Ann Phys 40: (1913).817

[35] C.G. Koop, Phys Rev 83 (1951) 121.

[36] S.H. Lee, H.M. Cheong, N.G. Park, C.E. Tracy, A. Mascarenhas, D.K. Benson, S.K. Deb, Solid State Ionics 140 (2001) 135-139

[37] J. Ross Macdonald, Impedance Spectroscopy: Emphasizing Solid Materials and Systems, Wiley Interscience Publication, New York (1987)

[38] R. Schmidt, W. Eerenstein, T. Winiecki, F. D. Morrison, and P. A. Midgley, Phys. Rev. B **75** (2007) 245111.

[39] N.K. Karan, D.K. Pradhan, R. Thomas, B. Natesan, R.S. Katiyar, Solid State Ionics 179 (2008) 689.

[40] D.K. Pradhan, B. Behera, P. R. Das, J. Mater. Sci.: Mater. Electron.23 (2011) 779-785

◆

Chapter - 6

THERMAL, STRUCTURAL, OPTICAL, MAGNETIC AND ELECTRICAL PROPERTIES OF $NiWO_4$/SnPc NANOCOMPOSITES

6.1 Introduction

Nickel tungstate as a p-type transition metal tungstate has some appealing properties and can be applied in various fields [1-3]. More properties can be explored by modifying and controlling structural and optical parameters. For better characterization and to elucidate the possible reasons, investigation on the improvisation on properties of $NiWO_4$ nanoparticles has to be done. Now wide varieties of inorganic/organic composites have been made and they find application in different fields [4-6]. Here inorganic transition metal tungstate ($NiWO_4$) is coupled with an organic compound (Tin phthalocyanine) to form a composite so that structural and optical properties of $NiWO_4$ can be modified for potential applications.

Tin phthalocyanines (SnPc) are important due to their chemical and spectroscopic properties, and their applications in photocatalysis and the biomedical field [7, 8]. In the case of tin phthalocyanine, Sn(II) ions induce some strain on the phthalocyanine framework as the ion is large. Due to this strain metal ion is slightly displaced leading to the breakage of planar symmetry of metal phthalocyanines [MPcs]. This non-planar symmetry modifies the crystalline properties of the compound.

In this chapter, the synthesis and characterization of nickel tungstate/tin phthalocyanine ($NiWO_4$/SnPc) nanocomposites, and the modification of structural, optical, magnetic and electrical properties of $NiWO_4$ by the formation of $NiWO_4$/SnPc composites are discussed.

6.2 Synthesis of $NiWO_4$/SnPc nanocomposite

The composite samples are prepared using a standard solvent evaporation method. Prepared $NiWO_4$, tin phthalocyanine [$C_{32}H_{16}N_8$] (Sigma Aldrich Chemicals); dimethylformamide[C_3H_7NO], dimethyl sulfoxide[C_2H_6OS] and ethanol[C_2H_6O] (Merck, Whitehouse Station, NJ, USA) are used for the synthesis of nanocomposite samples. Distilled water is used in all the synthesis procedures.

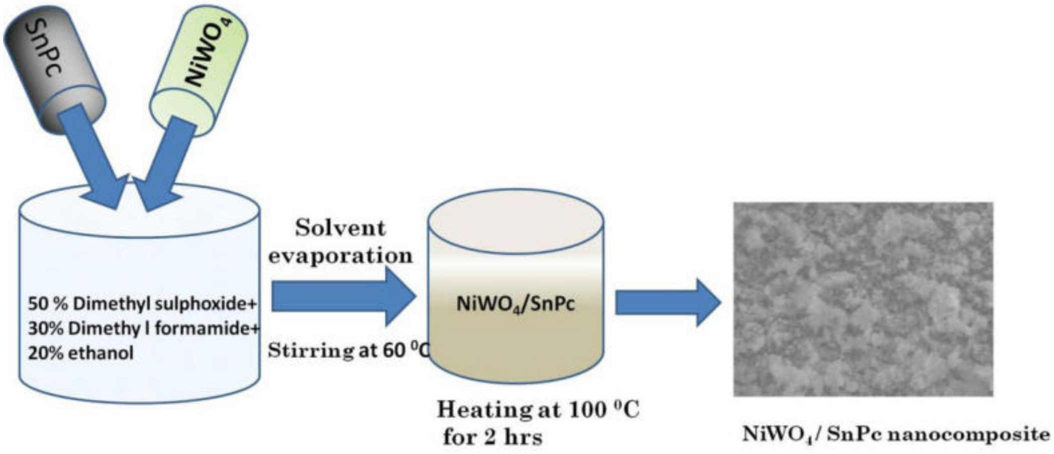

Fig. 6.1 The schematic diagram of the synthesis of $NiWO_4$/ SnPc nanocomposite.

Three composite samples are made by taking three different weight percentages of SnPc with $NiWO_4$ sample. Preparation of $NiWO_4$ nanoparticles calcined at 500^0C (S1) is described in *section 3.2*. SnPc (1 wt%) is dissolved in a solvent mixture containing 50% dimethyl sulfoxide, 30% dimethylformamide, and 20% ethanol. The required amount of synthesized $NiWO_4$ (S1) is gradually added to this solution under constant stirring. After attaining homogeneity, the solution is stirred using a magnetic stirrer at 60°C. After the complete evaporation of the solvent, the composite is dried at 100°C in a hot air oven for 2 h to get composite sample C1. A similar procedure is used to get the composite samples C2 (having 2 wt% SnPc) and C3 (having 3 wt% SnPc) [9].The schematic representation of the synthesis of nanocomposite samples is shown in Fig. 6.1.

6.3 Results and discussion

6.3.1 Thermal analysis

A study of the thermal stability of the $NiWO_4$/SnPc nanocomposite has done using thermogravimetric analysis, derivative thermogravimetry and differential thermal analysis using *Perkin Elmer STA 6000*. Fig.6.2 shows the TGA/DTG/DTA graphs of the composite sample. The sample is heated from ambient temperature to 800^0C. The curve indicates a weight loss of 1.5% within the temperature range of 45 to 545^0C. Only 0.5% of mass loss is seen up to 370^0C. The DTG curve shows three major peaks within this region, evidently owing to the removal of absorbed water content and non vaporized solvents. From 370 to 545^0C, there is a wide peak of intense decomposition. Almost 1% of the weight is lost during this temperature range. This might be due to the decomposition of the SnPc in the nanocomposite. The decomposition of SnPc can be confirmed from the DTA graph shown in Fig.6.2. It shows an exothermic peak with ΔH of 14.51 J/g within this region. This energy corresponds to the energy of the decomposition of SnPc [9]. After 545^0C the curve is almost stable. From the thermal analysis, it can be concluded that nanocomposite samples show thermal stability below 545^0C. Above this temperature, the phthalocyanine in the nanocomposite samples is removed by their decomposition. From the thermal analysis, the calcination temperature is chosen to be 100^0C.

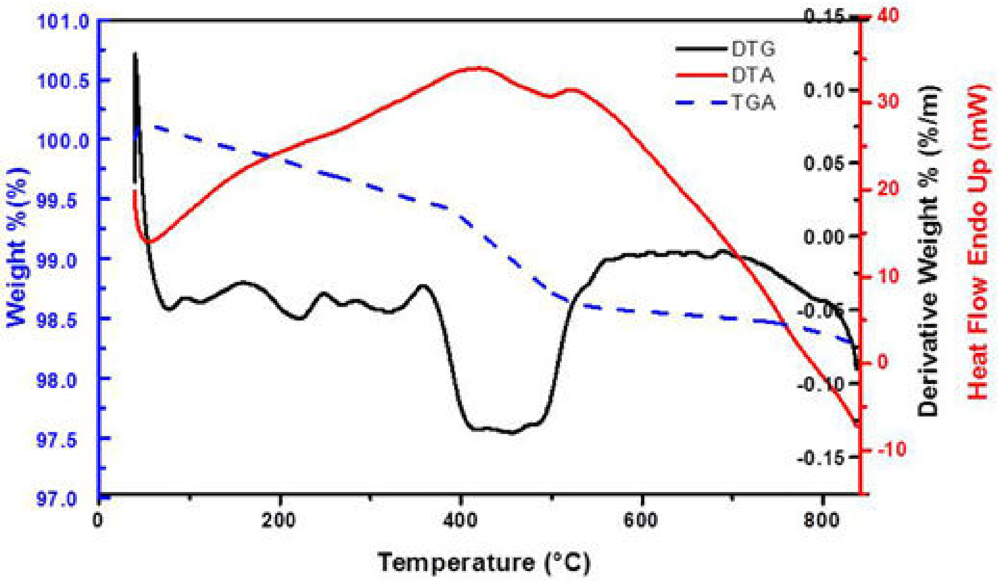

Fig. 6.2 TGA/DTA curves for $NiWO_4$ nanoparticles.

6.3.2 Analysis of structural properties

The structural analyses of synthesized $NiWO_4$/SnPc nanocomposite samples are carried out by following the procedure described in *section2.3.2.*

6.3.2.1 Powder XRD analysis

To study the crystal structure of pure sample (S1) and the changes take place in crystal structure by composite formation, XRD analysis is carried out with the help of *Bruker AXS D8 Advance* X-ray diffractometer with Cu-Kα radiation (λ = 1.5406 Å). Fig.6.3 shows the X-ray diffraction patterns of pure and composite samples. The XRD pattern of S1 agrees well with the JCPDS File No. 72-0480. It corresponds to the wolframite monoclinic structure with a space group *P2/c*. The same XRD pattern is observed for the composite samples also, which means the presence of SnPc doesn't change the crystalline structure of the pure sample (S1). This may be due to the low concentration of SnPc in nanocomposite samples. But there is a slight change in diffraction angle. The changes in diffraction angle for the composite samples are presented in Table 6.1 along with the details of d_{hkl} spacing. Intensities of diffraction peaks elevate and become sharper for C1 (Fig. 6.3), indicating an increase of crystalline nature. The reason is that the interaction of SnPc in the lattice may lead to changes in the scattering factor of the pure sample. For C2 and C3, there is a decrease in intensities compared to C1, and also the width of the obtained XRD peaks shows a broadening with an increase in the concentration of SnPc. These two observations imply the degradation of crystalline nature. It is probably associated with the lattice disorder and strain-induced in the $NiWO_4$ lattice due to the presence of a comparatively higher concentration of SnPc [9,10]. With the XRD data, lattice parameters of pure and composite samples are calculated using the formula given in *section 2.3.2.1.* The values are tabulated in Table 6.2.

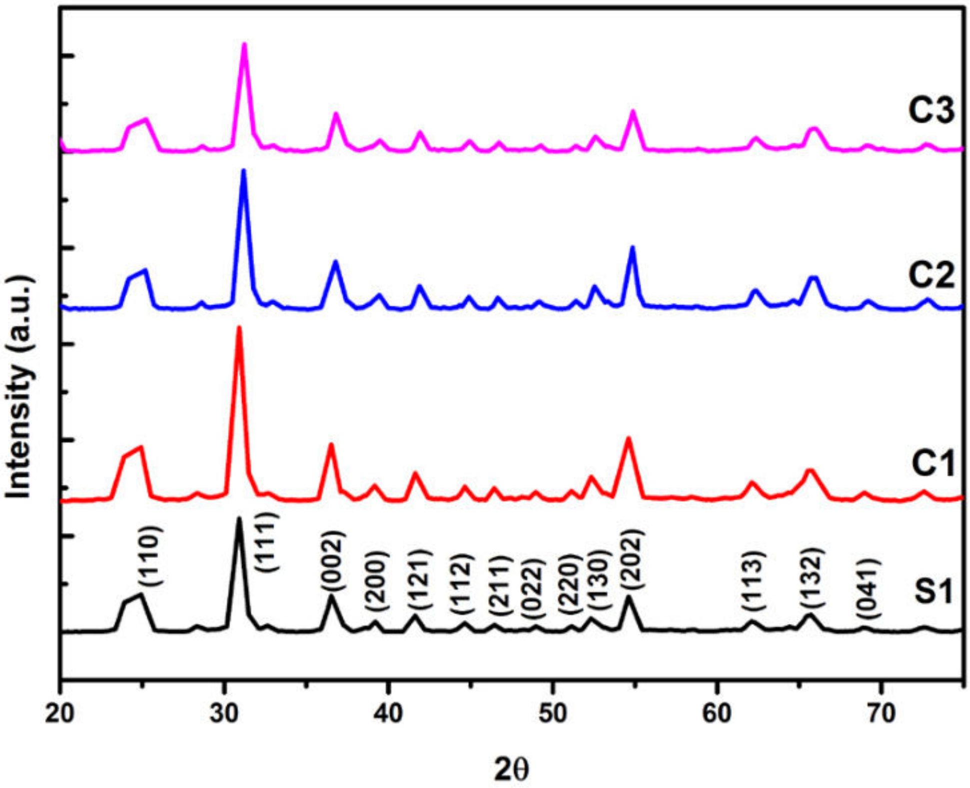

Fig.6.3. X-ray diffraction patterns of pure and composite samples.

Table 6.1 Changes in diffraction angle for the planes (111).

Sample	The peak position of (111) plane (2θ)	d spacing of (111) plane (A^0)
S1	30.918	2.889
C1	30.916	2.890
C2	31.182	2.866
C3	31.216	2.863

Table 6.2 Lattice parameters of $NiWO_4$ and $NiWO_4$/SnPc powder samples.

Lattice parameters	Sample (S1)	Sample (C1)	Sample (C2)	Sample (C3)	JCPDS values
a (Å)	4.655±0.093	4.442±0.088	4.536±0.090	4.694±0.093	4.599
b (Å)	5.439±0.108	5.481±0.109	5.628±0.112	5.481±0.109	5.660
c (Å)	4.986±0.099	5.759±0.115	4.857±0.097	5.052±0.101	4.906
β	91.943	89.175	88.99	89.298	90.030

The average crystallite size of S1 and composite samples are calculated from XRD patterns using the Scherrer equation. Average crystallite sizes estimated for samples S1, C1, C2 and C3 are 14.74, 19.16, 19.09 and 18.72 nm, respectively.

Williamson–Hall analysis is carried out to calculate the average crystallite size and micro-strain. Fig. 6.4 shows the W-H plots of the pure and composite samples. Geometrical parameters of S1 and composite samples are presented in Table 6.3.

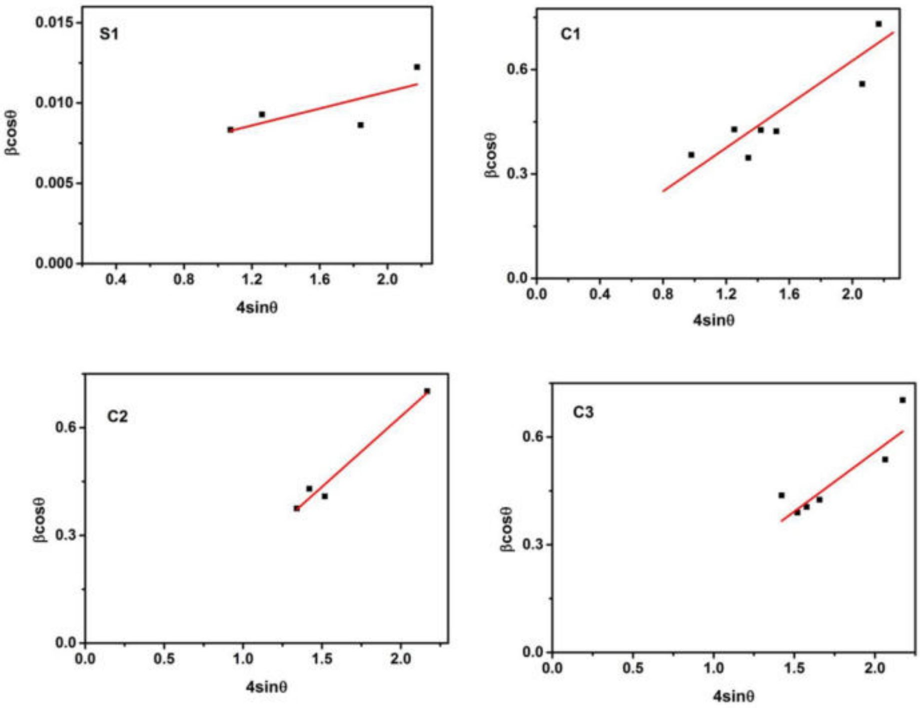

Fig.6.4. W-H Plots for pure and composite samples.

Table 6.3 Geometrical parameters of pure and composite samples

Sample	**Average crystallite size (Scherrer equation) (nm)**	**Unit cell volume (10^{-30} m^3)**	**W-H Method**	
			Average crystallite size (nm)	**Micro-strain (x 10^{-3})**
S1	14.74±0.29	126. 18	15.80±0.31	2.60±0.05
C1	19.16±0.38	140.18	20.57±0.41	302.90±6.06
C2	19.09±0.38	123.98	19.80±0.39	345.20±6.90
C3	18.72±0.37	129.94	17.33±0.34	375.80±7.51

It can be seen from Table 6.3 that the average crystallite sizes estimated from the Scherrer equation and W–H analysis for all the samples are almost in close agreement. The average crystallite size is increased for C1. But it is decreased for C2 and C3 samples having a higher concentration of SnPc. Table 6.3 shows that micro-strain values of the composite samples are larger than that of the pure sample. The addition of SnPc in S1 may cause structural imperfections and surface effects in the sample[9, 11, 12]. From the XRD analysis, it can be concluded that the geometrical parameters of $NiWO_4$ nanoparticles can be modified by the addition of SnPc.

6.3.2.2 TEM analysis

TEM analysis of pure and nanocomposite samples are carried out with the help of *JEOL/JEM 2100* (Source: LaB6 and voltage: 200 kV). Fig. 6.5 shows the bright field images of pure and $NiWO_4$/SnPc nanocomposite samples. Particle morphology is not changed significantly with the composite formation. But there is a slight change in the particle size of composite samples when compared with the pure sample. *Image J* software is used to calculate the particle size, and the average particle size is calculated by plotting a histogram shown in Fig. 6.6. The particle size ranges from 8 to 20 nm for S1, 12 to 30 for C1 and C2 and 12 to 26 for C3. The average particle sizes of samples S1, C1, C2 and C3 are 14.84, 20.62, 19.92 and 19.29 nm respectively. HRTEM image of pure and nanocomposite samples are shown in Fig. 6.7. From the figure polycrystalline nature of the samples can be identified. The selected area diffraction pattern of samples S1, C1, C2 and C3 are shown in Fig.6.8. The SAED patterns of samples S1, C1, C2 and C3 show bright spots that confirm the crystalline nature of the samples. The crystal planes which show high-intensity peaks in the XRD can be indexed from the SAED pattern. The calculated inter-planar spacing (d_{hkl}) values from SAED patterns are compared with the XRD results to index the planes. The calculated d_{hkl} values and corresponding planes are presented in Table 6.4. Variation in d_{hkl} values can be observed for the same (hkl) planes for different samples. This change in d_{hkl} spacing is due to the incorporation of SnPc into the $NiWO_4$ lattice. This variation in d_{hkl} values and the corresponding change in diffraction angles are explained in *section 6.3.2.1*.

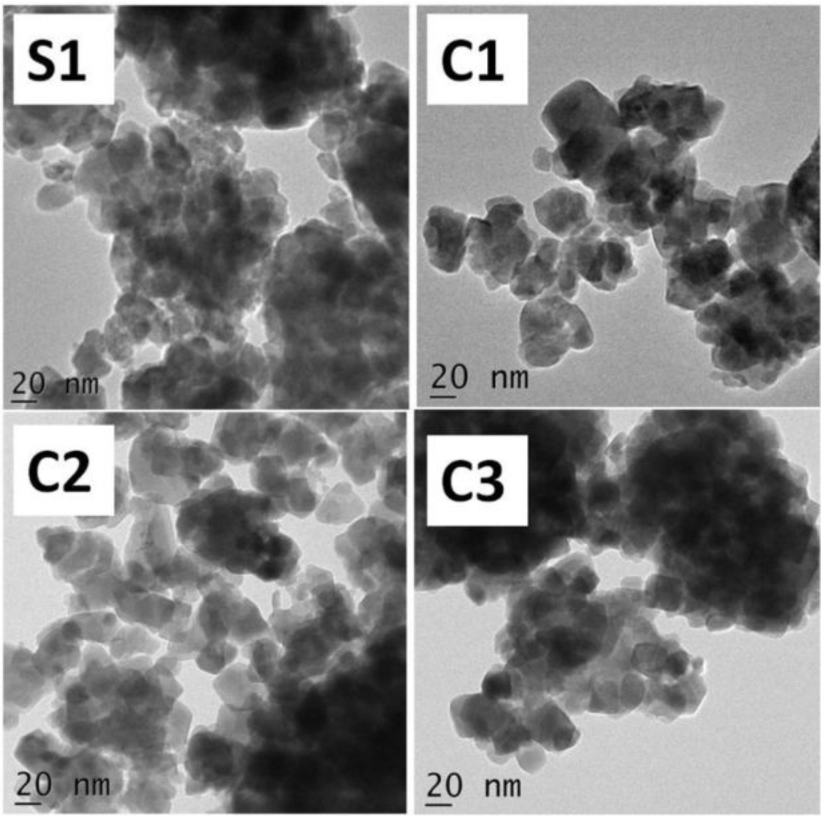

Fig. 6.5 Bright-field images of pure and $NiWO_4$/SnPc nanocomposite samples.

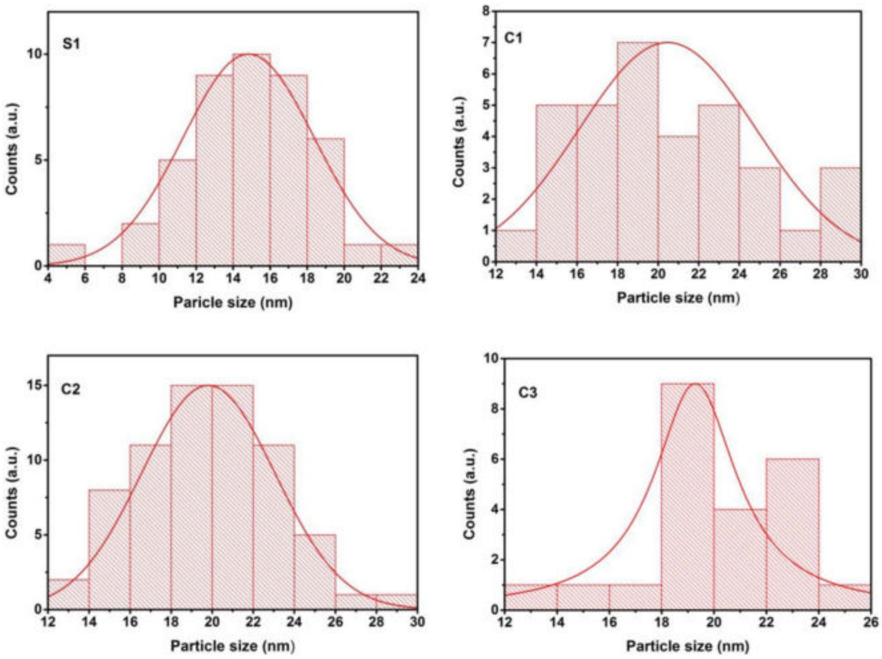

Fig. 6.6 Size distribution graphs for pure and $NiWO_4$/ SnPc samples.

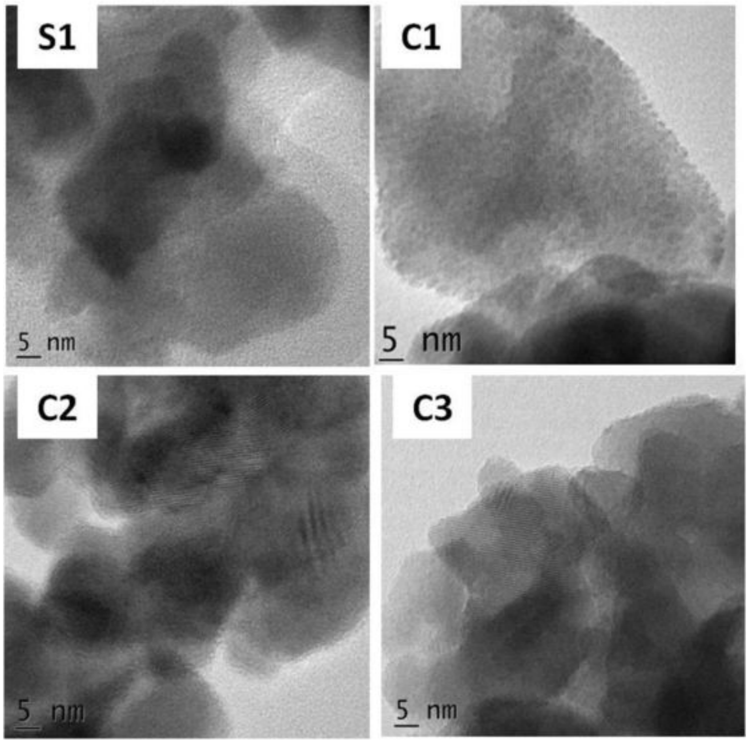

Fig. 6.7 HR-TEM images of pure and $NiWO_4$/SnPc nanocomposite samples.

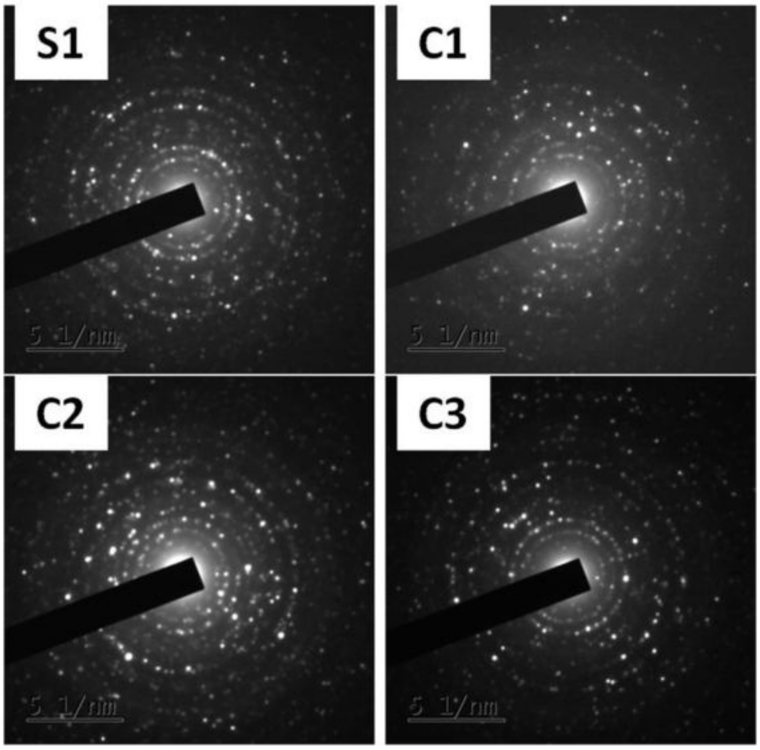

Fig. 6.8 SAED images of pure and $NiWO_4$/SnPc nanocomposite samples.

Table 6.4 Inter-planar spacing (d_{hkl}) and the corresponding planes of samples S1, C1, C2 and C3.

Sample	**Plane**	**Measured from SAED d (A^0)**	**Measured from XRD d (A^0)**
S1	(010)	5.543	5.587
	(100)	4.401	4.533
	(011)	3.448	3.537
	(002)	2.591	2.447
	(112)	2.046	2.017
	(130)	1.695	1.740
	(302)	1.268	1.298
C1	(100)	4.256	4.276
	(110)	3.388	3.567
	(002)	2.541	2.459
	(112)	1.998	2.028
	(202)	1.689	1.678
C2	(010)	5.376	5.574
	(100)	4.347	4.531
	(110)	3.404	3.674
	(111)	2.882	2.866
	(002)	2.506	2.442
	(112)	1.995	2.017
	(202)	1.681	1.672
C3	(010)	5.516	5.567
	(100)	4.239	4.524
	(110)	3.344	3.525
	(111)	2.907	2.863
	(002)	2.538	2.441
	(211)	1.975	1.950
	(202)	1.642	1.671

6.3.2.3 FE-SEM and EDS analysis

FE-SEM analysis of pure and NiWO$_4$/SnPc composite samples are done with the help of instrument *∑IGMA* ^{TM} operating at 5 kV. Fig. 6.9 shows the FE-SEM images of pure and composite samples. All the samples show agglomerated structures. The surface morphology of the pure sample is not varied much by the composite formation. But for the composite samples, clusters formed due to agglomeration are small in size compared to the pure sample.

EDS analysis of the samples reveals the chemical stoichiometry of the pure and composite samples. Fig. 6. 10 represents the EDS image of NiWO$_4$/SnPc nanocomposite sample C1. From the figure, it can be seen that element N present in the composite sample cannot be quantified with this analysis. The elemental data is presented in Table 6.5.

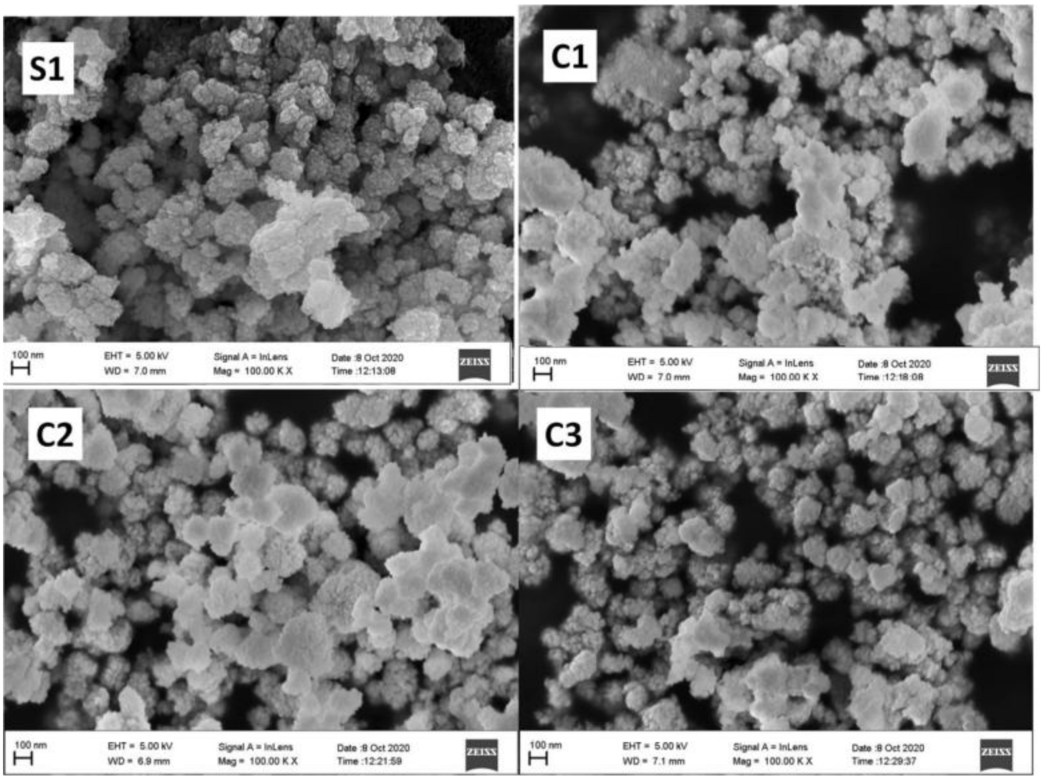

Fig. 6.9 FE- SEM images of pure and NiWO$_4$/SnPc nanocomposite samples.

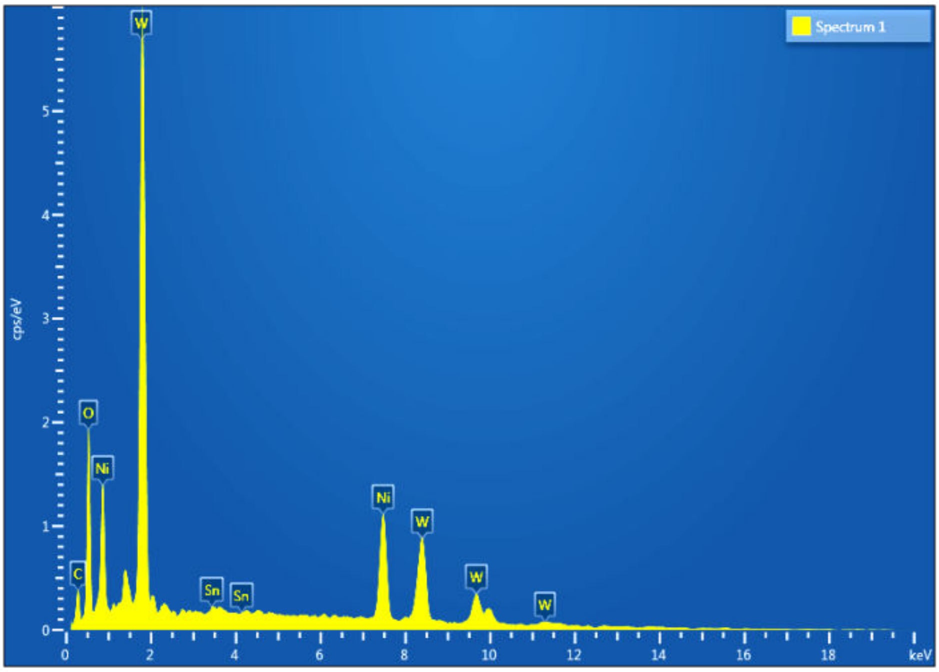

Fig. 6.10 EDS image of $NiWO_4$/ SnPc composite sample C1.

Table 6.5 EDS data for pure and $NiWO_4$ / SnPc nanocomposite samples.

Sample	Elements	Atomic number	Series	Wt. %	At.%
S1	W	74	L- Series	58.91	15.64
	O	8	K- Series	22.62	69.00
	Ni	28	K- Series	18.47	15.36
C1	C	6	K series	5.89	21.34
	O	8	K series	18.25	49.67
	Ni	28	K series	21.77	16.15
	Sn	50	L series	0.2	0.07
	W	74	M series	53.89	12.77
C2	C	6	K series	5.27	20.3
	O	8	K series	16.46	47.56
	Ni	28	K series	23.14	18.22
	Sn	50	L series	0.44	0.17
	W	74	M series	54.69	13.75
C3	C	6	K series	7.19	24.3
	O	8	K series	19.55	49.58
	Ni	28	K series	21.01	14.52
	Sn	50	L series	0.61	0.21
	W	74	M series	51.65	11.4

6.3.2.4 FT-IR analysis

The infrared absorption technique is used to identify the presence of SnPc in $NiWO_4$/SnPc composites as the IR spectrum is dependent on the chemical composition of the material. FT-IR spectra are recorded with the help of an FT-IR spectrophotometer (*Thermo Nicolet, Avatar 370*) in the range 4000 to 400 cm^{-1}. Fig.6.11 shows the IR absorption spectra of all the samples in which additional modes formed due to SnPc are marked. The spectra are nearly the same except some additional bands with much fewer intensities are in composite samples. These bands are due to the vibrational modes of SnPc components. Low intensities of the characteristic peaks may be due to the lower loading of SnPc. Intensities of the bands are found to be increasing as the increase in weight % of SnPc in the composite samples.

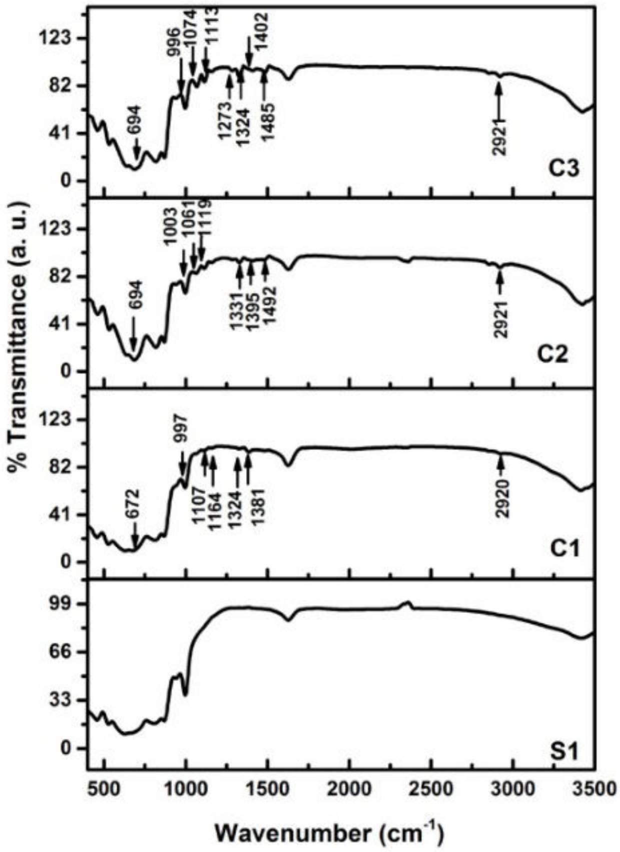

Fig. 6.11 FT-IR spectra of S1, C1, C2 and C3.

Table 6.6 represents a comparison of IR active modes of the composite samples with the literature values of SnPc. From the table, it can be concluded that out of 25 active modes of tin phthalocyanine, 17 modes are present in the composite samples [9]. So the presence of SnPc in the composite samples is confirmed.

Table 6.6. Comparison of IR active modes of composite samples with S1 and SnPc.

S1 (cm^{-1})	**C1 (cm^{-1})**	**C2 (cm^{-1})**	**C3 (cm^{-1})**	**SnPc (cm^{-1})**	**Band assignment [9, 13-19]**
	3411	3416	3423	----	Hydroxyl stretching vibrations of H_2O molecules
	2920	2921	2921	3020	Streching of aromatic C-H bond
	1623	1627	1621	1613	Aromatic C=C vibration
	1478	1492	1485	1493	Isoindole stretching
	1381	1395	1402	1416	C=N bond vibration
	1324	1331	1324	1333	Pyrrole stretching
	----	----	1273	1285	Pyrrole stretching
	1164	----	----	1160	Pyrrole stretching
	1107	1119	1113	1119	Benzene stretching
	1003	1061	1074	1074	C-H bending
	----	----	----	1062	
997	997	1003	996	1001	Isoindole deformation
944	944	945	938	952	Metal ligand vibrations
	----	----	----	887	
869	864	868	875	872	Vibrations of theWO_2 enitity
806	809	810	810	820	Vibrations of the WO_2 entity present in the W_2O_8
	----	----	----	780	
	----	----	----	770	
	----	----	----	745	
	----	----	----	726	
677	672	694	694	642	Macro ring breathing
623	624	630	617	628	Asymmetric stretching of two Obridge of W_2O_2
527	520	527	534	564	Asymmetric stretching vibrations of the NiO_6 polyhedra
	----	----	----	499	
	----	----	----	489	
455	455	462	462	437	Asymmetric stretching vibrations of NiO_6 polyhedra.

6.3.2.5 Raman analysis

The Raman spectra of pure and $NiWO_4$ /SnPc samples are taken by *Alpha 300 RA AFM & RAMAN*. Fig. 6.12(a) shows the Raman spectra of pure and nanocomposite samples. The Raman spectra of pure nickel tungstates and the details of its vibrational modes are explained in section 3.3.2.5. There are 18 Raman active modes for the $NiWO_4$ sample, in which 12 modes are present in the pure sample [20]. SnPc comes under C_{4v} point symmetry and it has 165 normal vibrational modes. With this C_{4v} symmetry, $22A_1 + 19\ A_2 + 21\ B_1 + 21B_2 + 41E$ fundamental modes are allowed. From this only 105 modes are Raman active which comes under the symmetry species A_1, B_1, B_2 and E [21]. Along with the 12 normal modes of vibrations of pure samples, $NiWO_4$/SnPc nanocomposite samples have 14 more weak vibrational modes due to the presence of SnPc. The modes of SnPc are seen as weak due to the high-intensity modes of the $NiWO_4$ in the composite samples as the weight percentage of SnPc is much less compared to the tungstate counterpart. Fig. 6.12 (b) shows the enlarged portion of Raman spectra in the range 1000-1600 cm^{-1} with peaks of SnPc highlighted.

SnPc has two characteristic vibrations at 680 and 1330 cm^{-1} due to macrocycle breathing and pyrrole stretching vibrations respectively [21-23]. The first one is not observable in the composite sample as it already has a peak due to B_g mode vibration of the $NiWO_4$ unit. The second band is observed in all composite samples with low intensity. Along with that other modes are also seen. The bands at 1005, 1029, 1077,1100, 1184,1309 cm^{-1} are due to the C-H bend. The bands 1141, 1152, 1156 cm^{-1} are formed by pyrrole breathing in the SnPc [21-23]. All composite samples show typical isoindole ring stretching vibration at 1398, 1402 and 1427 cm^{-1}. The Raman bands at 1484, 1488 and 1494 cm^{-1} are due to the C-N pyrrole stretching vibrations [21]. Raman peak at 1553 cm^{-1} is due to the C- N azagroup stretch. Modes 1612, 1617 and 1629 cm^{-1} are due to the benzene ring stretch [21]. From the Raman analysis, it can be concluded that SnPc is incorporated into the $NiWO_4$ lattice and this shows the successful formation of $NiWO_4$/ SnPc nanocomposite.

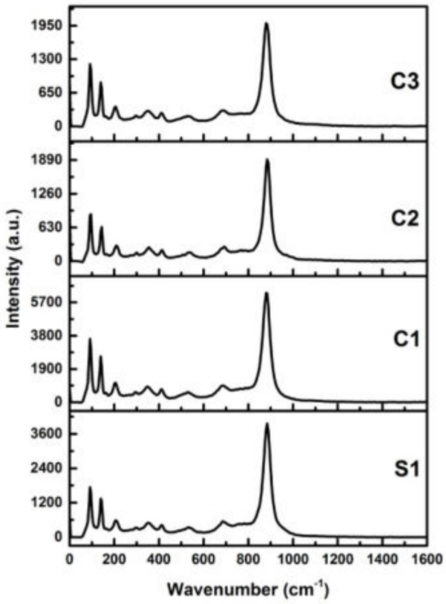

Fig. 6.12(a) Raman spectra of pure and $NiWO_4$/snPc nanocomposite samples.

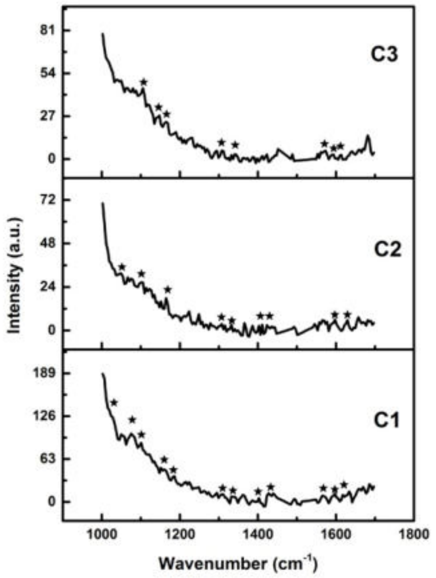

Fig. 6.12 (b) Enlarged Raman spectra in the range 1000-1600 cm^{-1} with peaks of SnPc highlighted.

6.3.3 Analysis of optical properties

UV-VIS-NIR absorption and photoluminescence properties of the synthesized $NiWO_4$/SnPc nanocomposite are investigated by following the procedure as given in *section 2.3.3*.

6.3.3.1 UV-VIS-NIR analysis

Absorption properties of S1 and composite samples C1, C2and C3 are studied using a double beam UV–Visible spectrophotometer (*Cary 5000 model*). Fig.6.13 shows the optical absorbance spectra of all the samples. All samples have good light absorption properties in UV, visible and IR wavelengths. The main absorption peak of S1 is at 271 nm, and additional peaks are observed in the visible region around 445, 740 and 823 nm [9,20]. In composite samples, these peaks are slightly shifted to longer wavelength due to attachment of SnPc to S1. Along with these peaks, C1, C2 and C3 show some other peaks due to the presence of SnPc. The spectra of SnPc originate from the orbital within the aromatic 18Π electron system and from overlapping orbital of the central metal atom [24]. These peaks correspond to the Q-band transition. The Q band is due to the intramolecular excitations [electronic transition $\mathbf{a_{2u}(\Pi) \longrightarrow e_g(\Pi^*)}$]. Here the Q band is split into two distinct peaks due to the strong interaction between the molecules [25, 26]. The two bands at 790 and 843 nm are due to the presence of SnPc. All samples show a broad absorption band in the IR wavelength range 1300-1600 nm. From the spectra, it can be seen that absorbance in the visible region increases with the increase in the concentration of SnPc in the composite sample. While a decrease of absorbance in the UV and IR regions are observed. So the absorbance spectra of S1 can be modified by SnPc, in all regions of the spectrum. The optical bandgap of pure and $NiWO_4$/SnPc samples are calculated from Tauc plot. Fig. 6.14 presents the curve, $(\alpha h\nu)^2$ as a function of photon energy. The optical bandgap energies of all samples are measured by extrapolating the linear portion of the curve to absorption equal to zero. The calculated bandgap values for S1, C1, C2 and C3 are 3.07, 3.20, 3.19 and 3.19 eV respectively (Table 6.7). With the variation in concentration of SnPc in the composite, the energy gap is also varied. That is optical bandgap of $NiWO_4$ can be modified by SnPc [27]. Fig 6.15 shows the curves $(\alpha h\nu)^{1/2}$ as a function of $h\nu$. The indirect energy gaps are also calculated and tabulated in Table 6.7.

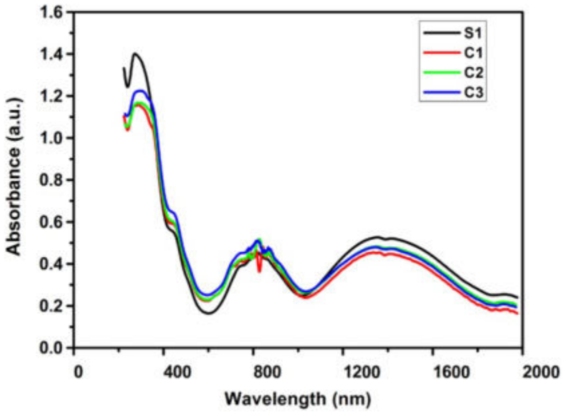

Fig. 6.13. Optical absorbance spectra of S1, C1, C2 and C3.

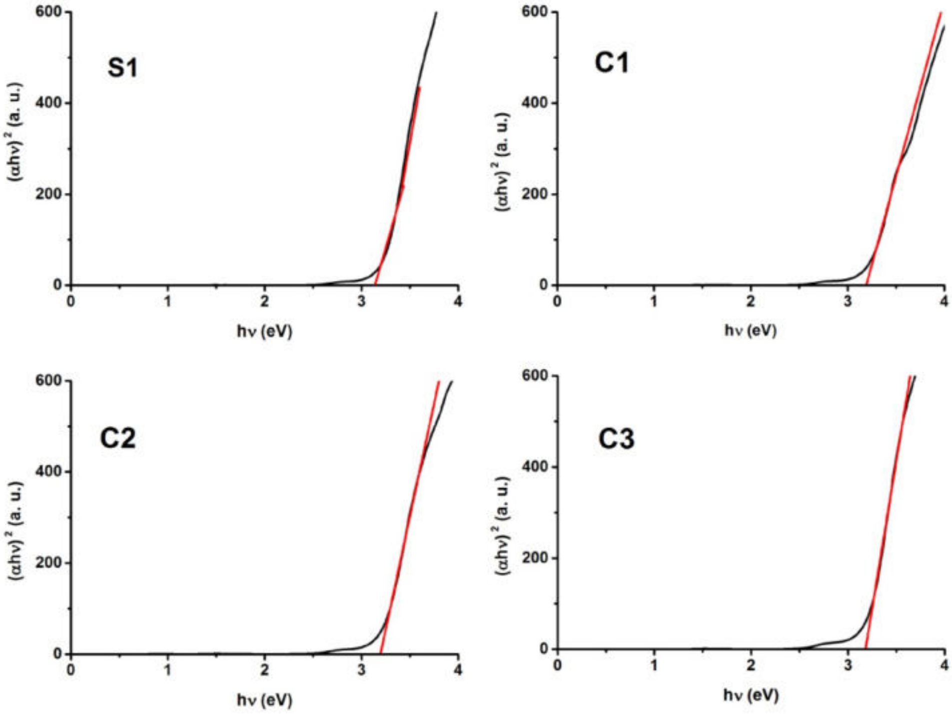

Fig. 6. 14 Tauc plots of pure and $NiWO_4$/SnPc nanocomposite samples for direct bandgap estimation.

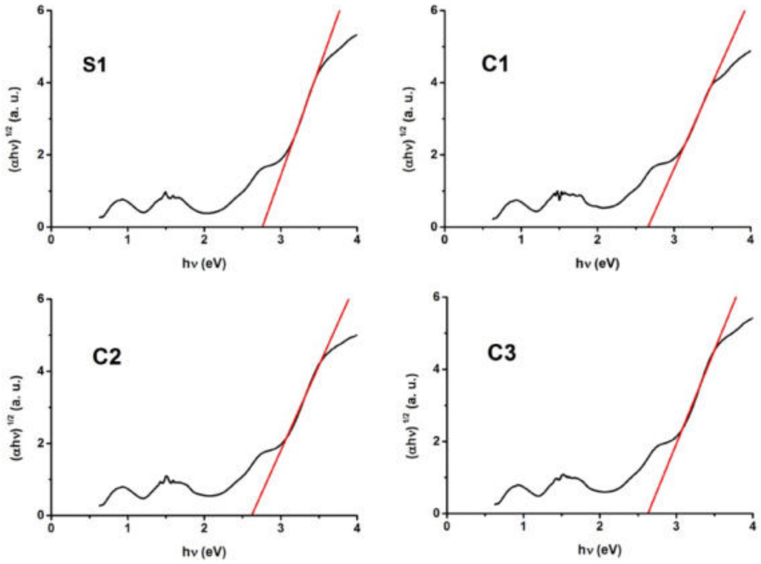

Fig. 6. 15 Tauc plots of pure and $NiWO_4$/SnPc nanocomposite samples for indirect bandgap estimation.

Table 6.7 Direct and indirect optical bandgap values of pure and $NiWO_4$/SnPc nanocomposite samples.

Sample	**Direct bandgap (eV)**	**Indirect bandgap (eV)**
S1	3.07	2.80
C1	3.20	2.68
C3	3.19	2.62
C5	3.19	2.65

6.3.3.2 Photoluminescence analysis

To analyse the PL properties of pristine and $NiWO_4$/SnPc nanocomposite samples, PL spectra of these samples are taken with the help of *Horiba fluorescence spectrometer* (slit width of 3.0 nm), with an excitation wavelength of 350 nm. Comparison of luminescence spectra of the pure and nanocomposite samples is shown in Fig.6.16. When excited with a wavelength of 350 nm at room temperature, all the samples show almost the same spectra with different intensities. The main peaks of the pure sample are observed at 412 and 434 nm respectively. In addition to that two peaks of low intensities are also observed at 454 and 481 nm. All the observed peaks are similar to other wolframite compounds [9, 20]. The composite samples show emission peaks with slight variation in wavelength. Fig. 6.17 shows the deconvoluted PL spectra of pure and composite samples. The sample C1 has emission peaks at 417, 439, 459 and 526 nm. Sample C2 has emission peaks at 417, 438, 464 and 470 nm. Sample C3 shows emission peaks at 417, 439, 465 and 481 nm. The variations in PL emission peaks may be due to the involvement of additional energy levels present within the bandgap of the composite samples [25]. From Fig.6.16, all the nanocomposite samples show low PL intensities than S1. Presence of SnPc in composite samples reduces the PL intensity. This may be attributed to the strong metal-ligand interaction in tin complexes [26]. The PL intensity is very low for C1. The SnPc modifies the lifetime of excitations in C1 and make it as a suitable candidate for solar cell, and photocatalytic applications. Samples C2 and C3 show a slight increase in PL intensity. This may be due to the defects introduced by the increase in the concentration of SnPc in C2 and C3, and that can be confirmed from the micro-strain values presented in Table 6.3.

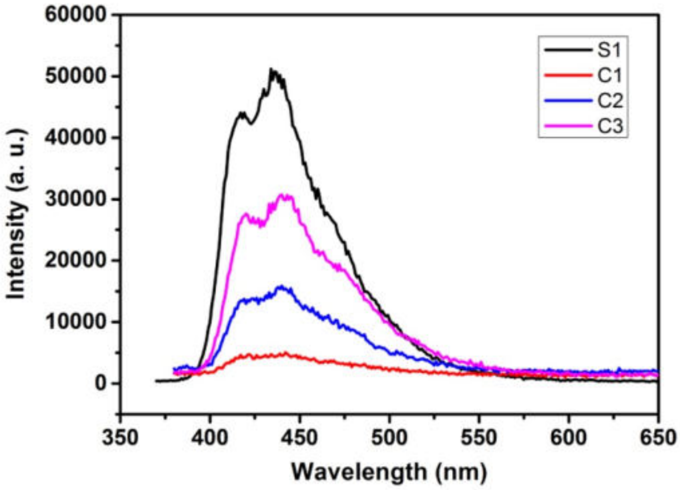

Fig. 6. 16 PL spectra of pure and $NiWO_4$/SnPc nanocomposite samples.

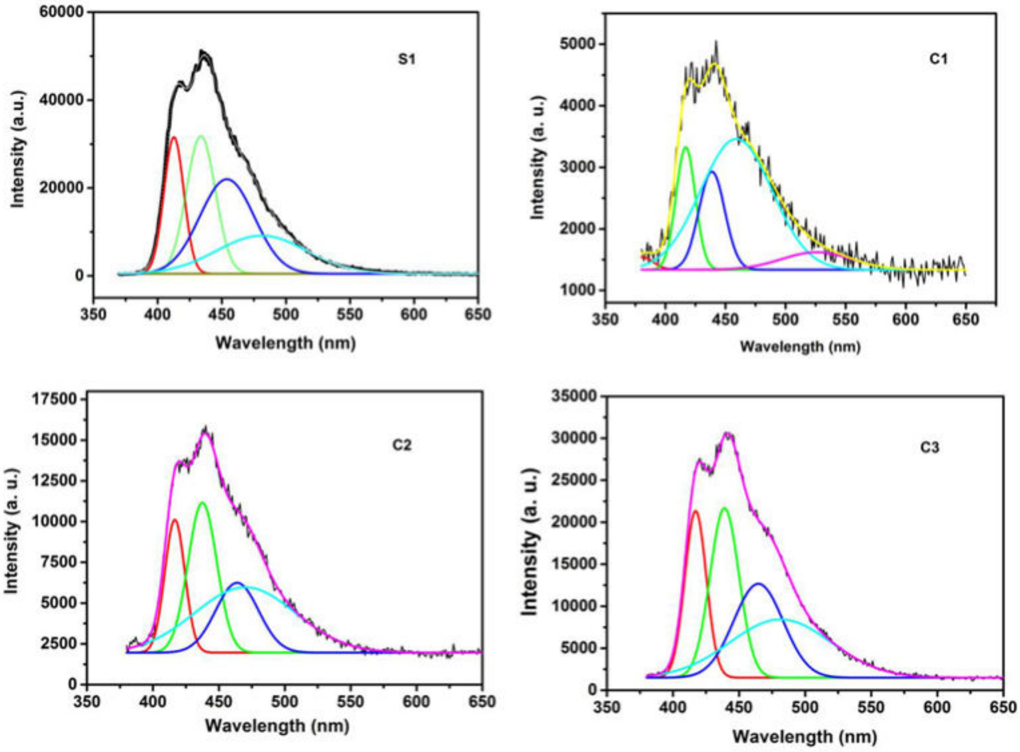

Fig. 6. 17 Deconvoluted PL spectra of pure and $NiWO_4$/SnPc nanocomposite samples.

Figure 6.18 shows the CIE Chromaticity diagram for the samples S1, C1, C2 and C3. The **x** and **y** chromaticity coordinates are calculated in the CIE XYZ colour space with an excitation wavelength of 350 nm. The CIE coordinates of the pure and composite samples are presented in Table 6.8. The sample S1 shows purplish-blue emission. The colour of the emission changes to white for C1. This is a significant change in the colour of emission. Samples C2 and C3 show purplish-blue emission. This data indicates that the colour of emission of samples can be tuned by varying the concentration of SnPc in the nanocomposite samples.

Table 6.8 Chromaticity co-ordinates of pure and composite samples.

Sample	**S1**	**C1**	**C2**	**C3**
x	0.1562	0.2564	0.2124	0.1769
y	0.0889	0.2534	0.1824	0.1406

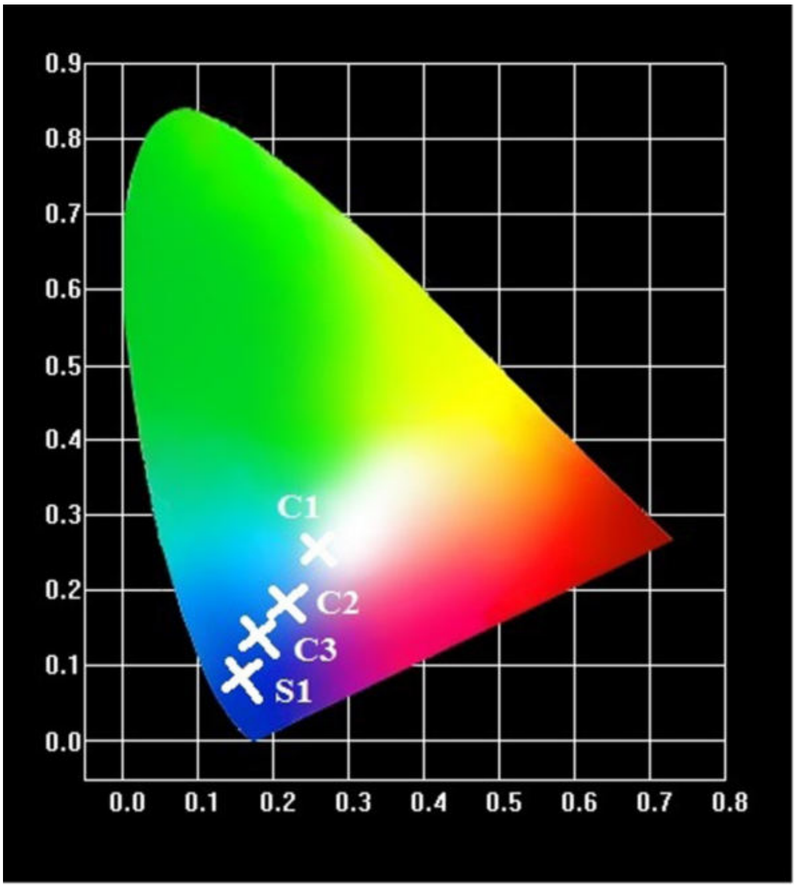

Fig.6.18 CIE chromaticity diagram of S1, C1, C2 and C3.

6.3.4 Analysis of magnetic properties

The magnetic measurements at room temperature for the pure and composite $NiWO_4$ nanoparticles are carried out using a vibrating sample magnetometer (*Lakeshore VSM 7410*) in an applied magnetic field sweeping between ± 15000 Oe. Fig. 6.19 represents the VSM curves of the pure and $NiWO_4$/SnPc nanocomposite nanoparticles. The pure sample shows paramagnetic behaviour at room temperature [13]. The magnetic behaviour of pure $NiWO_4$ is discussed in section 3.3.4. By making the composite with SnPc, there is no significant deviation from the magnetic nature of $NiWO_4$. All the nanocomposite samples show paramagnetic nature as the pure sample. But, a slight shift in the curve is observed. From the magnetic studies, it can be concluded that the presence of SnPc does not affect the paramagnetic nature of the $NiWO_4$ sample.

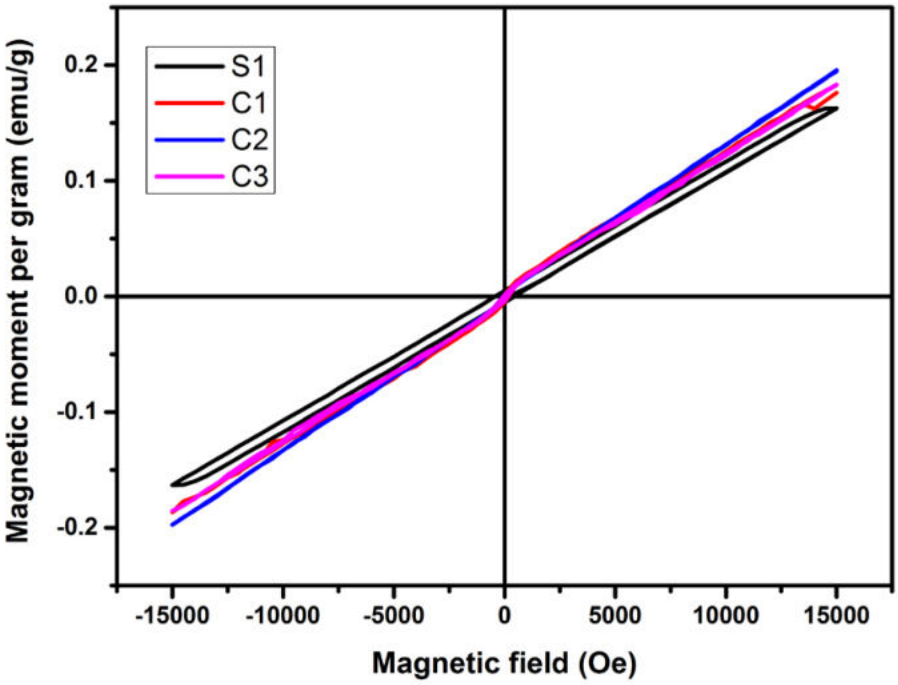

Fig. 6. 19 VSM curves of pure $NiWO_4$ and $NiWO_4$ /SnPc nanocomposites.

6.3.5 Analysis of electrical properties

Electrical studies are carried out by following the procedure given in *section 2.3.5*. The electrical measurements are performed by making cylindrical pellets of pure and $NiWO_4$/SnPc nanocomposite samples. Pellets are made using a hydraulic press by applying a pressure of 7 GPa. The thickness and diameter of the pellets are 1.7 and 13 mm respectively. The pellets are then sintered at 100^0C for 1.5 h. Here the comparatively low temperature is chosen as the sintering temperature. This is according to the thermal stability of the nanocomposite. When the temperature is increased further it may lead to the decomposition of the SnPc part in the nanocomposite. The silver paste is applied to both the faces of the pellets for good electrical contact. The dielectric and impedance spectra are measured in the frequency range of 50 Hz- 5 MHz at room temperature by using *Wayne Kerr H- 6500B* model impedance analyser.

6.3.5.1 Dielectric analysis

Fig.6.20 represents the frequency response of the real part of the dielectric constant of pure $NiWO_4$ and $NiWO_4$/SnPc nanocomposite samples at room temperature. From Fig.6.20, it can be seen that the real part of dielectric constant (ε') for the pure sample S1 is reduced significantly when the sintering temperature is lowered to 100^0C from 500^0C. All the composite samples show high value of ε' when compared to the pure sample. Both pure and nanocomposite samples show similar behaviour regarding the variation of the real part of dielectric constant (ε') with frequency. At low frequency, ε' is high for the pure and $NiWO_4$/SnPc samples. It shows a dispersion at lower frequency region 50-1000 Hz. The dispersion behaviour shown by the samples can be explained based on space charge polarization. It can be explained based on Maxwell–Wagner-type interfacial polarization [30, 31] and Koop's phenomenological theory [32]. The value of ε' decreases with the increase in frequency and becomes constant at high frequency region. The values of ε' for pure and nanocomposite $NiWO_4$ samples at selected frequencies are presented in Table 6.9.

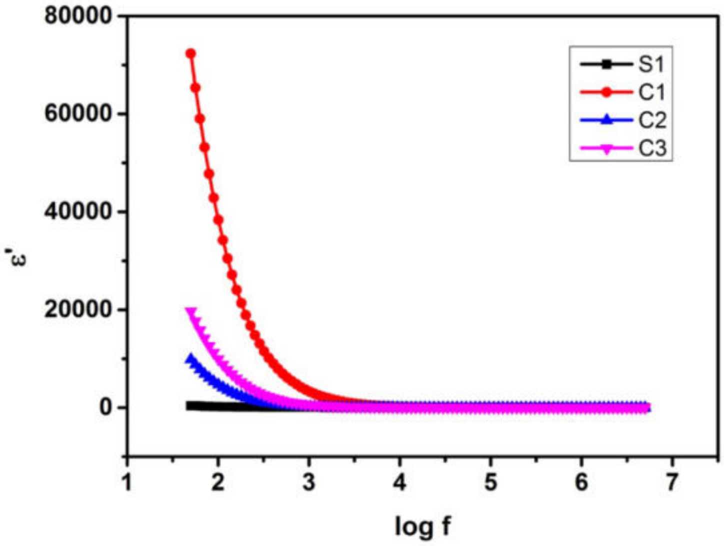

Fig. 6.20 Room temperature frequency response of the real part of dielectric constant for pure $NiWO_4$ and $NiWO_4$ /SnPc samples.

Table 6.9 Real part of dielectric constant at different frequencies for pure $NiWO_4$ and $NiWO_4$ /SnPc nanocomposite samples.

Sample	**ε' at 50 Hz**	**ε' at 1000 Hz**	**ε' at 10^5 Hz**
S1	391	52	16
C1	72340	3249	47
C2	9884	246	19
C3	19668	607	37

It can be seen from Fig. 6.20 and Table 6.9 that the $NiWO_4$/SnPc nanocomposite samples have a very high value of **ε'** in the low frequency region as compared to the pure sample. This can be attributed to the increase in space charge and dipole orientational polarization by the addition of SnPc into the $NiWO_4$ lattice. The delocalized π electron in phthalocyanine plays the main role in their conductivity. So the increase in the dielectric permittivity of the composite samples may be due to the increase in these electrons by the increase in the applied field [33]. When the frequency increases the effect of these polarizations gets reduced. All the samples attain a constant value of ε' at high frequency.

Fig.6.21 shows the frequency response of the dissipation factor of pure $NiWO_4$ and $NiWO_4$/SnPc nanocomposite samples at room temperature. For the pure $NiWO_4$ sample, the loss is maximum at the low frequency region. Its value decreases when the frequency is increased. Loss approaches zero value at high frequency. The nanocomposite samples show a peak in the loss curve. The peak in the tanδ curve implies the relaxation process taking place in the samples. Peaking behaviour occurs when the hopping frequency of the ions is equal to the frequency of the applied field. The nanocomposite samples show a loss greater than the pure sample. But at high frequencies, all the curves approach zero. From the dielectric analysis it can be inferred that by the formation of $NiWO_4$/SnPc nanocomposite, the dielectric constant of $NiWO_4$ can be increased by compromising the loss.

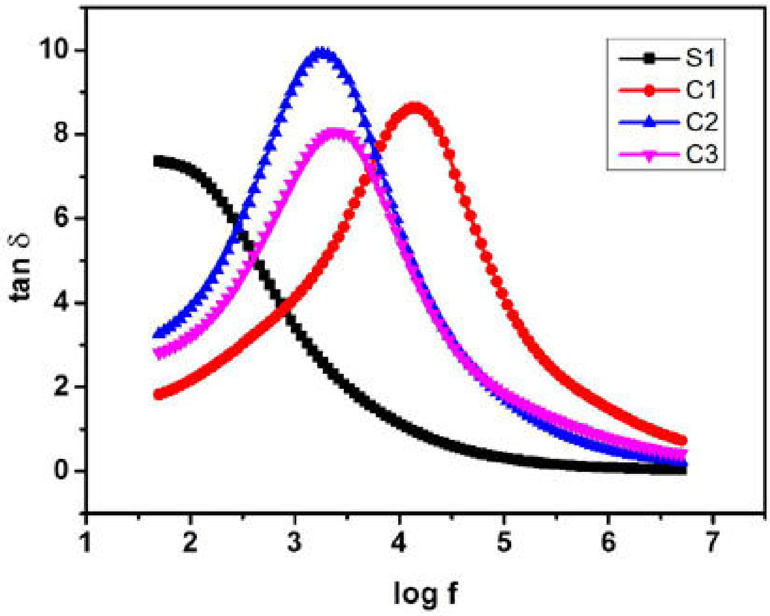

Fig. 6.21 Room temperature frequency response of dissipation factor for pure and nanocomposite samples.

6.3.5.2 Impedance analysis

Nyquist curves are drawn to analyse the conduction mechanism in the pure and $NiWO_4$/SnPc samples. The electrical properties of polycrystalline material have contributions from grains, grain boundaries and specimen electrode interfaces. Fig. 6.22(a) represents the Nyquist plots of the pure and composite samples. To analyse the behaviour of the composite samples, Nyquist plots of composite samples are enlarged and are presented in Fig. 6.22(b). All the samples show the non-Debye type relaxation process as the centre of the arcs lies below the real axis. The pure $NiWO_4$ sample shows high impedance at room temperature with a very small electrode polarization effect. At the same time, the composite samples show small values of real and imaginary parts of complex impedance which might be due to the additional charge carriers formed by the addition of the SnPc into the $NiWO_4$ lattice.

An equivalent circuit based on impedance spectroscopy gives an idea of the physical process happening inside the sample. The fitted Nyquist plots and corresponding equivalent circuits are shown in Fig. 6. 23. For the pure sample, two RC circuits connected in series to represent the conduction process. In the two RC circuits, one represents the grain and other represents the grain boundary contribution. In the RC circuits, capacitance is replaced by CPE which represents the non-Debye behaviour shown by the sample. For the nanocomposite samples also two RC elements are used to represent the grain and grain boundary contribution. Here also capacitance is replaced by CPE element to represent the non-Debye behaviour. The values of the parameters R, C and β for grain and grain boundaries, and CPE value are presented in Table 6.10.

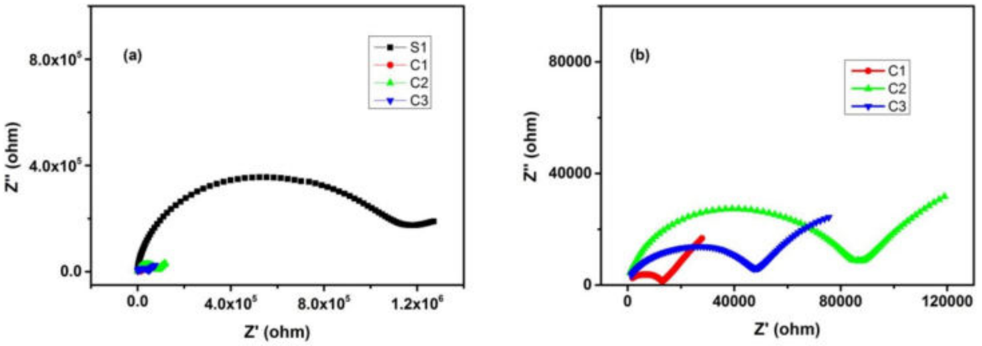

Fig. 6.22 Room temperature Nyquist plots of pristine and $NiWO_4$/SnPc nanocomposite samples.

Table 6. 10 Equivalent circuit parameters for pure and nanocomposite samples.

Circuit parameters	S1	C1	C2	C3
Rg (Ω)	1100000	13000	85000	50000
CPE_g (F)	4x 10^{-7}	1.6x10^{-6}	2x10^{-6}	2x10^{-6}
β_g	0.71	0.70	0.74	0.64
R_{gb} (Ω)	1100000	90000	100000	100000
CPE_{gb} (F)	2.2x 10^{-5}	7.2x 10^{-4}	5x10^{-4}	4x10^{-4}
β_{gb}	0.54	0.65	0.70	0.71

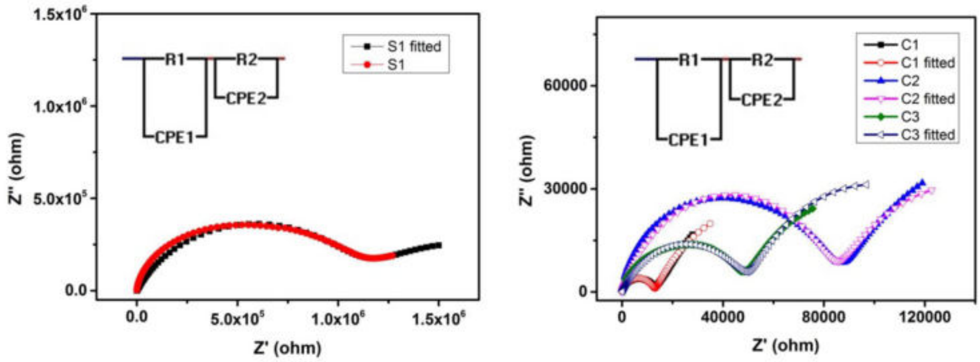

Fig. 6.23 Room temperature Nyquist plots and the corresponding equivalent circuit (inset) of pure and nanocomposite samples.

6.3.5.3 AC conductivity

The AC conductivity of pure and $NiWO_4$/SnPc samples are investigated to analyze their conduction mechanism. Variations of AC conductivity as a function of frequency at room temperature for pure and nanocomposite samples are shown in Fig. 6. 24.

The pure sample shows a frequency-independent region followed by a region where σ_{ac} increases with the frequency. The conductivity of the pure sample follows Jonscher's power law. In the case of the pure sample, an increase in conductivity occurs with the increase in frequency at the high frequency region. This may be due to the hopping of charge carrier from one site to a new site. The pure sample sintered at 100^0C show less value of conductivity compared to the pure sample sintered at 500^0C (*section 3.3.5.3*).

The nanocomposite samples show high AC conductivity. This may be due to the additional charge carriers introduced by the presence of SnPc. Sample C1 shows high conductivity. The conductivity of C1 shows a linear relationship with frequency in the low frequency region. This linear behaviour of the frequency against the AC conductivity in the low frequency region indicates the presence of conductivity influenced by the electrode polarization effect. But for the sample C2 conductivity decreases. This decrease in conductivity is due to a high density of defects. The presence of SnPc may introduce the defect ions in the system. This will reduce the conductivity. But for the sample C3 conductivity again increases. Composite samples also obey Jonscher's power law of conductivity. In short, it can be inferred that by introducing a matallothalocyanine into the lattice of $NiWO_4$, its conductivity can be improved. Additionally, the improved conductivity of $NiWO_4$/SnPc nanocomposite makes it a potential candidate in microelectronic devices.

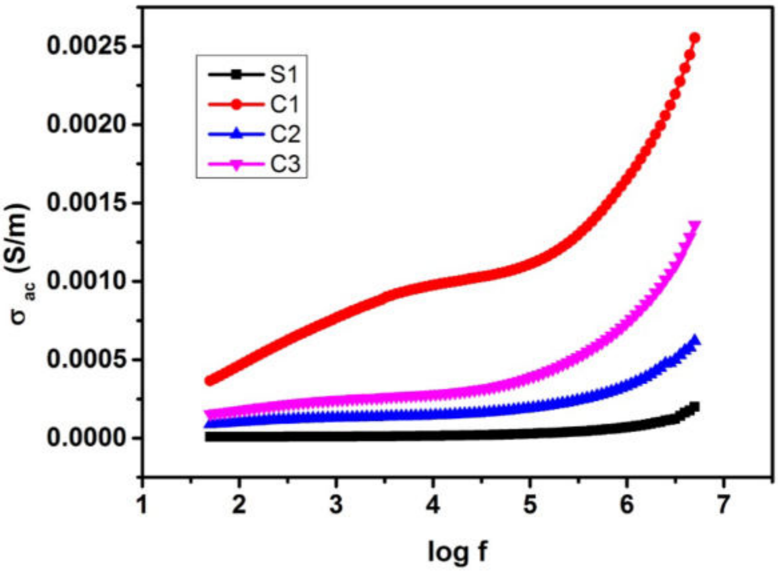

Fig. 6. 24 Variation of AC conductivity with frequency for pure and $NiWO_4$/SnPc nanocomposite samples at room temperature.

6.4 Conclusion

- $NiWO_4$/SnPc nanocomposite samples are successfully prepared by solvent evaporation method by taking three different weight percentages of SnPc with $NiWO_4$.
- From the thermal analysis, it is found that in between 370^{0}C to 545^{0}C decomposition of SnPc takes place. So above 545^{0}C, nanocomposite samples are not in the expected form.
- All the nanocomposite samples are found to have the same crystalline structure as the pure sample. The average crystallite sizes of the composite samples have values higher than that of the pure sample. But by considering the composite samples, there is a decrease in size with the increase in the concentration of SnPc in the composite samples.
- From the HRTEM images, it is found that all samples show polycrystalline nature and SAED patterns confirm the crystalline nature of the samples.

- FT-IR and Raman analysis confirmed the incorporation of SnPc in the $NiWO_4$ lattice to form $NiWO_4$/SnPc nanocomposite.
- From the UV-Vis-NIR spectra, it can be observed that absorbance in the visible region increases with the increase in the concentration of SnPc in the composite samples. Along with that a decrease in absorbance in the UV and IR regions.
- With the increases in weight% of SnPc in the composite, the energy gap is varied. That is the optical bandgap of the pure sample can be modified by SnPc.
- The Colour of emission of the pure sample can be changed from purplish-blue to white by 1 weight% of SnPc in the composite samples.
- The magnetic behaviour of $NiWO_4$ does not change much by the formation of nanocomposite with SnPc.
- Due to the presence of additional delocalized π electrons introduced by SnPc in the nanocomposite samples, the dielectric constant and conductivity are varied.
- The electrical properties of pure $NiWO_4$ can be modified by making nanocomposite with SnPc and that can find applications in electronic fields.

References

[1] D. L. Stern and R. K. Grasselli, J. Catal. **167**, 570 (1997)

[2] R. Sundaram and K. S. Nagaraja, Mater. Res. Bull. **39**, 581 (2004)

[3] P. S. Pandey, N. S. Bhave and R. B. Kharat, Electrochim. Acta **51**, 4659 (2006)

[4] S. Guo, Y. Zhu, Y. Yan, Y. Min, J. Fan, Q. Xu, Applied Catalysis B: Environmental 185 (2016) 315–321.

[5] J. Low, B. Cheng, J. Yu,Applied Surface Science 392 (2017) 658–686.

[6] D. Masih, Y. Ma, S. Rohani, Applied Catalysis B: Environmental 206 (2017) 556–588.

[7] Bogdan ML, Zgierski MZ, Bischoff C, Li M, Hu MY, Zhao J, Martin SW, Alp EE, Scheidt WR. Inorg Chem. 2013;52:9948–53.

[8] Gharaati S, Moghadamb M, Tangestaninejad S, Mirkhani V, Mohammadpoor-Baltork I, Barati B, Sadegh F. Organomet Chem. 2013;741–742:78–82.

[9] Hitha H, Anjaly Jose, Mathew John, Thomas Varghese, Materials Chemistry and Physics 239 **(2019)** 122080.

[10] P. Singh , A. Kaushal , D. Kaur, J Alloys and Compounds 471 (2009) 11.

[11] G. M. Fernandez, A. Martinez-Arias, J. C. Hanson, J. A. Ro-driguez, J. Chem. Rev. 104 (2004) 4063-4104.

[12] R. Di Monte, J. Kaspar, J. Catal. Today 100 (2005) 27-35.

[13] M. Daturi, G. Busca, M. M. Borel, A. Leclaire, P. Piaggio, J. Phys. Chem. B 101 (1997) 4358.

[14] V. V. Fomichev, O. I. Kondratov, Spectrochem. Acta A 50 (1994) 1113-1120.

[15] M. Maczka, J. Kanuza, S. Kojima and J. H. vander Maas, J. Solid state Chem. 158 (2001) 334-341.

[16] J. Hanuza, L. Macalik, Spectrochem. Acta A 43 (1987) 361-373.

[17] H. Wang, F. D. Medina, Y. D. Zhou, Q. N. Zhang, Phys. Rev. B 45 (1992) 10356-10362.

[18] J. M. Quintana-Melgoza, A. Gomez-Cortes, M. Avalos-Borja, React. Kinet. Catal. Lett.76 (2002) 131-140.

[19] M. M. EL-NAHASS, A. M. FARID, H. H. AMER, K. F. ABDEL-RAHMAN, H. A. M.ALI, Optoelectronics and advanced materials – rapid communications Vol. 3, No. 3, March 2009, p. 175 - 180.

[20] Hitha Harshan, Karathan Parakkandi Priyanka, Aikkara Sreedevi, Anjali Jose, Thomas Varghese, Eur. Phys. J. B(2018) 91: 287.

[21] C. Jennings, C, R. Aroca, A.M . Hor, R.O. Loutfy, Spectrochimica Acta Part A: Molecular Spectroscopy, 41(9) (1985) 1095–1099.

[22] R. Aroca, Z. Q. Zeng, J. Mink, Journal of Physics and Chemistry of Solids, 51(2) (1990) 135–139.

[23] D. R. Tackley, G. Dent, W. Ewen Smith, Physical Chemistry Chemical Physics, 2(18) (2000) 3949–3955.

[24] E.A. Ough, J.M. Stillman, Can. J. Chem. 71 (1993) 1891

[25] A. Jan Halvacc, The Technology of Glass and Ceramics-An Introduction, Elsevier, Amsterdam, 1983.

[26] G.A. Kumar, Vinoy Thomas, Gin Jose, N.V. Unnikrishnan, V.P.N. Nampoori, Materials Chemistry and Physics 73 (2~02) 206--2 I I

[27] K.P. Priyanka, S. Sankararaman, K.M. Balakrishna, T. Varghese, Journal of Alloys and Compounds (2017).

[28] S. Cavalcante, M.A.P. Almeida, W. Avansi, R.L.Tranquilin, E. Longo, N.C. Batista, V.R. Mastelaro, M.S.Li, Inorg. Chem. 51, 10675 (2012)

[29] Major MM, Horvath O, Fodor MA, Fodor L, Valicsek Z, Gramp G, Wankmu¨ ller A. Inorg Chem Commun. 2016;73:1.

[30] K.W. Wagner, Ann Phys 40: (1913).817

[31] C.G. Koop, Phys Rev 83 (1951) 121.

[32] S.H. Lee, H.M. Cheong, N.G. Park, C.E. Tracy, A. Mascarenhas, D.K. Benson, S.K. Deb, Solid State Ionics 140 (2001) 135-139

[33] S. Saravanan, C. Joseph Mathai, M. R. Anantharaman, S. Venkatachalam, P. V. Prabhakaran, J. of Appl. Polymer Sci., 91 (2004) 2529-2535.

◆

Chapter - 7

PHOTOCATALYTIC ACTIVITY OF $NiWO_4$, ITS DOPED AND COMPOSITE FORMS

7.1 Introduction

Environmental problems caused by the discharge of significant quantities of highly harmful and toxic contaminants into environmental systems is a consequence of the rapid development of modern industrial society and it is acknowledged as a major crisis all over the world [1]. There is an increased concern among the populace regarding alarming environmental issues and the protection of the environment for sustaining life. So the development of photocatalytic semiconductors for organic pollutant degradation in wastewater has turned into a demanding research area [2]. In particular, it is a great challenge to attain complete degradation of environmental contaminants in low-level concentrations in the course of conventional treatment processes [3]. Photocatalysis has found potential application in the degradation of low-level concentrations of environmental contaminants [4]. A low concentration of coloured organic compounds can result in the colouration of water in an aquatic system. This is harmful to aquatic organisms and plants, as it diminishes photosynthesis and affects the ecosystem [5]. Therefore, colour removal and purification of water have become an ecological concern and are essential for the sustainability of the environment.

On this background, the photocatalytic activity of $NiWO_4$ is a topic of concern. Literature reports [6-8] the photocatalytic nature of $NiWO_4$ under UV irradiation for a long time of exposure. Methylene blue

($C_{16}H_{18}ClN_3S$) and rhodamine blue ($C_{28}H_{31}ClN_2O_3$) are the two industrial dyes used to analyse the photocatalytic activity of the different catalysts. These dyes are toxic materials having synthetic origin with a very complex molecular structure. As these dyes are important agents in printing and textile industries [9] they are released to water bodies as industrial effluents. So the removal of these dyes by the photodegradation reaction is important.

This chapter deals with the study of photocatalytic activity of $NiWO_4$ sample and its different modified forms. These structurally and optically modified forms of $NiWO_4$ is expected to have improved photocatalytic activity. Here photocatalytic activity of pure $NiWO_4$ calcined at 500^0C (S1), $NiWO_4$ doped with 5% of Bi^{3+} ions (B5) and $NiWO_4$/SnPc nanocomposite having 1 weight % of SnPc (C1) under UV light are discussed.

7.2 Synthesis of photocatalysts

The synthesis methods of the selected photocatalyst are already explained in detail in the respective chapters. The synthesis of pure $NiWO_4$ calcined at 500^0C (S1) is explained in *section 3.2*. Synthesis of $NiWO_4$ doped with 5% of Bi^{3+} ions (B5) is given in *section 4.2*. $NiWO_4$/SnPc nanocomposite having 1 weight % of SnPc (C1) is synthesized using the solvent evaporation method. It is explained in detail in *section 6.2*.

7.3 Photodegradation test

The photocatalytic activity of the samples is evaluated using two representatives of organic pollutant dyes, Rhodamine blue (RhB) and Methylene blue (MB) under UV light irradiation.

Typically, 50 mg catalysts are mixed with 100 ml of dye solution containing 1 ppm of dye under ultrasonic treatment for 15 min in dark to get an adsorption-desorption equilibrium between dyes and the photocatalyst. The mixture is irradiated with UV light ($\lambda > 220$ nm) using a 30 W UV lamp, and aliquots are collected at 15 min intervals followed by centrifugation for 10 min. The supernatant solution is analysed using UV-Vis spectrometer (*Shimadzu 2600 UV- Vis spectrophotometer*). Wavelengths of 552 and 664 nm are used to analyse the photocatalytic degradation of RhB and MB respectively. Percentage degradation of dye is calculated using the formula,

$$\% \text{ degradation} = [(\mathbf{A_0}\text{-}\mathbf{A_t})/\mathbf{A_0}] \text{ X } 100, \qquad \mathbf{(7.1)}$$

where $\mathbf{A_0}$ is the absorbance of dye at the initial stage and $\mathbf{A_t}$ is the absorbance of dye at time t. The rates of photocatalytic reactions are obtained by drawing ln($\mathbf{C_0/C_t}$) *vs.* irradiation time graph. Another reaction is carried out using all the samples under the same reaction conditions in dark.

An indirect scavenger method is employed to examine the roles of active species such as $OH^{\bullet}$ and $O_2^{-\bullet}$ [10]. For this, isopropyl alcohol (IPA) and benzoquinone (BQ) are used as scavengers for $OH^{\bullet}$ and $O_2^{-\bullet}$ respectively [10-13]. The absorption spectra of the dye solutions with the scavengers are also obtained. From this absorbance data, % of degradation of RhB and MB dyes in 90 min is calculated and these results are compared with the results obtained without scavenger to understand the role of active species in pollutant degradation.

7.4 Results and discussion

7.4.1 Photocatalytic activity of $NiWO_4$ sample

The photocatalytic activity studies of $NiWO_4$ samples calcined at 500, 600 and 700^{0}C are carried out using RhB and MB dyes under UV light irradiation. Among these three samples, $NiWO_4$ sample calcined at 500^{0}C (S1) shows high photocatalytic activity compared to others. In this section photodegradation studies of RhB and MB dyes under UV light irradiation with S1 as photocatalyst are discussed. Fig. 7.1 represents the absorption spectra of RhB and MB dyes under the effect of catalyst S1. From the graph, it is found that absorbance of both dyes decreases with the increase in irradiation time. It shows the degradation of dyes by the irradiation of UV light with the presence of catalyst S1. The sample which is kept under dark conditions shows no dye degradation.

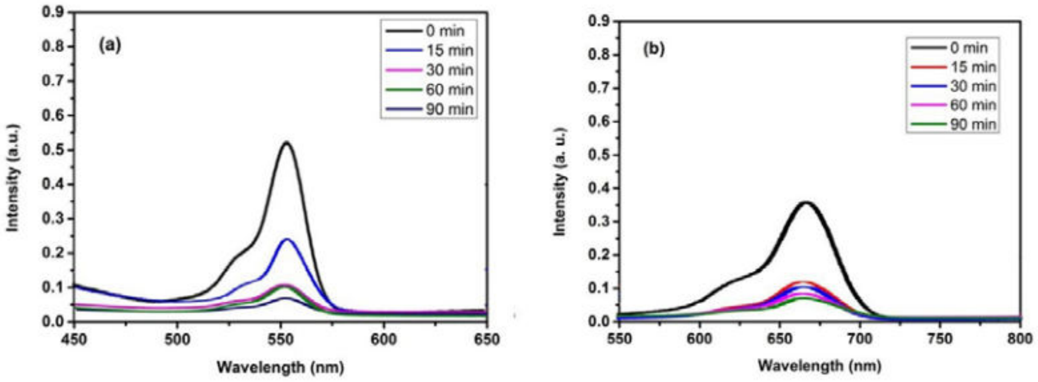

Fig. 7.1 Absorbance spectra of (a) RhB and (b) MB during decolourization over catalyst S1.

To analyse the kinetics of the photocatalytic reaction, the curve of $\ln(C_0/C_t)$ *vs.* irradiation time is drawn. By linear fitting the curve and finding the slope of the line, the reaction rate constant is calculated for the sample. Fig.7.2 represent $\ln(C_0/C_t)$ *vs.* irradiation time curves for photo-degradation of RhB and MB. From the graphs, it can be seen that both dye degradation follow pseudo-first-order kinetics. The rate constants for the photocatalytic degrading of RhB and MB are 0.0123 and 0.0027 min^{-1} respectively.

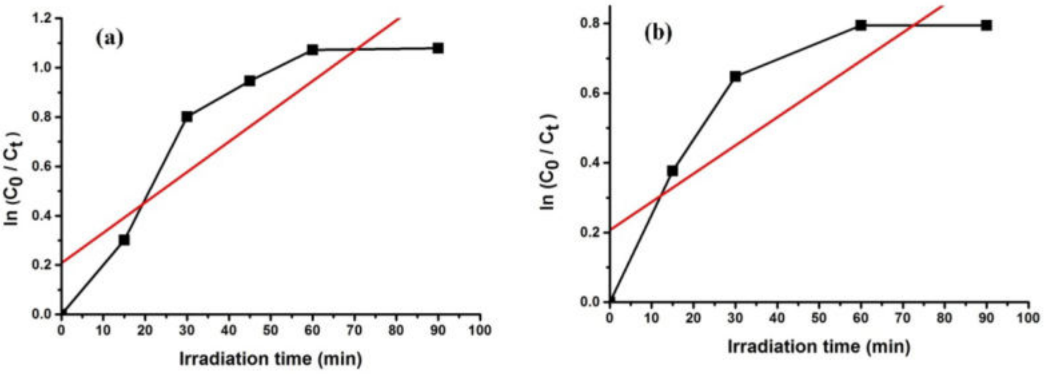

Fig. 7.2 Plot of ln (C_0/C_t) *vs.* irradiation time for degradation of (a) RhB and (b) MB for catalyst S1.

It is interesting to identify the plausible pathway for the degradation of organic pollutants in semiconductor photocatalytic degradation. When a semiconductor photocatalyst is irradiated by light energy which is equal to or greater than the bandgap energies, it excites the electrons from the valence band to conduction band. This results in the formation of a positive hole in the VB and an electron in CB. The photo-generated positive holes react with a surface hydroxyl group (–OH), or an adsorbed water molecule to produces hydroxyl ($OH^{\cdot}$) radical. This $OH^{\cdot}$ is a strong oxidizing agent. The electron in the CB reacts with electron acceptors such as O_2 adsorbed on the surface of the catalyst or dissolved in water to produce superoxide radical anion $O_2^{-\cdot}$ [10, 14]. Subsequently, the dyes react with these highly potential radicals. These reactions result in the generation of a range of intermediates followed by the complete mineralization of the dye.

The proposed mechanism of the photocatalytic degradation of RhB by S1 can be represented as:

$NiWO_4 + h\nu \longrightarrow NiWO_4^{\bullet} + e^- + h^+$ **(7.2)**

$h^+ + H_2O \longrightarrow OH^{\bullet}$ **(7.3)**

$e^- + O_2 \longrightarrow O_2^{-\bullet}$ **(7.4)**

$OH^{\bullet} + O_2^{-\bullet} + RhB/MB \longrightarrow$ Degradation products **(7.5)**

In the case of RhB and MB dye degradations, the efficiency of the catalyst S1 is 66% and 54.8 % respectively.

Scavenger test is carried for the catalyst S1 to study the active species involved in the photodegradation of dyes. The percentage of degradation of the dyes with and without scavengers are determined, and the results are presented in Fig. 7.3.

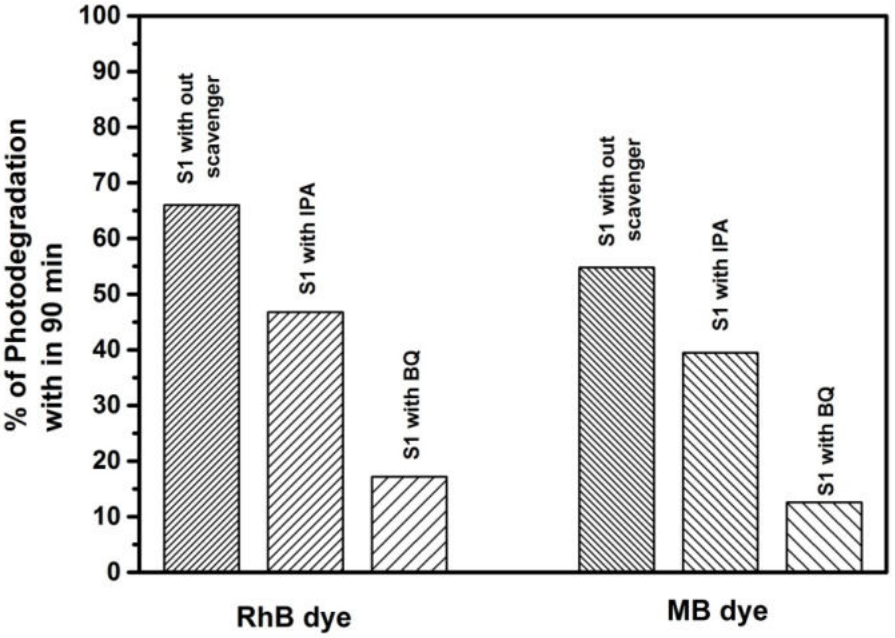

Fig. 7. 3 Comparison of percentage of degradation of RhB and MB over the surface of the catalyst S1 with and without scavengers.

From the graph, it can be found that in the presence of catalyst S1 the dye solution without the scavenger shows high degradation efficiency. In the presence of scavengers (IPA and BQ) the degradation efficiency is reduced. It indicates that the addition of IPA and BQ reduced the degradation efficiency. Since IPA and BQ eliminate the active species involved in the dye degradation ($OH^{\cdot}$, $O_2^{-\cdot}$), the degradation efficiency will be reduced. From the graph, it can be interpreted that superoxide free radicals play a major role in the catalytic action.

7.4.2 Photocatalytic activity of Bi-doped $NiWO_4$ samples

Photocatalytic activity of Bi^{3+} doped $NiWO_4$ samples is analysed using RhB and MB under the dark and UV irradiated conditions. The $NiWO_4$ sample doped with 5 molar% of Bi^{3+} (B5) shows high photocatalytic activity compared to other doped samples under UV irradiation. In this section, the photocatalytic activity of $NiWO_4$ sample doped with 5 molar% of Bi^{3+} is discussed. Fig 7.4 represents the absorption spectra of RhB and MB under the effect of catalyst B5. From the graph, it can be seen that both dyes show degradation in the presence of B5 under UV irradiation. The sample kept in dark show no degradation. Fig. 7.5 represents $\ln(C_0/C_t)$ *vs.* irradiation time graph. From the slope of the graph photodegradation rates are calculated for both the dyes. Degradation of both the dyes follow pseudo-first-order kinetics. The rate constants for the degradation of RhB and MB under the effect of catalyst B5 are 0.020 and 0.0057 min^{-1} respectively. In the case of RhB and MB dye degradations, the efficiency of the catalyst B5 is 86.71% and 75.21 % respectively.

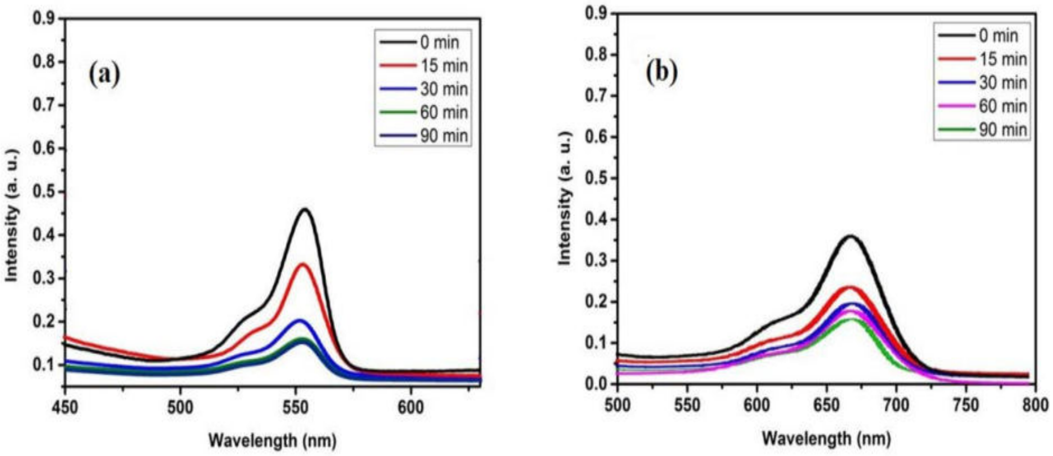

Fig. 7.4 Absorbance spectra of (a) RhB and (b) MB during decolourization over catalyst B5.

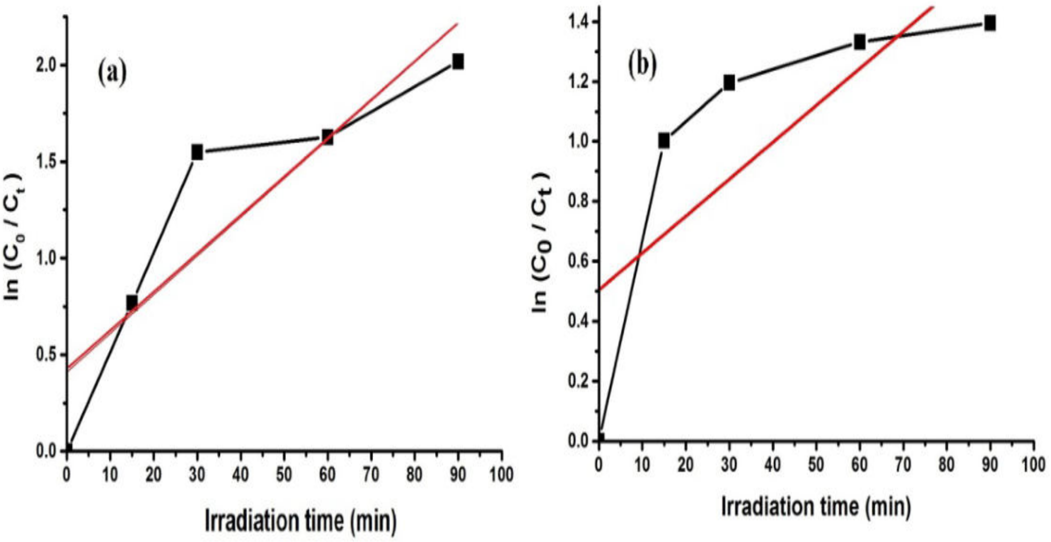

Fig. 7.5 Plot of ln (C_0/C_t) *vs.* irradiation time for degradation of (a) RhB and (b) MB for the catalyst B5.

In Section 7.3.1, the photocatalytic activity of the sample S1 is discussed. Comparing with S1, B5 shows high photocatalytic activity. Photocatalytic activity mainly depends on the separation efficiency of photogenerated electron and hole. This indicates that the B5 sample holds the highest separation efficiency of photo-generated charges during photocatalytic decolourization. The separation efficiency of photo-generated charges increases as Bi content increases [14-16]. In section 5.3.2, the structural modifications of S1 when doped with Bi^{3+} are discussed. The sample B5 has a lower particle size than S1. So surface area of B5 may be increased compared to S1. Since an increase in surface area can result in an enhancement of photocatalysis, B5 shows higher photocatalytic activity than sample S1. The schematic representation of photocatalytic decolourization of RhB is presented in Fig. 7.6.

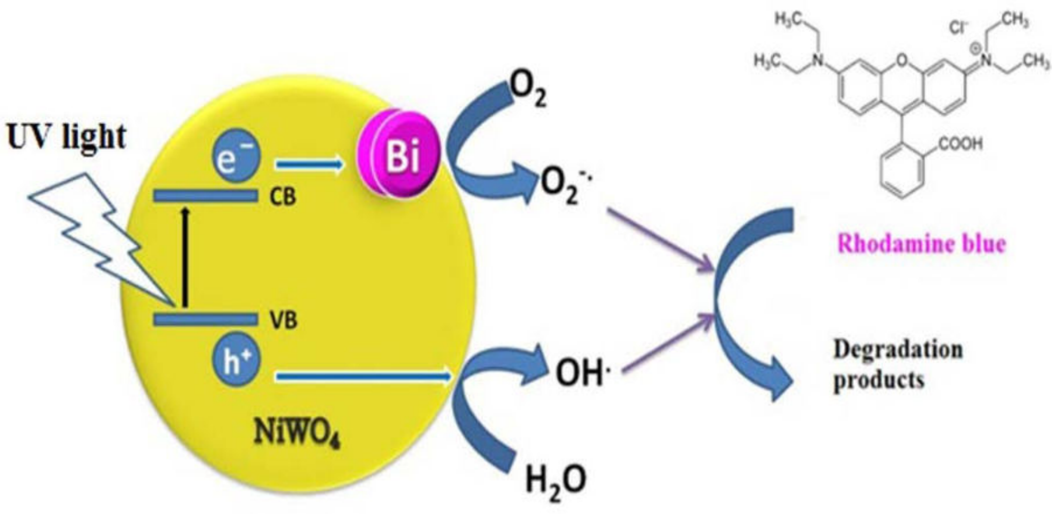

Fig. 7.6 Schematic representation of photocatalytic decolourization of RhB.

Scavenger test is carried out to analyse the active species involved in the photocatalytic degradation of RhB and MB dye. Photodegradation efficiency with and without scavengers over the surface of the catalyst B5 is presented in Fig. 7.7. The figure shows that the dye without a scavenger showed the greatest degradation. It is found that on the addition of scavengers for $OH^{\cdot}$ and $O_2^{-\cdot}$, dye degradation is suppressed. These results indicate that $OH^{\cdot}$ and $O_2^{-\cdot}$ species which are formed during UV-light irradiation play important roles in dye degradation [14]. As shown in Fig. 7.7, after adding IPA, degradation is suppressed rapidly both in the case of RhB and MB dyes. This indicates that $OH^{\cdot}$ is the main active species in the photocatalytic decolouration of dyes. By adding BQ, the efficiency of photocatalytic decolourization of dyes decreases, demonstrating that $O_2^{-\cdot}$ plays the second important role in photocatalytic decolourization of the dye solutions [14].

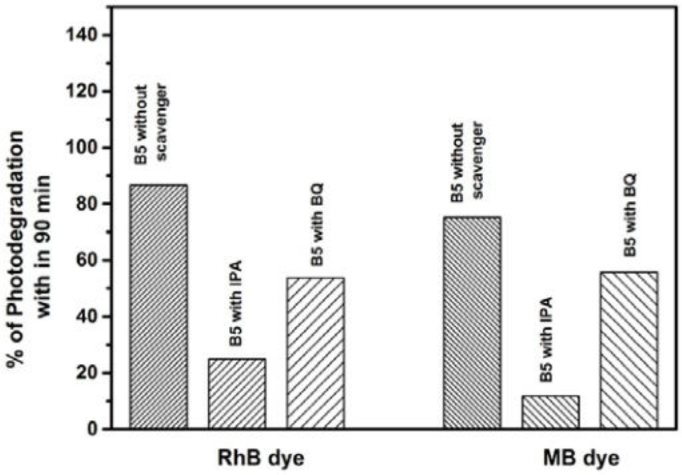

Fig. 7.7 Comparison of percentage of degradation of RhB and MB over the surface of the sample B5 with and without scavengers.

7.4.3 Photocatalytic activity of $NiWO_4$/SnPc nanocomposite samples

Photocatalytic activity of $NiWO_4$/SnPc nanocomposite samples namely C1, C2 and C3 are analysed. Among these samples, C1 shows improved photocatalytic activity than the pure sample S1. In section 6.3.3 optical properties of nanocomposite samples are discussed. Studies suggest that composite sample C1 can have good photocatalytic activity compared to other composite samples. Fig. 7.8 shows absorbance spectra of aqueous RhB dye over the surface of C1 under UV irradiation for 90 min.

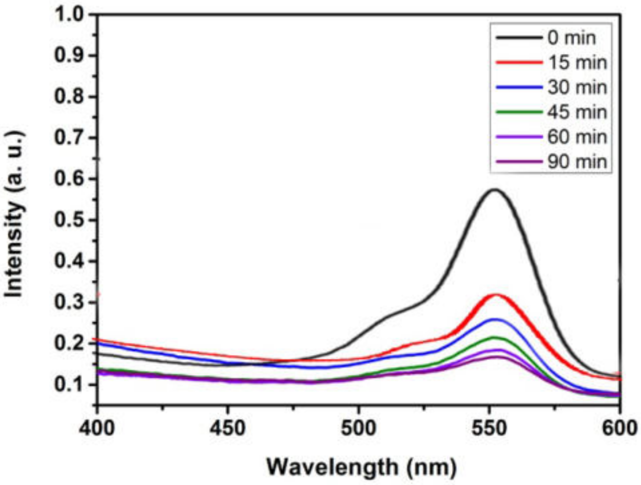

Fig. 7.8 Absorbance spectra during RhB decolourization over catalyst C1.

Fig.7.9 represents the graph between ln(C_0/ C_t) *vs.* irradiation time for the RhB dye degradation over the surface of catalyst C1. The $NiWO_4$/SnPc composite sample show pseudo-first-order reaction kinetics. The rate constants for the photocatalytic reactions are found to be 0.0127 min^{-1}. With C1 as a catalyst, RhB degradation is 70.88% within 90 min of UV irradiation. This degradation percentage is high as compared with the dye degradation with catalyst S1.

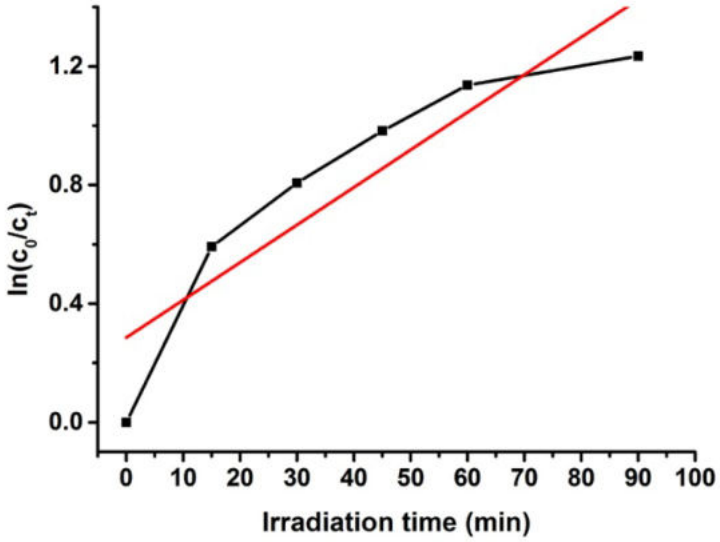

Fig. 7.9 Plot of ln (C_0/C_t) *vs.* irradiation time for degradation of RhB of catalyst C1.

The proposed mechanism of the photocatalytic degradation of RhB by $NiWO_4$/SnPc nanocomposite sample can be chemically represented as:

$h\nu + SnPc \longrightarrow SnPc^*$ **(7.6)**

$SnPc^* + O_2 \longrightarrow SnPc + {}^1O_2$ **(7.7)**

$SnPc^* + NiWO_4 \longrightarrow SnPc^* + NiWO_4(e^-)$ **(7.8)**

$NiWO_4(e^-) + (O_2 \text{ or } {}^1O_2) \longrightarrow NiWO_4 + O_2^{-\cdot}$ **(7.9)**

$O_2^{-\cdot} + H_2O \longrightarrow HO_2^{\cdot} + OH^-$ **(7.10)**

$HO_2^{\cdot} + H_2O \longrightarrow OH^{\cdot}$ **(7.11)**

$OH^{\cdot} + O_2^{-\cdot} + RhB \longrightarrow$ Degradation products **(7.12)**

$SnPc^* + RhB \longrightarrow$ Degradation products **(7.13)**

In Section 7.3.1, the photocatalytic activity of the sample S1 is discussed. The photocatalytic activity of S1 can be modified by making nanocomposite with SnPc. Improved photocatalytic activity of nanocomposite samples is due to the formation of additional free radicals due to the presence of SnPc. Moreover, SnPc itself changes to a free radical so that degradation of dye can be taken place. The $NiWO_4$/SnPc nanocomposite sample with 1 wt% of SnPc is suggested as a potential candidate to remove organic pollutants present in water by room temperature photocatalysis.

To identify the major active species involved in the photo-degradation reaction of the dye, the scavenger test is conducted. IPA and BQ are used to find the role of $OH^{\cdot}$ and $O_2^{-\cdot}$ in the photodegradation of the dye. Photodegradation efficiency is calculated with and without scavenger. Fig. 7. 10 represents the dye degradation efficiency in 90 min with and without scavenger. The results show that the solution without scavengers shows high dye degradation compared to the solutions with scavengers. The percentage of dye degradation is less for the solution with BQ. This result points to the fact that the primary active species involved in the RhB degradation are $O_2^{-\cdot}$ and $OH^{\cdot}$.

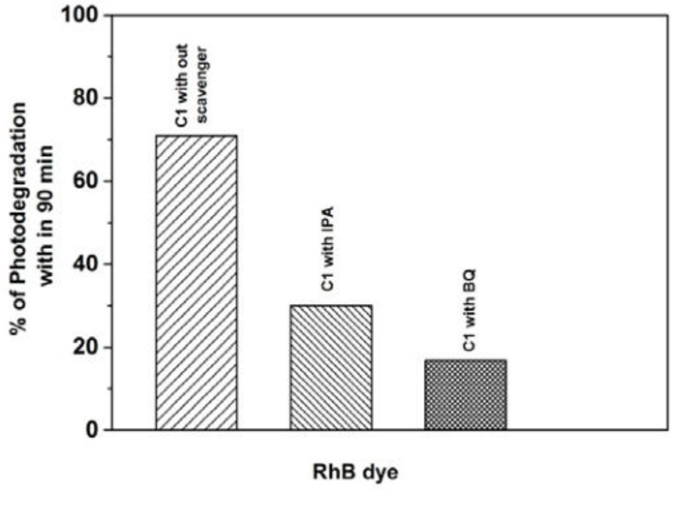

Fig. 7.10 Comparison of percentage of degradation of RhB over the surface of the sample C1 with and without scavengers.

7.5 Conclusion

- Photocatalytic activity of pure $NiWO_4$ (S1), 5% Bi-doped $NiWO_4$ (B5) and $NiWO_4$/SnPc (1wt%) nanocomposite (C1) are studied using organic pollutant dyes.
- Sample S1 shows dye degradation efficiency of 66% and 54.8 % for RhB and MB dyes respectively.
- The photocatalytic activity of $NiWO_4$ (S1) is improved by doping it with 5 molar % of Bi. The efficiency of the catalyst B5 for the degradation of RhB and MB dyes are 86.71 and 75.21 % respectively.
- Formation of nanocomposite with SnPc also exhibits improved photocatalytic activity, with the degradation of 71%.
- From scavenger test it is found that $OH^{\cdot}$ and $O_2^{-\cdot}$ are the main active species involved in the photo degradation of organic dyes.

References

[1] J. Han, X. Z. Zheng, L. W. Zhang, H. B. Fu, J. M. Chen, Environ. Sci. Nano. 4 (2017) 834–842.

[2] K.P. Priyanka, S. Sankararaman, K.M. Balakrishna, Thomas Varghese, J. Alloys and Compounds 720 (2017) 541-549

[3] G. Jiang, M. Lan, Z. Zhang, X. Lv, Z. Lou, X. Xu, et al, Environ.Sci. Technol. 51 (2017) 7599–7605

[4] T. Xiong, H. J. Zhang, Y. X. Zhang, F. Dong, Chin. J. Catal.8 (2015) 784–788

[5] S. Senthilvelan, V. L. Chandraboss, B. Karthikeyan, L.atanapatham, M. Murugavelu, Materials Science in Semiconductor Processing 16 (2013) 185–192

[6] X. A. Lo´pez, A. F. Fuentes, M. M. Zaragoza, J. A. Di´az Guille´n, J. S. Gutie´rrez, A. L. Ortiz, V. Collins-Marti´nez, Int. J. Hydrogen Energy 41 (2016) 23312–23317.

[7] T. Montini, V. Gombac, A. Hameed, L. Felisari, G. Adami, P. Fornasiero, Chem. Phys.Lett., 2010, 498, 113–119.

[8] M. M. Mohamed, S. A. Ahmed, K. S. Khairou, Appl. Catal.B, 150–151 (2014) 63–73.

[9] D. L. Postai, C. A. Demarchi, F. Zanatta, D. C. C. Melo, C. A. Rodrigues, Alexandria Engg. J., 55 (2) (2016) 1713-1723.

[10] J.Cao, B.Xu, H.Lin, B.Luo, S.Chen, Chem. Eng.J.185 (2012) 91–99

[11] J. Cao, B. Xu, H. Lin, B. Luo, S. Chen, Dalton Trans.41 (2012) 11482–11490

[12] T. B. Li, G. Chen, C. Zhou, Z. Y. Shen, R. C. Jin, J. X. Sun, Dalton Trans.40 (2011) 6751–6758

[13] M. Yin, Z. Li, J. Kou, Z. Zou, Environ. Sci. Technol.43 (2009) 8361–8366

[14] H. Hitha, Mathew John, Anjaly Jose, Soumya Kuriakose, Thomas Varghese, Journal of Solid State Chemistry 295 (2021) 121892.

[15] P. D. Kanhere,J. Zheng, Z. Chen, J. Phys. Chem. C 115 (2011) 11846–11853.

[16] X.T. Pian, B.Z. Lin, Y. L. Chen, J. D. Kuang, K. Z. Zhang, L. M. Fu, J. Phys. Chem. C 115 (2011) 6531–6539.

◆

Chapter - 8

SUMMARY AND SCOPE FOR THE FUTURE WORK

8.1 Summary of the present work

The present work describes the synthesis, properties and photocatalytic application of nanostructured nickel tungstate. The effect of doping by a transition metal and a semimetal on the structural, optical, magnetic and electrical properties of nickel tungstate is studied in detail. The formation of a nanocomposite structure of nickel tungstate and tin phthalocyanine and the modification in the various properties of nickel tungstate by composite formation is also studied. In addition, a focus is given to the photocatalytic activity of pure nickel tungstate and its doped and composite forms.

Nanocrystalline nickel tungstate particles are successfully synthesized by a simple direct chemical precipitation method. The effect of calcination temperature on the structural, optical, magnetic and electrical properties of the synthesized samples are studied. The average crystallite size of the nickel tungstate nanoparticles is found to be increased with an increase in calcination temperature. A reduction in the micro-strain is also observed with the increase in calcination temperature. The surface morphology is also modified with calcination temperature. Spherical shaped particles changed their shapes to cube-like shape. FT-IR and Raman spectra confirm the presence of characteristic bonds of nickel tungstate. UV-VIS-NIR analysis revealed the absorption properties of $NiWO_4$ samples. $NiWO_4$ absorbs all range of wavelengths due to its complex electronic structure. Most intense absorption is found in the UV region. Both direct and indirect optical bandgap may be present in $NiWO_4$. The bandgap is found to be decreasing with the increase in calcination temperature. The $NiWO_4$ shows a purplish-blue emission and calcination temperature affect the intensity of PL emission. The sample calcined at lower temperature show less PL emission and it can be used for photocatalytic application. The important idea regarding the magnetic property of $NiWO_4$ is obtained from VSM studies. It is found that nickel tungstate shows paramagnetic behaviour at room temperature. Electrical properties of $NiWO_4$ samples show significant changes with the change in calcination temperature. While the conduction mechanism remains unchanged. AC conductivity is mainly due to the polaron hopping mechanism and it obeys Jonscher's power law.

Doping of $NiWO_4$ with another transition metal cobalt in different doping concentrations leads to the modification of structural, optical, magnetic and electrical properties of $NiWO_4$. Cobalt ions are easily incorporated into the nickel tungstate lattice and lead to a decrease in the average crystallite size of the sample. Along with that reduction in micro-strain is also observed. The particle size reduction is also evident from the TEM images. Surface morphology is found to be almost similar for pure and doped samples. FT-IR and Raman spectra confirm the successful incorporation of Co ions into the $NiWO_4$ lattice. UV-VIS-NIR absorption spectra of Co-doped $NiWO_4$ samples show significant changes. An additional peak is formed corresponding to the Co absorption and the intensity of this peak increases with the increase in Co concentration. The energy gap of the Co-doped $NiWO_4$ varies with the varying molar concentration of cobalt. It can be explained based on the Burstein- Moss effect. Variation in dopant concentration also affects the PL emission intensity. The basic paramagnetic nature of the $NiWO_4$ is not changed by the introduction of a magnetically active Co into the $NiWO_4$ lattice. The change in the electronegativity of Ni and Co play an important role in the electrical properties of Co-doped nickel tungstate. Along with that oxygen-deficient nature of the doped samples also play a key role in the conductivity of Co-doped $NiWO_4$ sample. Cobalt doping in nickel tungstate improved the dielectric constant and conductivity, and reduced the dissipation factor of nickel tungstate. So Co-doping helps to tune the electrical properties of nickel tungstate.

Doping with a semimetal Bi^{3+} which is having a larger radius than nickel changed the structural, optical, magnetic and electrical properties of nickel tungstate nanoparticles. The average crystallite size increased for lower concentration of dopant. For higher doping concentrations, average crystallite size is found to be reduced. TEM analysis of Bi- doped $NiWO_4$ samples revealed the particle size variation and polycrystalline nature of the samples. Similar to pure sample, doped samples also show agglomeration and no significant change in morphology is observed for the Bi- doped $NiWO_4$ samples from FE-SEM analysis. FT-IR and Raman spectra confirm the incorporation of Bi^{3+} ions into the $NiWO_4$ lattice as there is a slight change in the characteristic peaks in the spectra of doped samples. UV-VIS-NIR spectra of Bi-doped nickel tungstate show additional peaks in the UV region corresponding to Bi^{3+} ions. The change in bandgap is observed with variation in Bi concentration. This may be due to the involvement of Bi in the formation of the valance band and conduction band. Doping with Bi also affects the PL emission of nickel tungstate. For the highest doping concentration, an emission peak corresponding to Bi is observed at 605 nm. PL analysis indicates that the photoluminescence emission of $NiWO_4$ can be tuned by Bi-doping. Magnetic properties of $NiWO_4$ show not much variation by Bi- doping. Bi-doped nickel tungstate show improved dielectric and conduction properties compared to the pure sample. This is due to the cation vacancy introduced into the $NiWO_4$ lattice by Bi^{3+} doping.

So the introduction of a heavier dopant ion into the $NiWO_4$ lattice changed the structural, optical, magnetic and electrical properties of $NiWO_4$.

Nickel tungstate is coupled with an organic compound Tin phthalocyanine to form a composite so that the structural and optical properties of $NiWO_4$ can be modified. The solvent evaporation technique is employed for the synthesis of nanocomposite samples. The thermal stability of the nanocomposite samples are analysed by thermal analysis. The nanocomposite samples are found to be thermally stable below 545^0C. The average crystallite size of the pure sample is found to be increased by the formation of nanocomposite with SnPc. Along with that, there is an increase in micro-strain too. The particle size variation is evident from the TEM images. The highly agglomerated and cluster forming nature of the samples are revealed from FE-SEM analysis. From FT-IR and Raman analysis the successful incorporation of SnPc into the $NiWO_4$ lattice is identified as the characteristic vibrations of SnPc are seen in both the spectra. UV-VIS-NIR analysis reveals the increase in absorption in the visible region with an increase in SnPc concentration. Presence SnPc tune the PL emission of the nickel tungstate. The nanocomposite sample with lowest SnPc concentration shows white emission. SnPc in the nanocomposite does not alter the magnetic nature of the nickel tungstate. $NiWO_4$/SnPc is found to be thermal stable below 545^0C, sintering is done at low-temperature. The low sintering temperature and the presence of delocalized π electrons which is introduced by SnPc, modify the electrical properties of nanocomposite samples compared to the pure sample.

Photocatalytic activity of $NiWO_4$, its doped and composite forms under UV irradiation are also studied. The photocatalytic activity is studied using RhB and MB dyes. The highest photocatalytic activity is found for the Bi-doped $NiWO_4$ sample. The second-highest efficiency is found for $NiWO_4$/SnPc nanocomposite with 1 weight percentage SnPc. Pure $NiWO_4$

has the lowest efficiency. So the photocatlytic activity of pure $NiWO_4$ can be modified by doping with Bi^{3+} and forming nanocomposite with SnPc of suitable weight percentage. For all the samples, the kinectics of dye degradation follow pseudo-first-order kinetics. Scavenger test is conducted to identify the reactive species involved in the dye degradation reaction. With these informations possible reaction pathways are propossed.

In short, the present study comprises the analysis of the properties of pure nickel tungstate nano particles, its doped and composite forms. The photocatalytic activity of the samples are also studied.

8.2 Major findings of the study

The main outcomes of the present research are listed below.

- Nanocrystalline $NiWO_4$ samples are successfully synthesized by direct chemical precipitation route.
- The structural, optical, magnetic and electrical properties of nanocrystalline nickel tungstate can be modified by changing the calcination temperature.
- Doping with cobalt changes the structural properties of nickel tungstate significantly and this results in the modification of optical and electrical properties.
- High values of dielectric constant and AC conductivity can be achieved by doping of $NiWO_4$ with suitable concentration of cobalt.
- Bismuth doping in $NiWO_4$ results in structural variations and it also leads to the extended absorbance in the UV range.
- Absorption of $NiWO_4$ in the visible range can be modified by incorporating SnPc with it to form a nanocomposite.
- Photoluminescence properties of $NiWO_4$ can be varied by the formation of nanocomposite with SnPc. Sample having 1wt% of SnPc shows white emission.

- The magnetic property of $NiWO_4$ remains unaltered by doping or nanocomposite formation.
- Photocatalytic properties of $NiWO_4$ can be improved with Bi-doping or making nanocomposite with SnPc.

8.3 Scope for the future work

The work presented in this thesis can be extended in quite a few directions and are briefly discussed here.

- Literature reports the sensing applications of nickel tungstate nanoparticles. Further studies are needed for the gas sensing applications of $NiWO_4$ samples.
- Cobalt doped nickel tungstate are reported to have electrochemical applications. So the electrochemical properties of Co-doped $NiWO_4$ are to be explored.
- A composite of bismuth tungstate and nickel tungstate are to be made so that bandgap of $NiWO_4$ can be tuned to visible range, and hence studies based on visible light driven photocatlytic activity can be done.
- Literature reports the application of $NiWO_4$ as an electrode material for super capacitors. Detailed studies on the electrochemical properties of $NiWO_4$ are needed to tune $NiWO_4$ for the fabrication of supercapacitors.
- Dependance of photocatalytic activity on the pH of the medium can be studied.

◆